Imperial College London
Department of Physics

RFQ DESIGN
FOR PAMELA INJECTOR

Matthew Joseph Easton

September 2011

Supervised by Dr. Juergen Pozimski

Submitted in part fulfilment of the requirements for the degree of
Doctor of Philosophy in Physics of Imperial College London
and the Diploma of Imperial College

Declaration

I hereby certify that all material in this thesis which is not my own work has been properly acknowledged.

M J Easton

Abstract

This thesis describes a new design method for a radio frequency quadrupole (RFQ), and its application to the first stage of acceleration for carbon ions in the *PAMELA* injector.

Radiotherapy is a valuable form of cancer treatment, but current methods using photons or electrons make it difficult to deliver an adequate dose to the tumour without damaging healthy surrounding tissue and organs. Charged hadron beams, such as protons and carbon, deposit most of the dose at the Bragg peak, which can be aligned with the tumour. This allows higher doses to treat the cancer while minimising damage to healthy surrounding tissue and organs.

The *PAMELA* project (part of the *BASROC* consortium) aims to design new charged particle therapy (CPT) facilities using non-scaling fixed-field alternating-gradient accelerators (ns-FFAGs). This new technology offers significant advantages over both cyclotrons and synchrotrons for CPT. The injector for the *PAMELA* FFAG accelerator includes separate pre-acceleration chains for protons and carbon ions, culminating in a shared injection system into the first FFAG ring. Carbon ions are pre-accelerated by an RFQ and a short linear accelerator (linac).

This thesis details the creation of an integrated system of software packages and custom code, which facilitates the design of RFQ vane tips, utilising computer-aided design (CAD) models for both simulation and manufacture, accurate multi-physics modelling of the electric field and particle tracking simulations. This design process is described, along with benchmark results for the *Front-End Test Stand* (*FETS*) RFQ and application of the code in optimising a new RFQ design for *PAMELA*.

Contents

Appendices

List of Figures

List of Tables

1 Introduction

The treatment of cancer is an important area of science that is constantly under development. Although radiotherapy is a vital component of this treatment, the radiation used causes many side-effects and is not universally effective, as there are types of cancer and locations in the body for which conventional radiotherapy cannot be used, or has limited utility. The application of the accelerating structure described in this thesis is for advanced radiotherapy using carbon ion beams. Chapter 2 provides a brief introduction to the subject of *charged particle therapy* (CPT), using beams of protons or ions of various species.

The charged-particle beams required for cancer treatment are produced by particle accelerators. Chapter 3 introduces some basic accelerator concepts and the major classes of accelerating structures, and describes their application to CPT. A glossary of terms and a general introduction for newcomers to the topic of Accelerator Physics are provided in § 3.1.

The particular accelerator for which the work of this thesis was developed is called the *Particle Accelerator for MEdicaL Applications*, or *PAMELA*. This project is part of an initiative by the *British Accelerator Science and Radiation Oncology Consortium* (*BASROC*) to develop a next-generation CPT facility in the UK, using *non-scaling FFAG* technology (an introduction to this technology is given in § 3.5), and has just completed the initial design phase. An introduction to the *PAMELA* project, the medical requirements of the accelerator and the translation into physical design requirements are given in Chapter 4. The subject of this thesis is part of the injector chain for the main *PAMELA* accelerator, and the requirements of this injector system are set out in § 4.4.

A team of accelerator physicists at Imperial College London have been working on the design of the injector for the *PAMELA* FFAG. This design work is described in Chapter 5, including an evaluation of the various pre-accelerator options (§ 5.1), the proposed injector design (§ 5.2) and an introduction to the component whose design is the main concern of this thesis, the *radio-frequency quadrupole* (RFQ), in § 5.3.

An RFQ uses an electrical quadrupole to produce a focusing force in one plane and a defocusing force in another, and oscillates this field at radio frequencies to produce alternating-gradient focusing. Modulations along the length of the RFQ also provide a longitudinal force that is used for bunching and accelerating the beam. An RFQ is used as the first stage of acceleration, as it is efficient in space and energy consumption for low energy acceleration. The next stage of acceleration typically uses a linear accelerating structure (*linac*), which is more efficient for medium energy beams. The theoretical background for the RFQ design process is introduced in Chapter 6.

The design method used for this thesis was an integrated computer design and simulation process. Chapter 7 describes the development of this process, and its application to the *PAMELA* project. A set of parameters that describe an RFQ are input into a computer-aided design (CAD) package to automatically generate a CAD model, which can then be used for both simulation and automated mechanical manufacture. This model is then connected to an electromagnetic solver, which produces a field map describing the field between the tips of the vanes of the RFQ. This field map in turn is used as an input for a particle tracking program, which simulates the beam in the model RFQ. The simulations are analysed by code, and numerical and graphical results are returned to the user.

This new simulation process has been applied to a series of RFQ designs for two accelerator projects: *PAMELA* and the *Front-End Test Stand* (*FETS*). The results of these simulations are presented in Chapter 8. Numerical and graphical results are detailed and discussed, and the stages of development of a working RFQ design for *PAMELA* are described. The main body of work for this thesis comprises the method and results presented in Chapter 7 and Chapter 8, respectively. Chapter 9 suggests future work to further develop the simulation process and to advance the design of the *PAMELA* RFQ. Chapter 10 summarises the simulation results and presents the final conclusions of this thesis.

Conventions

In this thesis, the term *charged particle therapy* (CPT) has been used to describe the kind of treatment discussed. Over time, many different terms have been used, but CPT is currently advised for proton and carbon therapy. Referring to the particles as charged excludes neutron therapy, which is included by alternative terms such as *hadron therapy* (HT). Neutron therapy produced significantly inferior results compared to proton therapy, and the charged nature of the particles used in CPT distinguishes the mechanism of ionisation from neutral interactions. CPT also has the advantage of avoiding terms such as hadrons, which are better known to physicists than to medical staff and the general public.

Online resources

An electronic version of this thesis is available from the author, and at the time of publication can be found at:

`http://www.matteaston.net/thesis.pdf`.

The code used for simulating the RFQ is available under the GNU Public Licence—although commercial software packages are also required—and at the time of publication can be found as a community project at:

`https://launchpad.net/modelrfq`.

2 Charged Particle Therapy

Charged particle therapy (CPT) is a method of treating cancer with charged hadron beams.

This chapter will describe some of the mechanisms of tumour control through radiotherapy (§ 2.1), then explain how CPT modifies the process of radiotherapy, and the advantages and disadvantages of using charged hadrons (§ 2.2). The rest of the chapter discusses existing and proposed treatment centres (§ 2.3), and the initiative in the UK for developing CPT (§ 2.4), organised by the *British Accelerator Science and Radiation Oncology Consortium* (*BASROC*), among others.

2.1 Radiotherapy

Charged particle therapy (CPT) is a subset of radiotherapy (RT), which uses radiation from external particle beams or internal radiation sources to cause damage to cancer cells. Radiotherapy is one of three modalities that are used, often in conjunction with one another, to try to remove cancer cells from the body. In some developed countries, radiotherapy is part of the treatment plan for up to 60% of all cancer patients [1, p. 21].

The most effective modality, defined by long-term survival rates, is surgery, removing the cancerous tumours by cutting them out of the body [2, p. 1]. The second most effective is radiotherapy, killing the cancer cells by irradiation. The final modality is chemotherapy, using targeted drugs to kill the cancer cells. Different types of cancer respond to different treatments, so the continuing development of all three modalities is essential. CPT is an important advance in the field of radiotherapy, providing increased dose to tumour cells with reduced dose to normal cells (see § 2.2).

Conventional radiotherapy uses photons or electrons to damage cancerous cells by ionising atoms within the cells. *Direct damage* to DNA can occur when ionisation occurs within DNA molecules. The *indirect effect* of ionised molecules on DNA is also important: ionisation of atoms within the cell ejects electrons, which interact with other atoms and cause secondary ionisation. Ionised water molecules, H_2O^+, can react with other water molecules to produce OH radicals, which are highly reactive, and other similar reactions can also damage DNA [3, p. 286].

Reaction of a biological system can be classed into three phases by the different timescales of these distinct responses. The *physical* phase lasts in the order of 10^{-12} seconds, and involves the passage of the charged particles across the cell, and the resultant ionisation. The *chemical* phase can last several seconds, and includes responses of the ionised atoms and molecules in rapid chemical reactions. The *biological* phase starts with enzymic reactions in response to physical and chemical changes within the cell, and includes all subsequent processes, such as repair, division, cell death and compensatory cell proliferation. This final phase can last for years after the initial ionising radiation [2, p. 3].

Type of damage	Number per Gy per cell
DNA double-strand breaks	40
DNA single-strand breaks	1000
DNA–protein cross-links	150
DNA–DNA cross-links	30
Base damage	2000
Sugar damage	1500

Table 2.1: Types and frequency of radiation induced damage [3, p. 287]

Direct damage to the DNA molecules in the physical phase, or indirect damage caused by free radicals in the chemical phase, produces breaks and lesions in the DNA structure. During the biological phase the cell attempts to repair the damage. Of the various types of damage that can occur to DNA molecules (see Table 2.1), the double-strand break (DSB, in which both strands of the double-helix are broken at the same point) is considered to be the most critical for lethal effects in the cell, although these make up a small proportion of the damage. The aim of radiotherapy is to produce a high density of broken links or molecular damage to the DNA molecule to the extent that the cell cannot repair itself, and therefore is unable to replicate and divide, and no longer contributes to the cancerous tumour. When multiple lesions occur in sites within a few nanometres of one another, this is known as a local multiply-damaged site (LDMS). This is much harder to repair, and therefore leads to a higher probability of cell death [2, p. 75].

These processes, however, cause damage to healthy cells as well as cancer cells. Managing the cost of normal tissue damage against the benefit of tumour damage is the most vital component when planning a treatment course [4, p. 59]. Some types of tissue are more radiosensitive than others [4, p. 30]. For example, the bone marrow is highly sensitive to radiation, and full-body radiotherapy for systemic diseases such as leukæmia is only possible with subsequent bone marrow transfer. Parts of the reproductive system are also highly sensitive, and sterility is a possible side-effect when the treatment area is close to the gonads. Other effects of radiation on normal tissues include desquamation of the skin and hair loss, damage to the intestinal epithelium resulting in diarrhoea or infection, reduction in white blood cell count leaving the body defenceless against infection, fibrosis and pneumonitis in the lungs, kidney, liver and brain damage [3, pp. 298–304]. Radiation can also induce mutation, cancerous tumours or leukæmia [1, p. 32].

A number of measures can be taken to maximise the damage to tumour cells while minimising damage to healthy cells. The first is fractionation. This is the division of the total dose into smaller fractions, administered at carefully planned intervals over a number of days or weeks. By planning the fractionation scheme based on the type of cancerous cells to be irradiated and the type of normal cells receiving an unavoidable dose, the tumour cells can be pushed past a viability threshold, below which the cells can no longer repair themselves, whilst the normal cells stay above this threshold. At the end of the treatment course, the tumour cells disintegrate but the the normal cells are able to recover [3, pp. 315–317].

Together with fractionation, manipulating the three-dimensional field of the radiation is important to deliver the highest possible dose to the tumour with the lowest possible dose to the surrounding tissue. The shape of the field can be constrained by the use of manufactured or adjustable shields, or by moving the beam entry points and angles [4, pp. 62–64]. Using multiple angles of attack can dramatically increase the dose at the tumour (where the multiple fields overlap) while spreading out the dose to normal tissue [5, p. 177]. The attack angles can be distinct, with multiple fixed beam directions, or continuous, by rotating a gantry around the patient during delivery.

Adjusting the intensity of the beam as it passes over different sections of the tumour can also optimise the dose distribution. This is known as *intensity-modulated radiation therapy* (IMRT). A computer-aided optimisation process calculates a customised intensity profile to match the shape of the tumour, and much closer control of the dose to tumour versus dose to normal tissue is achievable [5, p. 239].

Combining all of these methods provides the best control of the radiation and is vital for successful treatment with minimal side effects. The aim is always to maximise the dose delivered to the tumour and minimise the dose to healthy tissue, to balance effective destruction of the cancerous cells against the long-term survival of the normal cells.

2.2 Using charged particles

Charged Particle Therapy (CPT) continues the efforts to maximise dose to cancer cells and minimise dose to healthy tissue. In 1946, Robert Wilson suggested the future use of charged particles for cancer therapy [6]:

> “Except for electrons, the particles which have been accelerated to high energies by machines such as cyclotrons or Van de Graaff generators have not been directly used therapeutically. Rather, the neutrons, gamma rays, or artificial radioactivities produced in various reactions of the primary particles have been applied to medical problems. This has, in large part, been due to the very short penetration in tissue of protons, deuterons, and alpha particles from present accelerators.
>
> Higher-energy machines are now under construction, however, and the ions from them will in general be energetic enough to have a range in tissue comparable to body dimensions.”

Wilson went on to define and explain the dose distribution for charged hadrons as distinct from electrons and photons, based on the Bethe-Bloch equation for the passage of charged particles through matter [7, 8]. The qualitative differences are shown in Figure 2.1. The dose delivered is proportional to the ionisation per unit path length, or specific ionisation, which is in turn roughly inversely proportional to the energy of the particle. Plotting the specific ionisation of the particles, such as the protons in Wilson’s paper, or carbon ions, produces a low dose on entry to the body and a sharp peak in the dose, known as the Bragg peak, the depth of which depends on the energy of the particles. Therefore, by adjusting the energy of the particles, the majority of the dose can be delivered at the

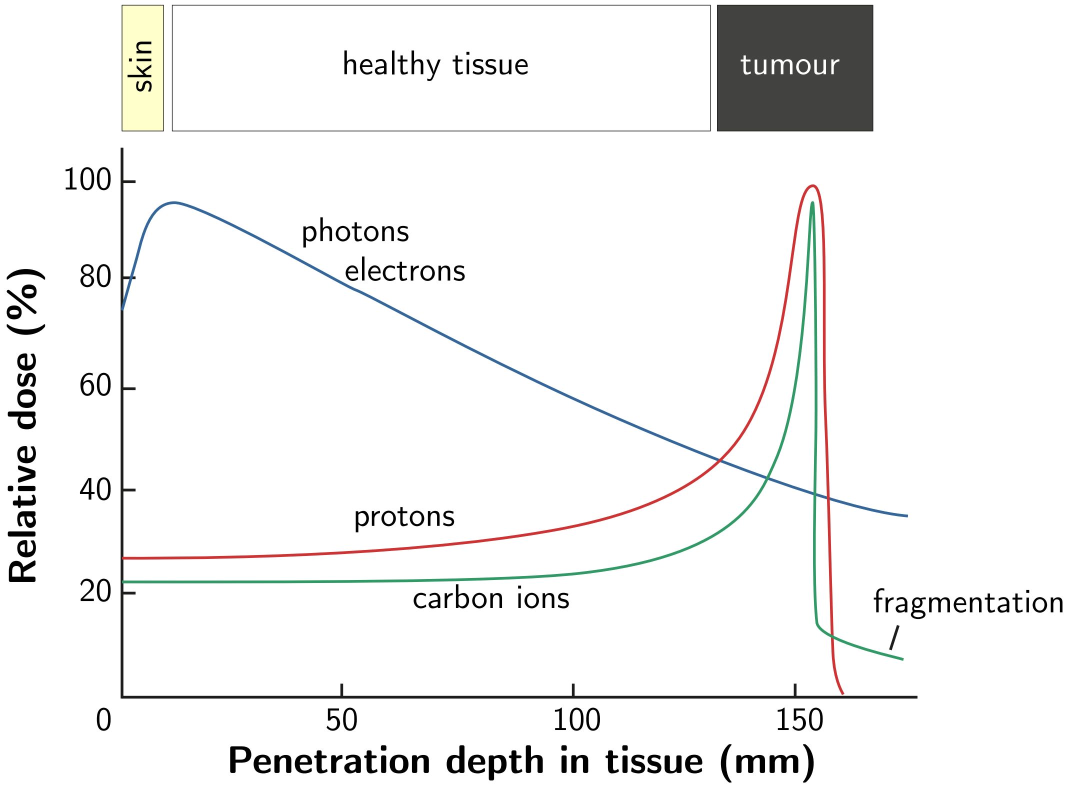

Figure 2.1: Dose profiles for different therapy beam options; adapted from Physics World [9]. Note that each graph is normalised to a percentage scale, so relative effectiveness is not displayed.

site of tumour [9]. Also, ionisation levels are significantly lower close to the surface of the body, and zero or very low deeper than the Bragg peak.

This is in contrast to the depth–dose curve for conventional radiotherapy, where the peak of maximum ionisation occurs near the surface of the body and drops off slowly as the particles go deeper into the body, towards the tumour. There is also a significant dose that passes through the tumour and causes damage further inside the body. This latter characteristic rules out conventional radiotherapy in cases where the tumour is in front of vital organs, as some ionisation would occur beyond the cancerous growth and damage the organs.

The Bragg peak for CPT allows its use in cases where conventional radiotherapy would be too dangerous, such as in front of organs [10]. Figure 2.2 demonstrates the extent of the reduction in normal tissue irradiation that can be achieved by CPT.

Due to the depth-specific nature of the dose distributions of CPT, a similar dose can be applied to the tumour while reducing the total energy deposition to between one-half and one-tenth of the radiation energy from conventional radiotherapy [11]. A reduction in this overall tissue irradiation is highly desirable, as many side-effects of radiation treatment, most notably the occurrence of secondary cancer, are correlated with the total energy deposition [12, 13]. Due to this effect, CPT offers advantages over conventional radiotherapy for a wide variety of tumour sites [see 14], including prostate, breast, oesophagus, lung, liver, kidney, brain and spinal cord. CPT can also offer advantages

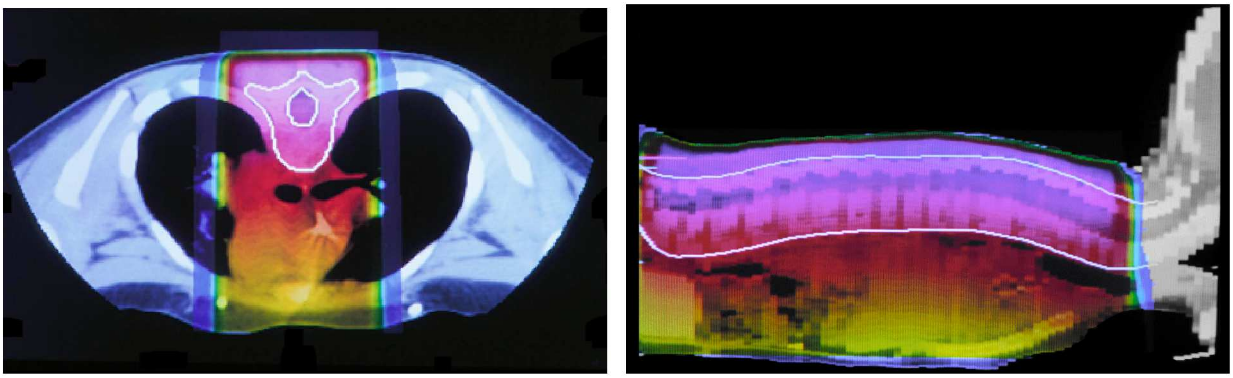

(a) Conventional radiotherapy **(b)** Conventional radiotherapy

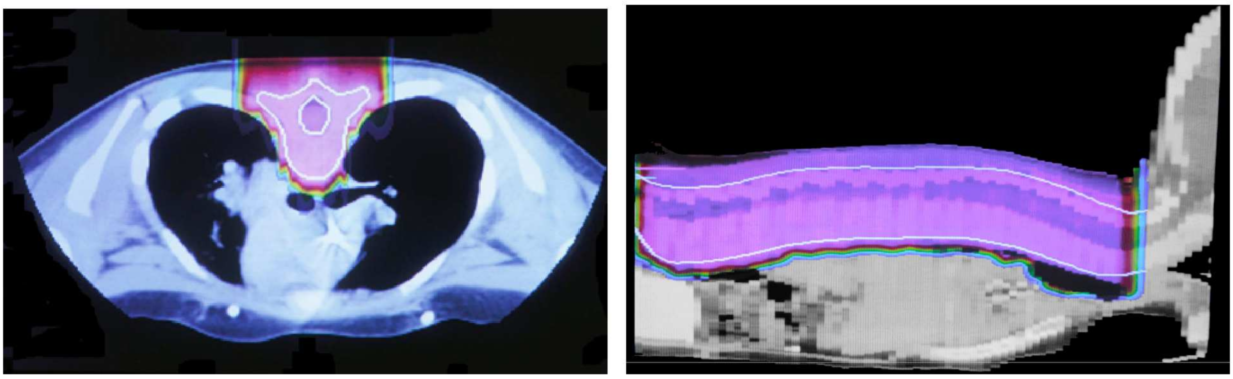

(c) CPT **(d)** CPT

Figure 2.2: Dose deposition cross-sections for treatment of child medulloblastoma of the spine, (a), (b) using conventional radiotherapy, and (c), (d) CPT using protons. The dose to vital and sensitive organs such as the heart and bowels is non-existent with CPT. Images courtesy of Prof. Ken Peach.

in treating sarcomas and lymphomas, and even in palliative care, for which the reduction of acute side effects is even more desirable as the treatment is intended to reduce suffering rather than to exterminate cancer cells. This reduction in total dose suggests that as the methods and equipment for CPT are developed further and reduced in cost, CPT may start to replace conventional radiotherapy in more and more treatment applications [15].

Not all particles interact with living cells to the same effect. This is due to different strengths of interactions, affected by mass, charge and kinetic energy, and the different relative importance of various types of interaction. The *relative biological effectiveness* (RBE) of a particle species in medical treatment is defined as the ratio to the dose of X-rays required to produce the same biological effect. Treatment by particles with an RBE higher than one will produce more damage to living cells, both cancerous and healthy, than treatment by X-rays at the same dose. Table 2.2 compares various aspects of different therapeutic beams, including their RBE.

Due to the high RBE of neutron beams, trials were run in the late twentieth century comparing neutron beams to X-ray beams for cancer therapy. However, due to the higher total biological dose caused by the high RBE being consistent across a long beam path with the same pseudo-exponential depth–dose profile, too much damage was caused to normal tissue. Also, conducting

	Attenuation with depth	Total dose	Average RBE
X-ray	Pseudo-exponential	High	1
Neutron	Pseudo-exponential	Highest	3
Proton	Bragg peak^a	Low	1.1
Helium ion	Bragg peak^b	Lower	1.4
Carbon ion	Bragg peak^c	Lowest	3

Table 2.2: Comparative aspects of different therapeutic beams in medicine [15]; superscripts ^{abc} refer to Bragg peak height where $c > b > a$.

the first comparative studies across different treatment beam options highlighted various problems of methodology in such studies [15]. Beams of charged particles such as protons and carbon ions utilise the Bragg peak depth–dose profile and higher RBE to increase the damage to tumour cells, while the reduced total biological dose due to the preferential depth attenuation reduces the damage to healthy cells. CPT therefore combines three advantages over conventional radiotherapy: increased dose to the tumour, reduced dose to healthy tissues, and low or zero dose beyond the Bragg peak, which can make CPT effective in locations where conventional radiotherapy is dangerous, ineffective or impossible.

The major disadvantage of CPT beams compared to photons or electrons is the difficulty involved in generating them at high enough energies, which requires a much larger and more complicated accelerator than conventional radiotherapy machines. Also, as CPT has not been studied for as long as conventional radiotherapy, there is still limited data and experience available for planning safe, efficient and effective treatment. Due to both of these factors, the cost of a CPT facility will be greater than for a comparable X-ray facility. For example, one study found that costs per fraction for an intensity-modulated proton therapy centre would exceed those for an intensity-modulated X-ray therapy centre by a factor of 2.4 ± 0.35, taking into account the higher setup costs for CPT technology in the form of capital repayments as part of the business costs [16]. For a carbon ion facility, or other heavy ions, the initial and continuing costs will be even higher than for a proton facility, due to the requirement for more powerful accelerators.

However, the cost-efficiency of CPT must take into account both the cost and the medical effectiveness of the treatment, and the final decision to invest in CPT will include plenty of other factors besides cost-efficiency.

2.3 Charged particle therapy centres

Protons were first used to treat patients in the 1950s, in particle physics laboratories in Berkeley (US) and Uppsala (Sweden) [17].

Britain established the first hospital-based proton therapy facility at Clatterbridge in 1989, using the Douglas cyclotron to treat cancer of the retina of the eye, and this has been a great success, with around 97% local tumour control [15]. This remains, as of 2011, the only UK proton therapy facility.

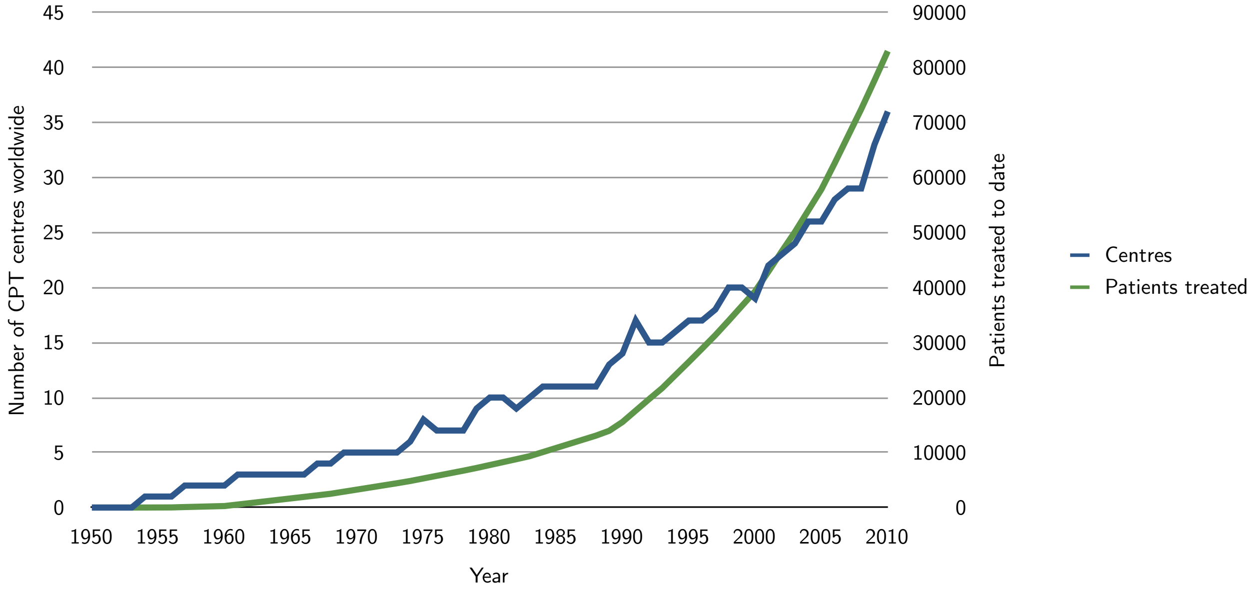

Figure 2.3: Number of working charged particle therapy centres increasing with time, and estimated cumulative total of patients treated (based on the simple approximation of constant rate of patients treated over the total lifetime of each centre); PTCOG data [17]

In the USA, the Loma Linda University Medical Center (LLUMC) has also been carrying out proton therapy since 1990. In that time, the centre has treated over 15 000 patients [17]. There are nine proton therapy centres in total in the USA, treating a total of nearly 27 000 patients since 1990.

In Japan there are eight working particle therapy centres, including three that use carbon ions, either exclusively or alongside protons. Over 12 000 patients have been treated since the first centre opened in 1994.

In Europe, there are fifteen working particle therapy centres, including carbon therapy at HIT, Heidelberg, Germany. Over 27 000 patients have been treated. Various pioneering studies have been carried out in Europe, such as investigations into RBE and the invention of spot-scanning both at GSI, Darmstadt, Germany [18], and the *Proton Ion Medical Machine Study* (*PIMMS*) at the *European Organisation for Nuclear Research* (*CERN*), which culminated in the Italian *National Centre for Oncological Hadron Therapy* (*CNAO*) being commissioned in Pavia, North Italy, using a synchrotron to accelerate both protons and carbon ions for treatment [19].

There are also working centres in Canada, China, South Korea and South Africa. A number of new centres have been proposed across Europe (at least fourteen), North America (at least four) and Asia (at least four).

Figure 2.3 displays the number of CPT centres in operation over time, and the number of patients treated to date. Figure 2.4 illustrates the different energies and number of patients treated for each of these centres. More details of the existing and proposed centres can be found in Appendix A. Details of the acceleration technology used in these centres is discussed in Chapter 3.

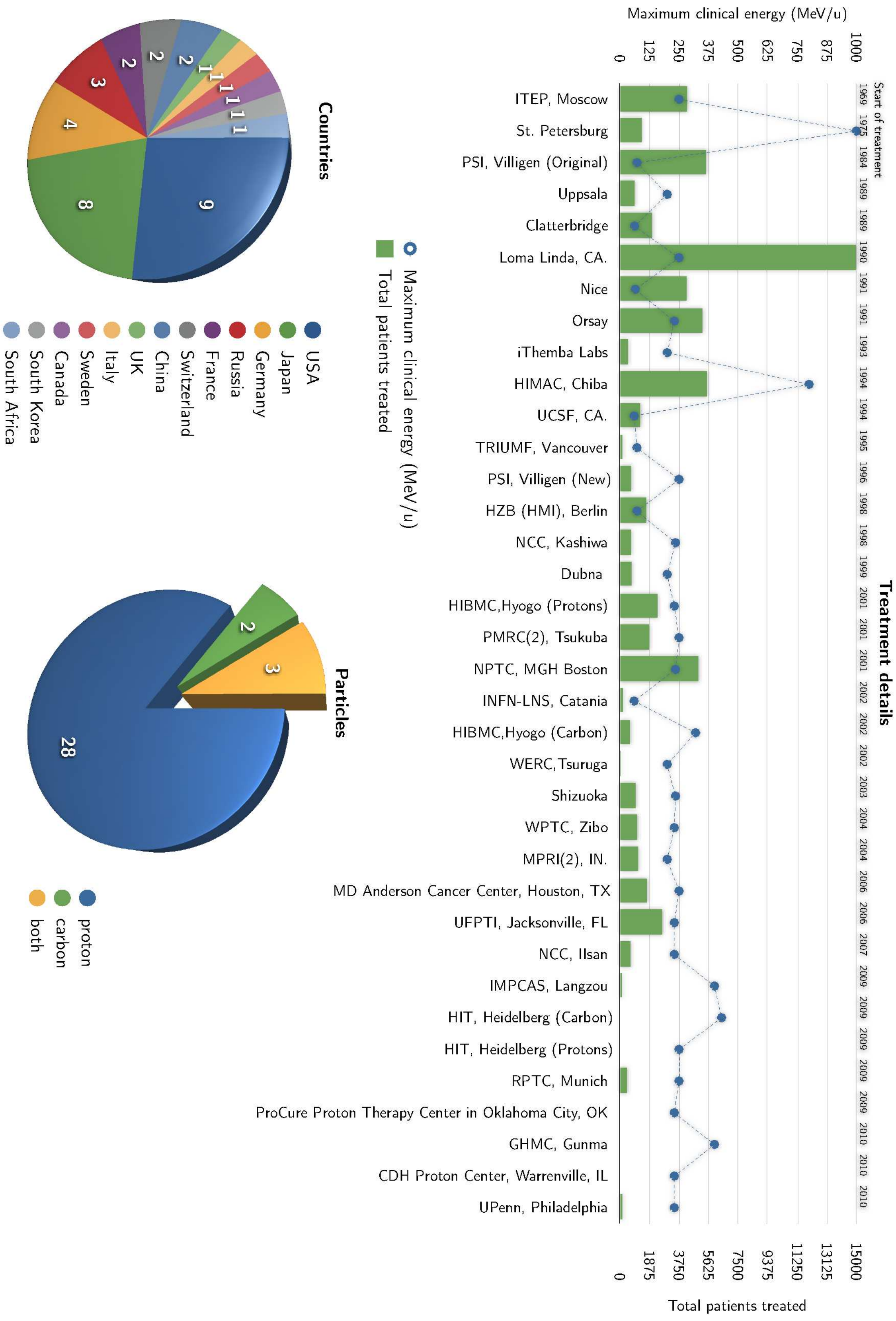

Figure 2.4: Details of existing CPT centres, including location, start date, treatment beam energy and number of patients treated; PTCOG data [17]

2.4 UK CPT Programme

The *British Accelerator Science and Radiation Oncology Consortium* (*BASROC*) was set up to develop the future of CPT in the UK. The consortium comprises many academic institutions, medical organisations and industrial companies working together to design the next generation of CPT facilities using ns-FFAG accelerators.

The current UK CPT situation is that there is only a single working treatment centre in the country, Clatterbridge Centre for Oncology, which only treats tumours of the eye. *BASROC* state their belief on their website,[1] that this is, "simply not good enough." The consortium aims to research and develop new technology that will make CPT possible in major UK hospitals. BASROC settled on FFAG acceleration technology (see § 3.5 for technical details) as a compromise between the high intensity and ease of use of a cyclotron and the beam control and variable energy capabilities of a synchrotron. The *BASROC* plan encompasses three major projects: *EMMA*, a technology prototype machine (see § 3.5.3), *PAMELA*, a treatment prototype machine (see § 3.5.4 and Chapter 4), and finally a working CPT treatment centre.

The UK Department of Health (DoH) has recently decided to accelerate the process for offering proton beam therapy on the National Health Service (NHS). The DoH called for applications from major hospitals for CPT centres using existing proton beam technologies. The contract was won by a two-site bid from University College London Hospitals (UCLH) and The Christie in Manchester, with the possibility of a third site at University Hospitals Birmingham. The project is now awaiting final approval. The London site would be close to the new UCLH cancer centre [20] and will use a commercially available cyclotron or synchrotron to deliver the proton beam for treatment [21].

The UK has also been involved in a number of collaboration projects. In 2011, *CERN* is embarking upon a new CPT study [22], following on from the *PIMMS* project that produced the *CNAO* CPT centre in Italy (see § 2.3 above). This new study is aimed at evaluating the feasibility of building a next-generation cancer therapy centre, and is calling for collaboration from all around Europe. This initiative offers a great opportunity for teams such as *BASROC* to advance CPT plans in the UK.

---

[1] `http://www.basroc.org.uk`

3 Charged Particle Therapy Accelerators

There are a number of considerations when designing an accelerator to deliver charged particle beams for cancer therapy.

Firstly, the energy range for both protons and carbon ions at extraction must cover the useful range for therapy in the human body. The lowest energy ions should allow treatment just below the skin surface, and the highest energy ions should reach to the deepest part of the body. To allow for treatment from any angle while avoiding vital organs, this deepest penetration should be right through to the other side of the body from the entry of the ions.

The intensity of the beam is also important, as a high intensity will reduce the length of time required for a given treatment. This improves the patient experience, because the patient does not need to remain still, sometimes in an awkward position, for too long. A reduced treatment time also means that more patients can be treated, increasing productivity for the therapy facility. The intensity must moreover be tightly controlled, so that the dose delivered to the patient is within a precise tolerance to match the treatment plan, and that the dose is uniform across the tumour.

Numerical constraints due to these criteria are examined in § 4.2 below.

Some principles and terminology for particle accelerator design are introduced in § 3.1. The three main types of accelerator are described in § 3.2 (linacs), § 3.3 (cyclotrons) and § 3.4 (synchrotrons). The application of these accelerators to cancer therapy is also discussed. § 3.5 introduces the alternative accelerator design selected for the *PAMELA* project: the *Fixed-Field Alternating-Gradient* accelerator.

Note that other accelerator alternatives could also be considered. For example, laser wakefield accelerators utilise a relatively new technology, in which laser propagation through a plasma produces very high electric fields by charge separation of electrons and ions in the plasma. These fields are used to accelerate particles, and the magnitude of the field means that laser wakefield accelerators can be very compact, and could possibly in the future provide treatment-energy beams from accelerators small enough to be mounted on a gantry in the treatment room. However, this technology is not yet sufficiently mature for such implementation [23].

3.1 Accelerator principles

This sections aims to define some of the terms used later in this thesis. It is not intended as a detailed introduction to theoretical concepts, but rather serves to introduce the non-specialist to pertinent terminology.

3.1.1 Fundamentals

Coordinates The particular application in this thesis is a type of linear accelerator, an RFQ, therefore the average motion of particles is along a straight line. This line is the central axis of the accelerator, and its dimension is denoted z. The transverse dimensions are orthogonal to z and are designated x and y, usually with x horizontal and y vertical. In circular accelerators, the average motion of particles is approximately circular, and is specified by a path coordinate s. The radial dimension is denoted x and the vertical y.

Units The earliest accelerators were electrostatic devices, where the final energy of the particles was given by the particle charge multiplied by the accelerator's potential difference, and therefore the primary units for particle energy in accelerator science are *electron volts* (eV), where one electron volt is the energy gained by a single electron across a potential difference of one volt [24, p. 3]. For atoms and ions, the energy is normalised by the number of nucleons u, so one electron volt per nucleon is denoted 1 eV/u.

Forces Starting from the Lorentz force,

$$\mathbf{F} = q\left(\mathbf{E} + \mathbf{v} \times \mathbf{B}\right), \tag{3.1}$$

it is clear that only the electrical force is applicable for acceleration. The magnetic force applies orthogonally to the particle velocity, which is useful for guiding particles but not accelerating them. Gravitational forces are too weak, and the strong and weak nuclear forces are too short-range in influence.

3.1.2 Focusing

Guiding a particle beam can be described by analogy with the guidance of an optical beam. The particles can be *focused* by *lenses* following the same mathematical framework, but the lenses for particle accelerators are electromagnetic rather than glass. Both electrical and magnetic forces can be applied for focusing; the magnetic force is proportional to the velocity of the particles, and so the relative strengths of the electrical and magnetic force are dependent on the energy of the particles being accelerated. For example, with a strong electric field of 30 MV/m and a strong magnetic field of 2 T, the forces would be equivalent for particles with a velocity of 1.5×10^7 m/s, or $\beta = 0.05$. For electrons, this only requires an energy of 0.6 keV, but for protons this velocity corresponds to an energy of 1.2 MeV. For carbon ions, this velocity requires an energy of 1.2 MeV/u, or 14 MeV in total.

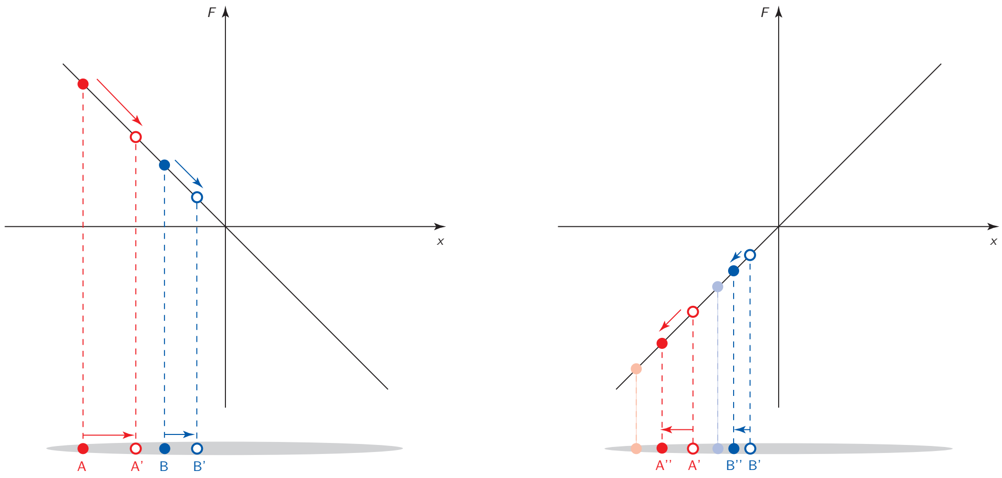

(a) Focusing

(b) Defocusing

Figure 3.1: An example of alternating gradients producing a net strong focusing force:
(a) Consider two particles at different x-positions in the bunch. Particle A is further from the bunch centre than particle B. The focusing quadrupole field is stronger further from the axis, so particle A receives a larger impulse than particle B, and the resultant movement from A to A′ is greater than the movement of particle B to B′ (all movements are relative to the bunch centre).
(b) The particles reach the defocusing quadrupole at x-positions A′ and B′. The defocusing force at point A′ is greater than that at B′. but crucially the defocusing force acting on both particles is significantly lower than the focusing force applied in (a). A′ is pushed back to A″, and B′ is pushed back to B″, but both particles are closer to the centre of the bunch than when they started.

A reference path, such as a straight line in a linear accelerator or a closed loop in a circular accelerator, describes the ideal motion of the particles, but the actual motion will diverge from this path, as particles enter the system with a distribution of both spatial and directional coordinates. Applying a focusing force constrains the particles to oscillate around the reference path, and remain within the influence of the accelerating force.

A dipole includes a natural focusing force in the bending (usually horizontal) direction, as the bending force acts to bring particles closer to the reference path in this plane. This force is weak compared to quadrupole focusing, so is known as *weak focusing* [25, p. 67]. By adding a field gradient to a dipole, a focusing force can be added in the vertical plane as well, although this also adds an unwanted defocusing force in the horizontal plane. By limiting the magnitude of the gradient so that this defocusing force is less than the natural dipole focusing force, the net effect can focus the beam in both planes. This method is commonly employed in cyclotrons to add stability [24, p. 15].

Quadrupole lenses, however, act to focus the beam in one plane and to defocus the beam in the other plane. By employing a sequence of lenses which alternate in orientation, a net focusing effect in both planes can be achieved. This process is called *strong focusing*, and is the method used in linear acceleration lines and annular rings such as synchrotrons [24, p. 16]. The net focusing effect is due to the increase of field strength with distance from the central axis, as illustrated in Figure 3.1. Particles that stray from the axis experience a strong focusing force and are moved closer to the axis, and therefore experience a lesser outward force in the next defocusing lens. As this process repeats with alternating gradients, the particles are focused closer to the axis in both transverse directions.

3.1.3 Phase space and emittance

The general term *phase space* refers to an abstract multidimensional space in which all the variables required to fully describe the state of the system in question are assigned as coordinates. In accelerator applications, the six variables required to define the motion of a single particle at a given time are the three spatial coordinates and the rate of change of each of those coordinates. A phase space distribution can be built as an ensemble of the six-dimensional phase coordinates of all the particles in the beam [26, p. 22].

The mathematics of such a space have been extensively developed and applied to many physical disciplines. One important mathematical result is *Liouville's theorem*, which describes the conservation of density and extension in phase space [27, p. 50], also described as the incompressibility of a phase fluid [28, p. 419]. When applied to an ensemble of particles in an accelerator, Liouville's theorem translates to the conservation of volume in phase space.

There are various possible definitions of the phase space coordinates for accelerator physics, but it is convenient to define the rate of change of the spatial coordinates as angles that are functions of the path of the reference particle s, such that

$$x'_i = \frac{\mathrm{d}x_i}{\mathrm{d}s}. \tag{3.2}$$

When all the particles in a beam—or more usually, in a beam packet, a subset of the beam currently undergoing acceleration—are plotted in a two-dimensional phase space,[1] such as x against x', then a distribution of particles can be seen. The area covered by the particle distribution is a measure of the quality of the beam—a narrower distribution in x or x' has a lesser spatial or angular spread, respectively—and is known as the *emittance*. This is a crucial parameter to be controlled in particle beam acceleration. There are many ways of defining, measuring and calculating emittance, so care must be taken when comparing values.

This definition of phase space in terms of coordinates and angles (sometimes called *trace space* to distinguish it from standard phase space [26, p. 89]) does not conserve area under acceleration. A Hamiltonian system would define coordinates and their momenta, x_i and p_i. The angles of Equation 3.2 are related to these momenta by $p_i = x'_i \beta\gamma m_0 c$ [26, p. 104]. Emittance measurements by angle must be normalised by a factor of $\beta\gamma$, such that the normalised emittance $\varepsilon_n = \beta\gamma\varepsilon$. This normalised emittance is conserved under acceleration.

Measuring the emittance exactly is often impossible, so various methods of estimating the emittance are used. The root-mean-squared (RMS) unnormalised emittance is defined as

$$\varepsilon_{\mathrm{RMS}} = \sqrt{\overline{x_i}^{\,2}\,\overline{x'_i}^{\,2} - \overline{x_i x'_i}^{\,2}}, \tag{3.3}$$

and the normalised version concerns momenta rather than angles [29].

---

[1] Or higher dimensions, if such can be visualised

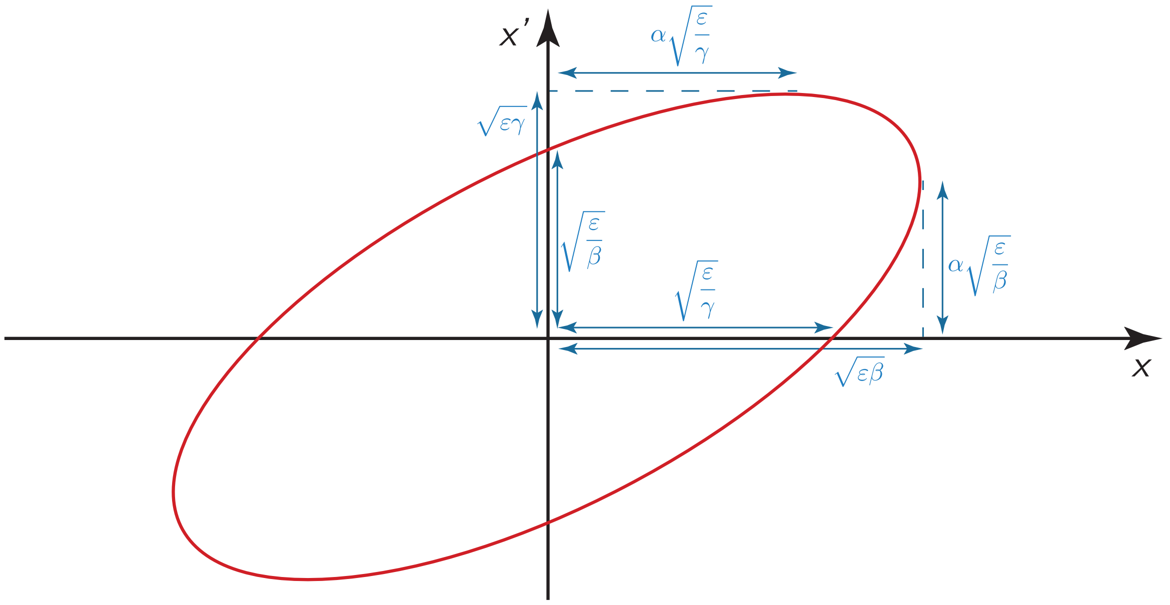

Figure 3.2: Twiss parameters α, β, γ and emittance ε, and the relation of these quantities to the geometry of a rotated ellipse

Ellipse equation A *phase space ellipse* can be drawn around a particle distribution to macroscopically describe the shape and size of the distribution and so provide a measure of the beam emittance. In simple acceleration schemes, the distribution closely resembles an ellipse, but as the situation increases in complexity the elliptical approximation becomes less accurate, so statistical methods are used to define an equivalent ellipse that is representative of the particle ensemble.

A general ellipse is defined by the equation $(x/a)^2 + (y/b)^2 = 1$, where a and b are the axes of the ellipse, and the area of the ellipse is given by πab. To include rotation of the phase space ellipse relative to the (x_i, x_i') axes, a cross term is required, and the full ellipse equation becomes

$$\gamma(s)x_i^2(s) + 2\alpha(s)x_i(s)x_i'(s) + \beta(s)x_i'^2(s) = \varepsilon, \tag{3.4}$$

where α, β and γ are known as the Twiss parameters,[2] and the beam emittance ε is the area of the ellipse divided by π. The Twiss parameters are related to the geometry of the phase space ellipse in Figure 3.2.

---

[2] The Twiss parameters $\beta(s)$ and $\gamma(s)$ are unrelated to the relativistic factors β and γ.

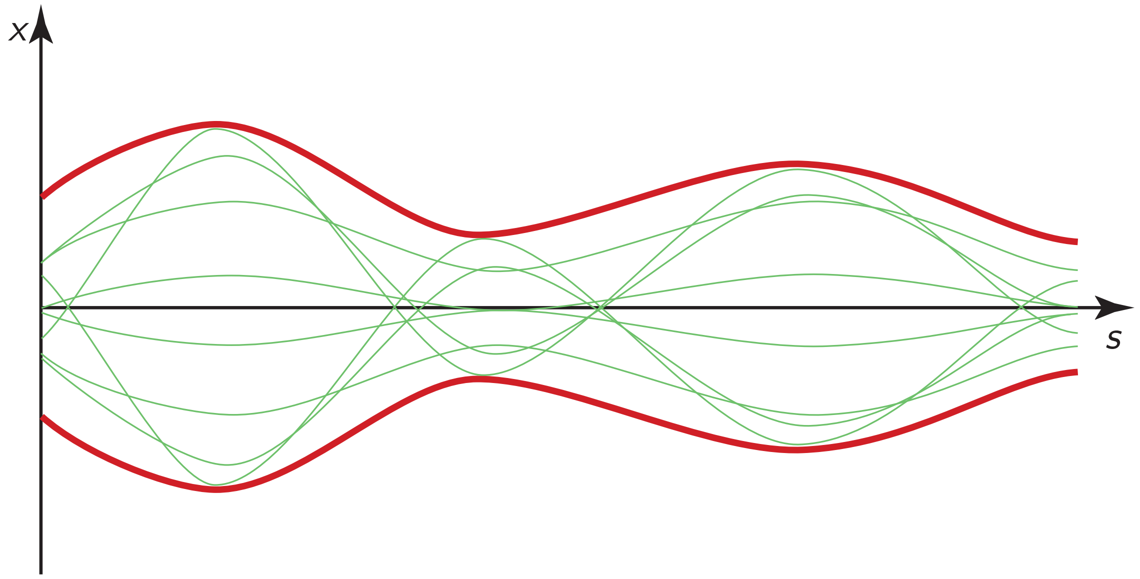

Figure 3.3: Paths of particles (green) oscillating around the stable path, showing the beam envelope (red) encompassing all paths

Betatron envelopes The *betatron* was an early electron accelerator, conceived when electrons were known as *beta particles*, hence the name. The particles in a betatron oscillate transversally about the equilibrium path, and this motion in all accelerators is now called *betatron oscillation* [25, p. 19].

Particles moving in a focusing field follow the Hill equation as their equation of motion, such that

$$x''(s) - k(s)x(s) = 0, \tag{3.5}$$

where $k(s)$ quantifies the strength of the focusing field—a negative k produces focusing in the horizontal direction x and defocusing in the vertical direction y, and a positive k produces the reverse [24, p. 32]. The solution to Hill's equation has the oscillatory form

$$x(s) = E(s) \cos\left(\psi(s) + \phi\right), \tag{3.6}$$

where $\psi(s)$ is the phase of the betatron oscillation, ϕ is a constant of integration, and $E(s)$ describes an *envelope* function that constrains the motion of all the particles [30, p. 65]. The envelope function satisfies $E(s) = \sqrt{\varepsilon\beta(s)}$ and is illustrated in Figure 3.3.

Although the envelope equation can be well defined, the motion of the individual particles within the envelope will depend on their starting conditions. Therefore, the envelope—and its evolution described in terms of the Twiss parameters—is a very useful concept in quantifying the action of accelerating structures. In the mathematical treatment of accelerating elements using matrix transformations, the Twiss parameters transform analogously to the individual paths of the particles, so can be used to find the beam envelope for all values of s, and hence define the entire beam without requiring the solution for every particle individually [31].

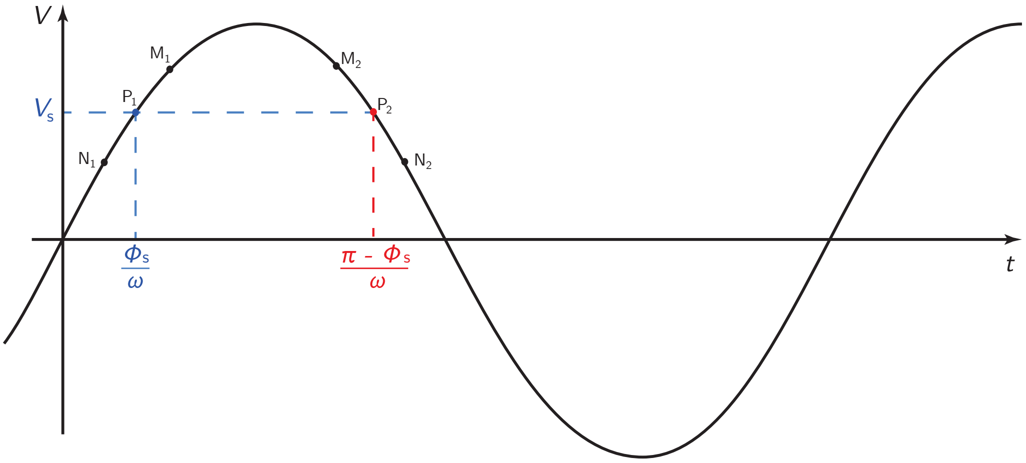

Figure 3.4: An illustration of phase stability: the RF potential is shown as a function of time at an accelerating gap in an accelerator. The synchronous particle has phase Φ_s, defined such that the phase is unchanged from one acceleration to the next. The synchronous phase (blue) is chosen in the range $0 < \Phi_\mathrm{s} < \pi/2$ so that particles close to this reference (such as M_1 and N_1) are focused towards the reference path and the oscillatory motion is stable. Adapted from *CERN Accelerator School* [33]

Phase stability The discussions above have focused on transverse particle dynamics. The longitudinal dynamics are concerned with the actual acceleration of the particles. Electrostatic accelerators are limited in the energy they can impart due to electrical breakdown [32, p. 283], and radio-frequency (RF) accelerators are used to attain higher energies, leading to accelerating phase considerations.

A particle that is in phase with the accelerating field, the *synchronous particle*, will steadily increase in energy as optimised for the particular accelerator. However, particles that slip forwards or backwards in phase relative to the synchronous particle will experience a slightly modified force, due to the phase of the accelerating field. The acceleration is stable if particles that fall behind the reference particle receive a greater energy increase, and those that slip ahead receive a lesser increase.

Figure 3.4 illustrates the phase focusing effect [33]. The synchronous reference particle is defined (in this simple case) as that with a phase that stays constant from one acceleration step to the next. The synchronous phase is in the range $0 < \Phi_\mathrm{s} < \pi/2$ (shown in blue) and the reference particle is incident at the accelerating gap at time $t_\mathrm{s} = \Phi_\mathrm{s}/\omega$, where ω is the applied radio frequency, and therefore sees a potential of V_s (point P_1 in Figure 3.4). A particle with a greater phase, such as that at M_1, will arrive later in time at the accelerating gap and will experience a potential greater than V_s. This greater potential leads to a greater accelerating force, and so the time to the next gap will be less than for the reference particle. This reduces the phase and brings the particle closer to synchronicity. Conversely, a particle with a lesser phase, such as that at N_1, will arrive earlier than the reference particle, see a lower accelerating potential, and therefore take a longer time to reach the next acceleration step. Its phase will increase and bring the particle closer to synchronicity. In this situation the area close to the reference path is stable, and a phase focusing effect will be seen.

In the area shown in red between $\pi/2 < \Phi < \pi$, a defocusing effect is seen: M_2 will arrive earlier than the reference P_2 but will be accelerated faster and so move further away in phase; conversely N_2 will arrive later than the reference but will be accelerated slower and so also move further away.

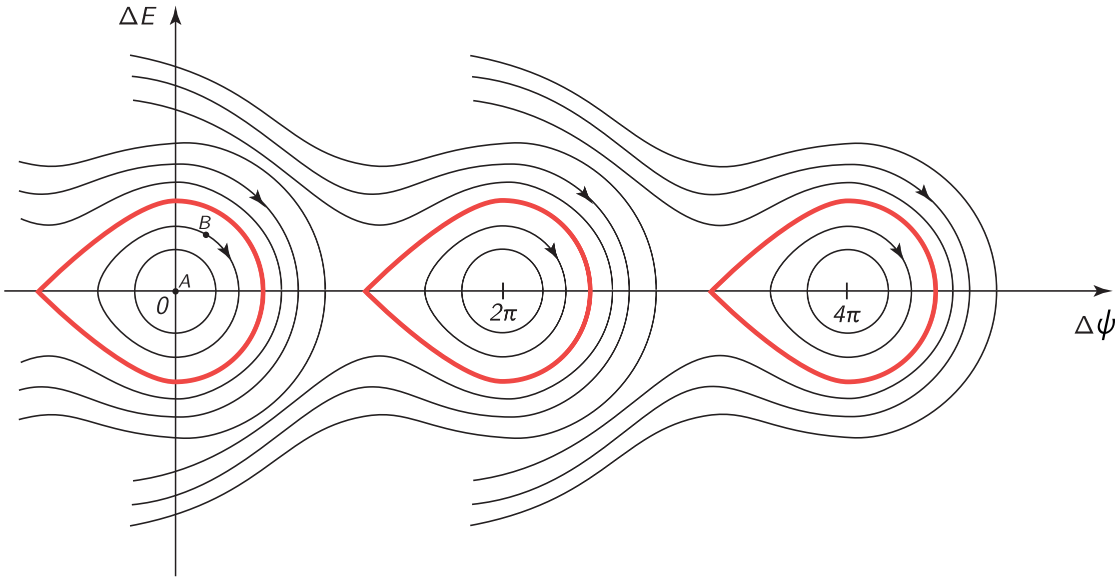

Figure 3.5: Motion of a particle B around the reference particle A in longitudinal phase space, showing multiple oscillation paths (black lines) and the separatrix (red line) that forms the boundary between stable and unstable motion; adapted from [25, p. 183]

Separatrix A *separatrix* is a general term defining a boundary in phase space between different behaviours. For example, there is a separatrix in the phase space of a pendulum that separates oscillation from rotation [34]. In particle accelerator physics, the separatrix in question is most frequently the boundary of stability of acceleration.

For particles close in phase to the stable reference particle, the longitudinal phase space motion (such as ΔE, the energy defect, against $\Delta\psi$, the phase defect, both relative to the synchronous particle) will circle around the reference particle and continue to be accelerated, as depicted in Figure 3.5. However, should the particle oscillations depart too far from the synchronous phase, they will no longer receive energy excesses or deficiencies enough to bring them back towards the reference particle. At this point the particles will no longer be accelerated correctly—they may fall within a different accelerating bucket, or may be lost from the accelerator altogether, or may be transported but at a greatly reduced energy. The boundary between the stable accelerating region and the region of lost energy is the separatrix.

3.2 Linear accelerators

Linear accelerators (linacs) can be any of a large class of accelerating structures. The basic principles can be explored in the context of a simple example that uses standing waves of electromagnetic fields in conjunction with drift tubes to accelerate particles. While the particles are within the drift tubes, they travel at a constant velocity. When they reach a gap between tubes, the voltage between the last and the next tubes produces an accelerating force on the particles. The electric field must be synchronised with the particle bunches to ensure that acceleration occurs at each gap between tubes.

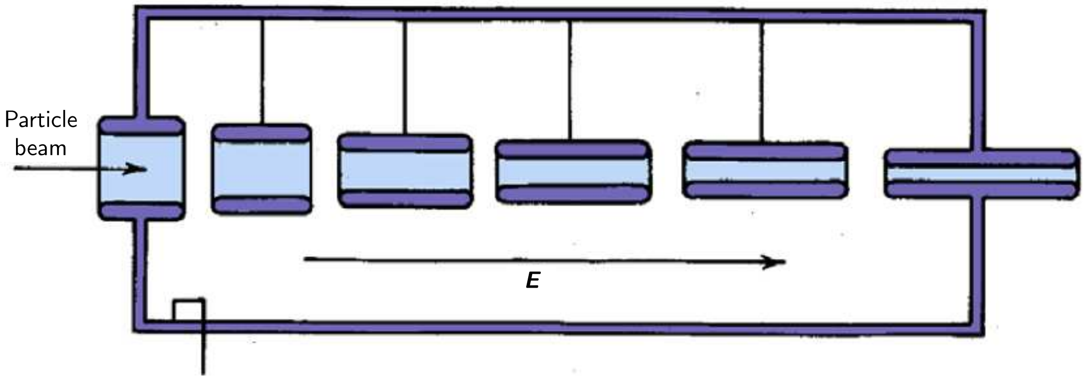

Figure 3.6: Alvarez linac with a single resonant cavity connected to drift tubes of increasing length [32, p. 461]

This is achieved by matching the lengths of the drift tubes with the frequency of the electric field. For a sinusoidally varying voltage $V(t) = V_0 \sin \omega t$, the energy gain at each gap ΔE is given by

$$\Delta E = qV_0 \sin \phi_\mathrm{s}, \tag{3.7}$$

where ϕ_s is the phase at which a synchronous ion will cross each gap in order to be accelerated. The total energy gain ΔE_n of the reference particle after crossing n gaps, each at phase ϕ_s, can be equated with the kinetic energy of the particle, as the final energy is several orders of magnitude greater than the initial energy:

$$\frac{1}{2} m v_n^2 = \Delta E_n = nqV_0 \sin \phi_\mathrm{s}. \tag{3.8}$$

In order to stay in phase, the length l_n of the nth drift tube must be defined by

$$l_n = \frac{v_n \lambda}{c} = \beta_n \lambda = \frac{2\pi}{\omega} \sqrt{\frac{2nqV_0 \sin \phi_\mathrm{s}}{m}}. \tag{3.9}$$

To reduce the length of the drift tubes to reasonable values for high energy acceleration of light ions (small m, large $1/m$), the tubes are located inside a resonant cavity to allow the use of high frequency (high ω, low $1/\omega$) electromagnetic fields. Figure 3.6 is a schematic of an *Alvarez* drift tube linac using resonant cavities and drift tubes with increasing lengths as the energy increases.

Linacs can also be designed and built using superconducting cavities. The primary advantage of superconducting technology is the reduced loss of RF power to the cavity walls [30, p. 576]. The quality factor of a cavity is defined as the ratio of the energy stored W_s to the energy dissipated per cycle W_d, multiplied by 2π: $Q \equiv 2\pi W_\mathrm{s}/W_\mathrm{d}$ [24, p. 148]. The Q-value for a superconducting cavity can reach values of the order of 10^9 or 10^{10}, compared to typical normal-conducting values of the order of 10^4. The higher Q-values equate to a reduction in power losses of the order of 10^5 or 10^6—for example, a 1 m-long, 500 MHz, 1 MV/m, normal-conducting structure may consume 35 kW of input power, whereas the equivalent superconducting structure may consume only 0.7 W.

More detailed discussion of modifications to this basic linac design for more efficient acceleration is included in § 5.1.2 as part of the discussion of the linear accelerator section of the proposed injector for *PAMELA*.

Electron linacs are widely used for conventional radiotherapy—many thousands of these accelerators are in use in hospitals producing beams of electrons with energies from 4–30 MeV [30, p. 33]. These electron beams are either aimed at targets to produce x-rays, or used directly for therapy. To use linear accelerators for charged particle therapy, however, is impractical for two reasons. Firstly, the length and cost of a linear accelerator scales with the target output energy. At energies requisite for CPT, the size and cost of a linear solution would be much too large. The maximum average field gradient for a proton linac is $\sim 3.5\,\mathrm{MV/m}$ [23], so for the target proton energy for *PAMELA* of 230 MeV, the shortest possible linac would be 65 m long. Also, variation of energy is harder to achieve than with a circular machine, as the cavities are synchronised to accelerate the particles for the whole length of the accelerator, and so produce a fixed final energy. The particle energy rises monotonically with length, and extracting with a lower energy requires switching off the later accelerating cavities and recalibrating all of the remaining beam optics for transport. In a circular machine, the particle energy rises with the number of turns taken around the ring, and therefore can be extracted at any point in the acceleration cycle.[3]

3.3 Cyclotrons

A cyclotron is a circular accelerator with a constant magnetic field magnitude and constant RF frequency.[4] Cyclotrons have large-area magnetic fields to allow acceleration from low energy near the centre to the output energy near the outer edge of the cyclotron. The field bends the particle trajectory into a circular path, allowing many accelerations from the same accelerating gap. Synchronisation between the oscillating accelerating fields and the revolution frequency of the particles can be achieved as long as the particle velocity is low enough that relativistic effects are negligible.

For a non-relativistic particle in a uniform vertical magnetic field, the balance of the centrifugal force with the magnetic force gives

$$qvB = \frac{mv^2}{r}, \tag{3.10}$$

$$\omega = \frac{v}{r} = \frac{qB}{m}, \tag{3.11}$$

such that the angular frequency ω is independent of the particle energy. As the particles accelerate and v increases, the radius r increases proportionally because the cyclotron frequency is constant. This means that ions at different energies travel at different radii in the cyclotron, therefore extraction at a fixed point in the structure necessarily means extraction at a fixed energy. This is unfavourable for CPT, as the large range of energies for treatment must be attained using an energy degrader,[5] but the fixed energy is appropriate for an injector.

The ions are accelerated in the gap between two electrodes, which are known as *dees* because of their traditional D-shape. One or both dees are connected to a resonator tuned to oscillate at the cyclotron frequency defined in Equation 3.11. Figure 3.7 shows the magnets and dees for a cyclotron and the particle orbits relative to each, in the case where both dees are connected to the RF generator.

---

[3] Designing an extraction system that can extract beams with such a wide range of energies is a separate challenge.

[4] Although variants exist that do alter these parameters

[5] A variable-thickness barrier, used to reduce the energy from the extraction energy to the target energy

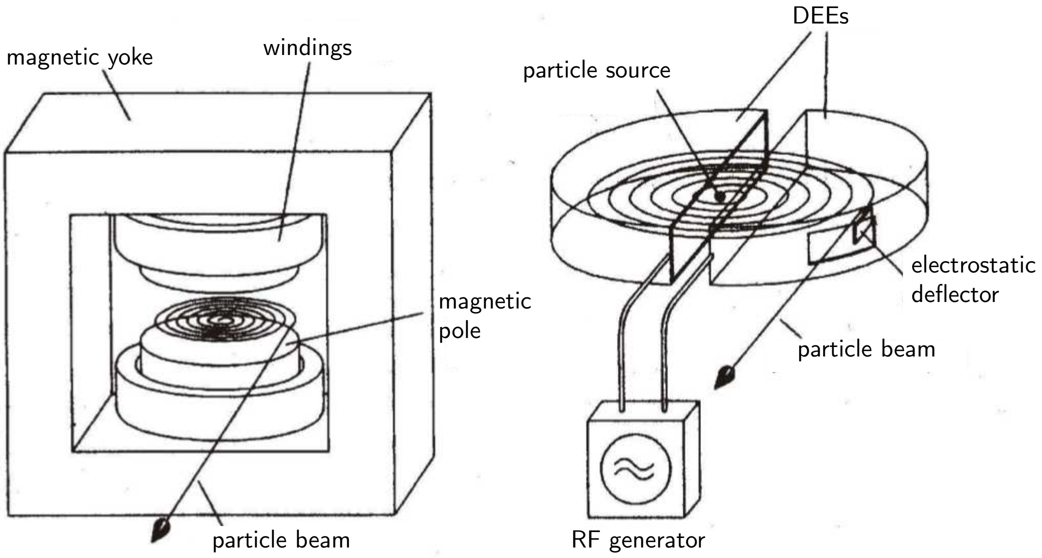

Figure 3.7: Magnetic and RF setup of a cyclotron; the fixed location of the electrostatic deflector for extraction leads to a fixed energy of extraction. Image adapted from [25, p. 15].

As an ion leaves the source near the centre of the cyclotron, it is accelerated by the voltage between the dees—the field at this time is polarised to apply a force in the direction of travel of the particle. An aperture ensures that particles leaving the source are in phase with the RF field [32, p. 506]. Once a particle enters the dee on the other side of the accelerating gap, it is shielded from the electric field and follows a fixed-energy circular path at the cyclotron frequency ω due to the magnetic field. After a time π/ω, the particle has turned a half-circle and has returned to the accelerating gap. As the RF resonator is tuned to oscillate at the same frequency ω, the accelerating voltage has advanced by half a period π and is now producing a force in the opposite direction, which accelerates the ion again across the gap and into the other dee. The particle is again shielded from the electric force and traces a path with a larger radius, due to its larger velocity after acceleration, but with the same angular frequency ω. This process continues, and the particle will always arrive at the gap between the dees in phase with the RF frequency to cause acceleration on each half-turn, as long as the velocity is kept low enough to avoid relativistic effects.

For relativistic energies, a synchrocyclotron or an isochronous cyclotron can be used. A synchrocyclotron uses time-varying RF frequencies in sync with relativistic revolution frequencies, but the duty cycle is relatively low, meaning that the beam current is significantly reduced. An isochronous cyclotron has a radially-varying magnetic field, which is designed so that the particle revolution frequency is in sync with the fixed RF field even at relativistic energies.

Superconducting cyclotrons bring similar power advantages as superconducting linacs. A superconducting *ACCEL Instruments* proton therapy cyclotron, for example, uses $\sim 40\,\mathrm{kW}$ compared to $\sim 200\,\mathrm{kW}$ power consumption of a normal-conducting cyclotron [35]. A superconducting cyclotron is also smaller and lighter than a normal-conducting version, due to the lack of a large iron core—

the *ACCEL* superconducting cyclotron weighs 90 tonnes, compared to ~ 200 tonnes for a normal-conducting equivalent. Other advantages include faster start-up time, as the coils can be continuously supercooled due to reduced running costs, whereas an iron magnet needs time to equilibrate; and also simpler methods of producing synchronous fields at relativistic energies—a normal-conducting magnet requires reduction of the pole-to-pole gap as the particles accelerate towards the extraction radius, leading to beam loss.

For proton therapy, cyclotrons can provide beams at sufficient energy and quality, but cannot provide energy variation—all protons from a therapy cyclotron will be extracted at a fixed energy and workarounds such as energy degraders must be used to counteract this disadvantage. For carbon ions, cyclotrons are in development to reach treatment energies, but none are in use at present.

3.4 Synchrotrons

Even with relativistic correction techniques applied, the maximum energy attainable in a cyclotron is limited. From Equation 3.10, the momentum of a particular orbit in the accelerator depends on the field strength and the radius of curvature, $mv = qBr$. To reach high energy values, even with the higher field available in a superconducting magnet, will require a large radius, and the poles of the cyclotron get larger and larger to accommodate the spiralling motion from the low energy at the centre to the high energy at the outer extraction radius.

Synchrotrons are circular accelerators in which the radius of curvature is held constant for all energies of the beam from injection to extraction. The particles are constrained to a narrow beam pipe at a large radius, and the spiralling motion is removed, so a series of much smaller magnets can be used. An extreme example is the *Large Hadron Collider* (LHC) at *CERN*, which has a radius of 4.3 km. Rather than two huge cyclotron magnet poles 9 km across, the LHC synchrotron uses over 1 500 superconducting dipole and quadrupole magnets, each half a metre across and up to 15 m long. Figure 3.8 shows a view of the beam pipe including one of the dipole magnets.

Figure 3.8: Section of LHC beam pipe, demonstrating the diameter and length of the bending dipole magnets; Image © CERN, `http://www.cern.ch`

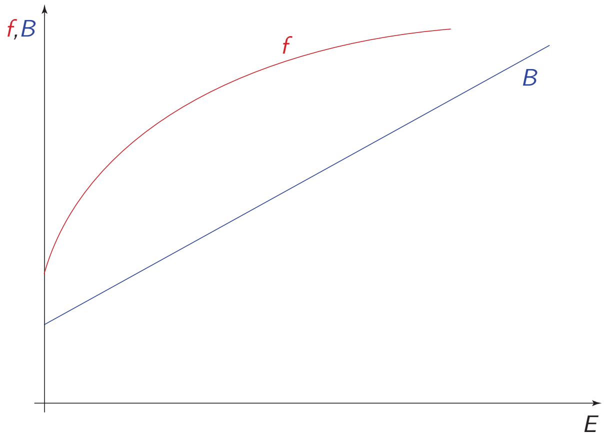

Figure 3.9: Field strength and radio frequency increasing with particle energy; adapted from [24, p. 13]

The magnet strength and RF parameters are varied during acceleration from injection to extraction energies, to maintain a constant radius of curvature. This requires precise synchronisation of both the magnet strength and the RF frequency, amplitude and phase with the energy and phase of the particles in the beam. Figure 3.9 plots the increase of magnetic field strength B and radio frequency f as the energy E of the reference particle increases. At higher energy, relativistic corrections to magnet strength and timings can be applied as part of the synchronisation algorithm, rather than requiring physical modification to the magnets.[6]

Australian physicist Mark Oliphant invented the synchrotron in 1943 and described the aim in a memo to the UK Atomic Energy Directorate [36]:

> "Particles should be constrained to move in a circle of constant radius thus enabling the use of an annular ring of magnetic field . . . which would be varied in such a way that the radius of curvature remains constant as the particles gain energy through successive accelerations by an alternating electric field applied between coaxial hollow electrodes."

Synchrotrons were the first accelerators to incorporate strong focusing (see § 3.1.2), which enabled much higher energies to be reached than had previously been attainable, such as the *CERN Proton Synchrotron* (PS) at 30 GeV, while using beam pipes only a few centimetres in diameter [24, p. 17]. Along with transverse stability provided by strong focusing, stability in the longitudinal dimension is required, otherwise particles that were slightly out of step with the accelerating voltage would be lost over the many turns through the synchrotron ring. The discovery of phase stability (see § 3.1.3) enabled the acceleration process to be stable in all dimensions, and the achievable particle energy in synchrotrons has continued to increase to the present day, with the LHC reaching energies of 7 TeV per beam.

As the lowest energy that can be accepted by the ring depends on the radius of the ring and the minimum reliable field strength in the magnets, particles cannot be injected directly from the ion source, as in a cyclotron. An injector is required—a smaller accelerator, or sequence of accelerators, that increase the energy to the correct injection value [37, p. 12].

---

[6] Note that relativistic corrections are not included in Figure 3.9

Synchrotrons are in use at existing carbon therapy centres such as *HIT* in Heidelberg [38]. Disadvantages of synchrotron technology include the size and complexity of the facility, which requires highly trained staff members to operate, and the low repetition rate due to the time variation of the magnetic fields, which leads to a low patient treatment rate. The use of FFAG accelerators is proposed to circumvent these issues.

3.5 FFAG accelerators

Fixed-Field, Alternating-Gradient (FFAG) accelerators were proposed by T. Okhawa and K. Symon independently in the 1950s [37, p. 219], based on a principle proposed by L. H. Thomas in 1938 [39]. The magnetic field is fixed in time, like in a cyclotron, and alternating gradient focusing is used to maintain stability of horizontal and vertical betatron oscillations [40], like in a synchrotron. The original FFAG designs are now classified as *scaling* FFAGs, to distinguish them from a more recent invention, the *non-scaling* FFAG.

3.5.1 Scaling FFAG accelerators

The fundamental difference between a synchrotron and an FFAG accelerator is the fixed magnetic field. In an FFAG, the RF frequency is still modulated during an acceleration cycle, but the magnetic field stays constant. This is achieved by applying a strong gradient to the magnetic field in the radial direction, and allowing the radius to increase slightly with energy. A fixed-field cyclotron has a wide range of radii from injection to extraction, requiring large circular magnets with a very large aperture. Varying-field synchrotrons take the opposite extreme, and constrain all particles to a constant radius for all energies by varying the magnetic field. FFAG accelerators lie between these extremes, with a smaller variation in radius with energy using fixed-field magnets with a strong radial gradient.

The fixed magnetic field allows a much higher repetition rate than synchrotrons; FFAG accelerators can reach a repetition rate in kHz, which compares favourably to Hz for standard synchrotrons and approximately 50 Hz for rapid-cycling synchrotrons (which use ceramic beam pipes to avoid inductance issues with rapidly changing magnetic fields). This fast repetition rate increases the output beam current, or alternatively allows a standard output average current to be achieved using a much lower peak current, which greatly reduces the space-charge effects in the accelerator. Using fixed magnetic fields also removes a number of technical difficulties in design and implementation of the accelerator as a whole. The smaller magnet size and greater ring compactness also adds both cost and operational benefits over synchrotrons.

FFAG accelerators also have advantages over cyclotrons, particularly for application to CPT. Cyclotrons produce ion beams at a fixed energy, and the energy variation required for therapy must be realised by passing the beam through absorbers. This has a drastic effect on beam quality and renders spot scanning—focusing the beam on the tumour and moving it across the extent of the tumour in three dimensions—impossible. Collimating moulds must be used instead, which are less accurate. Also, the collision of the protons with the absorbers releases unwanted radiation. FFAG accelerators, on the other hand, allow variation of output energy within the accelerators themselves, because particles with a wide range of energies can be extracted from a small spacial area.

An FFAG accelerator has a toroidal shape, as in a synchrotron, and the magnetic field pattern is designed so that all stable orbits, from injection at low energy to extraction at high energy, stay within the beam pipe. The first FFAG accelerators used *scaling* fields to accomplish this, utilising magnetic fields that increase rapidly with radius, so that the stable orbits at different energies have the same shape but different scales. The magnetic field must increase rapidly enough with radius to keep all the scaled orbits from injection to extraction within the beam pipe. For electron accelerators, this can be achieved with a relatively small machine, but for proton machines or heavier ions, the orbit excursion can be quite large to guarantee stable acceleration, requiring large-aperture magnets. One way to overcome this large orbit excursion is to remove the scaling constraint—this is the basis of the non-scaling FFAG [41].

3.5.2 Non-scaling FFAG accelerators

Non-scaling, fixed-field, alternating-gradient (ns-FFAG) accelerators were proposed in 1999 as an alternative to the scaling version [42]. Non-scaling accelerators produce beam dynamics with differently shaped stable orbits at different energies, so the orbits are no longer scaled with energy (see Figure 3.10 for comparison), hence the classification as *non-scaling*.

Relaxing the FFAG orbit-scaling law allows the use of simpler magnets with narrower apertures, as the orbit excursion can be reduced. However, the betatron tunes are no longer stable, and resonant conditions can cause beam loss. For fast acceleration scenarios, such as electrons or muons for a neutrino factory, the particles accelerate so rapidly that resonances cannot build up, and so there is no problem. For acceleration of thousands of turns, such as for protons and carbon ions for *PAMELA*, these resonances need to be avoided if acceleration is to be successful. Various methods for stabilising the tunes were investigated as part of the *PAMELA* design phase, culminating in the lattice proposed in [43] and [44].

Another advantage of the non-scaling design is a potential reduction in the outer radius of the machine, which is very important for a medical accelerator, as space in hospitals is at a premium. In general, an ns-FFAG will be larger than a cyclotron of equivalent maximum energy, but significantly smaller than the equivalent synchrotron.

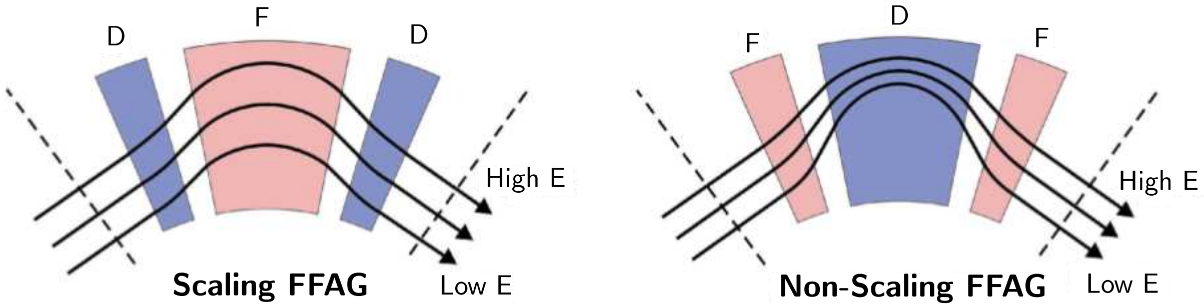

Figure 3.10: Comparative cell structure of scaling and non-scaling FFAG accelerators, showing shape of particle orbits. Image courtesy of Dr. R. Edgecock.

Non-scaling FFAGs are an untested technology, and as the lattice parameters and beam dynamics need to be studied in detail before a clinical ns-FFAG can be designed, *BASROC* intends to design two prototype machines, *EMMA* and *PAMELA*.

3.5.3 EMMA

The Electron Model for Many Applications (*EMMA*) is the first ns-FFAG accelerator to be designed. It is intended to be primarily a test machine, a proof of principle of ns-FFAG accelerators, to study their properties and learn how to best optimise the lattice structure. It is designed to be used to investigate some of the many possible applications of ns-FFAG accelerators, such as a neutrino factory, sub-critical nuclear reactors, and diverse medical and industrial uses. It is also proposed to remain in operation as a training machine after these various tests are complete.

The *EMMA* lattice is a densely-packed 42-cell ring that rapidly accelerates electrons at relativistic energies [45]. The focusing and bending forces are both applied using quadrupoles, where the horizontal offset between quadrupoles produces a net bending force. Electrons are injected from the *Accelerators and Lasers In Combined Experiments* (*ALICE*) accelerator at 12.5 MeV in a single 40 pC bunch. *EMMA* can accept a range of input energies, but for tests to date the input energy has been fixed and the momentum variation been simulated by scaling the quadrupole strengths. Successful acceleration has been demonstrated to 19.2 MeV within six turns. This very rapid acceleration is important for muon acceleration for a neutrino factory, among other applications [46].

3.5.4 PAMELA

The *Particle Accelerator for MEdicaL Applications* (*PAMELA*) is the second accelerator in *BASROC's* plans. It is to be a prototype for CPT machines, accelerating protons and carbon ions to the energies required for cancer treatment. It is being designed in parallel with *EMMA*, with the aim that the two projects can influence each other and accelerate the design process.

The *PAMELA* accelerator forms the context for the RFQ design of this thesis, and therefore Chapter 4 describes its design in more detail.

4 PAMELA Design

The *Particle Accelerator for MEdicaL Applications* (*PAMELA*) accelerator is designed to be the prototype for a new type of charged particle therapy (CPT) facility. The *PAMELA* team state [44]:

> "The aim of the *PAMELA* project is to design a highly efficient CPT facility, using the features of ns-FFAG technology to improve performance over existing facilities. The fixed field allows more rapid acceleration than is possible with a synchrotron (kHz rather than Hz) while still allowing variable energy extraction from 50 to 250 MeV (protons) or 70 to 450 MeV/u for light ions such as carbon, with excellent dose control and rapid transverse scanning. This should result in a much improved patient experience, greater patient throughput due to shorter treatment durations and in the case of carbon fewer treatment sessions (fractions)."

PAMELA is primarily a prototype for a clinical treatment machine, and the design must culminate in an accelerator capable of producing ions ready for treatment. The first design requirements, therefore, are specifications of the output beam. Other constraints include engineering and cost considerations.

The *PAMELA* design is described below. The clinical requirements for the treatment beam (§ 4.1) are translated into design requirements for the accelerator (§ 4.2). The accelerator lattice proposed to meet these requirements is introduced (§ 4.3), and this is used to formulate requirements for injection (§ 4.4). The values for these requirements are taken from the *PAMELA* Design Report [44].

4.1 Medical requirements

The requirements for the treatment beam relate to controlling the dose distribution within the body, delivering dose to the tumour in conformance with the treatment plan, while reducing the dose to healthy tissue to a minimum. There are two methods to achieve this beam matching: the *broad-beam* scheme that uses range modulators, degraders and collimators; and the active-scanning, or *spot-scanning* scheme that irradiates the tumour one small volume at a time with a pencil beam. Active scanning eliminates the significant particle losses and secondary radiation from the degraders and collimators, and greatly improves the conformity of the dose delivered to the body.

To enable the treatment of the hardest to reach and largest tumours, the range of the beam should reach up to 25 cm, the width of the *spread-out Bragg peak* (SOBP)—the resultant peak from adding together all the separate Bragg peaks—should reach up to 13 cm, and the transverse size of the field should reach up to 15 cm in both directions.

However, irradiating the volume involves more than just filling the space. The dose must meet standards of uniformity—the maximum deviation from the average dose—and tolerance—the deviation of the average dose from the prescribed dose. To meet the requirements of particle therapy, the uniformity should be below 2%, and the tolerance should be below 5%. However, to compete with other CPT centres, the tolerance target for *PAMELA* has been tightened to be below 2%.

Using active scanning, the time taken for each treatment is limited by the speed at which each *voxel* can be irradiated.[1] To be competitive with existing facilities, at least 100 voxels should be irradiated per second, to keep patient treatment times low and patient throughput high.

There is also a choice to be made as to how to adjust the intensity affecting each voxel. *Intensity-modulated radiation therapy* (IMRT) is a method of specifying different doses to different sections of the tumour, and the same principles can be applied to CPT. To achieve this end requires either adjusting the intensity of the beam rapidly for each voxel, or using a lower intensity and applying multiple bunches to each voxel. This latter method is simpler to realise but requires a higher repetition rate to meet the treatment time targets. It also allows *repainting* or *rescanning* of each voxel, when the beam returns later to previously irradiated voxels to produce the correct combined dose. This has significant advantages in regulating dose uniformity and tolerance, in dealing with organ motion due to respiration, in reducing the effects of beam positioning errors, and in allowing the tumour cells briefly to re-oxygenate during the treatment, as the presence of oxygen in the cells improves their susceptibility to irradiation. For a combination of these reasons, the multiple voxel painting method has been chosen for *PAMELA*.

In the following section, these medical requirements are converted to technical design requirements for the accelerator and beam lines. The medical and design requirements are summarised in Table 4.1.

4.2 Design requirements

The depth of the Bragg peak in the body is dependent on the energy of the particles. The range requirements described above translate into energy specifications of 70–230 MeV for protons and 110–450 MeV/u (MeV per nucleon) for carbon. To achieve the target uniformity and tolerance across the required longitudinal width of the SOBP, the energy needs to be adjusted in steps of 2 MeV at the lower end of the energy range and 0.5 MeV at the higher end for a proton beam, and 15 and 6 MeV/u respectively for carbon ions [47].

The beam spot size is limited by multiple scattering in the body to a minimum of 4 mm [48]. Allowing a larger beam spot size can help with uniformity in larger volumes when applied away from the edges of the volume, so for a transverse field size of 15 cm, the target beam spot size should vary in the range from 4–10 mm.

Using an active scanning system with multiple voxel painting to treat a tumour of the size specified requires a fast-cycling accelerator. This is a major factor in recommending an FFAG accelerator for this application. To achieve the target of over 100 voxels irradiated per second, with this particular choice of scanning, requires a repetition rate over 1 kHz [47].

---

[1] *Voxel* is a contraction of volume pixel, and refers to the practice of splitting up the target volume into smaller volumes that are irradiated one-at-a-time as the beam is scanned through three dimensions.

Medical Parameter	**Value**	**Design Parameter**	**Value**
Maximum range in body (cm)	25	Proton energy range (MeV)[1]	70–230
		Carbon energy range (MeV/u)	110–450
SOBP width (cm)	13	Proton energy step (MeV)	0.5–2
		Carbon energy step (MeV/u)	6–15
Field size (cm)	15×15	Beam spot size (mm)[2]	4–10
Dose field uniformity	$< 2\%$		
Dose field tolerance	$< 2\%$		
Scanning speed (voxel/s)	> 100	Repetition rate (Hz)	> 1000
Single dose(GyE)[3]	1–7	Intensity (nA)	0.05–1.5
		Proton bunch intensity (ppp)[4]	0.25–7.5$\times 10^6$
		Carbon bunch intensity (ppp)	0.75–22.5$\times 10^4$

Table 4.1: Summary of medical requirements and related design requirements for *PAMELA*

[1] The upper limit could be increased to 300 MeV to allow proton radiography.

[2] Full-width half-maximum (FWHM)

[3] GyE is the equivalent dose, adjusted for relative biological effectiveness (RBE), to the conventional radiotherapy dose in Grays (Gy).

[4] Particles per pulse

The beam intensity required to produce a particular dose is dependent on a number of factors, such as the size and shape of the tumour volume, the depth of the tumour in the body, the type of scanning and painting procedure selected, and the required treatment speed. To be able to treat a large tumour deep in the body with a 1 GyE dose in one minute requires a beam intensity of approximately 0.2 nA. The intensity scales linearly with the required dose, so the maximum dose of 7 GyE requires a beam intensity $\sim$ 1.4 nA. A single treatment dose may be split into four separate fields in the body, so to apply the minimum dose of 1 GyE across these four fields requires a minimum beam intensity of $\sim$ 0.05 nA. Therefore, *PAMELA* should be able to provide beam intensities from 0.05–1.5 nA. In terms of particle current, with a 1 kHz repetition rate (i.e. 1000 pulses per second), this corresponds to a proton count of 2.5×10^5 to 7.5×10^6 particles per pulse. For carbon 6+ ions, this corresponds to an ion count of 7.5×10^3 to 2.25×10^5 particles per pulse.

4.3 Lattice design

The original *scaling* FFAG accelerators were designed to keep the transverse betatron tunes constant throughout acceleration, and so avoid crossing any problematic resonances during acceleration. This was achieved by constraining the transverse magnetic field to follow the scaling law $B_y = B_0(r/r_0)^k$, where r and y are the radial and vertical coordinates respectively, the suffix 0 denotes the reference value, and k is the field index. The orbit excursion of such machines is of the order of 1 m, and therefore the magnets are large, complicated to manufacture, and expensive.

The first *non-scaling FFAG* (ns-FFAG) accelerator designs were proposed to decrease the orbit excursion and simplify the magnetic field profile, to reduce the difficulties and costs related to the magnets. Instead of following the scaling law, these designs use dipole and quadrupole fields with linear field profiles, hence they are classified as linear ns-FFAG accelerators. These achieve orbit excursions of the order of centimetres rather than metres, without increasing k to high values that lead to unstable increases in phase advance. However, the transverse betatron tunes are no longer constant, and resonances have to be crossed during acceleration. For many applications, making use of very fast acceleration means that resonances do not have the time to cause problems. For example, using a linear ns-FFAG for muon acceleration would only require 10 to 20 turns for full acceleration, and the machine tune changes a unit per turn. However, with a slower-cycling machine such as *PAMELA*, crossing these resonances over a significant number of turns leads to extremely strict tolerances in alignment of a few μm.

A number of methods have been proposed to avoid these problems, and one of these methods has been selected for the *PAMELA* lattice design. This method starts from a scaling FFAG design rather than from a linear ns-FFAG, and introduces a number of modifications that break the scaling law, while retaining a small variation in tune that can be implemented to avoid resonances altogether. This new design is neither scaling nor linear, so is classified as a non-linear non-scaling FFAG accelerator.

The design is based on a scaling FFAG using a radial-sector FDF (focusing, defocusing, focusing) triplet lattice. The first modification is to break the scaling law by expanding the magnetic field profile around the reference value and retaining only the dipole and first few multipole terms. This significantly affects the magnet design, allowing superconducting magnets to be employed rather than iron-cored magnets with complicated pole shaping used in a scaling FFAG. The magnets are further simplified by changing from sector-shape to square, and aligning the magnets of each triplet in a straight line rather than an arc. To reduce the orbit excursion, a high field index k is selected from the second stable region of the solution to Hill's equation, with a horizontal phase advance per cell greater than 180°.

The design uses two concentric, or near-concentric, rings. The first ring accelerates protons to their full energy, and also is the first stage for carbon acceleration. The carbon ions are then injected into the second ring to complete their acceleration to their full energy. The lattice layout for the proton ring is depicted in Figure 4.1. The energies and rigidities of the particles at injection, the reference energy and extraction are shown in Table 4.2 and the lattice parameters are shown in Table 4.3.

Ring	**Magnetic rigidity** $B\rho$ (Tm)	**Proton Energy** (MeV)	**Carbon Energy** (MeV/u)
1 injection	0.811	30.95	7.84
1 reference	1.621	118.38	31.0
1 extraction	2.432	250	68.36
2 injection	2.432		68.36
2 reference	4.401		208.75
2 extraction	6.370		400

Table 4.2: Particle kinetic energies and magnetic rigidities for the two-ring *PAMELA* lattice design [44]

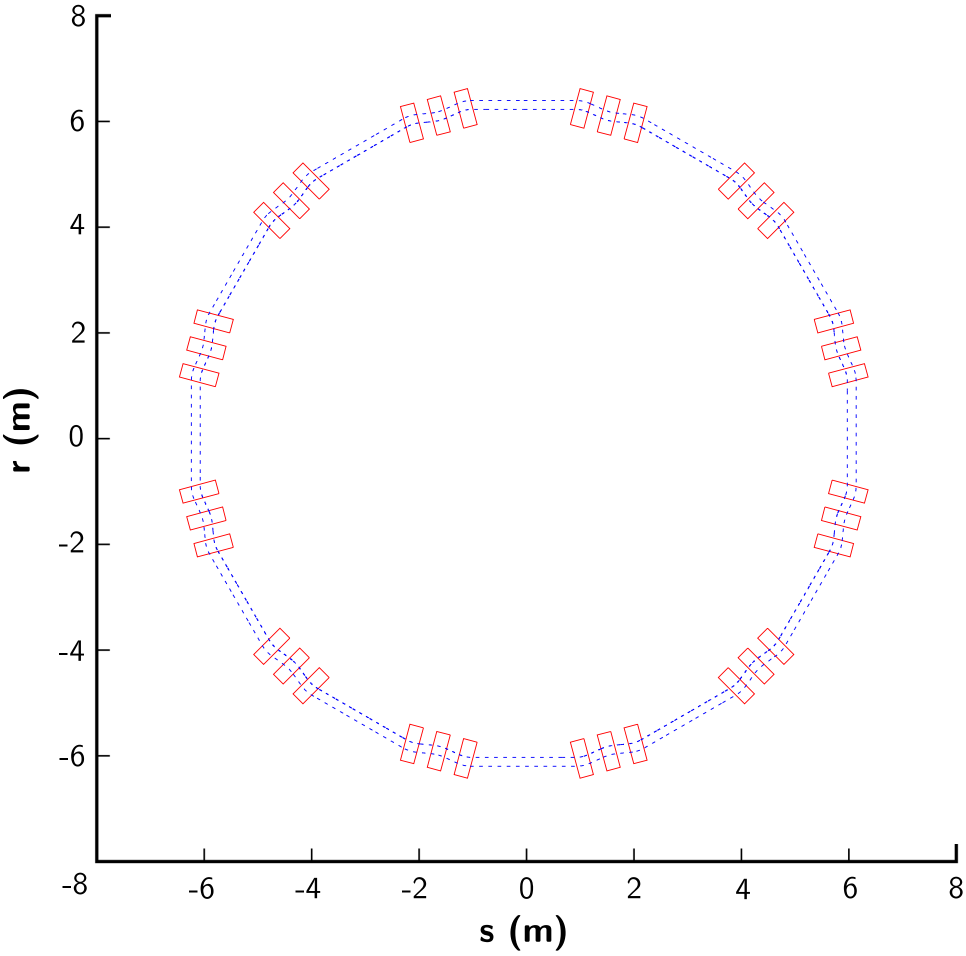

Figure 4.1: Layout of lattice elements in the first ring of the proposed *PAMELA* accelerator [44]

Parameter	**Proton ring**	**Carbon ring**
Cells	12	12
Reference radius r_0 (m)	6.251	9.3
Magnet length (m)	0.3144	0.6330
Packing factor $alpha$	0.48	0.65
Field index k	38	42
Orbit excursion (m)	0.176	0.217
Horizontal cell tune ν_x	0.72	0.0338
Vertical cell tune ν_y	0.27	0.0298
Maximum D magnet field (T)	4.0	4.5
Maximum F magnet field (T)	4.25	4.8

Table 4.3: Lattice parameters for the two-ring *PAMELA* lattice design; cell tunes are kept almost constant at the stated values [44]

4.4 Injection parameters

From the injection energies, ring geometry and beam time structure, the injection current requirements can be calculated. The results are summarised in Table 4.4. For 31 MeV protons, an injection current of 61 μA is required, whereas for 7.8 MeV/u carbon 6+ ions, the lower current of 576 nA is required. For both species, the target emittance at injection is 10 π mm mrad unnormalised.

To calculate the required current, the energy at injection can first be converted to a velocity and then to a time of flight around the ring circumference. This revolution period is 522 ns for protons and 1.012 μs for carbon 6+ ions. Assuming that about half of this time is available for the beam pulse (allowing time for the kickers to rise and fall and for filling the FFAG), the pulse time is of the order of 260 ns for protons and 500 ns for carbon. To produce enough current for treatment, 10^{11} protons or $3{\times}10^8$ carbon ions per second must be injected. With 1000 pulses of 260 ns each, this corresponds to a peak current of $10^{11}/(1000 \times 260 \times 10^{-9}\,\mathrm{s}) = 3.8 \times 10^{14}$ protons per second. For carbon, with 1000 pulses of 500 ns each, the value is $3 \times 10^8/(1000 \times 500 \times 10^{-9}\,\mathrm{s}) = 6 \times 10^{11}$ ions per second. The equivalent peak electrical current is 60.8 μA for protons and 576 nA for carbon.

Parameter	**Protons**	**Carbon 6+**
Injection energy (MeV/u)	30.95	7.84
Magnetic rigidity $B\rho$ (Tm)	0.811	0.811
Injection velocity β	0.2508	0.1294
Injection velocity v (m/s)	$7.524{\times}10^7$	$3.882{\times}10^7$
Ring 1 radius (m)	6.251	6.251
Ring 1 circumference (m)	39.276	39.276
Revolution period (ns)	522	1012
Pulse time (ns)	~ 260	~ 500
Harmonic number	10	17
RF period (ns)	52	59.5
RF frequency (MHz)	19	16.8
Mean particle current (s^{-1})	10^{11}	$3{\times}10^8$
Repetition rate (Hz)	~ 1000	~ 1000
Pulse particle current (ppp)	10^8	$3{\times}10^5$
Peak particle current (s^{-1})	$3.8{\times}10^{14}$	$6{\times}10^{11}$
Peak electrical current (μA)	60.8	0.576
Emittance (π mm mrad unnormalised)	10	10

Table 4.4: Injection parameters [44]

5 Injector Design

Various options for the *PAMELA* proton and carbon injector systems are considered in § 5.1, including cyclotrons (§ 5.1.1) and linear accelerators (§ 5.1.2). The choice of whether to use a single injector for both species or separate injectors is discussed in § 5.1.3.

The proposed final injector design is described in § 5.2. The protons and carbon ions are produced in separate ion sources (§ 5.2.1), allowing faster switching between species in a clinical situation and thereby improving productivity [38]. A 30 MeV proton cyclotron can be acquired for the proton beam injection, with an ion source included (§ 5.2.2). A low energy beam transport line (LEBT) transports the carbon ions from the ion source into a pre-accelerator, comprising a radio-frequency quadrupole (RFQ) for the first stage and a linear accelerator (linac) for the second stage (§ 5.2.3). The protons and carbon ions are combined into a medium energy beam transport section (MEBT), which transports the particles to the first *PAMELA* ring for injection.

An advantage of this separated pre-accelerator scheme is that the facility can be realised in three stages. Firstly, the cyclotron injector and a single FFAG ring can be used for proton therapy. Then, the installation of a carbon injector would allow clinical and biological studies using low power carbon beams. Finally, a second FFAG ring can be added to produce a carbon therapy beam.

5.1 Pre-accelerator options

The aim of the pre-accelerator and injector system is to produce beams of particles that match the design parameters for entry into the first FFAG ring, as set out in Table 4.4. The most crucial parameters for treatment are the particle energy and beam current, but the spatial and emittance profiles must also match the acceptance of the accelerator, otherwise particles will be lost and the current will decrease.

To produce the ion beams requires a source of ions, a pre-acceleration scheme, and a transport system. The ion source creates the particle beam, the pre-accelerator increases the energy to the correct value for injection, and the transport system guides the ions to the correct location, and also matches the real-space and phase-space distributions to the requirements. Although each aspect of the injector system is focused primarily on one or two of the design requirements, such as the pre-accelerator being focused primarily on increasing the energy, attention must still be given to the other parameters. For example, the particle losses must be considered at each stage to make sure that the maximum available current reaches the main accelerator rings, and that interactions from lost particles are minimised. Particles that are lost from the beam will collide with accelerator elements and produce radiation, and at energies above the Coulomb barrier this radiation will be long-lived and dangerous. There is also the chance of quenching of the superconducting magnets.

The pre-acceleration scheme must accelerate protons to 30.95 MeV and carbon ions to 7.84 MeV/u (see Table 4.4). At these relatively low energies, the conventional choices for acceleration are linacs or cyclotrons.

5.1.1 Cyclotron

The majority of proton therapy machines already in use are based on cyclotrons, in spite of the difficulties with fixed energy noted in § 3.3. Accelerators can be bought 'off-the-shelf' that will produce proton beams at a fixed energy, from lower energies aimed at biology studies and isotope production for industrial and medical uses, up to the higher energies required for proton therapy. Among the lower energy machines, 30 MeV cyclotrons are available that could be used to inject protons into the FFAG accelerator, which would then enable the delivery of protons at variable energies up to 250 MeV, as required for cancer therapy. The long heritage of cyclotron technology, and the high investment over the years for a wide range of scientific, industrial and medical applications, means that cyclotron technology is among the most reliable of the accelerator options. This high reliability and availability is crucial in an injector for a medical machine.

The transmission of these commercially available cyclotrons can be as low as 5% [23], so a high source current is required to get the correct output current for treatment. This is not a problem for proton sources, as proton sources can be found with currents far exceeding the injection requirements. Carbon 4+ ions can be produced at particle currents up to $\sim 400\,\mu$A, which still provides ample margin for losses in the system, but carbon 6+ ion currents are closer to $1\,\mu$A [49, 50]. A transmission of 5% in the injector would give a peak current of 50 nA. Although the magnet strengths do not need to be altered during acceleration, and the cyclotron can accept a DC source of current, the peak current is not available for the whole time because only a portion of the RF period is stable for acceleration. The space-charge forces act to spread out the beam, so this further reduces the available portion of the RF signal. Typically 30° of the RF is used for acceleration, so the average current could be as low as 4 nA. This places stringent constraints on possible losses through the rest of the acceleration chain in order to achieve the dose requirement of 1.5 nA for the treatment beam (see Table 4.1). A possible solution to this problem would be to accumulate the carbon beam in the FFAG ring before acceleration. Carbon therapy is generally only used for cancers that are resistant to proton therapy, and so carbon beams will not be required the whole time, allowing time for accumulation.

As well as current, the energy spread of the cyclotron beam must be considered, as too great a spread will lead to particles being lost longitudinally in the FFAG rings, and these losses can lead to radiation and superconducting-magnet quenching issues. Particles are extracted from a cyclotron when their increasing energy from acceleration increases their radius of motion to such an extent that they enter the extraction channel. The spatial width of this channel in effect determines the energy spread of the extracted beam. Reducing the width would reduce the energy spread, at the cost of also reducing the beam current. The optimisation of the extraction port width to produce sufficient current but with an acceptably small energy spread is important in the design of the cyclotron.

Parameter	**Value**
Energy (MeV)	15–30 MeV
Peak beam intensity (mA)	1.5
Transmission	10%
Weight (tons)	50
Cyclotron vault dimensions (m)	$8 \times 7.5 \times 4$
Power requirements (kW)	~ 200

Table 5.1: Selected technical specifications for the *IBA Cyclone 30 HC* cyclotron [51]

With current technology, the same cyclotron cannot be used for carbon as for protons (see § 5.1.3). A second, more powerful cyclotron could be used as a carbon injector, but this is likely to be larger and more expensive than a linear accelerator for carbon, as cyclotrons for carbon ions are not commercially available as they are for protons. Also, the higher charge and mass of the carbon ions means that problems with transverse focusing inherent in cyclotrons would be more pronounced than for protons, which would further reduce the transmission.

An example of a candidate for the proton injector is the *IBA Cyclone 30*, which is marketed for the production of radioisotopes for nuclear medicine.[1] This machine is capable of producing proton beams at 30 MeV with currents of 1.5 mA, which is more than adequate for the *PAMELA* injection requirements. Some of the technical specifications of one example of this technology are presented in Table 5.1.

5.1.2 Linac

Although linacs are not as compact as cyclotrons, they can be kept to a reasonable length by a sensible choice of RF parameters [52]. Other CPT facilities using carbon ions have selected linacs as an effective solution for injection where the main accelerator is a synchrotron [52, 53], due to their high reliability and stability, and their high current capacity. Linacs are established technology with a low risk, and can be made to be compact and relatively cheap. The same considerations apply for the *PAMELA* FFAG accelerator.

Accelerating carbon ions to 8 MeV/u would require a linac of approximately 5 m, including the RFQ and focusing lenses [54]. Accelerating protons to 30 MeV in the same accelerator would require a linac length closer to 25 m [55]. A longer linac takes up more space, costs more money and requires more RF power and extra power supplies. These factors exclude a linac as an injector for protons, but it is a feasible solution for carbon ions at the required energy.

The shunt impedance $Z = V^2/lW$ of an RF cavity determines the power lost in the cavity. The higher the shunt impedance Z, the lower the RF power loss W (for a fixed input field and cavity length l), and the more efficient the cavity. Figure 5.1 plots the shunt impedance for a variety of linac structures, and the variation with the velocity of the particles. For low velocity particles, the IH and CH structures provide much higher efficiency than conventional drift tube linacs (DTLs).

---

[1] `http://www.iba-cyclotron-solutions.com/products-cyclo/cyclone-30/`
® *IBA* and *Cyclone* are registered trademarks of IBA SA.

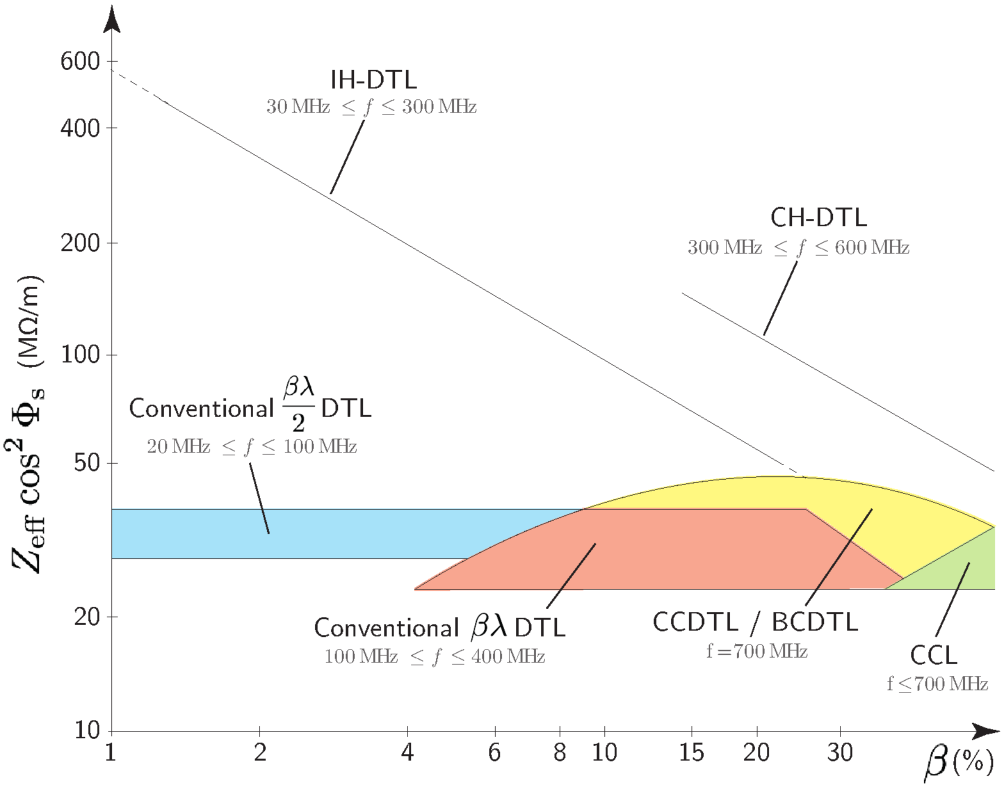

Figure 5.1: Shunt impedance of various linear accelerating structures as functions of particle velocity, including conventional Wideröe and Alvarez drift tube linacs, interdigital H-mode (IH), crossbar H-mode (CH), cell-coupled (CC) and bridge-coupled (BC) drift-tube linacs, and the higher energy cell-coupled linac (CCL); adapted from [56, p. 9]

DTLs (see § 3.2 and Figure 3.6) use the electromagnetic field shape known as an H-mode, based on the transverse magnetic (TM) field mode of an empty pillbox cavity, but modified by drift tubes to provide the longitudinal electric field required for acceleration. Traditional DTLs mount the drift tubes on one side of the resonant cavity, but an interdigital linac design mounts the drift tubes on alternating sides of the cavity [57, p. 90]. This uses a different resonant mode (H_{110}), which has the advantage of reducing the length for low frequency systems [58]. This design is known as an interdigital H-mode (IH) linac, as the alternating mounting scheme for the drift tubes appears similar to the fingers of two hands interlocked. A further refinement is the crossbar H-mode (CH) structure, where the alternate ‘fingers’ are rotated through 90°, which reduces the size of the accelerator even further, due to the different resonant mode used. As well as the reduced length, these machines also have a higher shunt impedance than an Alvarez DTL, which results in lower power requirements. Cutaway sections of an IH and CH linac are shown in Figure 5.2 and cross-sections and schematics for the two structures are compared in Figure 5.3, along with RFQ structures. Different structures are best suited to different radio frequency ranges and to different stages of the acceleration process, as summarised in Table 5.2.

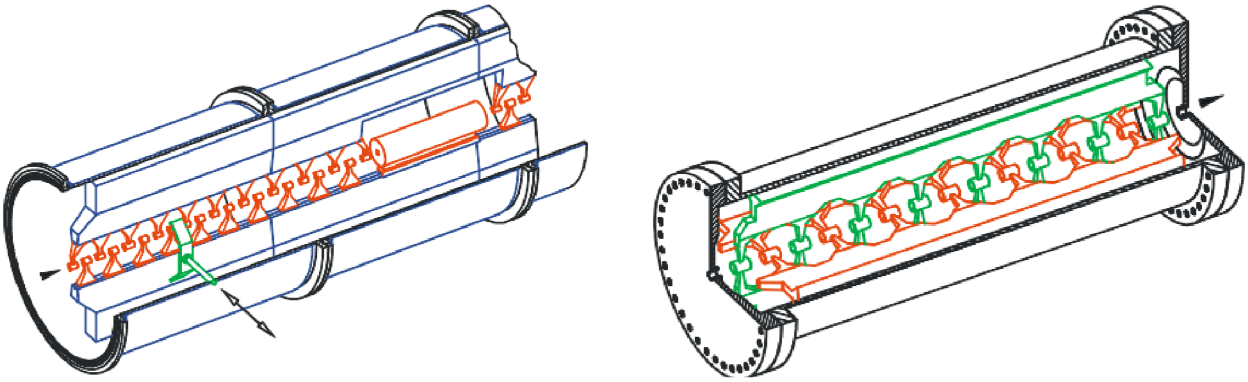

(a) IH linac **(b)** CH linac

Figure 5.2: Cutaway sections for (a) interdigital and (b) crossbar linacs

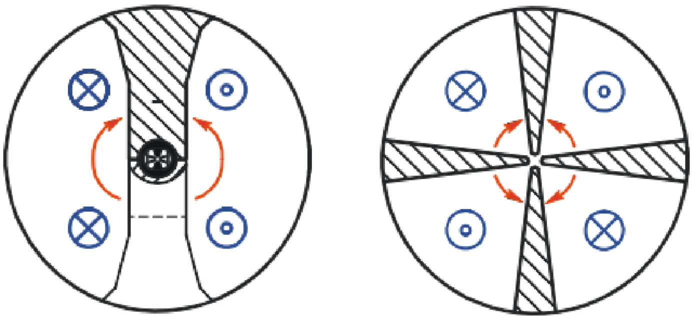

(a) 4-rod RFQ (H_{110}) **(b)** 4-vane RFQ (H_{210})

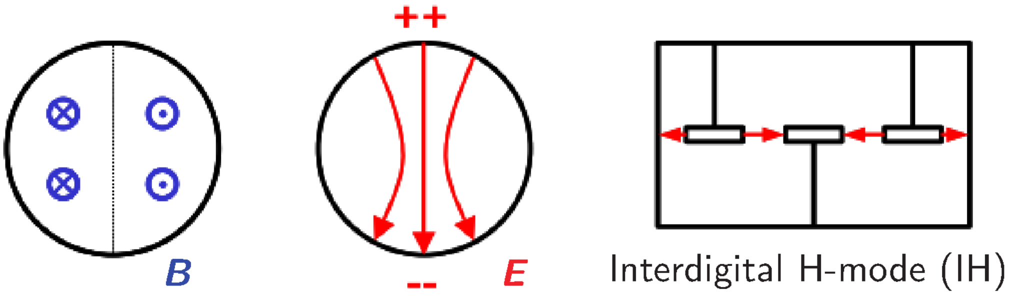

(c) IH linac (H_{110})

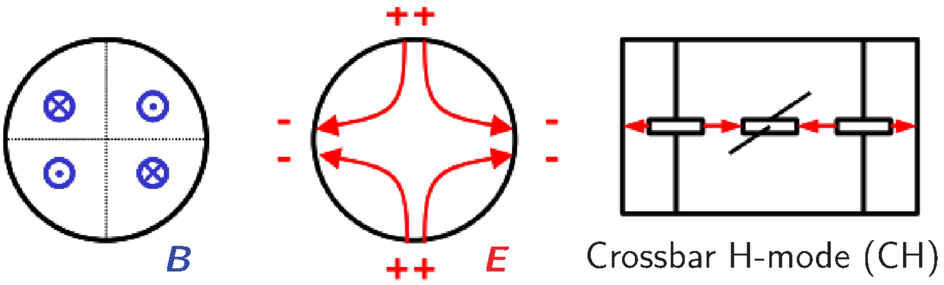

(d) CH linac (H_{210})

Figure 5.3: Schematic comparison of H-mode accelerating structures, showing physical features and field configurations; note that both (a) the four-rod RFQ and (c) the IH linac use the H_{110} mode, and both (b) the four-vane RFQ and (d) the CH linac use the H_{210} mode (see Table 5.2)

Structure	RF Mode	Frequency (MHz)	Particle Velocity β
4-rod RFQ	H$_{110}$	$\lesssim 100$	$\lesssim 0.03$
4-vane RFQ	H$_{210}$	100–400	$\lesssim 0.12$
IH linac	H$_{110}$	$\lesssim 300$	$\lesssim 0.3$
CH linac	H$_{210}$	250–600	$\lesssim 0.6$

Table 5.2: Comparison of H-mode accelerating structures, their operating frequencies and particle velocities

5.1.3 Combined pre-accelerator

The designs for the *PAMELA* FFAG lattices apply to both protons and carbon ions because they have the same magnetic rigidity $B\rho$,

$$B\rho = \frac{\gamma m v}{|q|}. \tag{5.1}$$

This constraint on rigidity determines a scaling law between the injection energies of protons and carbon 6+ ions. As the mass of carbon 6+ ions is approximately twelve times and the charge is six times that of protons, the product $\gamma\beta$ of the carbon ions must be about half that of the protons in order to match the rigidities at injection. Using accurate masses of the protons and carbon 6+ ions, the ratio is 1.9852. Taking 30.97 MeV as the kinetic energy at injection for protons T_p,

$$\begin{aligned}
T_\mathrm{p} &= 30.97\,\mathrm{MeV}, \\
\gamma_\mathrm{p} &= \frac{E_\mathrm{p}}{m_\mathrm{p}c^2} = \frac{T_\mathrm{p} + m_\mathrm{p}c^2}{m_\mathrm{p}c^2}, \\
\beta_\mathrm{p} &= \sqrt{1 - \frac{1}{\gamma_\mathrm{p}^2}} = 0.2508.
\end{aligned}$$

Asserting the equality of rigidities gives

$$\begin{aligned}
\gamma_\mathrm{c}\beta_\mathrm{c} &= \frac{6m_\mathrm{p}}{m_\mathrm{c}}\gamma_\mathrm{p}\beta_\mathrm{p} = \frac{\gamma_\mathrm{p}\beta_\mathrm{p}}{1.9852} \\
\beta_\mathrm{c} &= \frac{\gamma_\mathrm{c}\beta_\mathrm{c}}{\sqrt{1 + (\gamma_\mathrm{c}\beta_\mathrm{c})^2}} = \frac{\gamma_\mathrm{p}\beta_\mathrm{p}/1.9852}{\sqrt{1 + (\gamma_\mathrm{p}\beta_\mathrm{p}/1.9852)^2}} = 0.1294, \\
\gamma_\mathrm{c} &= \frac{1}{\sqrt{1 - \beta_\mathrm{c}^2}}, \\
T_\mathrm{c} &= (\gamma_\mathrm{c} - 1)m_\mathrm{c}c^2 \\
&= 94.73\,\mathrm{Mev} = 7.89\,\mathrm{MeV/u},
\end{aligned}$$

so a single FFAG ring that accepts 30.97 MeV protons at injection will also accept carbon 6+ ions injected at 7.89 MeV/u.

A cyclotron has a fixed magnetic field and a fixed radius at extraction, and therefore a fixed extraction rigidity. A cyclotron that produces 30.97 MeV protons would be able to accelerate carbon 6+ ions to 7.89 MeV/u, or carbon 4+ ions to 3.52 MeV/u.[2] A combined proton and carbon cyclotron pre-accelerator would therefore match the correct energies for injection into *PAMELA*, as long as a source of carbon 6+ ions were available for injection into the cyclotron. However, the carbon 6+ current from available ion sources is relatively low, and, coupled with the high beam losses in available cyclotrons, this would not give a high enough injection current for *PAMELA*. Carbon 4+ ions cannot be stripped at sub-MeV energies before the pre-accelerator, and stripping after the cyclotron would produce a mismatch in energy, so generating the carbon 6+ ions with this method is also not feasible. Therefore, a combined proton and carbon cyclotron pre-accelerator is challenging, if not impossible, with current technology.

Laser wakefield accelerators could possibly be used for a combined pre-accelerator, but this new technology has not been tested for this application and would be a very high risk option.

For these reasons, separate pre-acceleration stages have been designed for carbon and protons, and the ions then transported by a common MEBT to inject into *PAMELA*.

5.2 Planned injection system

A 30 MeV proton cyclotron can be acquired for the proton beam injection, and an RFQ and linac can be designed for the carbon injection. An advantage of this is that the facility can be realised in three stages:

1. A proton cyclotron injector and single FFAG ring for proton therapy;
2. A carbon linear injector into the same single FFAG ring for biological and clinical studies;
3. A second FFAG ring for carbon therapy.

The first stage would produce a proton therapy beam with all the advantages of FFAG accelerators over cyclotrons, especially the inclusion of spot-scanning technology. The second phase would allow vital clinical and biological studies to characterise cellular response to carbon ions. The accelerator would also be capable of accelerating beams of other ions that share the same charge-to-mass ratio, and this could be used to compare the biological effectiveness of different ions. Helium ions are of particular interest, as they release a relatively large quantity of energy, but are less massive than carbon and therefore easier to accelerate and less prone to fragmentation during therapy. The final phase would produce a carbon therapy beam with all the advantages of FFAG accelerators over synchrotrons. Figure 5.4 is a schematic of the proposed injector system including the LEBT, pre-accelerator and MEBT [see 59].

The first component in the injection system for each ion beam will be the ion source that provides a low energy current of particles. A commercially-acquired proton cyclotron will include a proton source inside the machine, so it is only the carbon ion source that needs to be considered.

---

[2] The value for carbon 4+ comes from requiring the same magnetic rigidity and therefore a velocity that is a third of the velocity of the protons, and using the same calculation as for carbon 6+ ions above.

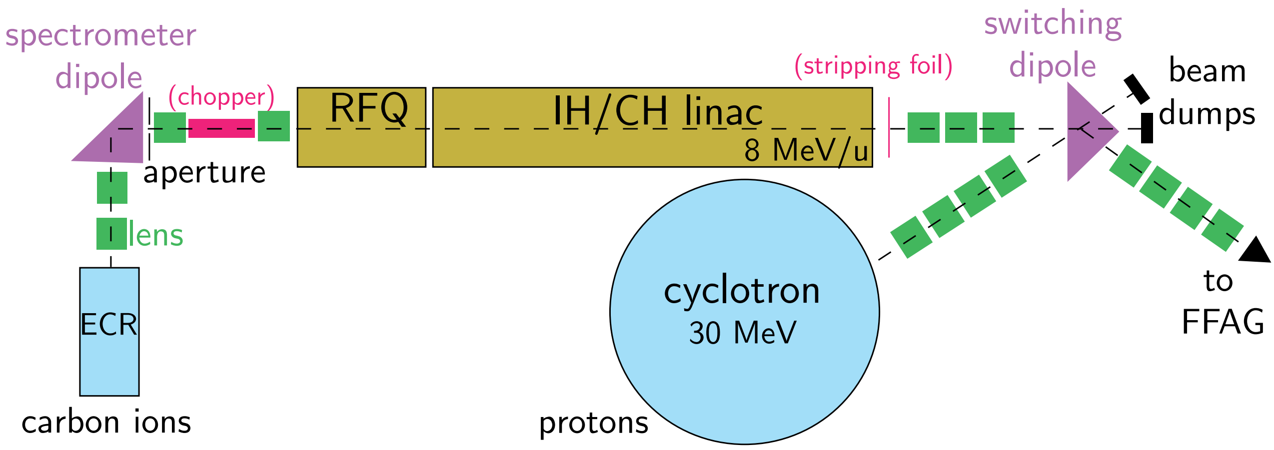

Figure 5.4: Schematic of proposed injector assembly from source to injection, including ion sources, LEBT, pre-accelerators and MEBT; the proton source is contained within the cyclotron.

Many different charge states of carbon will be produced in the ion source, and the unwanted charge states will need to be removed before pre-acceleration to avoid collisions with the injector assembly. The LEBT line must include a spectrometer dipole to select only the required charge state and remove the others. Different charge states will bend at different radii of curvature in the dipole (see Equation 3.10), and therefore will be focused to different locations by a magnetic lens before the spectrometer dipole. An aperture after the spectrometer dipole ensures that only the ions in the necessary charge state are allowed to enter the pre-accelerator. The final section of the LEBT line may include a chopper if this is required, together with two lenses that act firstly to ensure that the beam through the chopper is parallel and secondly to focus the beam into the RFQ, as the RFQ requires a convergent beam to yield a reasonable transmission. The chopper could be used to create the correct beam structure for acceptance into the linac and into *PAMELA* itself, and also to control the beam intensity at output from *PAMELA* to accomplish the correct dosage for treatment. The inclusion of the chopper depends on decisions about the beam delivery system and the acceleration scheme in the FFAG, as well as the injection parameters.

A stripping foil would not be required for a carbon 6+ RFQ and linac. However, the injector system has been designed to include the fall-back option of accelerating carbon 4+ ions from the ion source and stripping them after the linac, to increase the charge state from carbon 4+ ions to carbon 6+ ions. As the *PAMELA* project is still in the design phase, it is possible that changes to the FFAG accelerator or to the high energy beam transport (HEBT) lines, gantries and targeting systems require a greater current input from the injector. To achieve this higher current, the abundance of carbon 4+ ions from ECR ion sources could be utilised, along with the stripping foil, to produce higher current carbon 6+ beams.

A switching dipole will combine the proton and carbon beam lines into a single MEBT that will transport the ions to the injection point into *PAMELA*. The MEBT also prepares the beam structure to match the FFAG injection requirements, such that loss of current at injection is reduced as much as possible.

Parameter	Value
Beam radius	2 mm
Beam divergence	50 mrad
Beam emittances (normalised RMS)	0.25 π mm mrad

Table 5.3: Typical ECRIS beam parameters [44, 62]

5.2.1 Ion sources

The selection of a cyclotron for the proton injector will include a built-in ion source, but for the carbon injector, a separate source will be required.

An *electron cyclotron resonance* (ECR) ion source uses gases or vapours in a fixed magnetic field, with microwaves to excite electrons at their cyclotron resonance frequency (Equation 3.11). The electrons collide with the atoms in the gas and ionise them to produce the required ion beams. ECR sources provide beams of high quality, stability and reliability, and easy maintenance [60]. Depending on the injection scheme, different types of ECR ion source would be most suitable. For multi-term injection, a *super-nanogun* source can be employed. For a single-turn injection scheme, a *hyper-nanogun* source is more appropriate, although a super-nanogun ECR with a superconducting magnet could alternatively be used [52]. Since *PAMELA* takes advantage of a high repetition rate of 1 kHz, a single-turn injection is most likely, but a multi-turn injection should not be excluded as an option, as this would increase the available beam current.

The ions are extracted from the ion source by a fixed electrostatic potential. A typical extraction potential is 24 kV [60], which would extract carbon 4+ ions at $24\,\mathrm{kV} \times 4e\,\mathrm{C} = 96\,\mathrm{keV} = 8\,\mathrm{keV/u}$. Existing ECRIS devices can produce carbon 4+ ions at this energy with a beam current of 200 μA or higher [60, 61]. The same extraction potential of 24 kV would produce a carbon 6+ ion beam at 12 keV/u, but with a much reduced current, of the order of 1 μA [49, 50].

Typical output beam parameters are given in Table 5.3.

5.2.2 Protons

The beam from the cyclotron (see § 5.1.1) is transported to the first FFAG ring for injection by the *medium energy beam transport* (MEBT) line. Part of this line includes a switching dipole, which combines the proton beam with the carbon beam. The switching dipole has one set of parameters that accept the proton beam and direct it to injection, and another set of parameters that accept the carbon beam and direct this to injection instead. Before the switching dipole are four quadrupoles that control the parameters of the proton beam for matching into the FFAG accelerator (see Figure 5.4). After the switching dipole are four more quadrupoles that match both the proton and carbon beams into the main ring.

One possible injection scenario is displayed in Figure 5.5. Investigations for this scenario using the *MADX* code produced the beam optics plotted in Figure 5.6a.

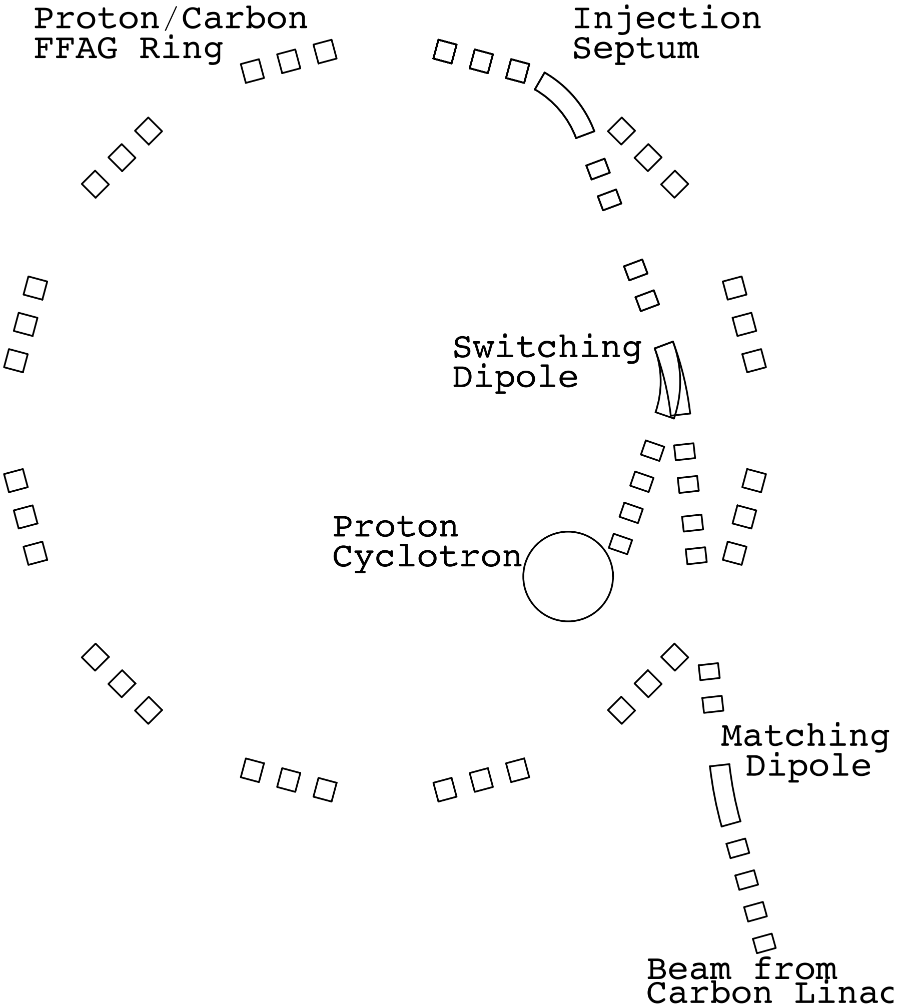

Figure 5.5: MEBT injection layout for *PAMELA*, based on a cyclotron inside the FFAG ring; Image courtesy of Dr. M. Aslaninejad

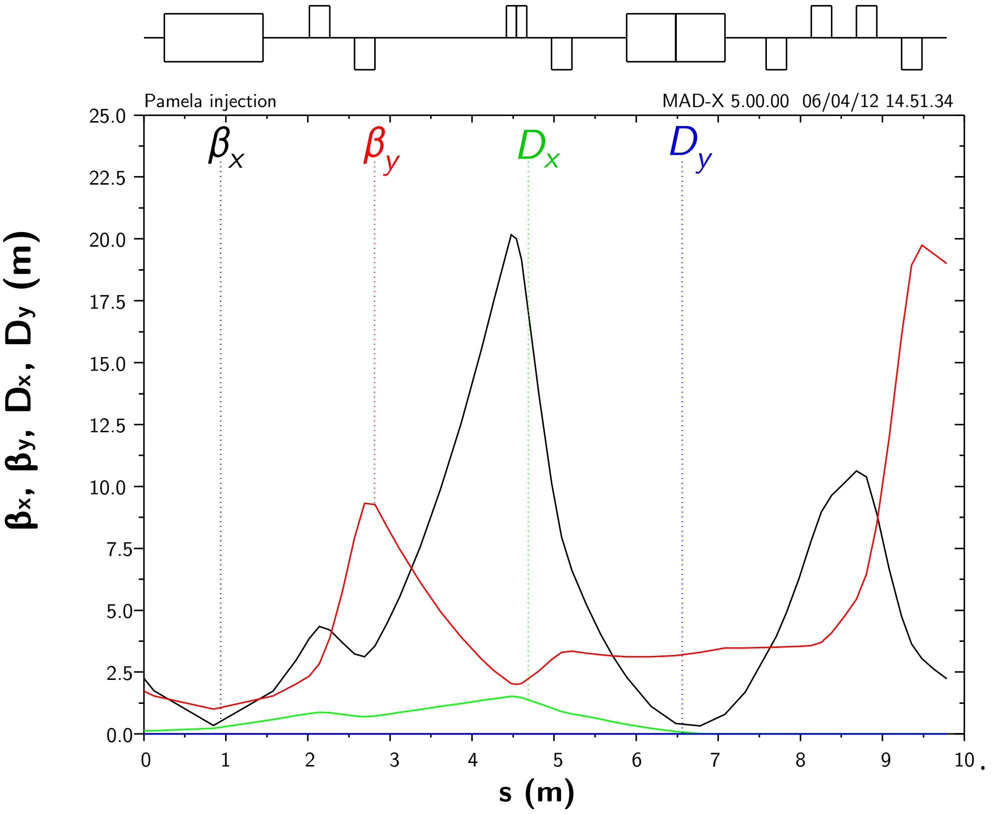

(a) Proton line

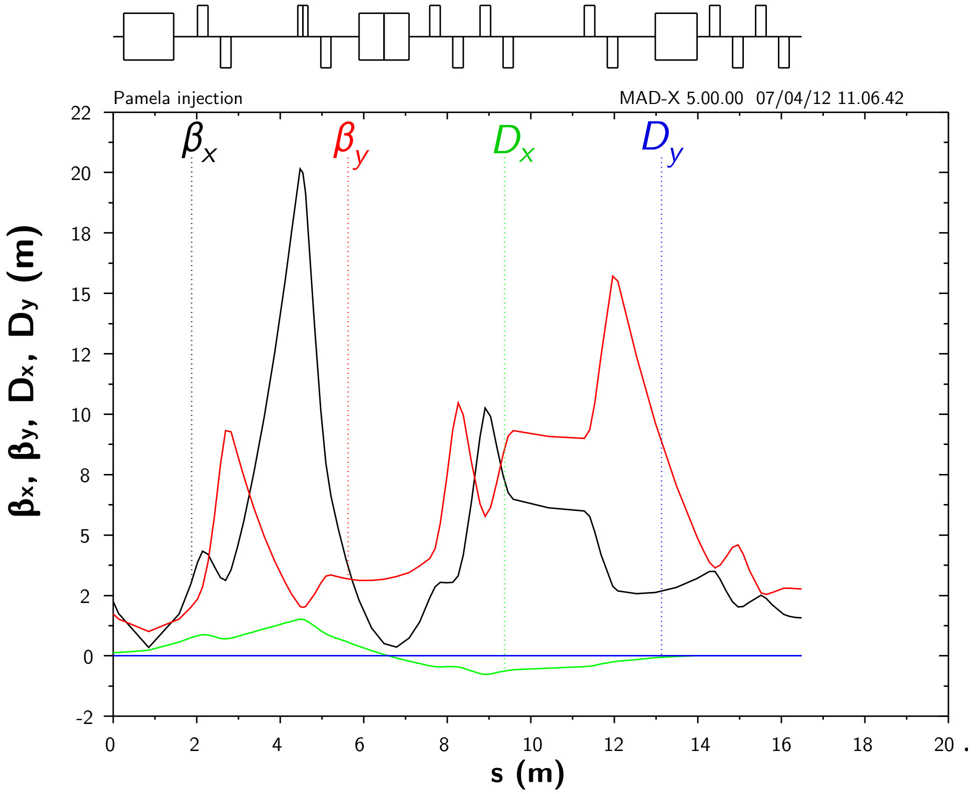

(b) Carbon line

Figure 5.6: Beta functions and dispersion for (a) the proton line, and (b) the carbon line, as shown in Figure 5.5—the optics are shown in the inverse configuration, such that the injector is located on the right and the FFAG cells on the left; Images courtesy of Dr. M. Aslaninejad

5.2.3 Carbon

The *low energy beam transport* (LEBT) line transports the particles from the ion source to the pre-accelerator (refer to Figure 5.4). Four solenoids (rectangular coils) are used as lenses for transversal focusing, and a spectrometer dipole and apertures for selecting the correct charge state. There is also the possibility of including a low-energy chopper for controlling the beam current.

The trajectories of carbon ions from the ion source to the RFQ are plotted in Figure 5.7. Two solenoids (S1 and S2) before the spectrometer dipole bring the beam parallel, and two more solenoids (S3 and S4) after the dipole focus the beam into the RFQ. The dipole itself (D1) bends the different charge states of carbon ions at different rates, and an aperture after the dipole selects only the carbon 6+ ions to continue. By adjusting the dipole field, different charge states can be selected, such as the carbon 4+ ions, should this be required. Figure 5.7 demonstrates the selection of the carbon 6+ ions using two apertures and a switching dipole: the first aperture removes many of the lower charge-state ions that have not been selectively focused by the solenoids, and the second aperture removes almost all remaining lower charge-state ions that have bent at lesser angles through the spectrometer dipole.

The carbon ions are then accelerated. The first stage of acceleration is an RFQ, which is the subject of the rest of this thesis. Following the RFQ, a linear drift-tube accelerator (linac) is used to bring the carbon ions to full injection energy. As noted in § 3.2, a linac is likely to produce a maximum average accelerating field gradient of $\sim 3.5\,\mathrm{MV/m}$, which means that for a full proton therapy machine to bring the protons to 230 MeV would require a 65 m linac. For a carbon injector, however, the total length would be approximately 5 m, and a linac brings the advantages of high current limit and transmission [44]. An CH structure would be used for carbon 6+ ions, whereas an IH structure would be better for carbon 4+, as this is more effective at low velocities than the CH structure, in terms of the power requirements [57, p. 90].

In an RFQ the accelerator provides both accelerating and focusing forces. In a linac, however, there is no focusing force. Therefore, the resonant cavities must be interspersed with quadrupoles to keep the beam focused.

Downstream of the linac are more quadrupoles and a dipole to match the beam for acceptance into the FFAG accelerator and reduce the dispersion, and then the carbon MEBT merges with the proton MEBT at the switching dipole. Similar *MADX* simulations for carbon as for the proton MEBT show a good match to the FFAG injection parameters (see Figure 5.6b).

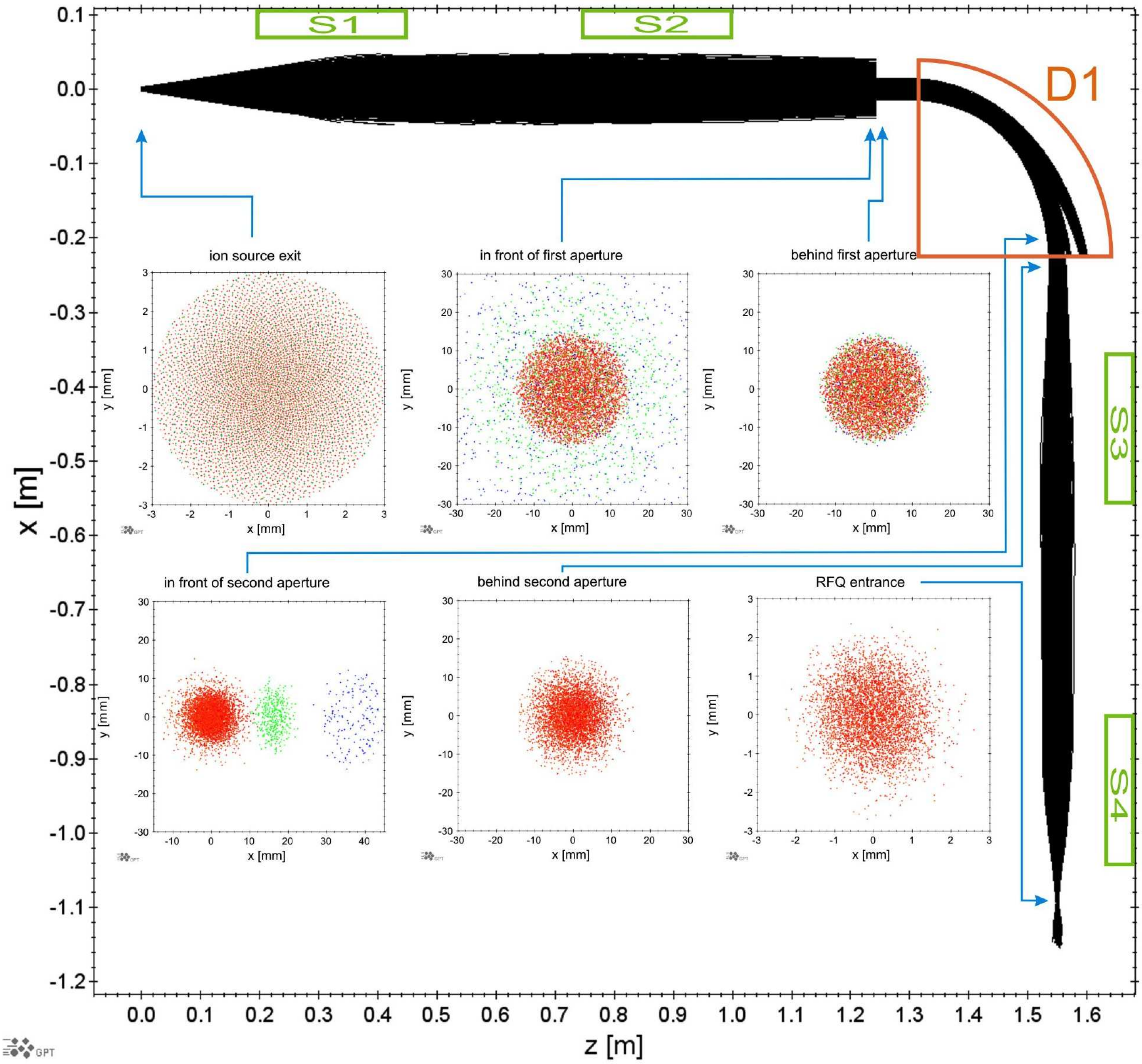

Figure 5.7: Trajectories of carbon 6+ (5000, red), 5+ (1000, green) and 4+ (1000, blue) ions through the LEBT, showing transverse beam profiles at important locations (note the smaller scale at the focal points in the first and last profiles) and indicating the positions of solenoids and spectrometer dipole; images courtesy of Dr. J. Pozimski

5.3 RFQ

A linac is not efficient for accelerating particles from the very low energies of the ion source. For this reason, a first-stage acceleration structure must precede the linac. This structure is the *radio-frequency quadrupole* (RFQ), which is the subject of the remainder of this thesis. The primary function of the RFQ is to increase the particle energy to a value that is an efficient starting point for the linac, but it also performs the secondary function of bunching the beam—converting the continuous (DC) beam from the ion source to a pulsed beam that can be easily accelerated in a periodic structure.

Chapter 6 describes how the RFQ performs these bunching and accelerating functions. Chapter 7 details the novel method developed for this thesis to design, simulate and optimise an RFQ accelerator, and the application of this method to the *FETS* and *PAMELA* RFQs. Chapter 8 presents the results of these simulations, Chapter 9 suggests further evolution of the current work, and the conclusions are submitted in Chapter 10.

6 RFQ Theory

In the first stages of acceleration, the electric force $q\mathbf{E}$ overpowers the magnetic force $q\mathbf{v} \wedge \mathbf{B}$. For example, in the *Front-End Test Stand* (*FETS*) RFQ, the maximum electric field is $\sim 30\,\mathrm{MV/m}$ with $q = 1$, producing a force of the order of $3{\times}10^7\,\mathrm{N}$. At the start of the RFQ, with particle energies of $65\,\mathrm{keV}$ and therefore velocities of $3.5{\times}10^6\,\mathrm{m/s}$, the magnetic field strength required to produce the same force would be at least $8\,\mathrm{T}$. An electrostatic quadrupole is therefore much more effective than a magnetic quadrupole for focusing the particles at these low energies.

A *radio-frequency quadrupole* (RFQ) uses electric forces both for focusing and for acceleration. RFQs provide multiple functions in low-energy pre-acceleration: firstly, strong focusing in the transverse plane (see § 3.1.2), due to the alternating gradient effect of the RF field. Secondly, bunching the beam, creating the correct time structure for acceleration. Thirdly, acceleration of the particles. Combining all three functions into a single device saves space and energy, but more importantly for high current applications such as *FETS*, the space-charge effect can be more efficiently controlled—focusing at the same time as acceleration constantly counteracts the space-charge forces, as opposed to a drift tube linac (DTL) where the space-charge forces defocus the beam between the focusing quadrupoles [63]. At the low beam energies for which electrical forces are more efficient, space-charge forces are also stronger, so the application of RFQs to this energy range is doubly apposite.

This oscillation of the RF is vital for transverse focusing, as a static quadrupole would focus in one transverse direction but defocus in the other. As the field oscillates in time and the particles travel down the length of the RFQ, the field produces a net focusing effect in both transverse dimensions. § 6.1 deals with the transverse focusing of the RFQ.

The quadrupole is created by rods or vanes within a resonant cavity carrying the oscillating field. If these rods were uniform along the length of the RFQ, then the field would be transverse only and produce focusing forces but no acceleration. Modulations on the rods or vanes of the RFQ are used to create a longitudinal accelerating field. § 6.2 treats the accelerating force along the RFQ.

The phase of the modulations must be matched to the velocity of particles as they move through the RFQ, and the length of the modulations adjusted as the particle energy increases. The modulation patterns also change along the length of the RFQ to create the required time structure in the beam and thereby ensure coherent acceleration. The DC beam must first be bunched so that the particles are in phase with the accelerating force, which is achieved with a certain pattern of modulations. The particle bunches can then be accelerated, by a different pattern of modulations. § 6.3 describes the design of the modulation patterns.

The rods or vanes of the RFQ must be contained within a resonance cavity to shape the RF field as required, and tune the frequency. The design considerations for the cavity are discussed in § 6.4.

The equations governing the field and particle motion within the RFQ are described in Appendix B.

6.1 Quadrupole focusing

The transverse electric quadrupole field (see Figure 6.1) focuses in one transverse dimension and defocuses in the other transverse dimension. As the field oscillates, the direction of the focusing force alternates, and produces a net focusing force in both transverse directions over time (see § 3.1.2).

The two-term potential function (see § B.1) approximately describes the potential in the RFQ,

$$V(r, \theta, z) = \frac{V_0}{2}\left[A_{01} r^2 \cos 2\theta + A_{10} I_0(kr) \cos kz\right]. \tag{B.4}$$

The electric field is calculated from this potential, which in the x-coordinate gives (see § B.2),

$$E_x = -\frac{V_0}{2}\left[2A_{01}x + kA_{10} I_1(kr)\frac{\partial r}{\partial x}\cos kz\right]\sin(\omega t + \phi). \tag{B.10}$$

To analyse the motion in the x-direction of a particle with mass m and charge q, the displacement is assumed to be small, such that $I_1(kr) \approx kr/2$. For the synchronous particle, the equation of motion is shown to fit the form of the Mathieu equation (Equation B.18), the solution of which is,

$$x = C \sin \sigma_{0t}\tau \left[1 + \varepsilon \sin 2\pi\tau\right], \tag{B.22}$$

where the first sinusoidal term describes the betatron phase oscillation and the second sinusoidal term is the *flutter factor* describing a variation at the radio frequency.

Similar derivations for the y-direction show that the quadrupole field successfully contains the beam in both transverse directions.

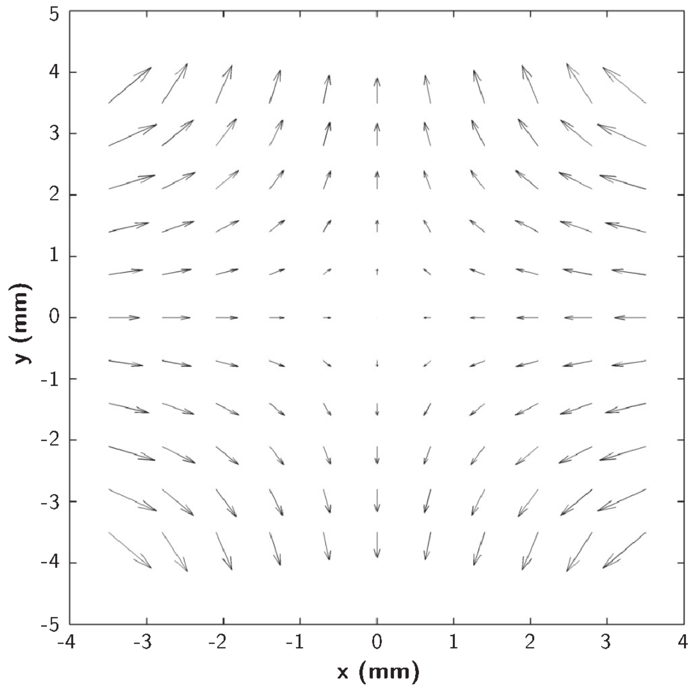

Figure 6.1: Transverse field map for the *FETS* RFQ design; Image courtesy of Dr. S. Jolly

6.2 Acceleration

A quadrupole with no modulations would have no longitudinal field and hence no accelerating force, as the transverse fields would have the form $E_x = -Cx \sin \omega t$ and $E_y = Cy \sin \omega t$, where C is a constant, and, as the quasi-electrostatic field satisfies the Laplace equation,

$$\frac{\partial E_z}{\partial z} = -\left(\frac{\partial E_x}{\partial x} + \frac{\partial E_y}{\partial y}\right), \tag{6.1}$$

and the boundary conditions exclude a constant E_z field, this would leave $E_z = 0$ as the solution.

With the modulations along the length of the RFQ, the transverse fields instead take the form

$$E_x = -Cx\,(1 + \epsilon \cos kz) \sin \omega t, \tag{6.2}$$

$$E_y = Cy\,(1 - \epsilon \cos kz) \sin \omega t, \tag{6.3}$$

where ϵ is the magnitude of the modulation in the field relative to the standard quadrupole field [32, p. 489]. The first term in each expression gives the transverse focusing effect and the second term gives the acceleration effect.

Substituting into Laplace's equation (Equation 6.1) gives

$$\frac{\partial E_z}{\partial z} = 2\epsilon C \cos kz sin\omega t, \tag{6.4}$$

and integrating gives the longitudinal field

$$E_z = \frac{2\epsilon C}{k} \sin kz \sin \omega t \tag{6.5}$$

$$= \frac{\epsilon C}{k} \left[\cos\left(kz - \omega t\right) - \cos\left(kz + \omega t\right)\right]. \tag{6.6}$$

This longitudinal electric field resolves into two travelling waves, one moving with the ion beam and one moving against it. The wave moving with the particles will provide an accelerating force.

More detailed versions of these equations can be derived from the two-term function, as detailed in § B.3.

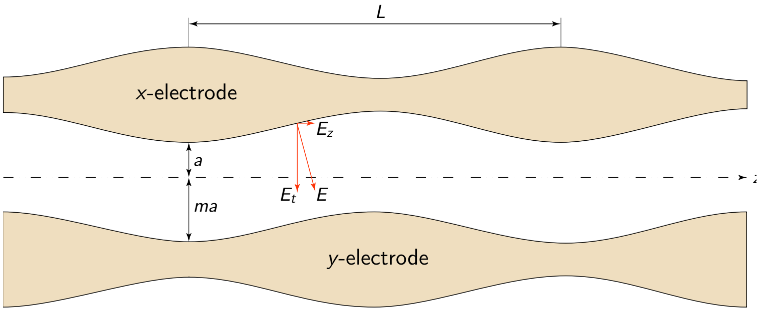

Figure 6.2: Schematic of rod modulations creating a longitudinal electric field

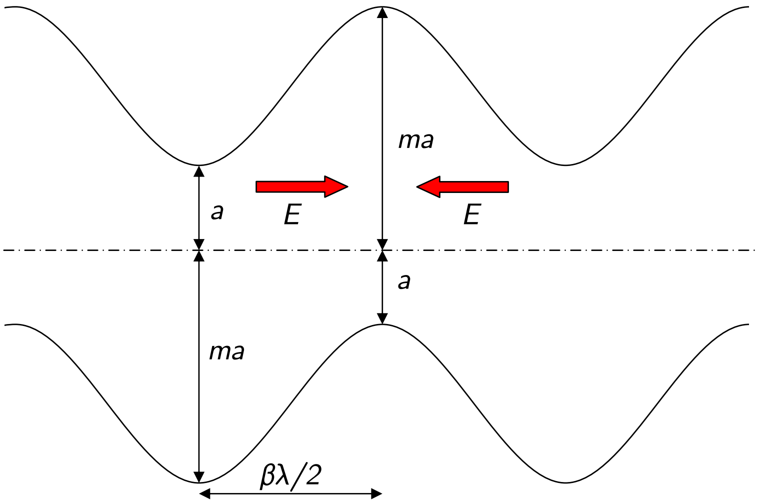

Figure 6.3: Schematic of RFQ modulations, showing definitions of modulation parameters a and m and cell length $\beta\lambda$; one of the two electrodes shown is a horizontal electrode, and the other is a vertical electrode; one will be at a positive potential at a given time and the other will be at a negative potential; Image courtesy of Dr. J. Pozimski

The horizontal and vertical electrode pairs are modulated in anti-phase (see Figure 6.2 and Figure 6.3) to produce the sinusoidal E_z field pattern. The modulation period is set to $\beta\lambda$ where β is the velocity of the synchronous particle and λ is the wavelength of the RF. λ will remain constant along the length of the RFQ but β will increase as the particles are accelerated. Adjusting the modulations to keep in phase with the motion of the particles ensures that the particles will continue to be accelerated coherently along the length of the RFQ.

6.3 Modulation design

The design of the modulation profile along the length of the RFQ must be optimised for the particular application of the accelerator. For example, the high current of the *FETS* RFQ means that reducing the impact of high space-charge forces is a defining consideration, whereas the physical space constraints of a hospital environment and the relatively low current of the the *PAMELA* RFQ mean that achieving maximum acceleration in a shorter length is more critical.

An RFQ is often described in four sections [63]: the *radial matching section*, which collects the incoming beam and matches it to the RF phase, the *shaper*, which captures the continuous (DC) beam and adjust the synchronous phase to allow the beam to be bunched, the *gentle buncher*, which bunches the beam ready for acceleration, and the *accelerating section*, which does the actual work of accelerating the particles. These functional sections may overlap spatially.

Radial matching section The transverse motion of particles (Equation B.22) in the RFQ is dependent on the phase of the RF field through the factor $\sin\phi$ in the term Δ_{RF} (Equation B.21). This means that the input acceptance of the RFQ is time-dependent. To accept the whole beam from the ion source, a radial matching section is used at the front of the RFQ, in which the electrodes

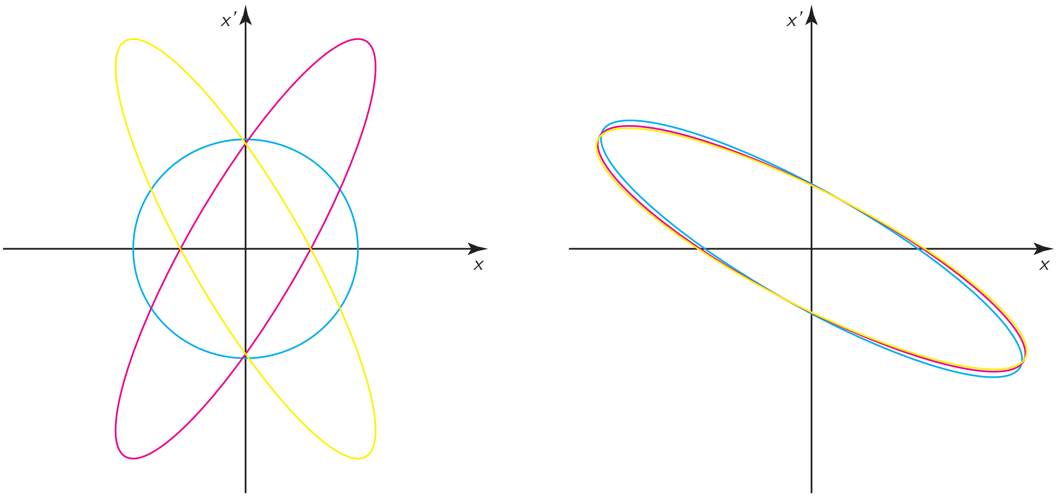

(a) End of matching section **(b)** Start of matching section

Figure 6.4: Phase space ellipses at (a) the end and (b) the start of the radial matching section, showing ellipses for three different RF phases separated by 90°; image adapted from [63]:
(a) the acceptance at the end of the RFQ is highly time-dependent, and the overlap between different phase ellipses is small;
(b) the matching section is designed to remove this dependence, such that the acceptance at the start of the matching section is independent of time.

curve away from the beam axis, so the focusing strength at the start of the radial matching section is effectively zero. The focusing strength increases with z over a number of periods of RF oscillation so the beam is slowly squeezed into the acceptance of the RFQ in both transverse dimensions. There are no modulations on the vanes in the matching section as the required effect is purely transverse. The acceptance at the start of the matching section should be as close to time-independent as possible.

Figure 6.4 illustrates the acceptance of an RFQ with and without the matching section. Three ellipses correspond to three different times, separated by 90° of RF phase. The matching section rotates the phase space so that all three ellipses coincide at the start of the matching section, and so the acceptance of the RFQ is independent of time. This is important for collecting the maximum current from a continuous ion source.

Shaper Once the beam is successfully captured into the RFQ, it must be prepared for acceleration. To capture a continuous beam, the synchronous phase ϕ_s about which all the particles oscillate must be at a stable point of the RF sinusoidal oscillation. That means the synchronous phase at the start of the RFQ must be $-90°$. For successful acceleration, however, the phase should be around $-30°$. The function of the shaper is to apply an accelerating force to begin to move the synchronous phase, and to start the bunching process.

Gentle buncher To achieve the highest possible capture efficiency of the DC particle beam from the ion source, adiabatic bunching and acceleration should be employed in the RFQ. The gentle buncher is the functional section of the RFQ that creates the bunches or pulses required for acceleration, so that all particles in the beam end the gentle buncher in phase with the accelerating force.

For a high current beam, compressing the DC beam into bunches increases the space-charge forces, so a method of adiabatic bunching is used that keeps constant the longitudinal small angle oscillation frequency, the spatial length of the separatrix ψ in phase space that defines the stable accelerating phase, and the transverse focusing strength [64].

By observing various relations (see Appendix B), the values for the modulation parameters can be determined, given the required values at one point. The point at the end of gentle buncher can be used, as the optimal parameter values for the start of acceleration are known, and from this point the modulation parameters can be worked backwards towards the start of the RFQ.

Accelerating section Once the beam is bunched and matches the phase of the RF to catch the accelerating force, the depth of the modulation determined by a and m can remain constant and only the length of the cells change to keep synchronicity with the increasing velocity of particles, $l_{\mathrm{c}} = \beta_{\mathrm{s}}\lambda$. The synchronous phase ϕ_{s} is typically kept constant during acceleration, but can continue to increase slightly to increase the accelerating force, providing the stability of the acceleration bunch is not compromised.

Figure 6.5 displays an example set of cell parameters along the length of the RFQ. There are the modulation parameters, a, the closest distance from the beam axis to the electrode, ma, the furthest such distance, m, the ratio between these two distances, r_0, the average of these two distances, and L, the length of the cell. There are also energy parameters, W, the energy of the reference particle, and ϕ, the phase of the reference particle. The modulation parameters are the physical values used to construct the machine. The energy parameters describe the dynamics of the particles, and are derived from the modulation parameters. When designing an RFQ, the ideal pattern of W and ϕ for coherent acceleration is the target, and the design process involves adjusting the modulation parameters to achieve this goal.

The energy parameters in the example show the energy W (blue dashed line) staying mostly constant through the matching, shaping and bunching sections, and then accelerating consistently through the acceleration section. The phase ϕ (red dashed line) is also adjusted from $-90°$ at the start of the shaper to collect the full continuous input beam, up to $-30°$ for stable acceleration. As this is varied, the accelerating force begins to appear, so the acceleration section cannot easily be separated spatially from the other sections.

The changes in dynamics are realised by adjusting the physical attributes of the vanes. Through the shaping and bunching sections, the distances from the beam axis are increased reasonably symmetrically to keep the average distance r_0 roughly constant. Figure 6.5b shows the increase in a (blue) and symmetric increase in ma (red)—produced by varying the parameter m (violet)—and the constancy of the average distance r_0 (yellow) between these. Throughout the accelerating section these values do not change significantly. The length of each cell L (green) increases as the energy of the particles increase to keep the accelerating force in phase with the particles as their velocity increases.

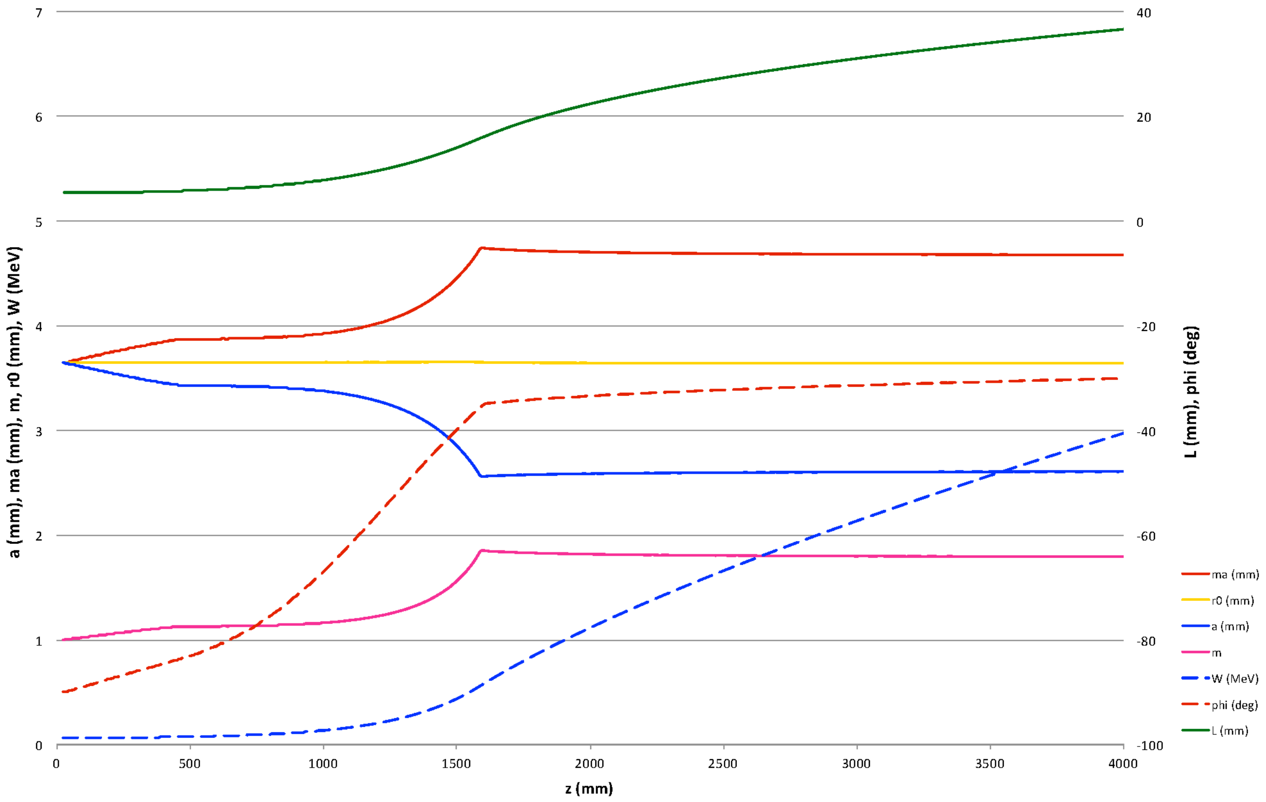

(a) Cell parameters

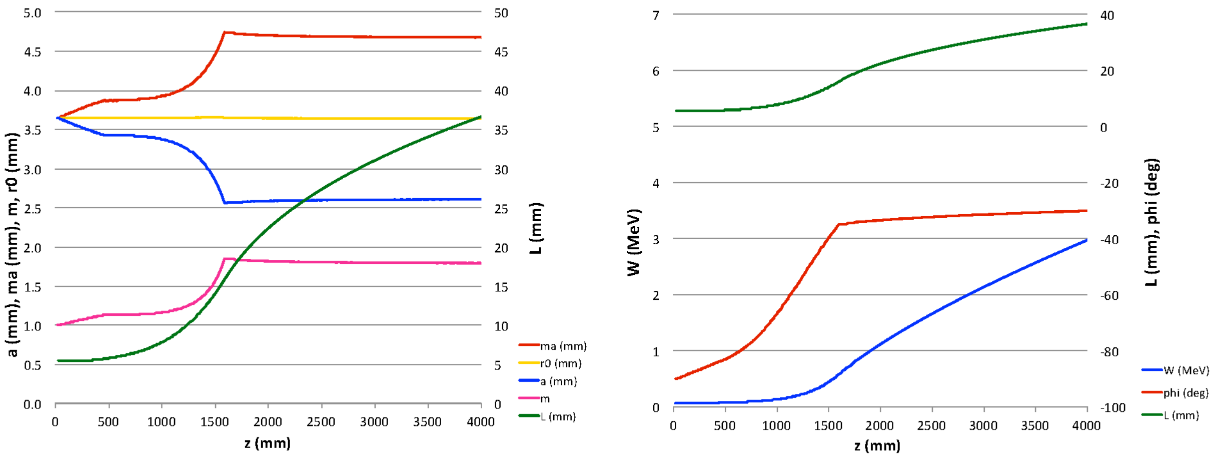

(b) Modulation parameters

(c) Energy parameters

Figure 6.5: (a) Cell modulation parameters for the *FETS* RFQ, and the same parameters split into separate plots relating to (b) vane modulations and (c) particle dynamics

There are many further details to take into account when deciding upon the optimal target parameters, to which the physical modulations are to be fitted. One example is the coupling of oscillations in the transverse and longitudinal dimensions leading to emittance growth along the length of the RFQ, dependent upon space-charge forces. A method called *equipartitioning* describes the matching of the magnitude of the velocity spreads in all coupled directions, so that the emittance growth is be kept to a minimum [65, 66]. Another example is halo formation—a diffuse halo of particles forms around the core of the beam, and these halo particles are much more likely to collide with the walls, be lost from the beam and possibly cause heat and radioactivation problems. Detailed equipartitioning can also help reduce halo formation, as can smoothing of parameter changes and non-linear field components [67, 68].

6.4 Resonant cavity

The vane tip potential is produced by inducing radio-frequency (RF) waves within a resonant cavity, such that the components of the electromagnetic field on the vanes tips or rods are the required electric potentials oscillating sinusoidally in time. The correct design of the resonant cavity is crucial in order to produce the appropriate field near the beam axis for particle transport.

Many features of the cavity are similar to the cavities used for H-mode drift tube linacs, as discussed in § 3.2, as both use H-mode RF fields. The transverse field between the vanes or rods must be a quadrupole field, in order to provide strong focusing, as depicted in Figure 6.6a (see also Figure 5.3 for comparison of field cross-sections). Longitudinally, the wavelength of the field must also be matched to the combination of intended velocity of the particles and the modulation on the vanes, such that the reference particle stays in phase with the field. Once the vanes have been manufactured, the modulation patterns cannot be altered, so any tuning to match the beam velocities must affect the resonant frequency. For this purpose, tuning plugs can be added to the RFQ structure for fine tuning of the frequency [69, 70], as depicted in Figure 6.7.

For the *FETS* RFQ as an example, the initial design of the resonant cavity involved a series of electromagnetic models, in which various parameters were modified and the RF eigenmodes calculated to find the resonant frequency. This frequency was then optimised to match the available RF sources, coupling technologies, and required acceleration profiles, and to facilitate the most efficient use of energy by maximising the cavity's quality factor. Further optimisation of the design was also carried out to control the surface currents, and so constrain the worst of the heating effects to areas of the cavity that can be easily cooled [69]. The next stage was the construction of a cold model of the RFQ, which has no accelerating modulations, for verification of the modelling and manufacturing process. The resonant characteristics of this model were measured and compared with the model [71], and improvements suggested for modelling and construction of the final RFQ, which is currently underway.

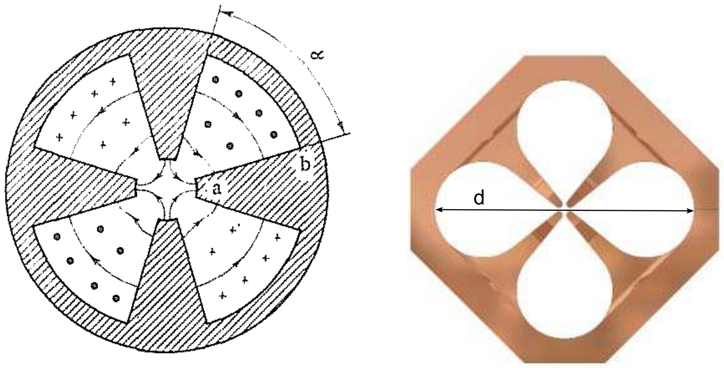

(a) 4-vane field cross-section [64] **(b)** 4-vane cross-section [69]

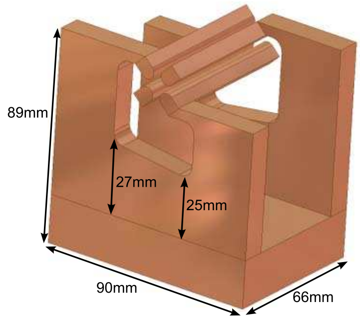

(c) 4-rod schematic [69]

Figure 6.6: RFQ cavity design parameters

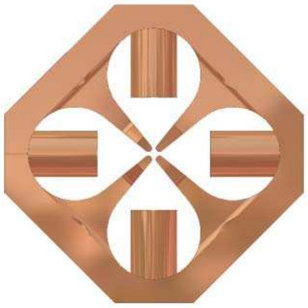

Figure 6.7: *FETS* 4-vane RFQ cross-section with tuning plugs fully inserted [69]

The RFQ requires much more engineering than simply the modulation pattern and a hollow resonant cavity. During the addition of extra features such as cooling channels, tuning plugs, front and rear flanges and end-plates, and diagnostic devices, care must be taken to preserve the resonant characteristics of the cavity [71]. Also, any of these features that come close to the beam axis must be considered in the particle tracking simulations.

7 RFQ Simulations

The majority of the work carried out and presented in this thesis was focused on the development of highly resolved simulations of the electric field around the RFQ vane tips, and particle tracking simulations based on these fields, in an integrated approach based on one global RFQ model.

This chapter sets out the reasons for taking this approach (§ 7.1), describes the software packages used and the code written to interact with them (§ 7.2), and then describes the content and parameters of the simulations themselves, for benchmarking with the existing *Front-End Test Stand* (*FETS*) design (§ 7.3), the preliminary scaling studies for a *PAMELA* RFQ (§ 7.4) and the working and final *PAMELA* RFQ designs (§ 7.5). The partition of the description of the simulation code and process into these particular sections is functional rather than chronological, as much of the work was carried out simultaneously, and only near the end of the project were all these separate—yet interdependent—strands woven together into a cohesive whole.

This chapter describes the simulations, and the process of developing them, and the next chapter presents the results of these simulations in detail.

7.1 Models and simulations

The description of the particle dynamics within an RFQ are only part of the design process. The other major concerns are the engineering design and the radio frequency (RF) resonator.

The engineering design covers a huge array of parameters that must be considered before an RFQ design is complete and ready for manufacture. It must be possible to provide the specified field to the particle beam within certain tolerances, otherwise the simulated beam dynamics will be unachievable, and the RFQ will not fulfil its goal. Considerations such as machining accuracy and reasonable alignment errors can affect the final field detrimentally. Also, myriad other interactions will take place within the RFQ, and the engineering design must heed the temperature, mechanical stresses and strains, vacuum seals and electromagnetic coupling, to name but a few.

The potential at the vane tips is wholly dependent on the resonant electromagnetic field within the bulk of the RFQ, and so this field must be described precisely, and all factors that affect this field must also be investigated. In fact, the electromagnetic field distribution is coupled very strongly to the engineering design, so simulating the interactions between these is very important. For example, the manner in which the separate sections of the RFQ are joined together affects the machining and assembly difficulty, the alignment accuracy and the local field flatness.

In previous methods of modelling the beam dynamics of an RFQ, the models have been based on mathematical approximations of the vane tip field (as described in Chapter 6 and Appendix B). For this project, an alternative approach was taken, where the beam dynamics simulations were integrated with the engineering design and the electromagnetic modelling. The basis of this approach is to use *computer-aided design* (CAD) software to produce an accurate model of the whole RFQ, including the vane tips. The same model would be used for the engineering design—and finally used in a *computer-aided manufacture* (CAM) method to cut the copper to produce the vanes—as for the electromagnetic modelling and the beam dynamics simulations. This means that, when evaluating measures such as the electromagnetic field flatness, all the mechanical features are taken into account, and when simulating a particle beam, the field in the simulation will match closely with the real field in the manufactured RFQ. In practice, there must always be simplifications, such as the field modelling having small features of the design removed, and the beam dynamics simulations working from a simplified field map, due to the limitations of computer power, but there are still many advantages to this integrated design method.

This CAD-based modelling enables the theoretical investigation of many hypothetical situations that methods based on field expansions would find difficult or impossible to model. For example, a hypothetical situation could be set up in which two adjacent sections of the RFQ are misaligned by some error factor, or in which a cooling channel is clogged and stops working. The effects of these situations can be explored by modifying the CAD model and running the modelling software, producing a field map and particle tracks, which can be compared with the results without the modifications. In this way, many problems can be simulated and solutions tested, before the manufacturing process has even begun. The multi-physics modelling also allows the investigation of the interactions between different physical processes, such as how the paths of the cooling channels affect the electric field quality between the vanes.

Models based on analytic solutions or truncated field expansions seek, by their very nature, periodic solutions for motion through the RFQ. Using computer simulations allows the exploration of alternative, non-periodic solutions. This means that a solution that may be preferable—based on cost, manufacturing simplicity or myriad other concerns—could be found using simulation methods, while more traditional methods may not find it.

Also, using CAD modelling allows many different aspects of the design process to interact with one another. Having a unified approach to modelling avoids incompatibility problems when trying to relate different models to each other, for example, to evaluate the effect of various joining techniques on the electromagnetic field flatness. Using complete CAD models also brings the simulations closer to the reality of the manufactured device.

Computer modelling also enables the consideration of fringe fields and higher order modes without requiring complex or approximated analytic models. In some cases, analytic solutions cannot be found, so CAD modelling again provides solutions otherwise unattainable.

Similar work is being carried out [72, 73] to solve for the field in the RFQ by a custom, open-source, iterative Poisson solver, rather than using commercial packages like the present work. This work focuses on rewriting the electromagnetic solver section of the analytic method rather than using CAD models and multi-physics simulations. However, the Poisson solver also includes space-charge and image-charge effects with the full geometry of the vane tips, where the CAD simulations only include space-charge simulations with very generalised vane geometry, and do not include image charge. Combining the advantages of both methods would be very desirable (see Chapter 9).

7.2 Simulation code

The method of simulating the beam dynamics for the RFQ involves a number of steps, requiring various software packages and customised code for driving the simulation through these packages.

The first step (§ 7.2.1) uses the *RFQSIM* code to generate a series of modulation parameters to define each cell of the RFQ. This code is a numerical solver for the potential function described in Appendix B. This produces a periodic solution, which is then used as the first step in an iterative process to find an optimised solution using CAD modelling techniques.

The second step (§ 7.2.2) models the RFQ vane tips in *Autodesk Inventor*. The modulation parameters from the first step are imported into *Inventor* via a spreadsheet, then some *Visual Basic for Applications* (VBA) code constructs the vane tips from these parameters.

The third step takes the CAD model from *Inventor* and models the electric field in the quasi-static approximation. Two different software packages have been tried for this step: firstly *CST EM Studio* (§ 7.2.3) and secondly *Comsol* (§ 7.2.4).

The final step (§ 7.2.5) takes the field map from the electrostatic modeller, modulates it with the resonant frequency of the cavity, and tracks the particles through this field. The tracking software is called *General Particle Tracer* (*GPT*).

The modelling process is controlled from *Matlab* by custom code (§ 7.2.6). Unfortunately, it is not yet possible to interact with *RFQSIM* or *Inventor* in this way, but the rest of the simulation process is launched, controlled and analysed within *Matlab*. The code is written to enable the future addition of optimisation scripts to model multiple simulations and iteratively approach an optimal solution.

Figure 7.1 shows a schematic of the simulation code. Output files include the field map and CAD model. Input files include the modulation parameters spreadsheet, the particle parameters specification file and the field map produced by *Comsol* as an input for the particle tracking.

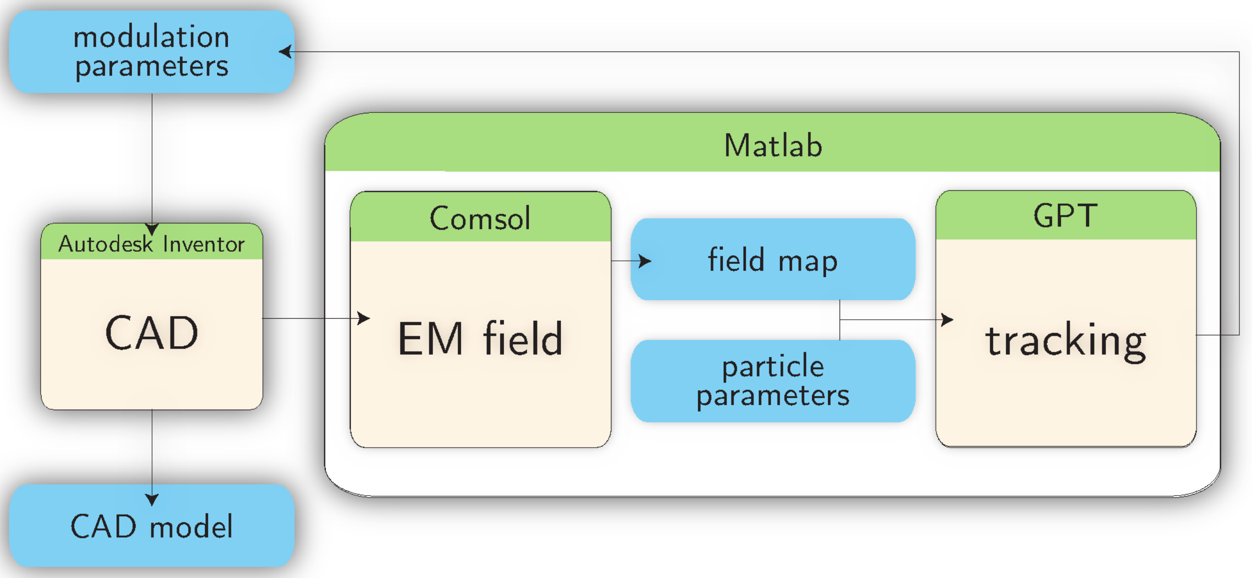

Figure 7.1: Schematic of simulation code, showing software packages, data flow and input and output files

7.2.1 RFQSIM

RFQSIM is a numerical code authored as part of the development of the RFQ pre-injector for the ISIS Spallation Neutron Source at the Rutherford Appleton Laboratory in the UK [74]. The code starts from the infinite series describing the RFQ electric field, as described in § B.1. First of all, design recipes from Kapchinskij and Teplyakov [64] and others [63] are used to produce a set of values for each cell for the acceleration efficiency A and the focusing force factor B, which correspond to the terms in Equation B.3 by $A = A_{10}$ and $B = q\lambda^2 A_{01} V/m_0 c^2$.

Next, the two-term approximation (Equation B.4) is used to find a starting set of modulation parameters that define the shape of the the RFQ tips. The code then expands the approximation to include the first eight terms of the potential function, rather than just the first two, and calculates the coefficients for this eight-term function by means of a *least-mean-squared* (LMS) error fit to the RFQ tip geometry defined by the current modulation parameters. *RFQSIM* then begins an iterative process of refining the modulation parameters, recalculating the eight-term potential function coefficients, and comparing the values of A and B to the design values, which continues until both are within 1% of the design values. This whole process continues cell-by-cell until all the modulation parameters are defined and the field is within tolerance of the design values.

In the current, CAD-based system, *RFQSIM* is used to produce a set of modulation parameters that are then converted into a CAD model and solved by the finite element method, rather than using potential function approximations. This combines the speed of the numerical methods with the power of the CAD-based systems.

7.2.2 Autodesk Inventor

The role of *Autodesk Inventor* in beam dynamics simulations is to convert the one-dimensional modulation parameters into a three-dimensional CAD model that can be used for simulating the electric field near the beam axis, for cutting the shape of the vane tips with a CAM machine, and for integrating with the other CAD elements of the RFQ design for integrated simulations.

The process of constructing a vane is implemented by custom *Visual Basic for Applications* (*VBA*) code that runs within *Inventor*. First, the modulation parameters are read from a spreadsheet. A vane profile (see Figure 7.2a) is sketched as a semi-circle with the radius of curvature specified by the spreadsheet, together with two rectangles. The upper rectangle is attached to the semi-circle and moves vertically as the vanes modulate.The lower rectangle stays at a fixed distance from the beam axis and overlaps the moving rectangle, so the final vane has a base which is parallel to the beam axis. The path along the length of the RFQ, which defines the longitudinal modulations of the vanes, is constructed in a second sketch in *Inventor* (see Figure 7.2b) using a *spline* function to fit a pseudo-sinusoidal path to the points specified in the modulation parameters spreadsheet. By combining the profile with the path, a three-dimensional vane-tip model is generated (see Figure 7.2c).

The vanes are constructed in sections, to reduce the load on computer memory. The horizontal and vertical vanes are generated separately, as they move in anti-phase and so trace different paths along the length of the RFQ. These sections are combined with matching-in and matching-out sections and end flanges (see Figure 7.3) to produce a full CAD model for the next stage of the simulations.

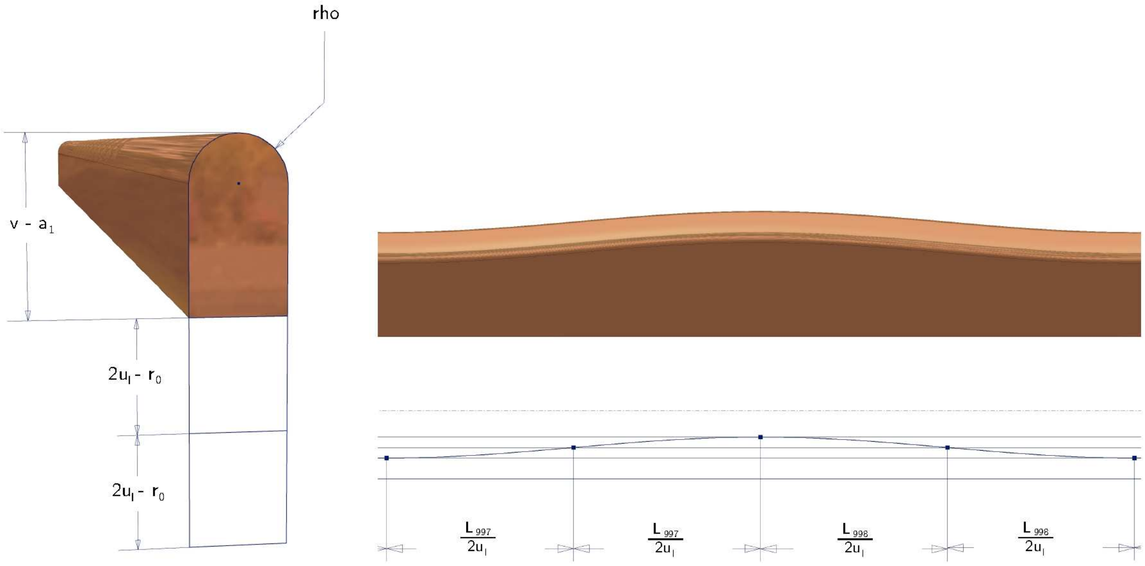

(a) Vane profile **(b)** Vane spline

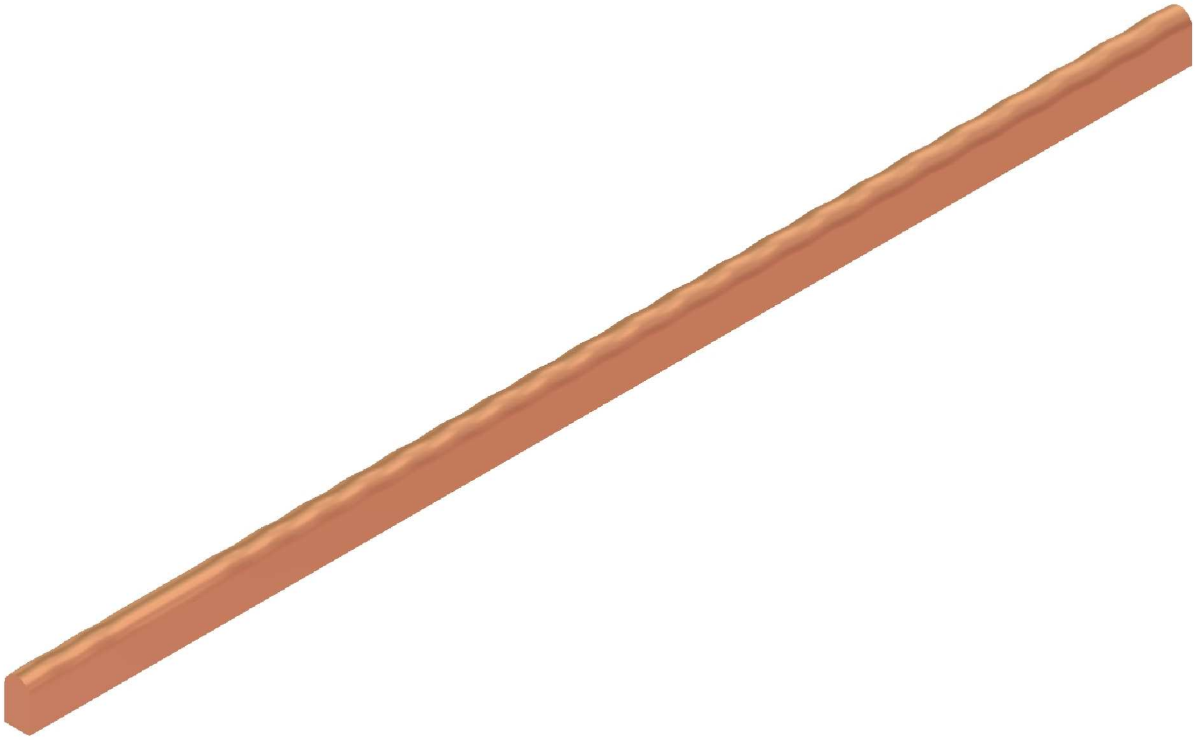

(c) Constructed vane

Figure 7.2: Vane construction:
(a) the vane profile, constructed from a semi-circle that tracks up and down along the length of the RFQ, and a solid rectangular section that maintains a constant distance from the beam axis;
(b) a spline path defined by the modulation parameters, along which the vane profile moves to construct the length of the RFQ;
(c) the three-dimensional vane constructed from the two two-dimensional elements

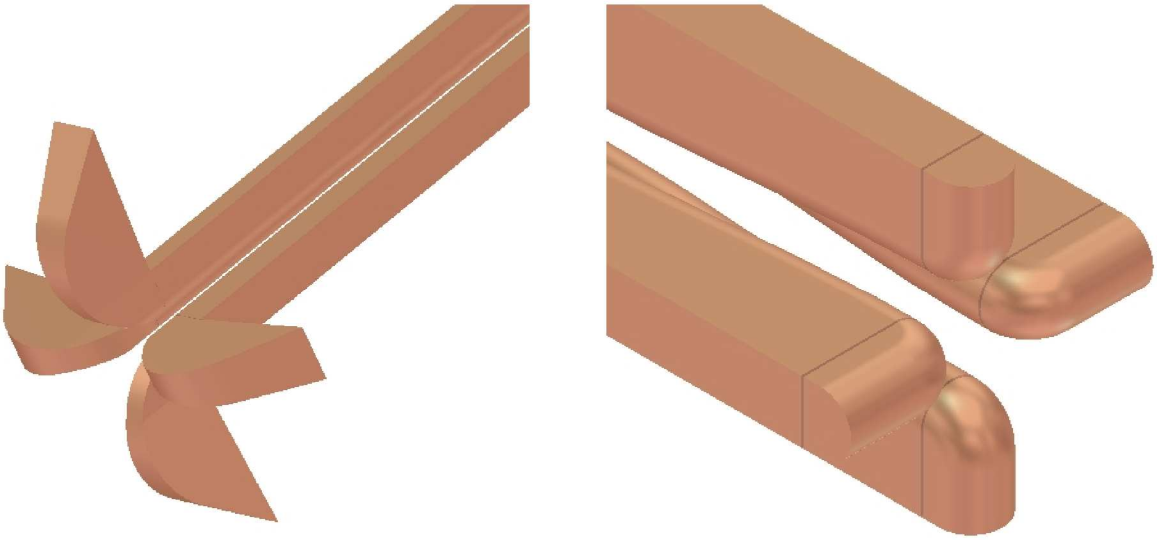

(a) Matching-in section **(b)** Matching-out section

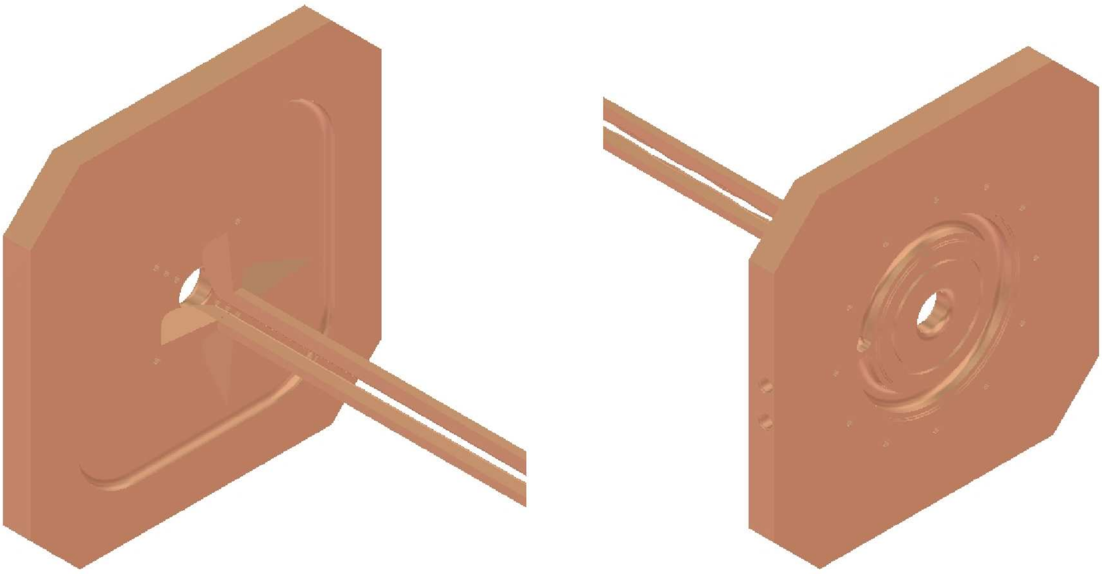

(c) Front flange **(d)** End flange

Figure 7.3: Detail at the ends of the RFQ vanes:
(a) matching-in section to gradually increase field magnitude to capture DC beam;
(b) matching-out section to smooth electric field gradient at end of vanes;
(c), (d) flanges at front and rear of the RFQ that form part of the resonant chamber and define ground potential with respect to the vanes for modelling

7.2.3 CST EM Studio

Once the CAD model of the vanes is constructed, the electric field between these vanes must be calculated. Originally, the software used for this purpose was the *CST EM Studio*.

The CAD model would be imported, and the voltage on each vane at a particular time would be specified. *CST* would then solve the electrostatic problem and produce a field map of the electric field between the vanes at this particular time (see Figure 7.4 for an example). This field map could later be modulated by a sinusoidal time variation to produce a time-dependant field map. This is the *quasi-static* approximation. More details of the *CST* simulation process are described in § 7.3.2.

For a number of reasons, later in the project (see § 7.3.3), *CST* was replaced for this purpose in the simulation chain by *Comsol Multiphysics*.

Firstly, *Comsol* allows greater interaction with other packages, via *LiveLink* modules. This means that *Comsol* can exchange control and data signals with both *Inventor* and *Matlab*. In the former case, this enables iterative workflows, where the outcome of *Comsol* simulations can affect the parameters of an *Inventor* model. In the latter case, this permits programmatic control of the modelling process, which is invaluable in optimising the meshing and solving process for accurate reconstruction of the RFQ field map.

Secondly, *Comsol* integrates well with other simulations required for the RFQ, such as the resonant frequency, stress and strain, and cooling models. *Comsol*'s multi-physics approach allows multiple solvers to act upon the same model and interact with one another in automated iterative steps to find a solution to all physical problems defined, rather than solving for each application separately. A number of other factors contributed to the decision to switch solvers, such as cost, licensing model and platform compatibility.

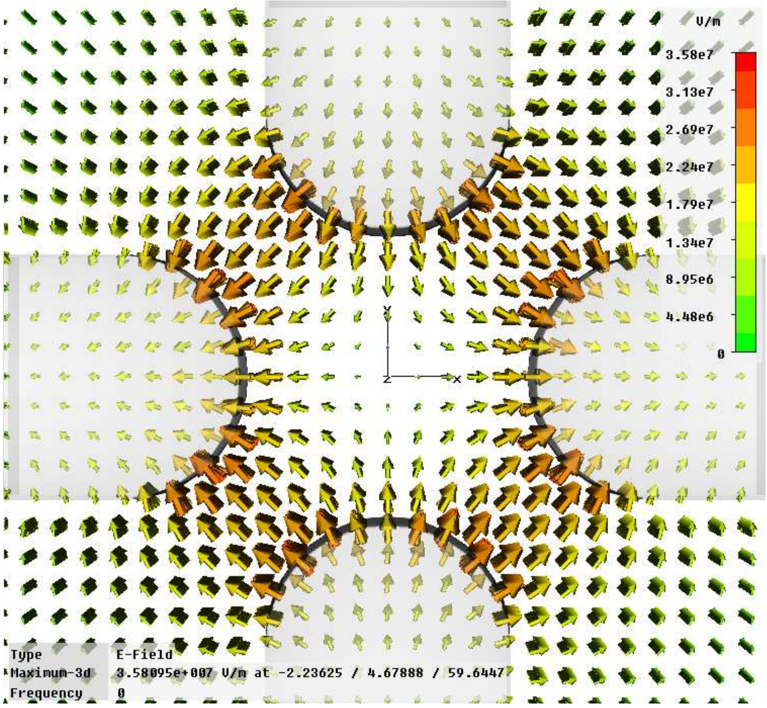

Figure 7.4: Example cross-section of an RFQ field map produced by *CST EM Studio*

7.2.4 Comsol

Comsol offers two methods of importing the CAD model from *Inventor*. The first method imports a static model, similarly to *CST*, which is often the simplest and most efficient method. The second method creates a live link to an open *Inventor* session, so that changes in one software package are reflected in the other. This can save time while constructing and testing the models.

Once the model features are imported into *Comsol*, a particular section of the model can be selected to be solved. The selection is cut out, and the rest of the model is temporarily discarded. A typical section to be solved is one quadrant of three modulation cells: half of one horizontal vane and half of one vertical vane (see Figure 7.5a). The aim of taking such small models and later combining the field maps is to reduce the errors due to the coarseness of the mesh used to solve the equations numerically. *Finite element modelling* (FEM), such as that employed by *CST* and *Comsol*, produces answers that are dependent on the size of the finite elements used to approximate a continuum. The smaller the elements, the closer the solution approaches the continuum value. The tradeoff is the computing power and time required to solve the equations, which is a strong function of the number of mesh points. Smaller elements mean more mesh points and slower solvers. There is often an optimum point beyond which reducing the element size makes little difference to the result. A coarser mesh will solve faster but be less accurate. A denser mesh will take longer to solve but not produce a significant improvement in the result. By splitting the RFQ vanes into three-cell sections, we can produce a much denser mesh than for a larger model, so the accuracy is greatly improved when compared to models with much larger volumes being modelled at once.

Comsol offers several methods for creating a custom mesh of points, on which the solver produces solution values. By creating blocks in the vacuum (see Figure 7.5b) and defining regular mesh points throughout these blocks (see Figure 7.5c and Figure 7.5d), the solver can be forced to produce field values at the locations to be exported to the field map. This removes errors produced by interpolating the field. The flexibility of *Comsol*'s meshing system allows important areas to be densely meshed while less important areas remain relatively coarsely meshed, so the computing power is concentrated intelligently.

Once the model is imported, cut and meshed, the vane tips are defined as electric terminals at a fixed potential, as previously in *CST*, and an electrostatic solver generates the fixed-time potential (see Figure 7.5e) and field map (see Figure 7.5f).

After the model is meshed and solved, the field map of the central cell is exported, then the selection moves along longitudinally one cell. The outer cells are included in each selection to define the boundary conditions to the central cell field, but only the field in the central cell is exported. The exported field maps are combined by *Matlab* code, and then reflected in both transverse axes to recover the full field map from the quadrants.

A major advantage of *Comsol* is the interface with *Matlab*. This allows the whole process detailed above to be automated. The selection of each segment to solve and export can be carried out by a programmatic loop, rather than requiring each of the 300+ cells to be selected, built and solved manually. See § 7.2.6 below for details of the *Matlab* code that carries out the automated simulations.

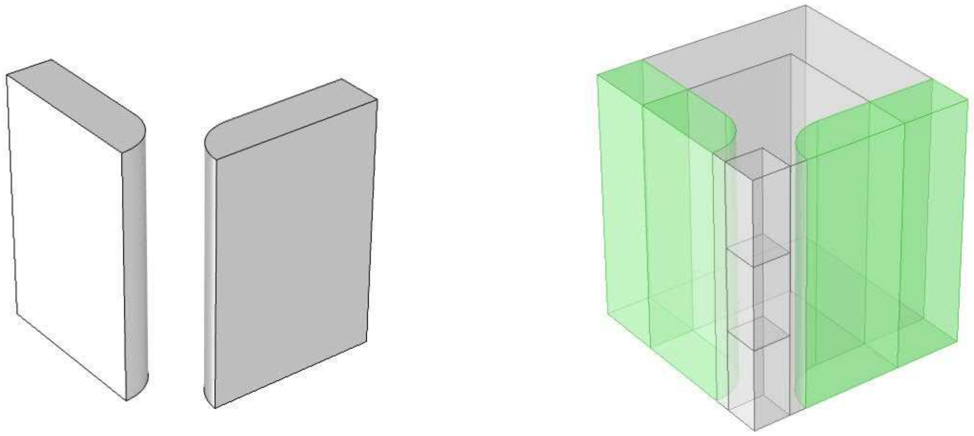

(a) Vane quadrant **(b)** Vane quadrant with beam boxes

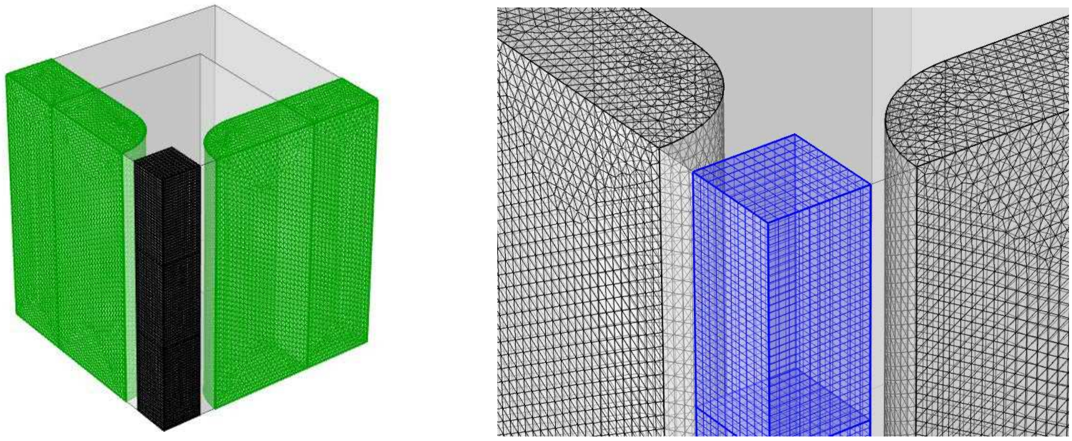

(c) Mesh **(d)** Mesh detail

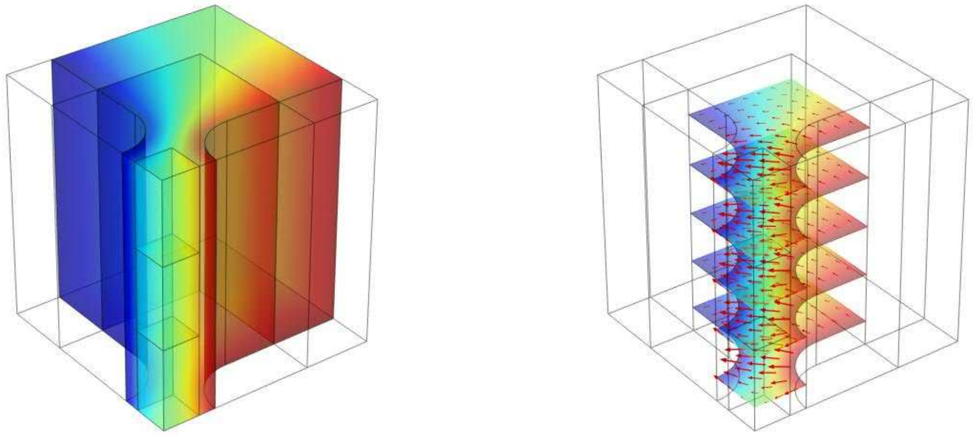

(e) Electric potential **(f)** Electric field

Figure 7.5: *Comsol* three-cell vane cell quadrant models:
(a) a short section of the RFQ vanes, cut to a quadrant including half of the horizontal vane and half of the vertical vane, from which the whole vane section can be reconstructed;
(b) five additional structures that define the volumes in which to apply different meshes, with the densest mesh near the axis, in the central of the three cells, and the coarsest mesh in the furthest volume from the beam axis;
(c), (d) finest mesh volumes, including fine tetrahedral meshes on the surfaces of the vane sections and fine regular rectangular mesh near the beam axis; and
(e), (f) electric potential and field respectively between the vane sections

7.2.5 General Particle Tracer

The field map is combined with the initial particle distribution in *Pulsar Physics'* tracking code, *General Particle Tracer* (*GPT*).[1] At this point, the sinusoidal time component of the electric field is added to the static field generated in *CST* or *Comsol*. The starting conditions are defined in an input text file or particle data file, including the spatial, temporal, and kinetic distributions (the beam parameters), along with the parameters of the tracking simulation (the field parameters and the scope of the simulation). *GPT* then tracks the paths of the particles through the RFQ field, taking space-charge effects into account (see below for details).

GPT outputs the location and trajectories of each particle at fixed time-steps, at fixed locations along the length of the RFQ, and the trajectory of each particle from the start to the finish of the RFQ. By analysing the tracks of any lost particles, the probable causes of the losses can be inferred. *GPT* also provides a graphical environment for analysing the motion of particles through the RFQ,[2] although in the present work the majority of post-processing analysis is implemented by custom code run in *Matlab*.

To track the particles, *GPT* takes the equations of motion for each particle,

$$\frac{\mathrm{d}\mathbf{p}_i}{\mathrm{d}t} = \mathbf{F}_i = q\left(\mathbf{E} + \mathbf{v}_i \times \mathbf{B}_i\right), \tag{7.1}$$

where

$$\mathbf{v}_i = \frac{\mathrm{d}\mathbf{x}_i}{\mathrm{d}t} = \frac{\mathbf{p}_i c}{\sqrt{\mathbf{p}_i^2 + m_i^2 c^2}}, \tag{7.2}$$

and combines them into a vector equation,

$$\frac{\mathrm{d}\mathbf{y}(t)}{\mathrm{d}t} = \mathbf{f}(t, \mathbf{y}(t)), \tag{7.3}$$

where $\mathbf{y}(t)$ is a vector containing all six coordinates $(\mathbf{x}_i, \mathbf{p}_i)$ of every tracked particle and $\mathbf{f}$ is a force function combining Equation 7.1 and Equation 7.2. *GPT* acts on this vector equation to solve for all particles simultaneously, because each particle influences the others [75, p. 22]. The solver uses a fifth-order *Runge–Kutta step algorithm* [76] to advance from $\mathbf{y}(t)$ to $\mathbf{y}(t+h)$, where h is a small time step [75, p. 23]. *GPT* checks the results against estimates from a fourth-order algorithm and adjusts h until the error is within tolerances. The final value is then the starting point for the next time step.

GPT also offers a number of different methods of including space-charge effects, along with the ability to write custom code for any elements or effects. Figure 7.6 shows the additional spread of particles in a drift space due to space charge. The built-in effects range from a simple cylindrically-symmetric calculation, to a full 3D point-to-point interaction, to a sophisticated non-equidistant moving-mesh method using a Poisson solver. Figure 7.7 compares the latter two codes for a simple drift space, demonstrating good agreement between them; the moving-mesh method is significantly less resource-intensive as a computing method. A custom bunch-based calculation has been written

---

[1] `http://www.pulsar.nl/gpt`

[2] In the *Windows* version only

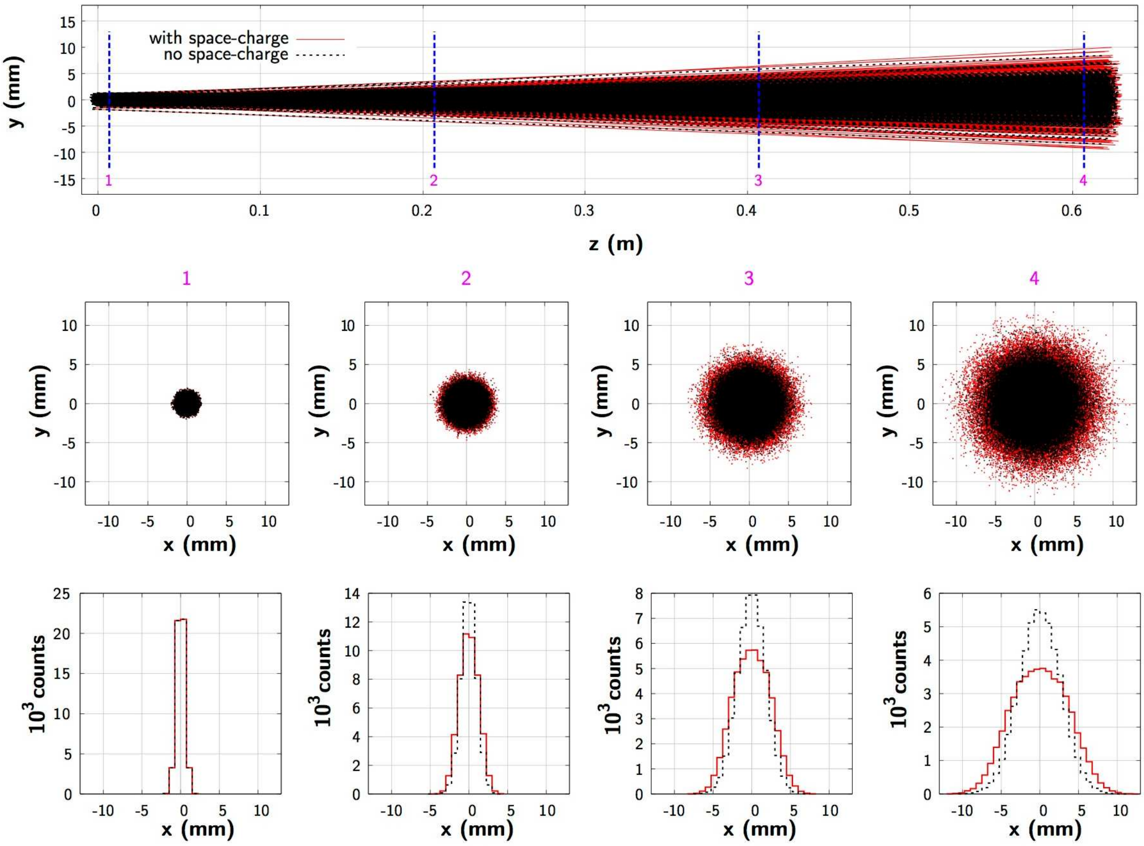

Figure 7.6: Simulated trajectories of particles in a drift space without (black) and with (red) space-charge forces; Plots courtesy of C. Bonţoiu

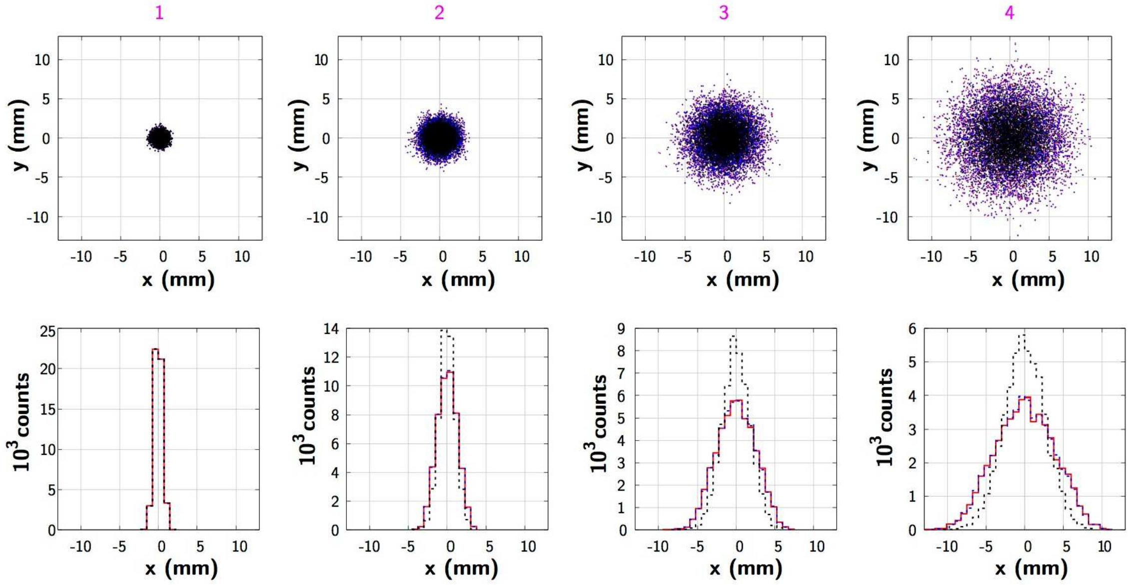

Figure 7.7: Comparison of *GPT* simulations with no space-charge effects (black), with full 3D point-to-point calculation (blue), and with non-equidistant moving-mesh method (red); Plots courtesy of C. Bonţoiu

as part of the *FETS* project, which simulates the bunches in front and behind the current bunch by analogy with the particles in the current bunch. This, however, does not include image charges due to the conductive vane tips, which has been highlighted as a significant process in RFQ design [73]. This effect could theoretically be included in the moving-mesh method (see Chapter 9).

Space-charge effects are more important in some applications than others. The *generalised perveance* K is a dimensionless measure of the magnitude of space-charge forces in the equation of motion. Larger values of K correspond to larger space-charge forces. For particle beams,

$$K = \frac{I}{I_0} \frac{2}{\beta^3 \gamma^3}, \tag{7.4}$$

where I is the beam current, $I_0 = 4\pi\epsilon_0 m_0 c^3/q$ is a characteristic current for the particle species, and β and γ are the relativistic velocity and Lorentz factor respectively [77]. Space-charge is most important for high-current, low-velocity accelerators.

The *FETS* RFQ will accelerate 70 mA of H^- ions from a minimum energy of 65 keV. Table 7.1 calculates the generalised perveance to be 2.7×10^{-3}, which is a significantly large value. For *PAMELA*, the beam has a much lower current of $1\,\mu$A, producing a tiny generalised perveance of 2.46×10^{-7}. Therefore, the space-charge handling capabilities of *GPT* are vital for simulating the *FETS* RFQ and other high-current drivers, but much less crucial for simulating the *PAMELA* RFQ and similar low-current applications.

	FETS	*PAMELA*
Ions	H^-	C^{6+}
Nucleons (u)	1	12
Charge (C)	$-e$	$6\,e$
Characteristic current (A)	31.3×10^6	62.1×10^6
Current I (A)	70×10^{-3}	1×10^{-6}
Kinetic energy T (keV/u)	65	12
Relativistic velocity β	0.0118	5.1×10^{-3}
Generalised perveance K	2.7×10^{-3}	2.46×10^{-7}

Table 7.1: Generalised perveance for *FETS* and *PAMELA* RFQ designs

7.2.6 Matlab

Matlab is "a high-level language and interactive environment," optimised to handle large datasets efficiently.[3] The post-processing code for RFQ simulations takes the trajectories of all the particles and calculates various values, such as the mean energy and energy spread, the transmission and the emittance. Trajectories through the RFQ and final energy, space and phase space distributions are also plotted. Videos in real space and phase space can be produced by plotting the properties of the particles at each time-step as frames in the video.

As well as post-processing tools, *Matlab* provides a programming environment and offers an interface to run system commands and input and output various file types. Additionally, *Comsol* offers an API that *Matlab* can control, and *GPT* offers a command line that runs the particle tracking and conversion tools. For this thesis, a rapid development process was undertaken to automate the existing, time-consuming, manual simulation method by writing custom code in *Matlab* that runs the RFQ design process from the CAD model onwards. The steps taken in the code:

1. Create a *Comsol* model and import the geometry from the CAD model;
2. Extract the cell coordinates from the modulation spreadsheet;
3. Build, mesh and solve the *Comsol* model, one cell at a time;[4]
4. Combine the separate field maps and convert the file format for particle tracking;
5. Run *GPT* with the field map from *Comsol* and the parameters from the spreadsheet;
6. Import the particle tracking data into *Matlab* arrays;
7. Analyse the data to characterise the simulation results and produce figures, images and videos.

These steps are run from a number of nested custom functions, which are combined with various data files to form the *ModelRFQ* distribution.[5] For more details on the program code, see Appendix C.

The following sections summarise the evolution of the design code and its application to designing RFQs for *FETS* and *PAMELA*. The detailed results of these simulations are described in Chapter 8.

---

[3] Quoted from `http://www.mathworks.com/products/matlab`

[4] In fact, three cells are selected and solved, but only the central cell is exported (see § 7.2.4).

[5] See `https://launchpad.net/modelrfq`

7.3 Front-End Test Stand (FETS) RFQ Simulations

7.3.1 RFQSIM

The first step in developing the RFQ for *FETS* was to run *RFQSIM* to find a field map using the truncated series approximation (Equation B.3). This approximation produces a field map that creates an accurate field representation near the beam axis but an inaccurate representation further away (see Figure 7.8). As discussed in § 7.3.3, with high space-charge forces, more particles are pushed outward into these regions further from the beam axis, and the inaccuracies of the field become more significant. As well as a field map, *RFQSIM* produces the modulation parameters that define the vane modulations along the length of the RFQ.

The results of the particle tracking simulations using the *RFQSIM* field map are presented in § 8.1.1. 100% of particles entering the RFQ are transmitted and accelerated to 3.03 MeV with an RMS energy spread of 14 keV. These are very encouraging results and meet the requirements of the RFQ, so all further simulations were benchmarked against these results.

7.3.2 CST

The next stage was to take these modulation parameters and create a CAD model. The process described earlier in § 7.2.2 was developed gradually over the course of this thesis—initially, the process required a lot of manual manipulation to import the modulation parameters and construct a coherent model of the vane tips, but by the end of development, the code can take a spreadsheet with the parameters of any RFQ with up to 1000 cells and automatically construct the CAD model.

Early electrostatic modelling was carried out using *CST*, as described earlier in § 7.2.3, and the whole CAD model was imported and solved at the same time. The particle tracking simulations with this field map transported 99.9% of the particles, but none of them reached the full acceleration energy (see Figure 8.2 and the discussion in § 8.1.2.1). By virtue of having a CAD model rather than an analytic solution, a number of different scenarios were able to be tested to try and find the cause of the discrepancy.

Firstly, the shape of the transverse electric field was investigated. Although the high transport result seems to indicate that there are no problems with the transverse field, comparing the *RFQSIM* and *CST* field maps showed that the transverse field strength was higher for the *RFQSIM* solution. This difference could not be ignored, as the transverse and longitudinal dynamics are strongly coupled.

To attempt to bring the simulation closer to the truncated series potential function, two different alterations to the CAD model were simulated. The ideal (but unphysical) quadrupole has hyperbolic surfaces for its electrodes. The eight-term potential function modifies this potential by bringing the electrodes closer to a physical, circular vane-tip geometry. To investigate the difference between the *RFQSIM* potential and the *CST* potential, the first family of models added wedges tangential to the circular vane tip at various angles (see Figure 7.9), and the second increased the radius of curvature of the vane tips while keeping the distance from the beam axis constant (see Figure 7.10). Each of these scenarios brings the simulation closer to the ideal hyperbole.

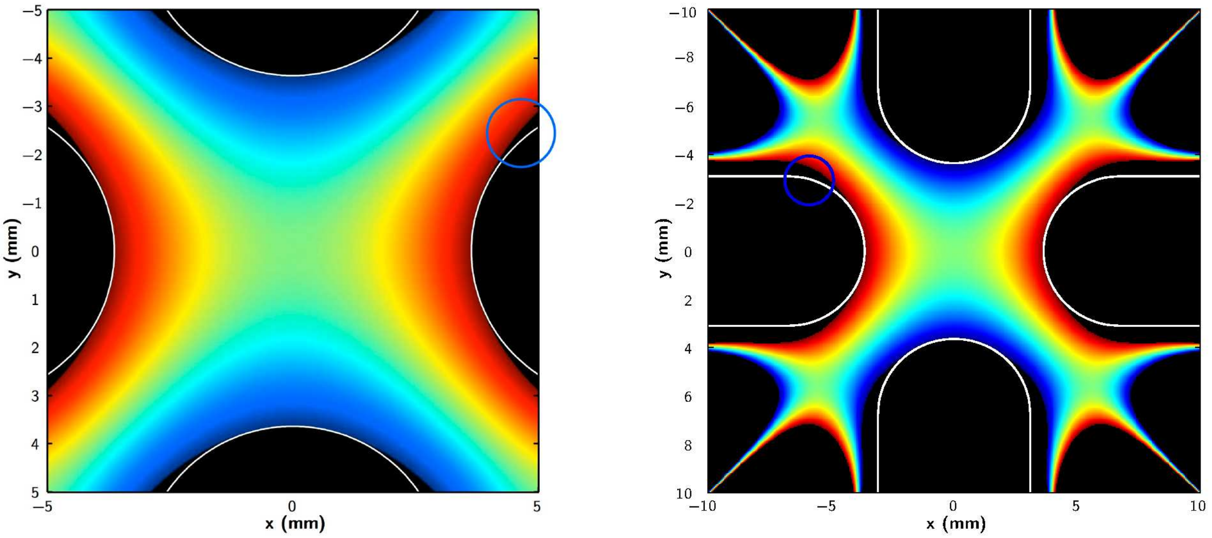

(a) *RFQSIM* vane tip electric potential cross-section **(b)** *RFQSIM* electric potential cross-section

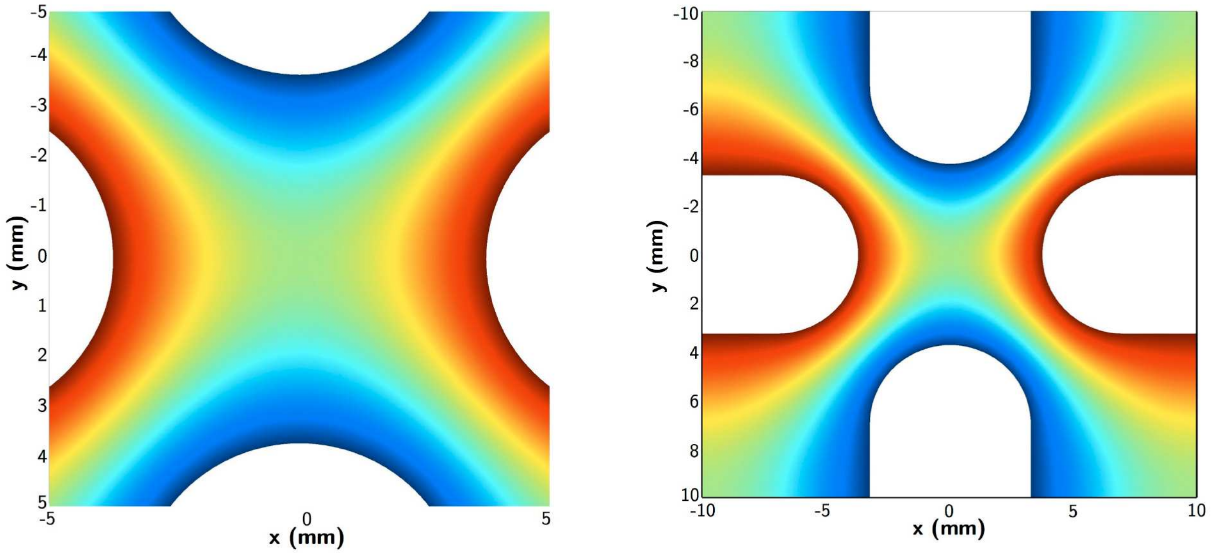

(c) *Comsol* vane tip electric potential cross-section **(d)** *Comsol* electric potential cross-section

Figure 7.8: Comparison of field maps produced using *RFQSIM* and using CAD methods:
(a) electric potential cross-section from *RFQSIM* close to the vane, with real vane tip profiles shown by white lines;
(b) electric potential cross-section from *RFQSIM*; and
(c), (d) similar electric potential cross-section from *Comsol*.
Note the artificial objects and incorrect potential in the corners of the the *RFQSIM* potential, away from the vane tips, and more significantly, deviation from the real vane tip profile away from the central axes, such as the areas circled in blue.

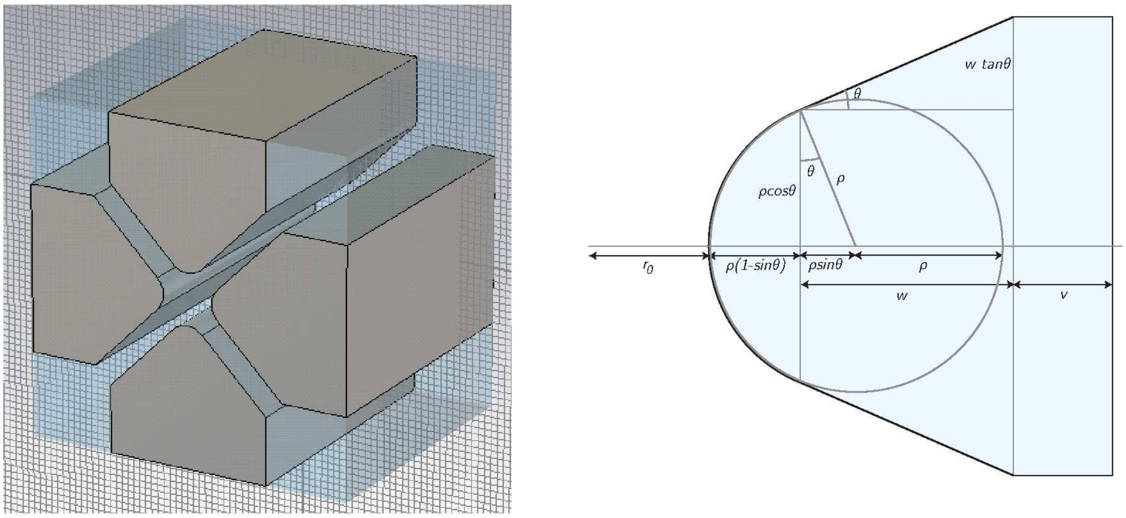

(a) Vanes with added wedges **(b)** Wedge geometry

Figure 7.9: RFQ vanes with wedges added in an attempt to bring potential closer to a hyperbolic function

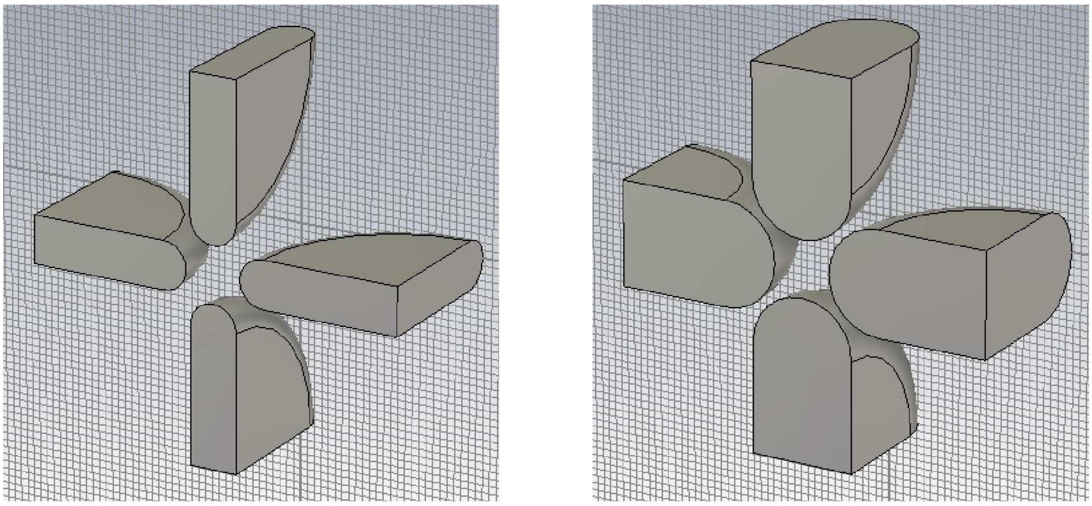

(a) Standard vane radius **(b)** Vanes with radius increased to 7 mm

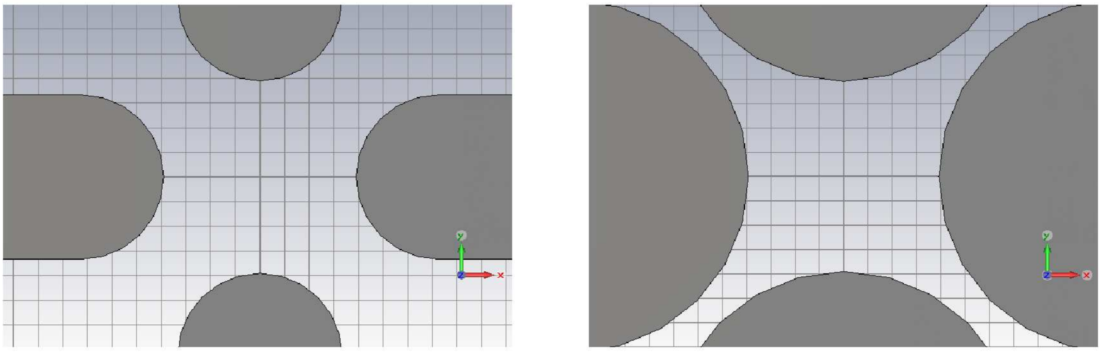

(c) Standard vane tips **(d)** 7 mm vane tips

Figure 7.10: RFQ vanes with radius increased in an attempt to bring potential closer to a hyperbolic function

The wedge geometry made little difference to the results, as described in § 8.1.2.2, but increasing the radius of curvature to twice its nominal value brought the simulations nearly in line with the *RFQSIM* field map (see Figure 8.4 and the discussion in § 8.1.2.3). This caused investigation into the source code for *RFQSIM* and a problem was discovered with the input file, relating to conversion between different units. Once this problem was corrected, a new set of vane modulation parameters was produced that could be simulated in *CST*. However, as detailed in § 8.1.2.4, these updated simulations still did not accelerate the particles correctly, despite the transverse field map now matching the successful *RFQSIM* field map.

Investigations into the longitudinal field map found problems relating to the mesh used to solve the electrostatic problem in *CST*. The ratio of the length of the RFQ to the size of the modulations was too high, and the mesh was not detailed enough in the longitudinal dimension. To address this problem, the CAD model was split into five sections, and each of these sections was solved separately. This reduced the ratio of longitudinal to transverse dimension, and allowed a denser mesh to be used, but increased the computing time required for a solution. The results (detailed in § 8.1.2.5) improved, but the particles were still not coherently accelerated.

The final problem was related to the method of reconstruction of the full RFQ field from the five sections. A bug in the *MATLAB* code meant that the field map sections were not connected to the correct geometry. After fixing this bug, the particle tracking simulation produced a fully transported and accelerated beam, matching the results using the *RFQSIM* field map (see § 8.1.2.6).

Once the simulations were producing a field map that matched the expected RFQ field, the next step was to optimise the simulation process. Firstly, the meshing options were investigated to find the most accurate electrostatic solution process. Figure 7.11 shows how the transmission, final energy, and emittance converge as the number of mesh points increases. To achieve a number of mesh steps in each dimension higher than 1 000, the model needs to be split into sections. The discontinuity in the convergence is due to the jump from single full RFQ models, to separate section models.

Figure 7.12 displays the convergence when varying the field map output mesh. This secondary mesh is applied after the electrostatic solver has completed, and interpolates the calculated field to the specified output points. The results show that mesh steps greater than 2 mm introduce interpolation errors that significantly affect the particle tracking results. The value of 0.5 mm steps was selected as a compromise between field accuracy and computing time.

To test the differences in field flatness between different mesh types, a CAD model was created without any vane modulations. This pure quadrupole should produce zero field in the longitudinal direction. The results depicted in Figure 7.13 show that a tetrahedral mesh comes a lot closer to producing this flat field than a hexahedral mesh, and that splitting the RFQ into sections also improved the field accuracy for this model.

To test the effect of different boundary conditions on the electrostatic solver, the same CAD model without vane modulations was simulated in four sections, each 1 m in length, with the boundary conditions at the each end of each section set to either *open* or *tangential*. Figure 7.14 demonstrates the problem with open boundaries: at the end of each section is a large spike in electric field due to the abrupt termination of the material. Tangential boundaries do not have this problem, and are closer to the real boundary condition of vanes continuing beyond the end of the simulation.

However, a number of technical problems prevented the use of a tetrahedral mesh with tangential boundaries for the CAD models produced in five sections for the *FETS* RFQ. To address these issues, the model needed to be split into much smaller sections to simplify the geometry. To carry out this process efficiently requires a level of automation that *CST* does not offer, and at this point the simulation effort turned to *Comsol* instead.

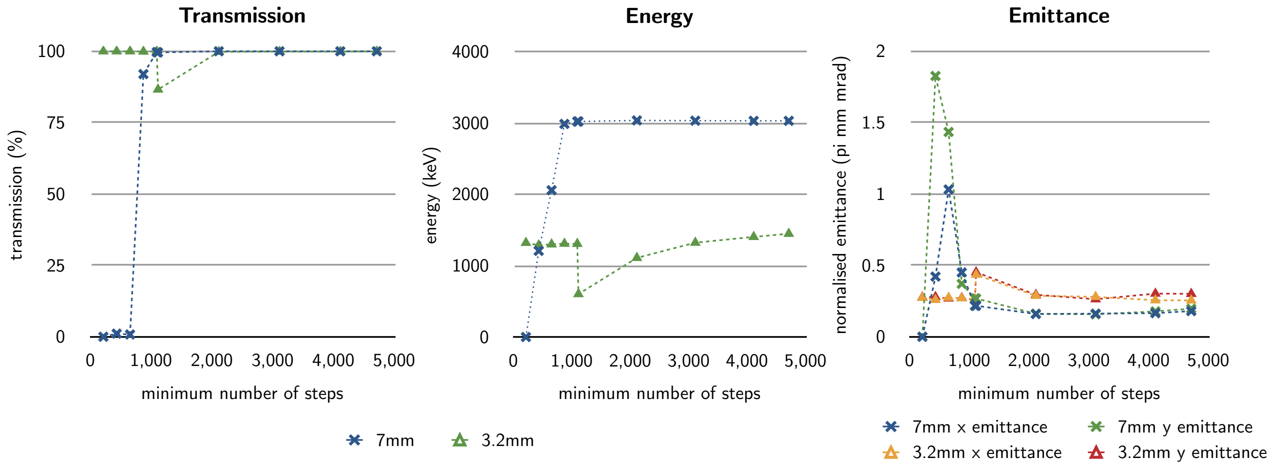

Figure 7.11: Convergence when varying *CST* mesh density, showing transmission increase, energy increase and emittance decrease as number of mesh points increases; two models shown with different vane-tip radii. The discontinuities for the 3.2 mm model are due to the switch from a single 4 m-long model to four 1 m-long sections; the 7 mm model used four 1 m-long sections throughout.

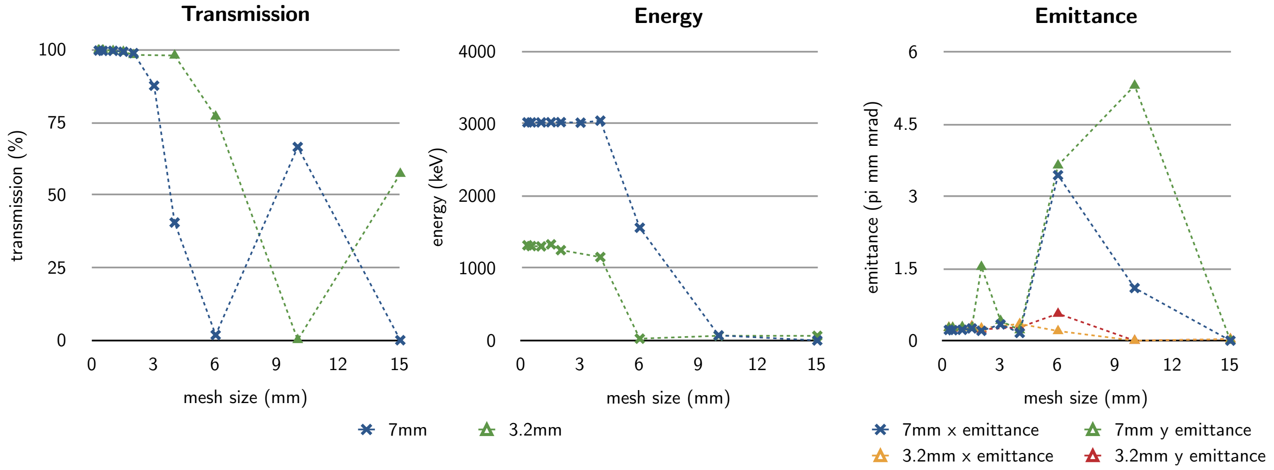

Figure 7.12: Convergence when varying field map output mesh density, showing transmission increase, energy increase and emittance decrease as the output mesh spacing size decreases; again two models shown with different vane-tip radii

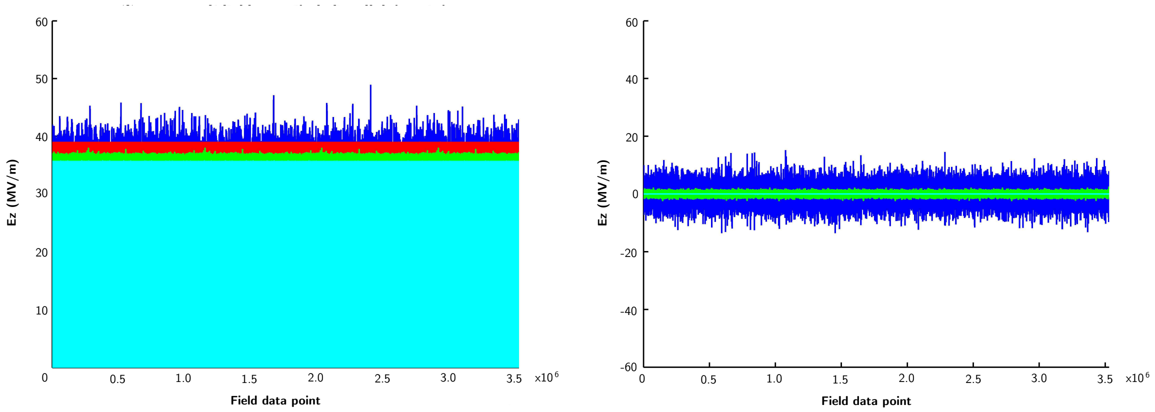

(a) transverse electric field **(b)** z-component of electric field

Figure 7.13: Comparing *CST* mesh types for an RFQ model with no modulations—the four mesh types are hexahedral mesh in one 4 m model, tetrahedral mesh in one 4 m model, hexahedral mesh in four 1 m sections, tetrahedral mesh in four 1 m sections. Results show the tetrahedral mesh is less prone to noise and therefore closer to the theoretical result.
(a) Transverse electric field. The blue plot is a 4 m model using a hexahedral mesh, showing a lot of noise on the theoretically flat result. The red plot with a flat response uses a tetrahedral mesh, still with a 4 m model. The green plot is a model in four 1 m sections using a hexahedral mesh, still showing noise but at a lesser field value and with a smaller relative noise component. The cyan plot is a model in four 1 m sections using a tetrahedral mesh.
(b) The z-component of the field in this RFQ model with no modulations should be zero. Both tetrahedral models (red and cyan) show as a straight line at zero, so narrow as to be hard to detect in the image. Both hexahedral models show noise around zero, with the larger, blue plot being the 4 m model and the smaller, green plot being the model in four 1 m sections.

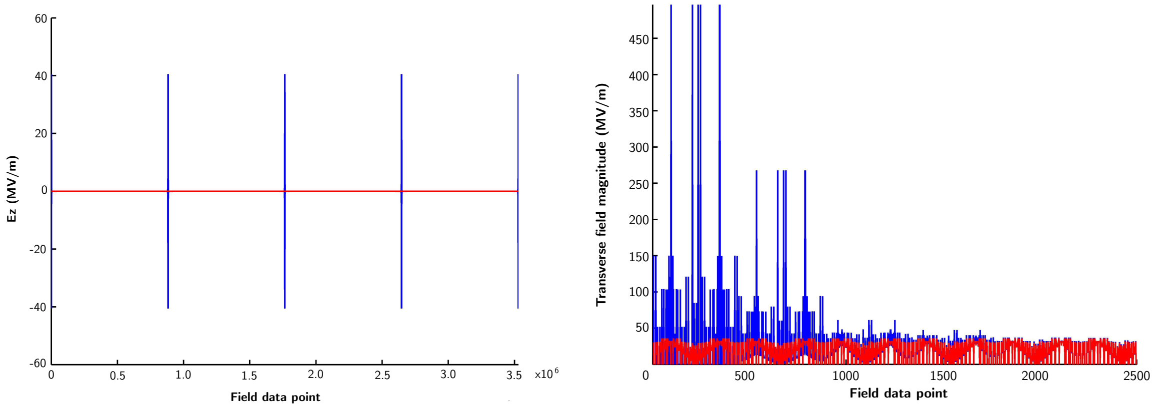

(a) z-component of electric field **(b)** close-up of transverse electric field

Figure 7.14: Comparing *CST* boundary types for an RFQ model with no modulations—the red plot uses tangential boundaries and the blue plot uses open boundaries:
(a) with tangential boundaries, no z-component of the field exists, as is correct for an RFQ with no modulations; with open boundaries, large unphysical spikes in field are created; and
(b) unphysical field components also appear in the transverse field near the boundaries.

7.3.3 Comsol

The first tests using *Comsol* were like-for-like comparisons with *CST* to test that similar solutions were reached with both software packages. Figure 7.15 shows the transverse field directions at a slice through the RFQ at the end of the matching section, and Figure 7.16 shows the longitudinal field magnitude along the length z of the RFQ. While the shape of the fields match closely, the details show interesting differences. The *Comsol* longitudinal map shows a much higher signal-to-noise ratio, and this difference is also present in the transverse field map, visible as smaller arrows near the beam axis in the centre of the plot. The reduced noise is due to the increased mesh density using *Comsol*'s custom mesh functions. Differences in the directions of the field on the axes in the transverse slices are due to different mesh systems in the two software packages—in a theoretical model, the field on axis would be exactly straight, but with a finite element model these values will approach the theoretical limit as the mesh density tends to infinity.

The *Comsol* longitudinal map shows large, unphysical spikes between the separate sections, similar to those in previous tests in *CST* (see Figure 7.14). The spikes are due to the abrupt ends of each section with incorrect boundary conditions. Periodic conditions were attempted to remove the spikes, but technical issues made these conditions difficult to apply. Later models overcame these difficulties by using the cell-by-cell method described above—by including extra cells either side of the central cell, the boundary conditions of the central cell are correct, and the number of extra cells is chosen so that the further boundaries do not affect the results in the central cell.

Up to this point in the simulation process, all comparisons had been carried out without the addition of space-charge models in the particle simulations. Including the space-charge forces greatly increases the simulation time, but for the *FETS* RFQ, space-charge effects cannot be ignored. The transverse effect of space-charge forces is to push the particles out from the beam axis towards the electrodes, due to the repulsive force between particles of like charge. Increasing the space-charge current in the simulations from zero to the full beam current has the effect of probing deeper into the field map and checking for problems further from the beam axis. The results of tracking simulations with increasing space-charge currents for the three field maps (generated in *RFQSIM*, *CST* and *Comsol*) were compared. Figure 7.17 shows good agreement between the *CST* and *Comsol* field maps in five sections. Figure 7.18 shows that both simulated field maps (tagged 'CST' and 'Comsol 1') produced lower transmissions at higher currents than the *RFQSIM* field map, as the simulations do not reproduce the field in enough detail due to the limited mesh density.

The next stage of simulations started from the finest mesh quality possible, to avoid these detail issues. A single cell was modelled at a time, with extra cells either side included in the simulation to provide the most accurate boundary conditions, but only the field in the central cell was exported. This cell-by-cell approach was made possible by the interaction between *Matlab* and *Comsol*. The position and dimensions of each cell were stored in a spreadsheet. These values were read in by *Matlab* and then exported to *Comsol* as parameters, which then determined which part of the CAD model was selected and solved. Once the model had been solved, *Matlab* read out the field map data and saved it to file. Once this process was complete and all cells had been solved and the field map combined into a single whole, the particle tracking simulations produced good transmission

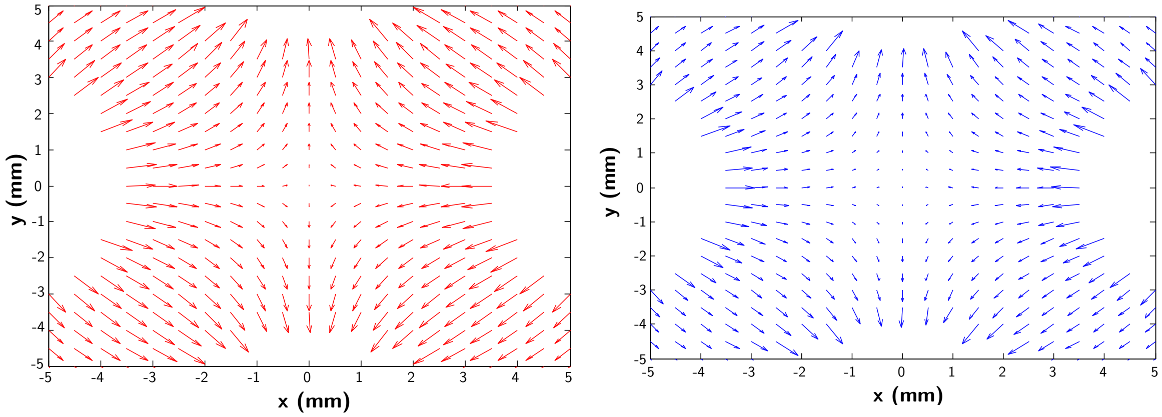

(a) *CST* transverse field slice **(b)** *Comsol* transverse field slice

Figure 7.15: Transverse field slices from *CST* and *Comsol* models, showing slightly smaller magnitudes near the central beam axis for *Comsol*, and slight directional differences near the symmetry axes

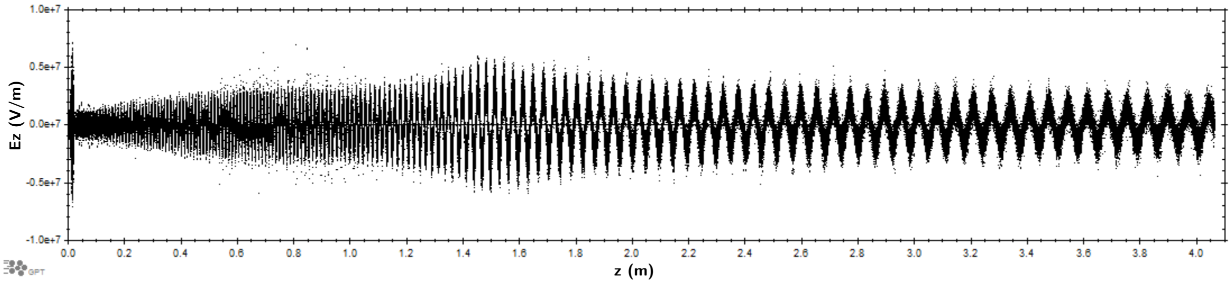

(a) *CST* longitudinal field data points

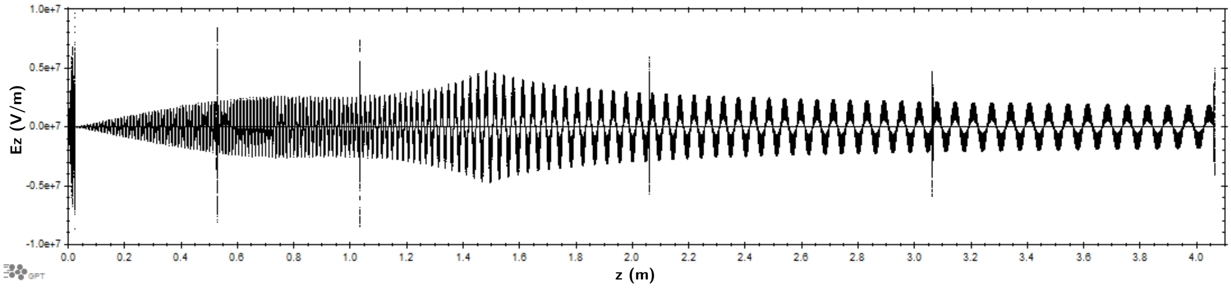

(b) *Comsol* longitudinal field data points

Figure 7.16: Longitudinal field data points from *CST* and *Comsol* models, showing better signal-to-noise ratio in *Comsol* but also large spikes due to incorrect boundary conditions

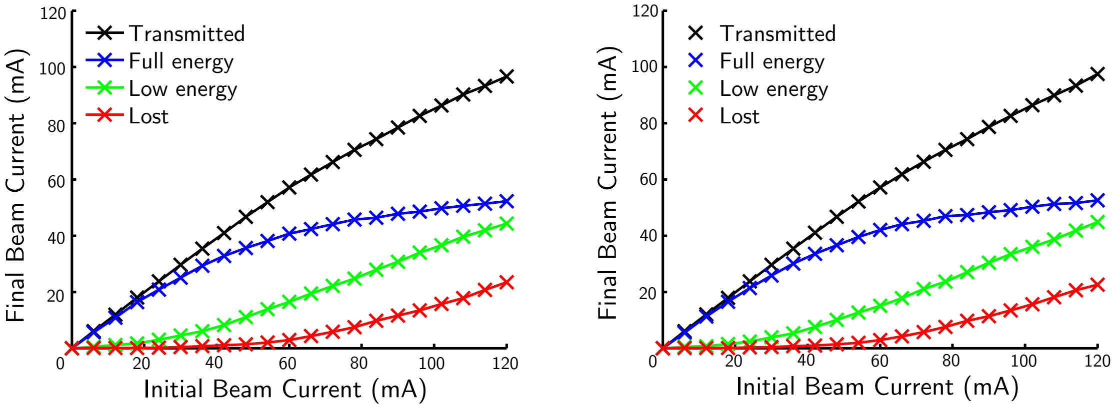

(a) *CST* transmission

(b) *Comsol* transmission

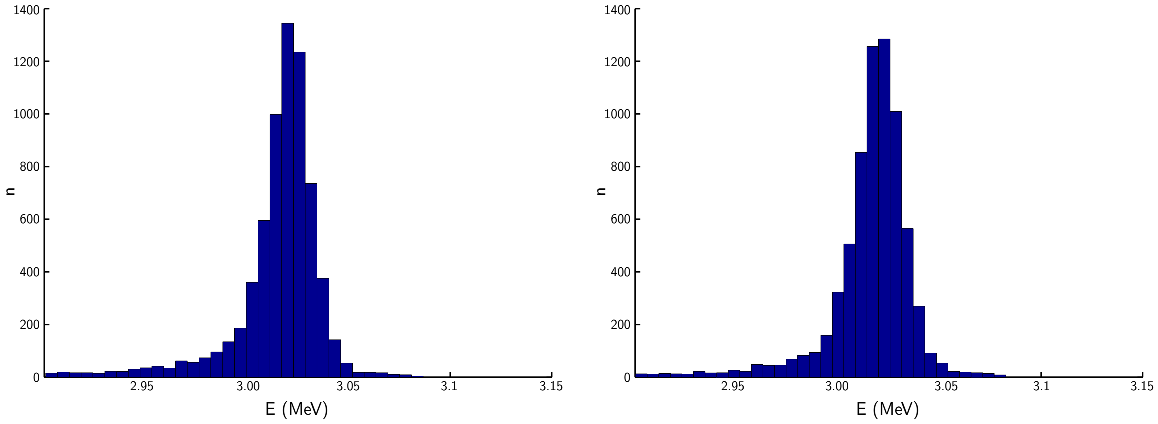

(c) *CST* final energy

(d) *Comsol* final energy

Figure 7.17: Transmission profiles and final energy histograms for beam simulations through the field maps produced by *CST* and *Comsol* models, where the final beam current is split into three categories: correctly accelerated to 3 MeV; transmitted to the end but not reaching full energy; and lost particles that do not reach the end. The histograms show the energy of the particles that are correctly accelerated.

at all space-charge currents, shown in Figure 7.18 with the tag 'Comsol 2'. These results were similar to the results with the truncated series method of *RFQSIM*. The differences at higher beam currents demonstrate the effect of the truncated field expansion used in the *RFQSIM* calculations, as illustrated above in Figure 7.8, where the shape of the vane tips is larger in the *RFQSIM* field map than the physical size of the vanes. The high mesh density *Comsol* models now seemed more accurate than the truncated series method.

In summary, the simulations for the *FETS* RFQ have generated field maps that are producing expected results and possibly more accurate maps than previous methods, especially far from the beam axis, where the assumptions of the truncated series do not hold. These areas are more important when space-charge effects are significant. The numerical differences between *CST* and *Comsol* models are simply due to different mesh schemes, rather than differences in the codes or solvers. However, *Comsol* was selected primarily for its ease of automation of the very high mesh density cell-by-cell models, and for other secondary factors such as cost and compatibility.

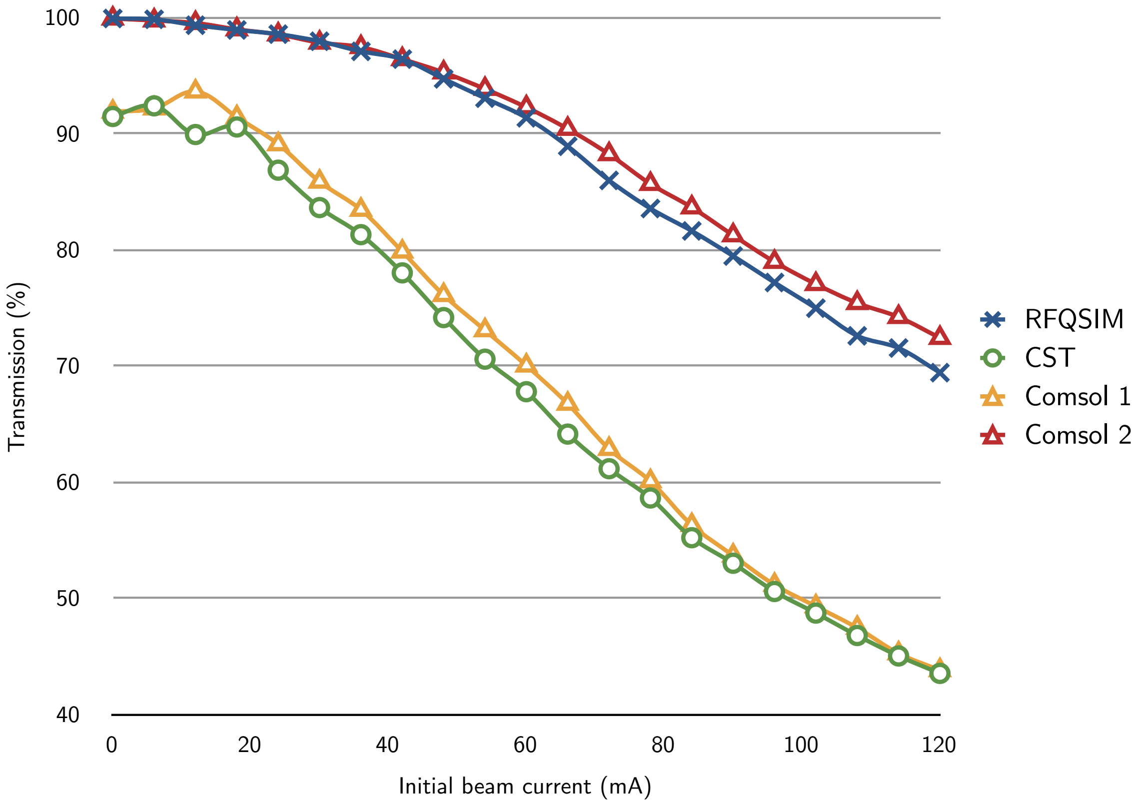

Figure 7.18: Transmission of various RFQ models as space-charge current increases: the *CST* model and first *Comsol* model produce significantly poorer responses than the calculated *RFQSIM* field map, but are in good agreement with each other; switching to the cell-by-cell solving method in the second *Comsol* model increased the accuracy of the field map and produced a response much closer to that of the *RFQSIM* field map. Differences far from the beam axis (see Figure 7.8) are more apparent with higher space-charge current, as particles are pushed out transversally into these areas due to mutual repulsion.

7.4 RFQ scaling laws applied to FETS parameters

The first models for *PAMELA* were generated by scaling the *FETS* field map appropriately. Various scaling laws were investigated to determine the changes required to produce a carbon RFQ. The use of both carbon 4+ and carbon 6+ ions was investigated. Similar scaling considerations can be applied to the design of various other RFQs.

The *FETS* RFQ is designed to accelerate a high-current proton beam from 65 keV to 3 MeV. Replacing the proton beam with a carbon beam without modifying the RFQ parameters requires a carbon input beam at 65 keV/u, or a total energy of 780 keV, which is impractical for a hospital-based carbon ion source [60]. The magnitude of the electric field also needs to be increased to accelerate the carbon ions. As a carbon 4+ ion has a charge-to-mass ratio a third of that of a proton, the electric field magnitude needs to be increased three-fold (see Equation 7.6 below). Studies using *GPT* confirmed these results: Figure 7.19 shows that acceleration only starts to occur with electric field magnitude three times larger than that for protons, and initial energy at 65 keV/u. Additionally, accelerating carbon ions to 3 MeV/u in an RFQ is very inefficient in terms of energy and therefore not cost-effective, and the transition to a linac structure should rather take place below 1 MeV/u.

To produce a carbon RFQ that avoided these issues of excessive input and output energy and field magnitude, the next stage of simulations involved reducing the length of the RFQ and reducing the frequency of the electric field, scaling the modulation pattern with the length of the RFQ. An operating frequency of 200 MHz was chosen for carbon 4+ ions, for the ease of production with available RF power sources, and because reducing the frequency increases the Q-value of the cavities, increasing the shunt impedance and thereby reducing the power requirements. The synchronous velocity β_s of an ion in the RFQ is given by,

$$\beta_\mathrm{s} = \frac{D\omega}{2\pi c}, \tag{7.5}$$

where D is the spatial period of the modulations and ω is the frequency of the RF field [32]. The *FETS* RFQ is designed for protons with an energy of 65 keV, and therefore a synchronous velocity of $\beta_\mathrm{s} = 0.0117$. A reasonable energy from available carbon 4+ ion sources is 8 keV/u, or total energy of 96 keV, which for carbon 4+ ions can be achieved with a voltage of 24 kV. This corresponds to a velocity $\beta = 0.00414$, so the carbon RFQ for *PAMELA* needs a reduction in the synchronous velocity by a factor of 0.37. Reducing the frequency from 324 MHz to 200 MHz produces a reduction in velocity by a factor of 0.62, so a further factor of 0.60 is required, which can only be achieved by reducing D. *GPT* allows transformations of the field map by a fixed factor,[6] so a number of simulations were run, in which the z-axis is compressed by a fixed factor. Compressing the entire axis will reduce D by the same factor. Figure 7.20 shows how the resonant input energy of maximum acceleration varies with length of the RFQ with the frequency of the electric field fixed at 200 MHz. As expected, a factor of 0.6 produced the best acceleration (reaching a final energy of 382 keV/u) with an initial energy of 8 keV/u. This compression factor results in an RFQ length of 2.3 m.

---

[6] This transformation is not ideal for producing accurate field maps, as discussed at the end of this section, but it does enable the rapid investigation of scaling laws.

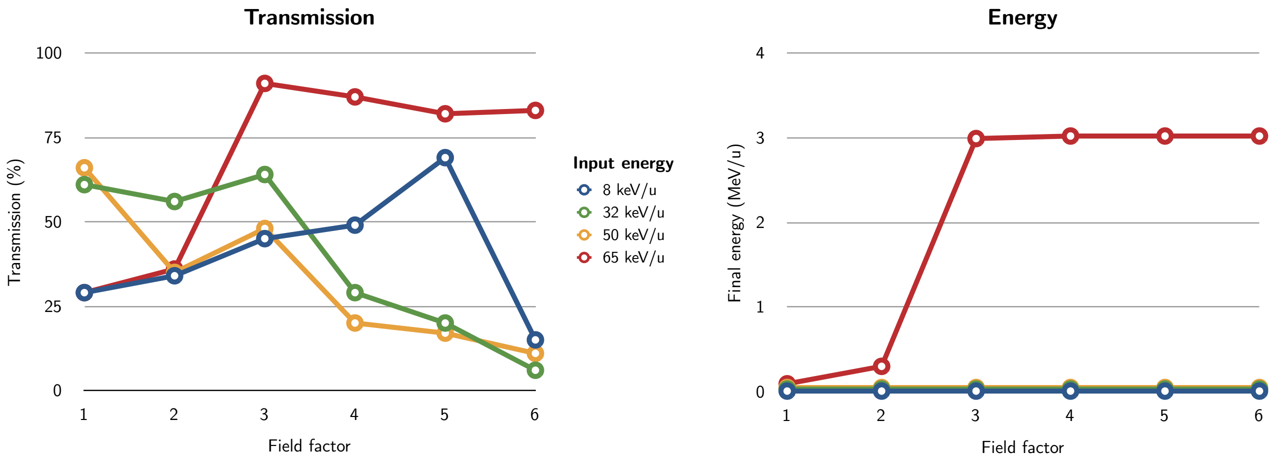

Figure 7.19: Graphs of transmission and final energy for scaled carbon RFQs at different initial energies and different field factors. The RFQ has the same frequency (324 MHz) and length and modulation patterns as the *FETS* design for proton acceleration. The electric field profile is obtained by multiplying the electric field at each point by a fixed field factor. Results show that, although transmission is reasonable for a number of initial energies, significant acceleration can only take place when the initial energy is close to 65 keV/u and the field factor is at least 3. This confirms that with the same frequency and length and input velocity per nucleon, with alterations to the velocity gain per cell by increasing the field magnitude, the same RFQ can accelerate carbon ions as well as protons.

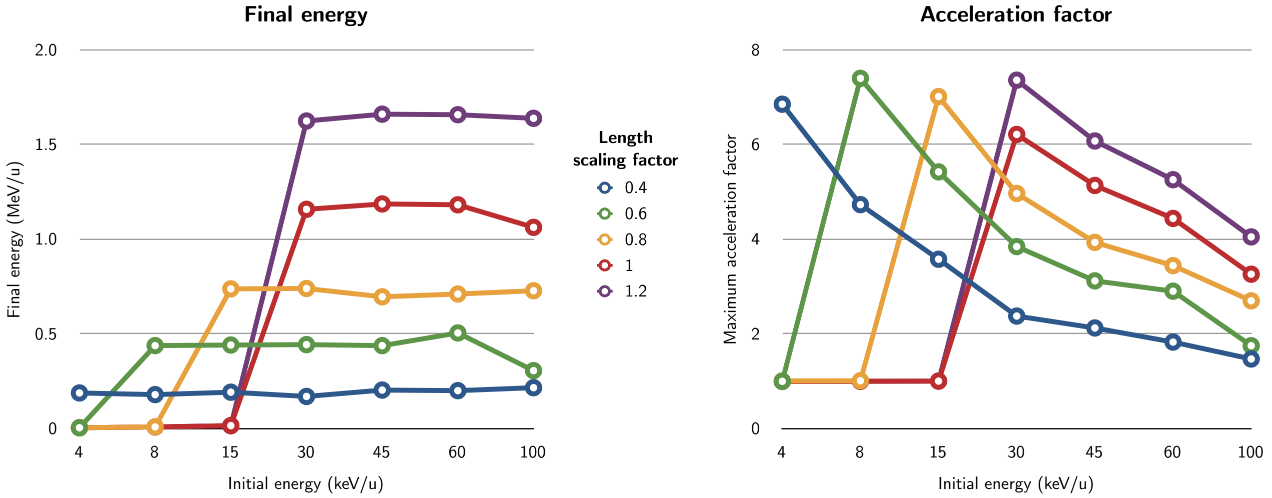

Figure 7.20: Graphs of final energy and maximum acceleration factor against input energy for different lengths of RFQ; maximum acceleration factor is defined as the largest ratio of final velocity to initial velocity when varying the electric field magnitude. The acceleration graphs show that the actual acceleration factor at the resonant input energy is roughly the same for each different length, which is not obvious from the final energy graphs, as these increase with input energy.

The modulations of the vanes or rods of the RFQ produce the longitudinal field that enables particle acceleration, but they also affect the transverse field, and act to reduce transverse focusing. Net focusing can still occur as long as the modulations in the electric field are not too large in magnitude (see Equation B.10 and Equation B.11), requiring,

$$\epsilon \leq \frac{qE_0}{ma\omega^2 \cos\phi}, \tag{7.6}$$

where ϵ is the magnitude of the modulating electric field, a is the distance between the electrodes and the axis and ϕ is the phase of the particle relative to the phase of the electric field [32]. As these preliminary simulations do not alter the relative magnitude of the modulating electric field nor the transverse dimensions of the RFQ, the values ϵ and a are fixed. For a carbon 4+ ion, the charge is four times greater than for a proton, and the mass is very close to twelve times greater. To satisfy Equation 7.6 and achieve net focusing, a carbon 4+ beam needs an electric field three times greater than a proton beam in the same RFQ. However, reducing the frequency of the electric field allows a reduction in the magnitude of the electric field as well. Simulations show that net focusing can be achieved with the electric field reduced in magnitude by a factor of 0.8 relative to the magnitude used for proton acceleration. This translates to an inter-electrode potential of approximately 80 kV.

The limits for RF breakdown were investigated experimentally by Kilpatrick [78], leading to a formula for the electric breakdown limit now known as the Kilpatrick limit V_K:

$$V_\text{K} = \left(\frac{2\pi d}{\lambda}\right)^2 \frac{m_\text{p}c^2}{\pi e}, \tag{7.7}$$

where d is the smallest gap distance between electrodes, m_p is the mass of a proton and e is the charge of an electron. Often a linear approximation is used to evaluate the Kilpatrick limit:

$$V_\text{K}\,(\text{kV}) = 10 \cdot (1 + d\,(\text{mm})) \cdot \left(1 + 1.5 \times 10^{-3} \cdot f\,(\text{MHz})\right), \tag{7.8}$$

which gives a value of 56 kV when using a minimum gap distance of 3.3 mm and a frequency of 200 MHz. The ratio between the Kilpatrick limit and the actual electrode voltage is known as the Kilpatrick factor, and using current technology Kilpatrick factors up to 2.0 are acceptable for an RFQ, and this value is likely to increase as research advances. The required voltage of 80 kV corresponds to a Kilpatrick factor of 1.4, so is well within achievable limits.

The same scaling laws were applied to a carbon 6+ RFQ, and a number of frequencies were investigated, settling on a frequency of 280 MHz. Similar investigations as for carbon 4+ produced similar results. The parameters and results of the simulations are summarised in Table 8.4 and displayed in § 8.2.

The scaling method used in these simulations was designed for coordinate transformations rather than for making physical changes to the field magnitudes. This means that, although the z-coordinate was scaled correctly, the relative magnitudes of the transverse and longitudinal field components were not altered. This coordinate-based scaling method is useful for investigating the parameter space, as the acceleration is dependant on the RF field direction matching the location of the particles longitudinally in the accelerator, and so scaling the z-coordinate to synchronise the field with the particle motion will determine the length of the RFQ. However, a physical scaling of an RFQ—such as taking the *FETS* modulation parameters and applying them to a shorter RFQ length—would adjust the distribution of the electric field as the modulations became relatively deeper due to the contraction of the longitudinal dimension. This means that finding a scaled field map that correctly accelerates carbon ions is not a sufficient solution to the problem, because this field map cannot be obtained by simply scaling the modulation parameters accordingly. The next stage of simulation was to create a CAD model for an RFQ scaled for carbon acceleration, and adjust the modulation pattern to produce coherent acceleration with a real physical field map. This may produce a field map similar to the artificially scaled field maps investigated above, or may produce a different solution with similar transport characteristics.

7.5 PAMELA RFQ simulations

Results of simulations from four different models for the *PAMELA* RFQ are presented in § 8.3. The results are compared in Figure 7.21 and Table 8.5, and the final energy profiles are shown in Figure 7.22.

The Mark 1 *PAMELA* RFQ design was a directly scaled version of the *FETS* RFQ. By this stage, simulations focused on carbon 6+ ions in a superconducting RFQ with a radio frequency of 280 MHz. This higher frequency reduced the Kilpatrick factor and gave more scope for varying the maximum potential. The method of simulation was very straight-forward, as it involved taking the spreadsheet of modulation parameters for *FETS* and scaling the z-dimensions by the scaling factors calculated for the earlier models scaled in *GPT* (in § 7.4 above). This adjusted spreadsheet was then taken as the starting point for the established simulation process, as described above in § 7.2. The Mark 1 design accelerated some particles to the correct energy, but only 23% of the beam: 68% of particles were lost transversally in the RFQ—that is, the particles would hit the vane tips—and a further 9% were lost longitudinally—that is, were not accelerated correctly and fell behind the bunch, and ended the simulation with their energy too low.

The Mark 2 *PAMELA* RFQ design returned to *RFQSIM* to generate a completely new set of modulation parameters, tailored to the application of carbon 6+ ions, rather than modifying the proton parameters. This spreadsheet was then used to generate a new CAD model, field map and tracking simulation. The results were very promising, with 97% of particles transported to the end of the RFQ and accelerated to the correct energy. However, this design was 3.8 m long, rather than the 2 m of the Mark 1 design. For a space-limited hospital environment, increasing the length by such a factor is a major drawback. Also, to maintain the same voltage across the vane tips for almost twice the length requires almost twice the RF power. The increased length was due to a much gentler bunching section for the Mark 2 design. This is a product of the focus of the *RFQSIM* software on high-current accelerators, in which space charge is a driving force for the modulation pattern. As discussed in § 7.2.5, the low current of the *PAMELA* RFQ means that space charge is almost negligible, so such a conservative long bunching section is not necessary and is a waste of RF power.

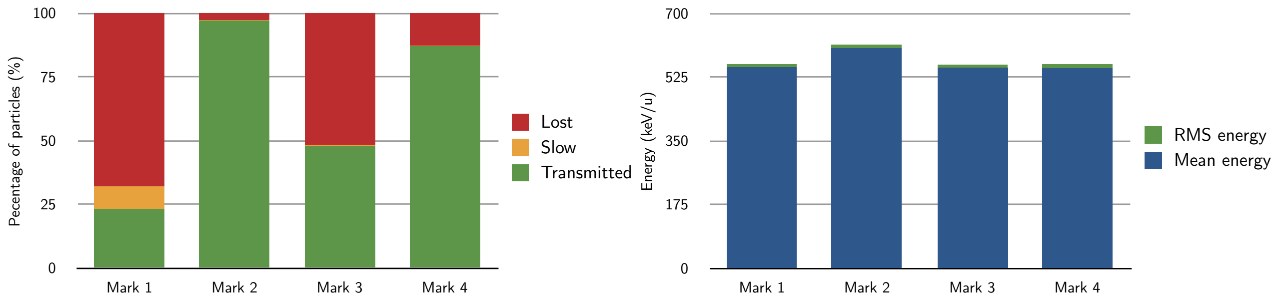

(a) Transmission **(b)** Energy

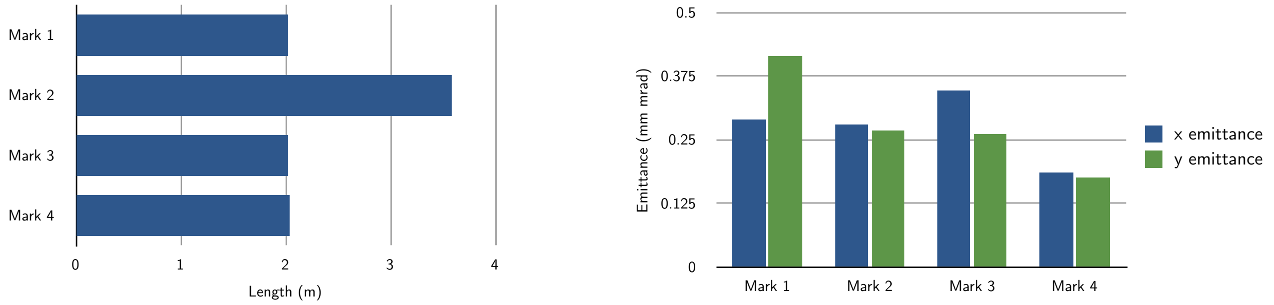

(c) Length **(d)** Emittance

Figure 7.21: Comparison of different model simulations for the *PAMELA* RFQ:
(a) particles transmitted (green), lost longitudinally (amber) and lost transversally (red);
(b) mean energy and RMS energy spread of transmitted particles;
(c) length of RFQ; and
(d) final emittance of transmitted particles in x (blue) and y (green) directions

The Mark 3 *PAMELA* RFQ design took a different approach in generating modulation parameters. The Mark 1 parameters scaled from the *FETS* design were taken and modified, and these parameters run through the normal process to produce a CAD model and field map for tracking. After each simulation, the results were analysed to find the cause of the particle losses, and suggest modifications to the design to reduce these losses. Modifications included adjusting the depth of the modulations in different sections of the RFQ, and adjusting the position of the vane tips with respect to the beam axis. The design method constructed above made this process very simple, and modifications that would not be possible with a numerical solver could be investigated simply by adjusting the spreadsheet and running through the design code. The modifications were mainly relating to the shaper and buncher sections, to attempt to bunch the beam more strongly than the long bunching regime from the Mark 2 design. The most effective modification involved reducing the separation r_0 of the vanes from the beam axis by 10%. The Mark 3 design accelerated 48% of the particles correctly, with the majority of the remaining particles hitting the vane tips in the bunching section due to the greater force from the increased transverse field. This increased transverse force is applied to both the focusing and de-focusing directions in the RFQ, and so the oscillations of the particle tracks around the beam axis are increased in amplitude, bringing more of the particles into contact with the vane tips.

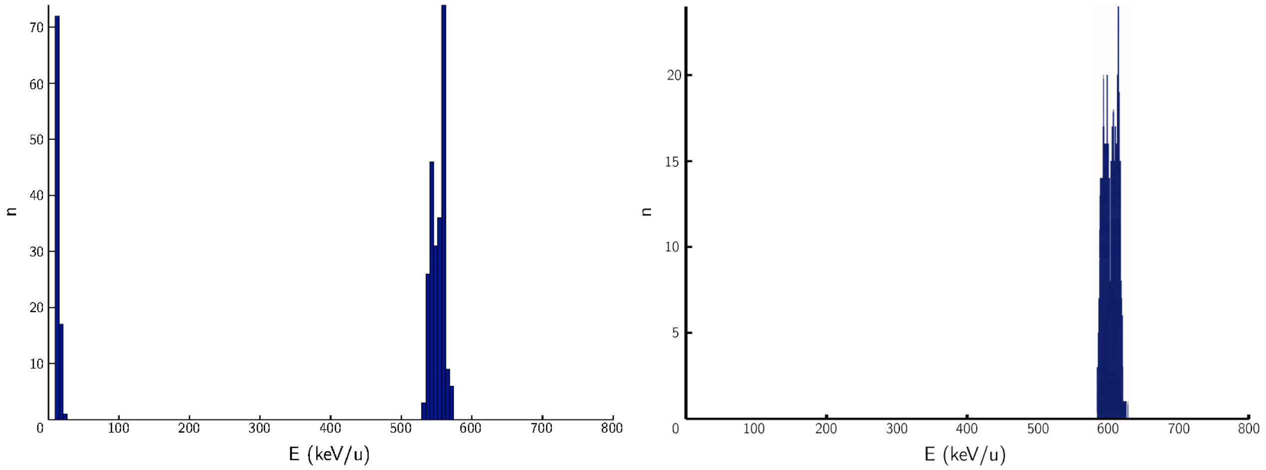

(a) Mark 1 **(b)** Mark 2

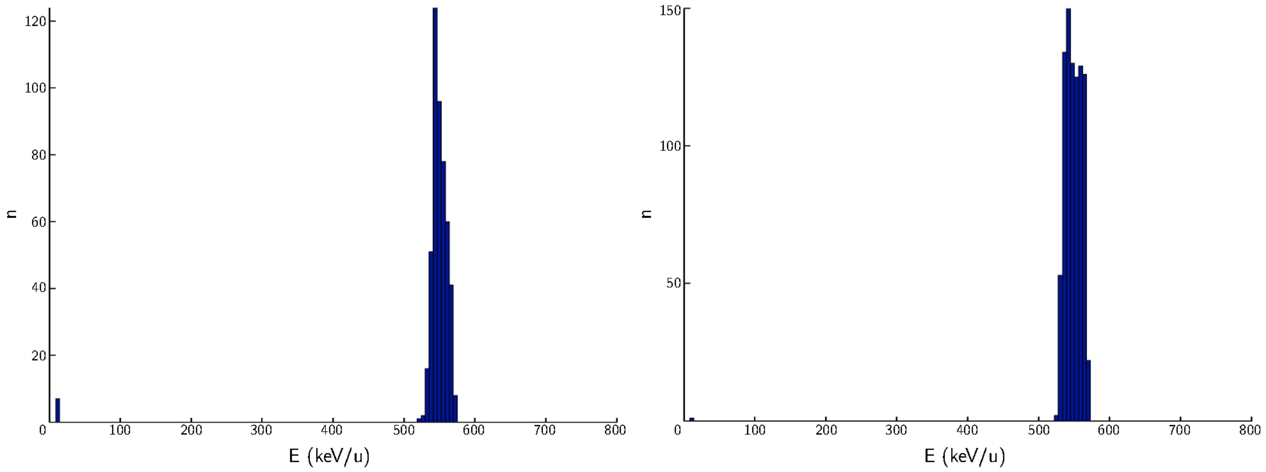

(c) Mark 3 **(d)** Mark 4

Figure 7.22: Comparison of final energy profiles for the *PAMELA* RFQ simulations

The evolution of the phase-space of the particle beam through the Mark 3 field showed that particles were slipping out of phase very early in the RFQ, soon after the matching section. The Mark 4 *PAMELA* RFQ design doubled the length of the matching section, so the particles would have more time to adjust to the correct phase of entry to the RFQ. A number of other modifications were also tested, with the most effective being the reduction of the separation r_0 by a further 10%. This increased the Kilpatrick factor (see Equation 7.7 and Equation 7.8, and discussion in § 7.4) to 1.21, which is still a conservative value, and reduced the acceptance of the RFQ by 10%, which is an acceptable compromise. The Mark 4 design accelerated 87% of particles to the correct energy. This value was accepted as sufficiently high to mark the completion of this stage of design for a *PAMELA* RFQ.[7]

---

[7] Any further optimisation would be dependent on the precise input distribution and the required matching parameters for the output distribution, which are not completely finalised at this time. As these parameters are set, further iterations of the same design process should be carried out to match the RFQ input and output to the rest of the injector system. See the recommendations for further work in Chapter 9.

8 RFQ Simulation Results

The methods for developing and simulating RFQ designs based on CAD models were set out in the previous chapter, and important results were presented and discussed. This chapter details the particle tracking results of these simulations, including numerical comparisons between different models and graphical representations of the particle dynamics.

The first sets of results (§ 8.1) were models of the *FETS* RFQ, based on field maps produced by three different codes: *RFQSIM* (§ 8.1.1), *CST* (§ 8.1.2) and *Comsol* (§ 8.1.3). These simulations were used for benchmarking the new code. The next set of results (§ 8.2) concerns preliminary carbon RFQ models based on scaled versions of the *PAMELA* field map. These models were intended as studies in the scaling laws in an RFQ and to define the parameter space for a carbon 4+ or 6+ RFQ. The final set of results (§ 8.3) were produced from models designed for *PAMELA* to accelerate carbon 6+ ions for injection into a linac and then into the FFAG rings.

The particle tracking results presented are based upon simulations of 10 000 particles, unless otherwise stated.

8.1 FETS RFQ

The design for the *FETS* RFQ was produced using *RFQSIM* (see § 7.2.1). The first stage of developing the new simulation method involved comparing the particle tracking results from the *RFQSIM* code with the results from the new code using *General Particle Tracer* (see § 7.2.5). *RFQSIM* has been extensively tested and compared against other accepted codes [74], so confirmation of the new code using the same field map acts as a validation of the *GPT* section of the process. The next stage of development was to model the RFQ structure in a CAD package, *Autodesk Inventor* (see § 7.2.2), and calculate the electric field using simulation software, either *CST EM Studio* (see § 7.2.3) or *Comsol Multiphysics* (see § 7.2.4). The methods used are described above in § 7.3, including the steps taken as the simulation process matured over time. The results of each of these simulations are presented below.

8.1.1 RFQSIM field map

The development of the modelling code started with the particle tracking, as a field map was already available, generated using *RFQSIM*. The field map was imported into *GPT* and used as the basis of a linear simulation lasting the length of the RFQ. Various technical issues needed to be overcome, but once the code was producing reliable results, the *RFQSIM* field map produced 100% transmission and acceleration of all particles to 3 MeV, in the absence of space-charge forces. As noted in § 7.2.5, space-charge effects are important for the *FETS* RFQ, but inconsequential for the *PAMELA* RFQ. However, space charge increases the processing requirements by a significant amount, so these early simulations did not include this effect for the *FETS* RFQ either. The results are plotted in Figure 8.1 and summarised in Table 8.1.

Result	Value
Length (m)	4.060
Transmission (%)	100
Transverse losses (%)	0
Longitudinal losses (%)	0
Mean energy (MeV)	3.033
RMS energy spread (keV)	14
x-emittance (mm mrad)	0.198
y-emittance (mm mrad)	0.203

Table 8.1: Summary of results of simulations for the *RFQSIM FETS* RFQ field map
Note that emittances quoted here and in following tables are normalised RMS values

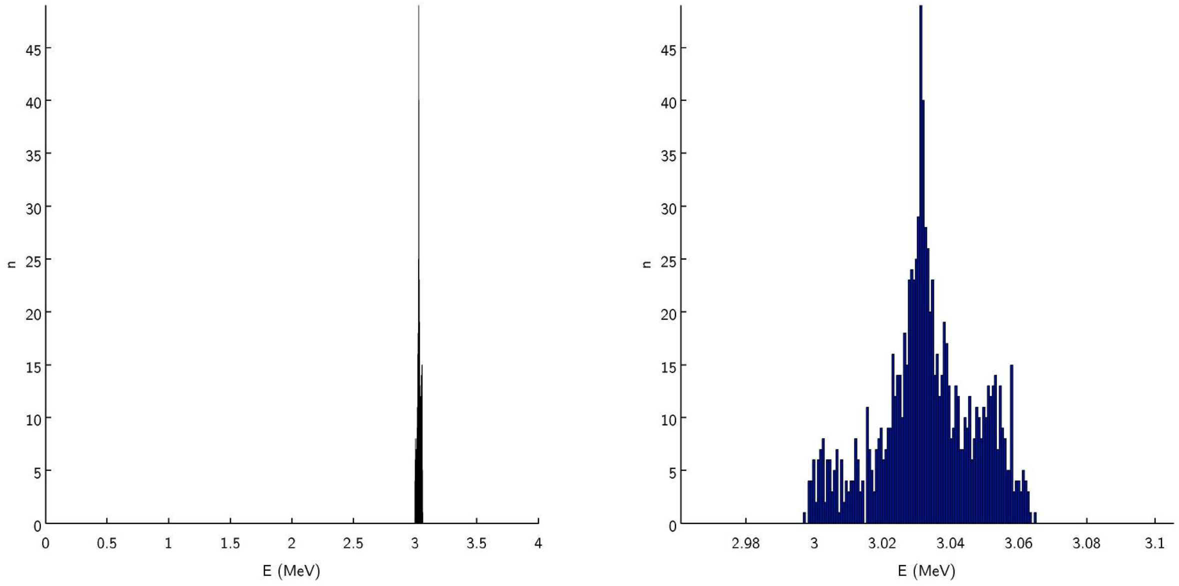

(a) Final energy distribution

(b) Final energy peak detail

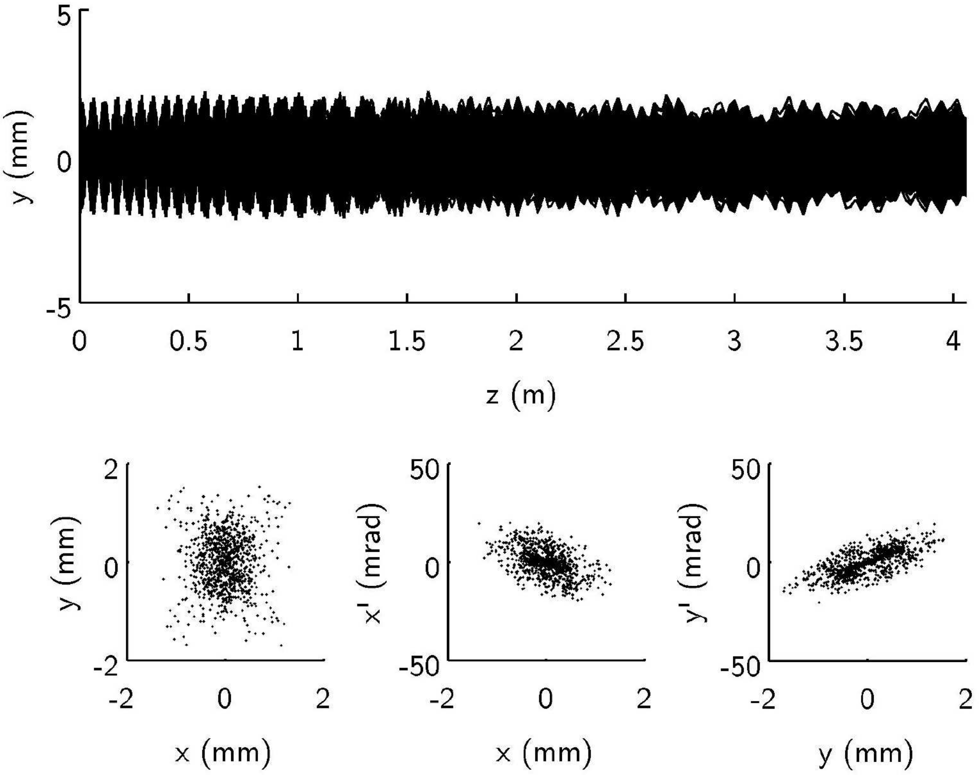

(c) Particle trajectories and final phase space

Figure 8.1: Results of *FETS* RFQ simulations using the *RFQSIM* field map:
(a) Histogram of energies of particles at the end of the RFQ;
(b) Detailed histogram of energies of fully accelerated particles at the end of the RFQ;
(c) Particle distributions, showing tracks through the RFQ and final phase space—lost particles would be marked in colour

8.1.2 CST field map

Once the *GPT* section of the code produced reliable results, the development process moved to using CAD models and solving for the electric field. The first stage was to produce the CAD model, as described in § 7.2.2. The aim of the CAD modelling is to produce the correct particle dynamics, so the results below deal with the process once a CAD model was completed and electrostatic simulation could be carried out by importing the geometry from *Inventor*.

8.1.2.1 CST1: First simulation

The first complete field map produced using *CST* did not produce the coherent acceleration predicted by the *RFQSIM* field map. Almost all particles (99.9%) reached the end of the simulation, but much slower than designed—in fact, many of the particles did not reach the exit by the end of the simulation time. The average energy was 1.3 MeV with a large spread of 261 keV, compared to the previous results of 3 MeV with a narrow 14 keV spread. The results are plotted in Figure 8.2 and included in the summary in Table 8.2.

	CST1	**7 mm**	**CST2**	**CST3**	**CST4**
Transmission (%)	0	99.6	56.3	0	100
Transverse losses (%)	0.01	0.4	6.7	0.2	0
Longitudinal losses (%)	99.9	0	37.0	99.8	0
Mean energy (MeV)	1.31	3.02	2.99	1.977	3.03
RMS energy spread (keV)	261	14	444	378	12
x-emittance (mm mrad)	0.298	0.229	0.242	0.244	0.225
y-emittance (mm mrad)	0.244	0.248	0.248	0.349	0.205

Table 8.2: Summary of results of simulations for the *CST FETS* RFQ field maps

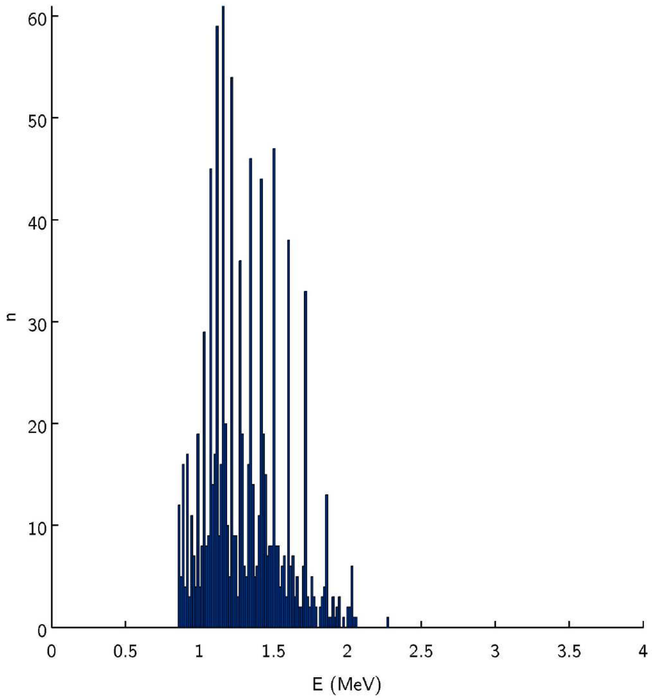

(a) Final energy distribution

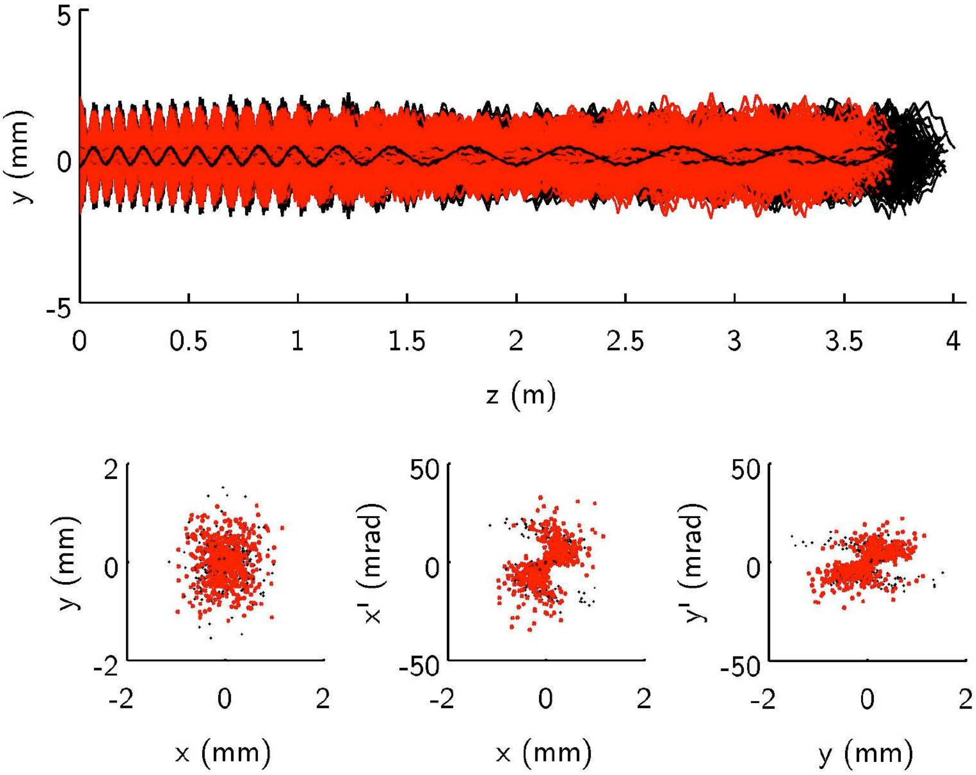

(b) Particle trajectories and final phase space

Figure 8.2: Results of *FETS* RFQ simulations using the first *CST* field map; particles marked in red did not reach the end of the simulation

8.1.2.2 Wedge geometry

The most apparent difference between the *RFQSIM* and *CST* field maps was found in the the transverse field directions. Although it is counter-intuitive that the problem would lie in the transverse field, as the particles were focused correctly but not accelerated correctly, the transverse and longitudinal fields in an RFQ are intrinsically linked. The action of the transverse field to guide the particles influences the accelerating force, and hence an incorrect focusing field can damage the acceleration effects. Figure 8.3a shows the departure of the *CST* transverse field from the *RFQSIM* field. The deviation could be due to the difference in the modelling methods—*RFQSIM* starts from a pure hyperbolic quadrupole and adds terms to make this more circular, whereas CAD-based models start from the circular geometry. To attempt to bring the models closer to a hyperbolic model, wedges were added to the sides of the vanes, as previously illustrated in Figure 7.9. A simplified vane model without the modulations was used to test the transverse field map and see whether the wedges produced a closer fit to the *RFQSIM* data. Various widths, angles and depths of wedges were tested. Figure 8.3b shows virtually no change in the area of field of interest between the vane tips, using the largest wedges tested. The wedges only affected the field far from the central beam axis, so this difference from a hyperbolic model cannot explain the difference between the *RFQSIM* and *CST* field maps. The wedge model was therefore not incorporated into the full RFQ model, so no tracking results are included here.

8.1.2.3 Radius of curvature

Another method to bring a circular geometry closer to a hyperbolic shape is to increase the radius of curvature of the vane tips. This method is discussed in § 7.3.2 and illustrated in Figure 7.10. Tests were carried out with the simplified vane model without vane modulations for a variety of different radii of curvature. Figure 8.3c shows the field comparison for a radius of 5 mm and Figure 8.3d shows the same comparison with a radius of 7 mm. The results show that the larger the radius, the closer the model approaches the *RFQSIM* field shape. Models larger than 7 mm were also tested, but the vanes were by this point so large as to begin to touch each other. The full RFQ model with the vane modulations included was rebuilt with a radius of curvature of 7 mm, and the particle tracking code run with this model. The results are plotted in Figure 8.4 and included in the summary in Table 8.2.

The 7 mm results seem similar to the *RFQSIM* results, which is initially puzzling, as interrogating the *RFQSIM* field map clearly shows clear vane tips with a radius of curvature closer to 3 mm (see Figure 7.8). Additionally, by increasing the radius of curvature of the vane tips without increasing the separation of the vanes or decreasing the potential difference, the electric field strength increases to levels at which electrical breakdown is almost certain to occur.

These results sparked investigation into the parameters produced by *RFQSIM*. It was found that, while all internal calculations in the code were self-consistent, some differences in measurement unit handling produced inaccuracies in the parameter output procedure. This meant that the field map produced by *RFQSIM* and the field map produced by modelling the same parameters in a CAD package *would not be modelling the same RFQ*. Some minor alterations to *RFQSIM* produced a new set of parameters, and these were used for the next phase of CAD modelling.

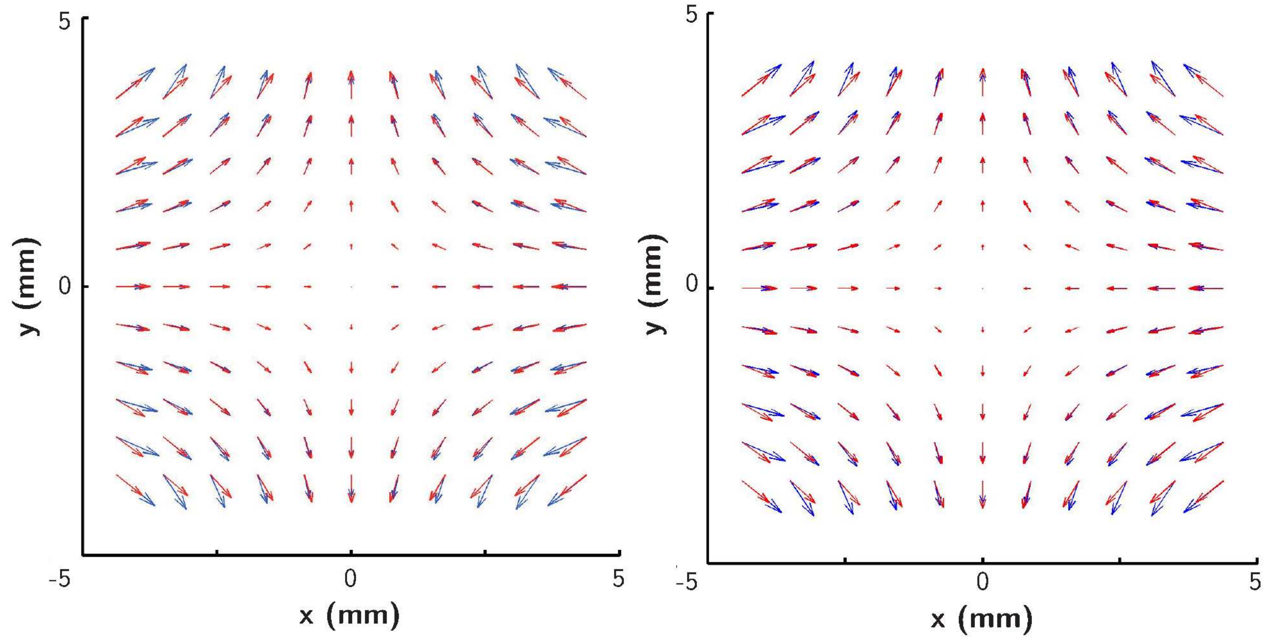

(a) *RFQSIM* and first *CST* field maps **(b)** *RFQSIM* and wedged *CST* field maps

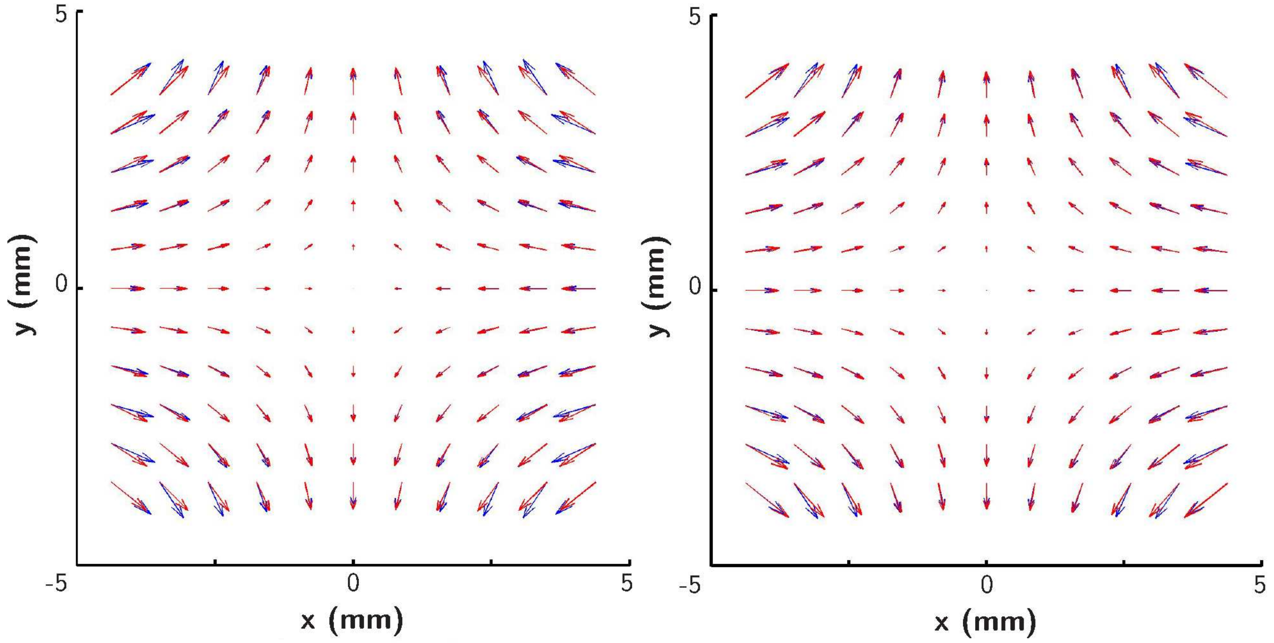

(c) *RFQSIM* and 5 mm radius *CST* field maps **(d)** *RFQSIM* and 7 mm radius *CST* field maps

Figure 8.3: Comparison of transverse slices through the *RFQSIM* (blue) and *CST* (red) field maps:
(a) the original CST model;
(b) with wedges applied, showing virtually no difference produced by the wedges;
(c) with radius of curvature increased to 5 mm;
(d) with radius of curvature increased to 7 mm, showing closest agreement

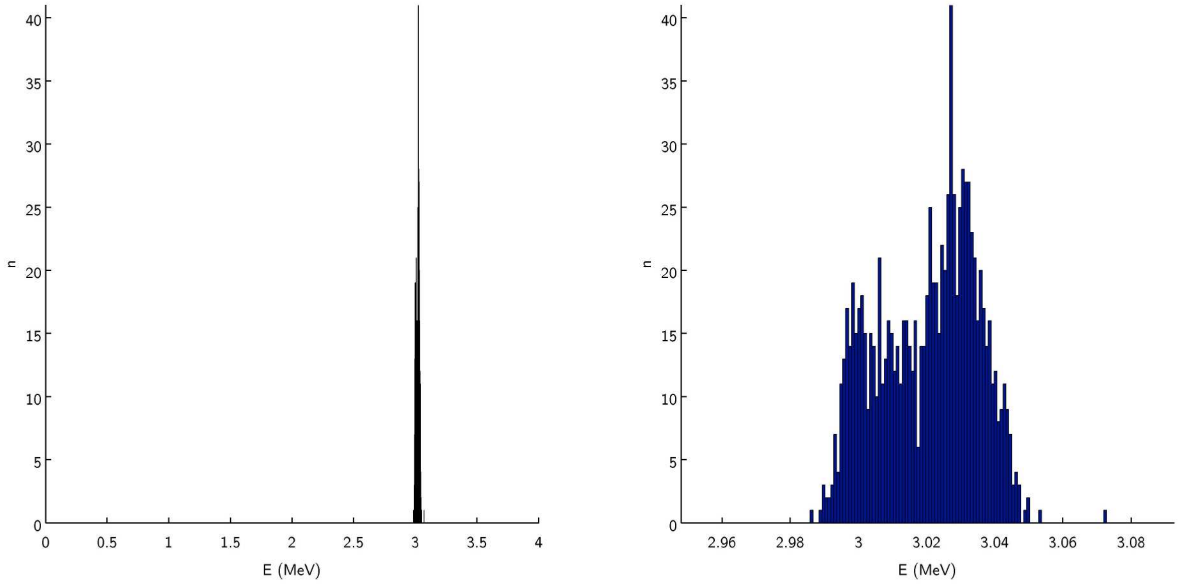

(a) Final energy distribution

(b) Final energy peak detail

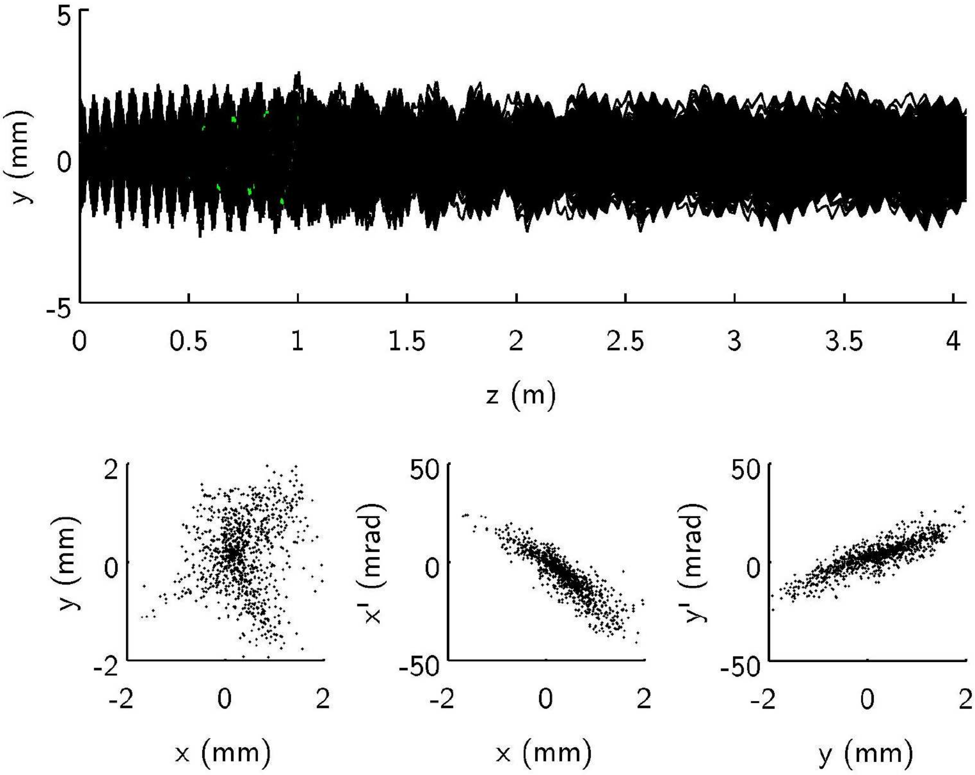

(c) Particle trajectories and final phase space

Figure 8.4: Results of *FETS* RFQ simulations using the first *CST* field map adjusted to use a radius of curvature of 7 mm:
(a) Histogram of energies of particles at the end of the RFQ;
(b) Detailed histogram of energies of fully accelerated particles at the end of the RFQ;
(c) Particle distributions, showing tracks through the RFQ and final phase space—lost particles would be marked in colour

8.1.2.4 CST2: Corrected input parameters

With the new CAD model from the corrected *RFQSIM* output parameters, a new field map was produced in *CST* and particles tracked through this field map using *GPT*. The results of these tracking simulations are presented in Figure 8.5 and included in the summary in Table 8.2. With this field map, 93.3% of the particles reached the end of the RFQ, and many of these were correctly accelerated to the full energy of 3 MeV, but a large number of particles did not reach the full energy. With an accurate field map, all the particles were expected to reach the full energy, as demonstrated above with the first *CST* field map modified to have a larger radius of curvature (compare Figure 8.4). It was found that the inaccuracies in this new field map were rooted in the mesh used in *CST*, as discussed in § 7.3.2. The mesh determines the accuracy of the electric field solution, and in this case it wasn't dense enough to produce an accurate solution. Unfortunately, the software could not easily produce a denser mesh for the full RFQ. The next phase of the simulations took the same CAD model but split it into five sections, so each section could be solved separately with a denser mesh, and the results of these models combined into a single field map for the particle tracking.

8.1.2.5 CST3: Reconstruction from sections

The field map built in five sections and combined in *Matlab* produced worse results than the previous single field map, which was not expected. The results of the tracking simulations are presented in Figure 8.6 and included in the summary in Table 8.2. Although a higher proportion (99.8%) of the particles reached the end of the RFQ, in this case none of them reached the full energy. A number of possible causes of this discrepancy were tested, and the models refined further, but the problem was finally resolved after finding a bug in the recombination code written in *Matlab* that had not correctly rebuilt the sections into a coherent field map.

8.1.2.6 CST4: Final results

The final *CST* model, built in five sections from an *Inventor* CAD model, produced clean results, as shown in Figure 8.7 and included in the summary in Table 8.2. All the particles reached the end of the RFQ at the full energy of 3 MeV, with an RMS energy spread of just 12 keV.

As the simulation effort switched priority from building an accurate model to optimising the design and simulation process, a number of issues gradually came to light that prompted a change of electrostatic modelling software. The technical reasons are set out in § 7.3.2—in summary, boundary conditions require the splitting of the model into much smaller pieces than the five already used, if tracking with space-charge forces was to be effective. To carry this out in *Comsol Multiphysics* using the built-in *Matlab* application programming interface (API) would be much more efficient than the existing methods using *CST*. Other factors such as cost and the integration of particle tracking modelling with existing *Comsol* models for structural and RF engineering also favoured *Comsol*, so this package was adopted for the next stage of simulations.

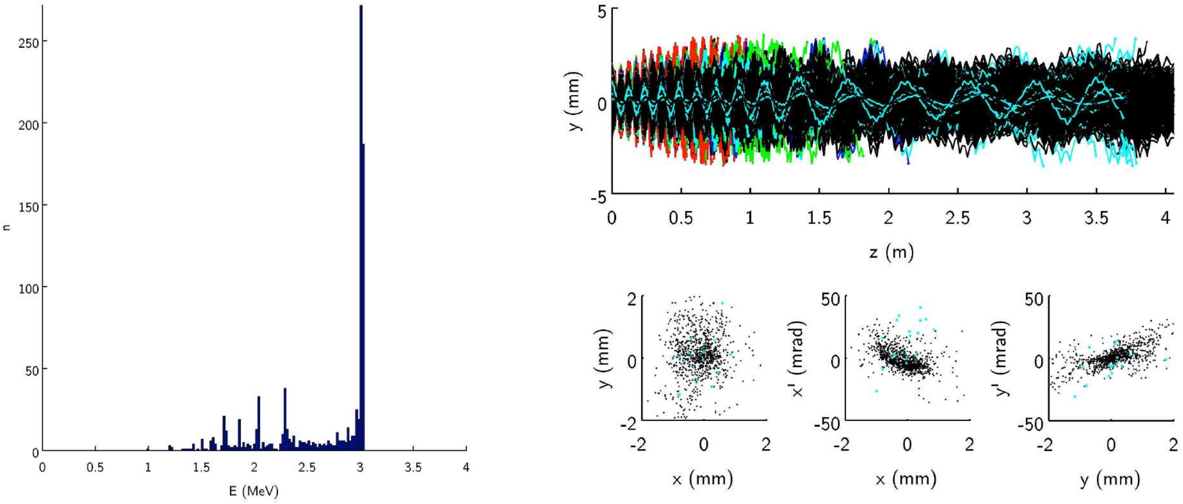

(a) Final energy distribution

(b) Particle trajectories and final phase space

Figure 8.5: Results of *FETS* RFQ simulations using the second *CST* field map, based on corrected parameter values from *RFQSIM:*
(a) Histogram of energies of particles at the end of the RFQ;
(b) Particle distributions, showing tracks through the RFQ and final phase space, with lost particles marked in colours dependent on the area of the RFQ in which they are lost

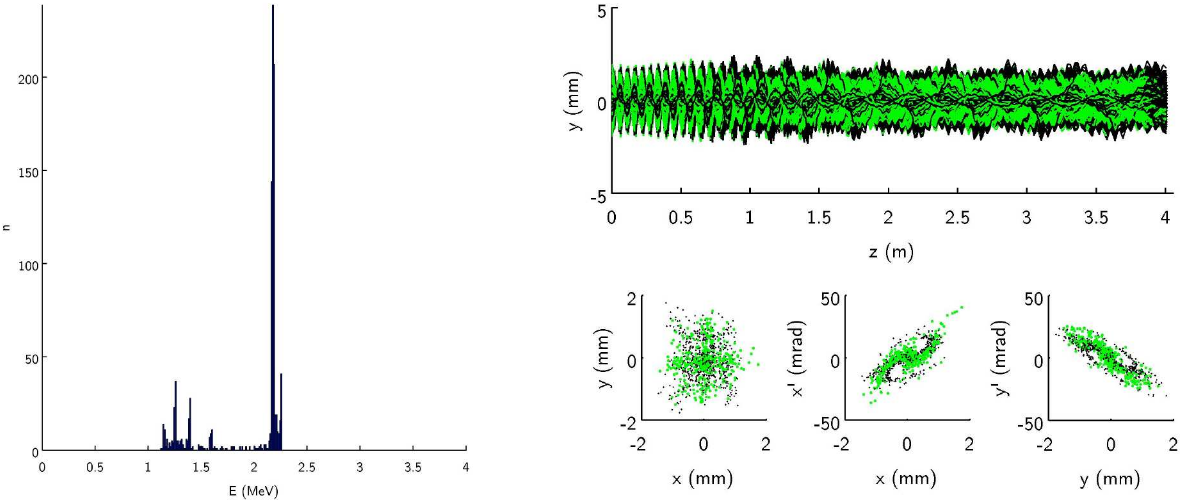

(a) Final energy distribution

(b) Particle trajectories and final phase space

Figure 8.6: Results of *FETS* RFQ simulations using the third *CST* field map, built in sections to improve mesh density:
(a) Histogram of energies of particles at the end of the RFQ;
(b) Particle distributions, showing tracks through the RFQ and final phase space, with lost particles marked in colours dependent on the area of the RFQ in which they are lost

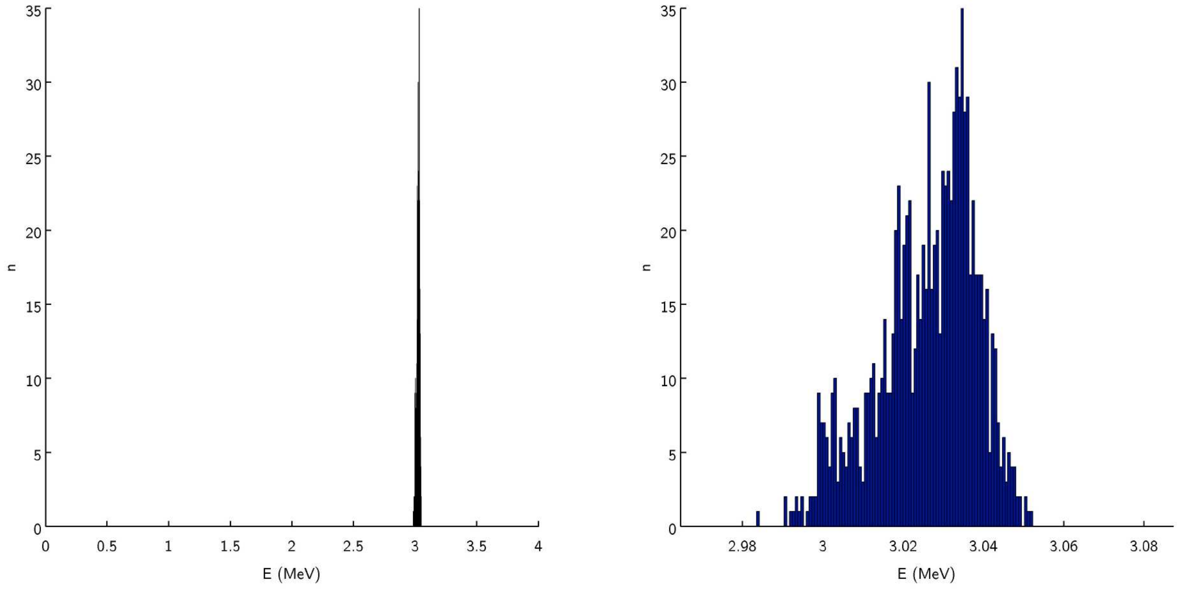

(a) Final energy distribution

(b) Final energy peak detail

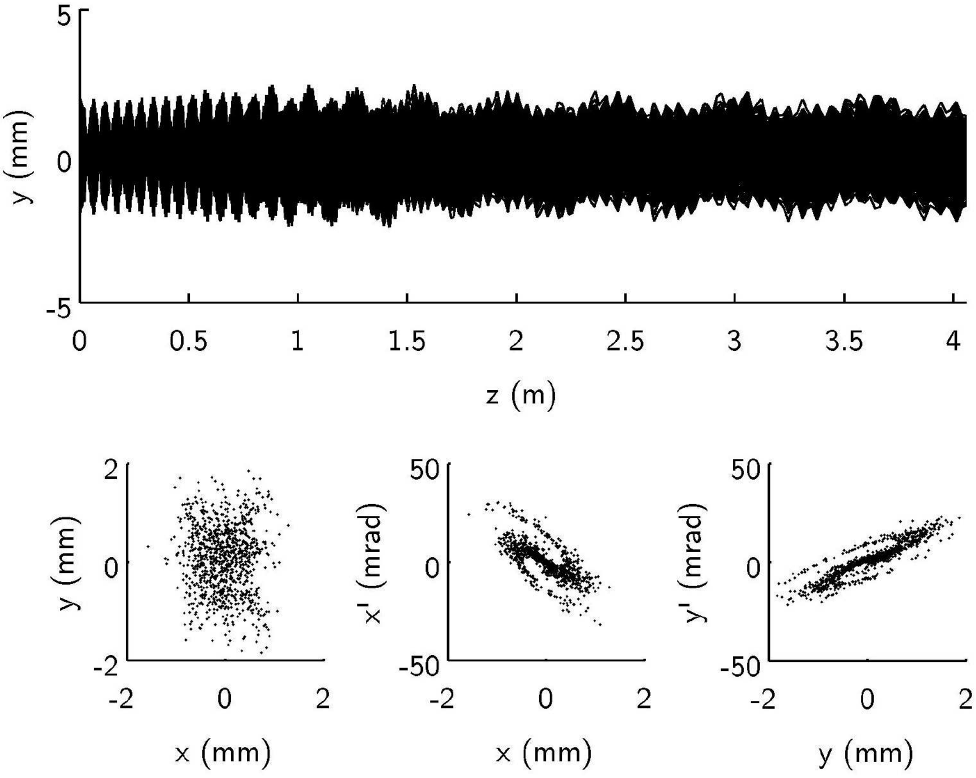

(c) Particle trajectories and final phase space

Figure 8.7: Results of *FETS* RFQ simulations using the fourth and final *CST* field map, built in sections and correctly reconstructed into a full RFQ field map:
(a) Histogram of energies of particles at the end of the RFQ;
(b) Detailed histogram of energies of fully accelerated particles at the end of the RFQ;
(c) Particle distributions, showing tracks through the RFQ and final phase space—lost particles would be marked in colour

8.1.3 Comsol field map

The first activity carried out in *Comsol* involved verifying that the new process produced sensible field maps that simulated the field inside an RFQ at least as accurately as the existing *CST* method (see § 7.3.3). Once this comparative analysis was complete, and the new method verified, particle tracking through the *Comsol*-generated field map was carried out. The results of the tracking simulations are presented in Figure 8.8 and included in the summary in Table 8.3. The results match the *RFQSIM* (Figure 8.1) and *CST* (Figure 8.7) models in many details, but when space-charge forces are included, the CAD-based and expansion-based codes differ significantly in their response to increasing current (see § 7.3.3, and Figure 7.18 in particular).

In order to produce more accurate field maps, and to remove unphysical anomalies due to meshing and boundary errors, the modelling method as described in § 7.2.4 was devised. The electric field map is produced for each cell separately in *Comsol* and then combined in *Matlab*, before being imported into *GPT* for the particle tracking. The results of the tracking simulations are presented in Figure 8.9 and included in the summary in Table 8.3. The results for all space-charge currents act as expected, and differences between the *RFQSIM* and *Comsol* can now confidently be attributed to the increased accuracy of CAD modelling over the Taylor expansion method (see § 7.3.3).

	Comsol1	**Comsol2**
Transmission (%)	100	100
Transverse losses (%)	0	0
Longitudinal losses (%)	0	0
Mean energy (MeV)	3.03	3.02
RMS energy spread (keV)	10	15
x-emittance (mm mrad)	0.243	0.168
y-emittance (mm mrad)	0.111	0.178

Table 8.3: Summary of results of simulations for the *Comsol FETS* RFQ field maps; *Comsol 1* refers to the field map in five sections, and *Comsol 2* refers to the field map built one cell at a time

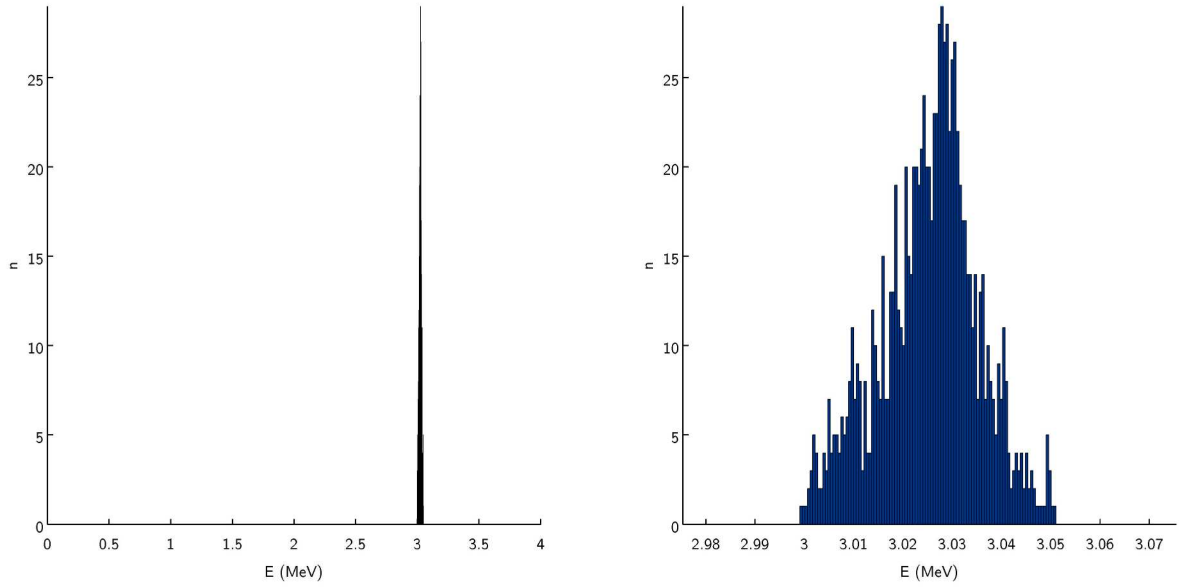

(a) Final energy distribution **(b)** Final energy peak detail

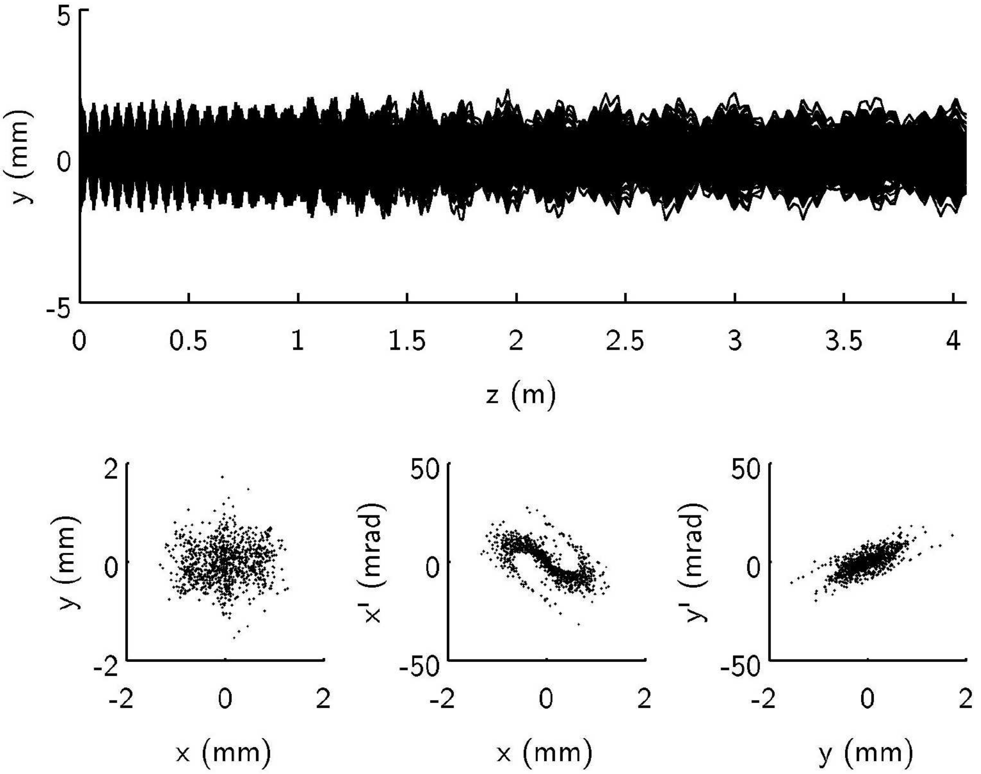

(c) Particle trajectories and final phase space

Figure 8.8: Results of *FETS* RFQ simulations using the first *Comsol* field map, built in five sections:
(a) Histogram of energies of particles at the end of the RFQ;
(b) Detailed histogram of energies of fully accelerated particles at the end of the RFQ;
(c) Particle distributions, showing tracks through the RFQ and final phase space, with lost particles marked in colours dependent on the area of the RFQ in which they are lost

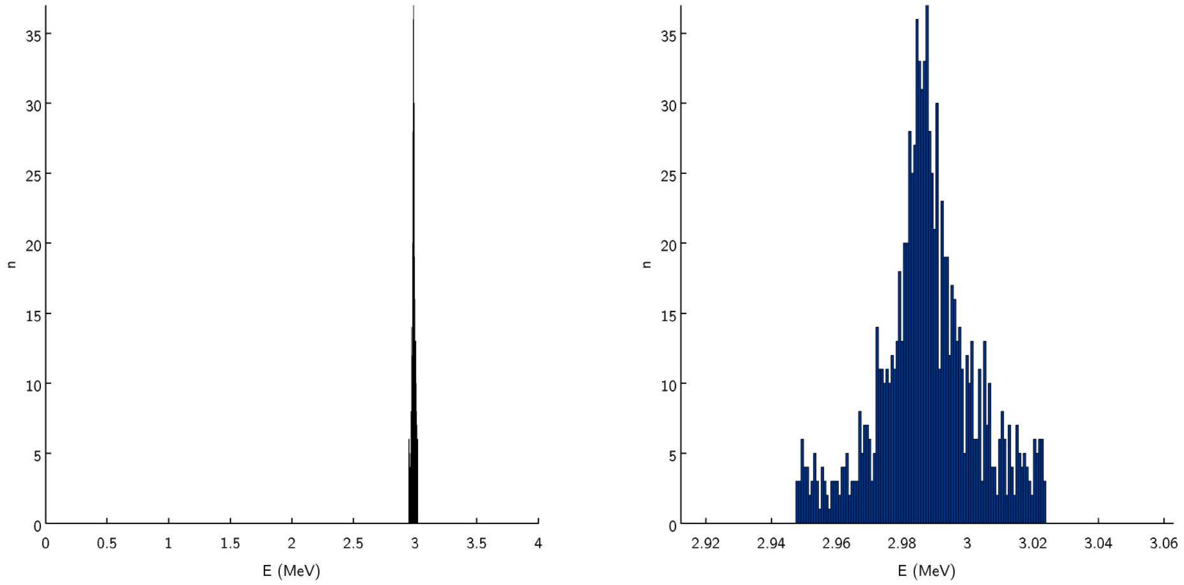

(a) Final energy distribution

(b) Final energy peak detail

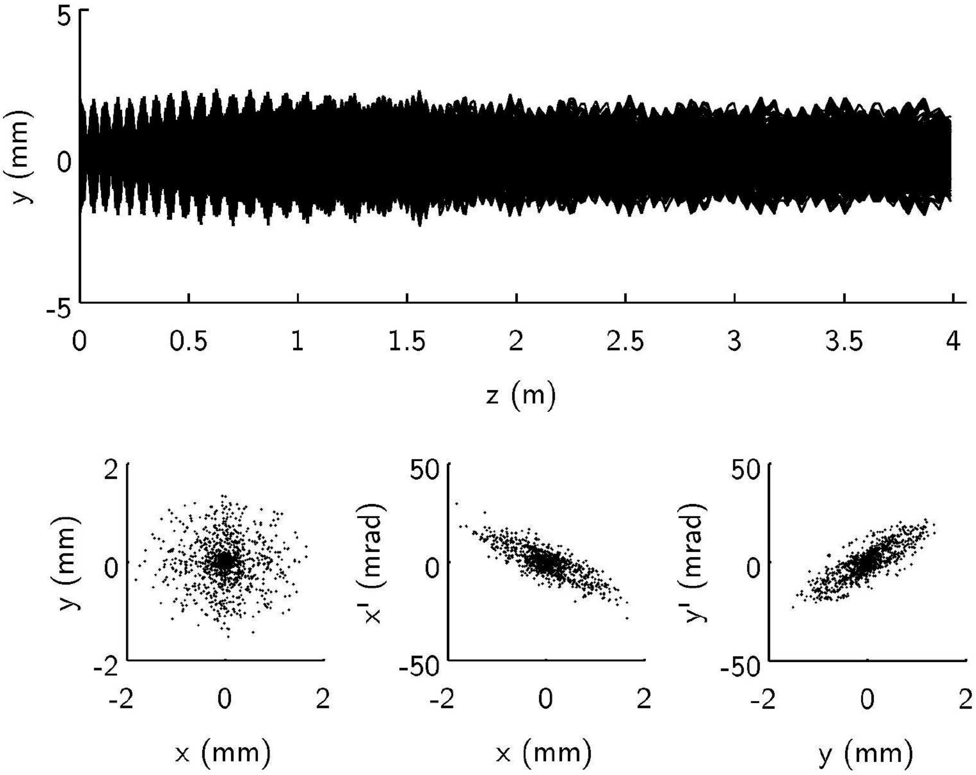

(c) Particle trajectories and final phase space

Figure 8.9: Results of *FETS* RFQ simulations using the final *Comsol* field map, built cell-by-cell:
(a) Histogram of energies of particles at the end of the RFQ;
(b) Detailed histogram of energies of fully accelerated particles at the end of the RFQ;
(c) Particle distributions, showing tracks through the RFQ and final phase space, with lost particles marked in colours dependent on the area of the RFQ in which they are lost

8.2 Scaled FETS RFQ for PAMELA

The method of scaling the *FETS* RFQ for use with carbon ions is described in § 7.4, and results for different scaling factors are summarised. The current section sets out the results of the final particle tracking simulations with the scaled field maps using *CST* (§ 8.2.1) and *Comsol* (§ 8.2.2). As previously discussed (also in § 7.4), the scaled field maps are not the same as the field from a real RFQ with the scaling factor applied, so these scaled simulations are just a preliminary step to define the parameter space before developing new RFQ parameters. There were no differences in the method used for simulating the scaled RFQ with the *CST* and *Comsol* field maps, only different field maps used as the starting point for the scaling process.

8.2.1 CST

The results of the tracking simulations based on the *CST* field map are presented in Figure 8.10 for carbon 4+ and Figure 8.11 for carbon 6+, and are included in the summary in Table 8.4. 99% of the particles were accelerated to the full energy for both ion species. Note that the lower frequency (200 MHz) of the carbon 4+ RFQ would be more efficient with a four-rod RFQ, but these models based on the *FETS* RFQ are four-vanes models.

8.2.2 Comsol

The results of the tracking simulations based on the *Comsol* field map are presented in Figure 8.12 for carbon 4+ and Figure 8.13 for carbon 6+, and are included in the summary in Table 8.4. The carbon 6+ RFQ was scaled to run at 280 MHz in this version, which reduces the length of the RFQ, but resulted in a slightly poorer transmission of 93%. Further optimisation of the scaling function for this increased frequency could improve this result, but as these simulations are aimed to explore the parameter space rather than produce an optimised field map, this refinement is not necessary at this point.

	CST Carbon 4+	**CST Carbon 6+**	**Comsol Carbon 4+**	**Comsol Carbon 6+**
E-field frequency (MHz)	200	240	200	280
Initial particle energy (keV/u)	8	12	8	12
RFQ length (m)	2.32	2.36	2.32	2.03
Electrode potential (kV)	75	78	85	85
Transmission (%)	98.7	99.2	98.9	93.0
Transverse losses (%)	1.2	0.8	1.1	7.0
Longitudinal losses (%)	0.1	0	0	0
Mean energy (keV/u)	371	557	365	554
RMS energy spread (keV/u)	5	8	6	8
x-emittance (mm mrad)	0.111	0.158	0.124	0.216
y-emittance (mm mrad)	0.137	0.167	0.150	0.208

Table 8.4: Simulation parameters and comparison of results for scaled carbon RFQ models

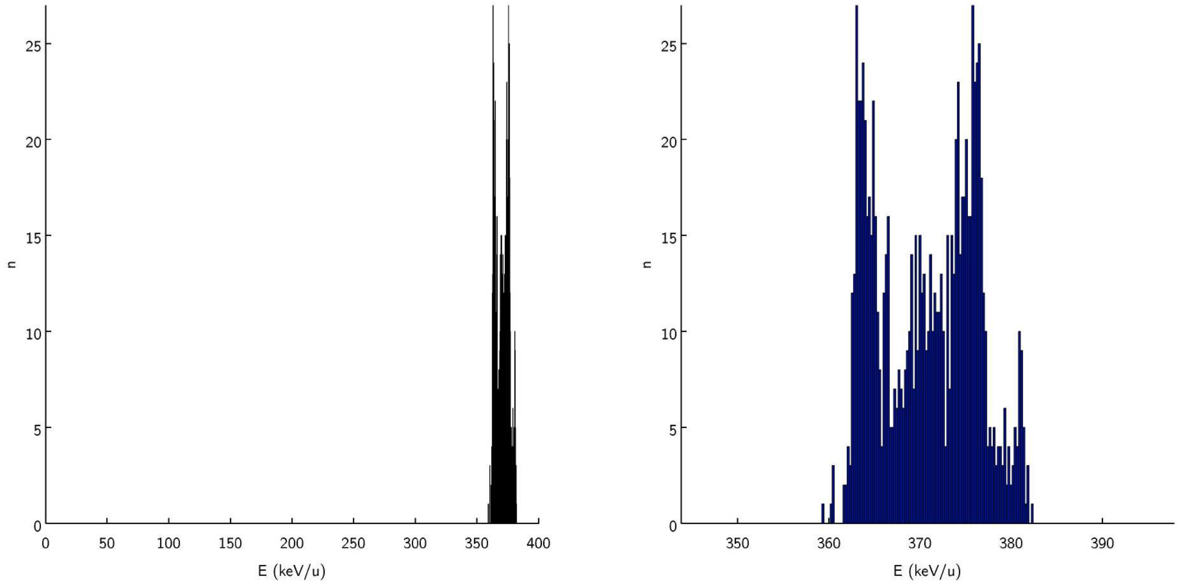

(a) Final energy distribution

(b) Final energy peak detail

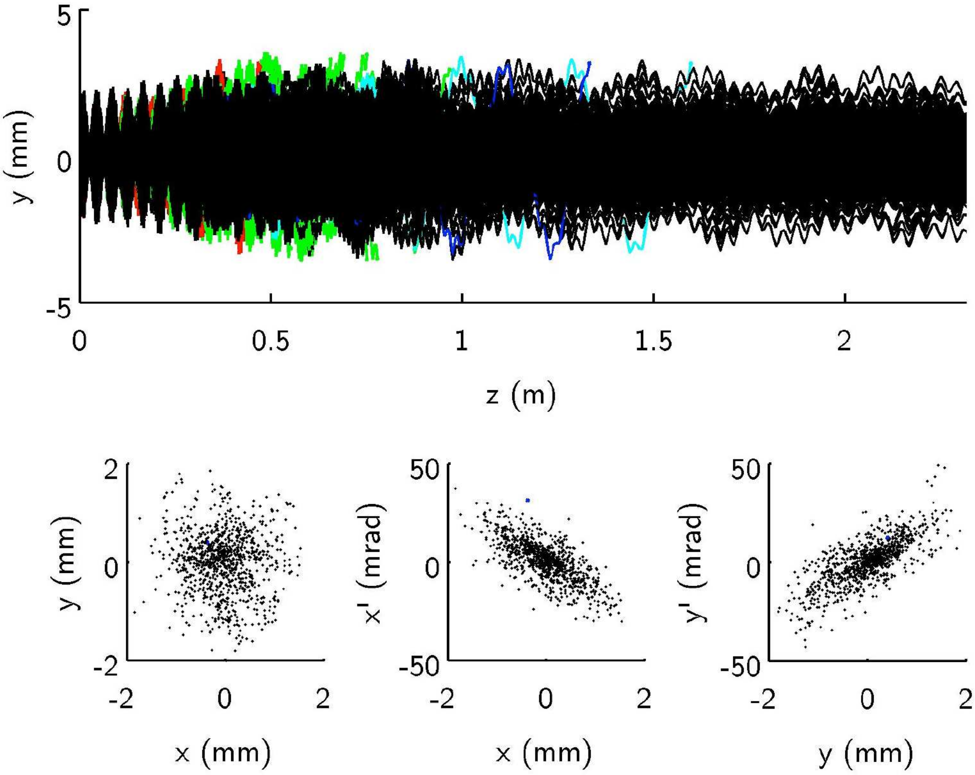

(c) Particle trajectories and final phase space

Figure 8.10: Results of carbon 4+ RFQ simulations using the final *CST* field map scaled in *GPT*:
(a) Histogram of energies of particles at the end of the RFQ;
(b) Detailed histogram of energies of fully accelerated particles at the end of the RFQ;
(c) Particle distributions, showing tracks through the RFQ and final phase space, with lost particles marked in colours dependent on the area of the RFQ in which they are lost

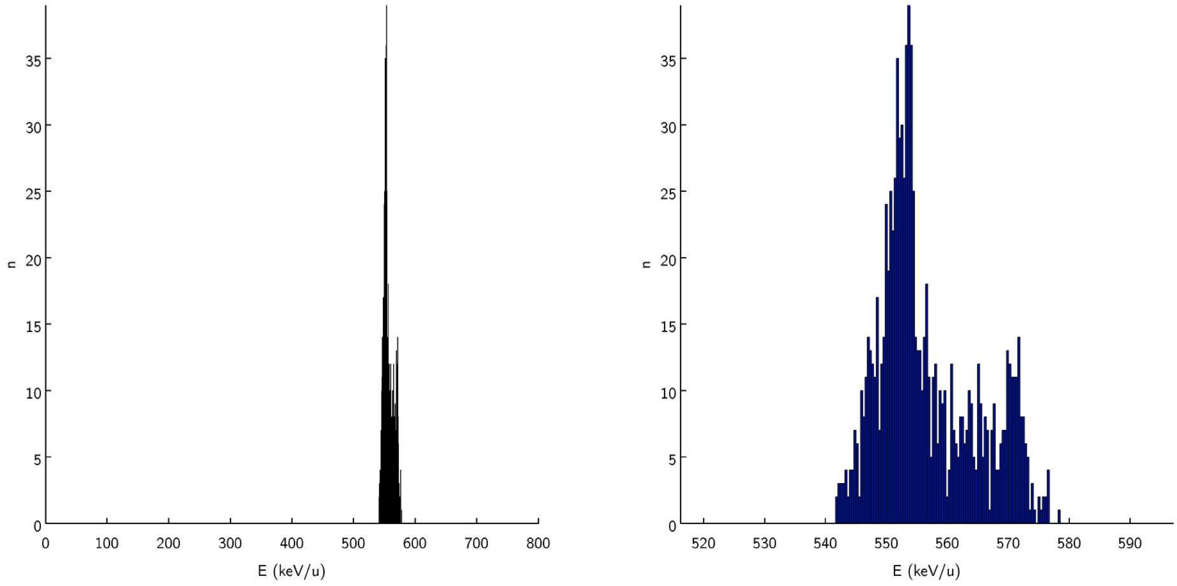

(a) Final energy distribution **(b)** Final energy peak detail

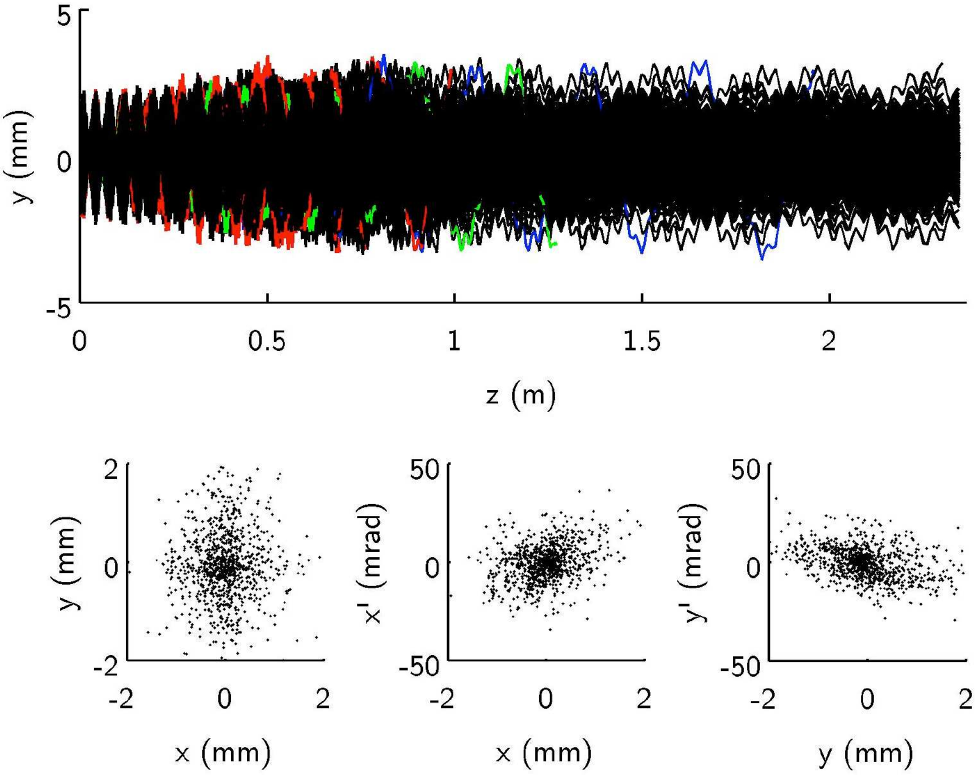

(c) Particle trajectories and final phase space

Figure 8.11: Results of carbon 6+ RFQ simulations using the final *CST* field map scaled in *GPT:*
(a) Histogram of energies of particles at the end of the RFQ;
(b) Detailed histogram of energies of fully accelerated particles at the end of the RFQ;
(c) Particle distributions, showing tracks through the RFQ and final phase space, with lost particles marked in colours dependent on the area of the RFQ in which they are lost

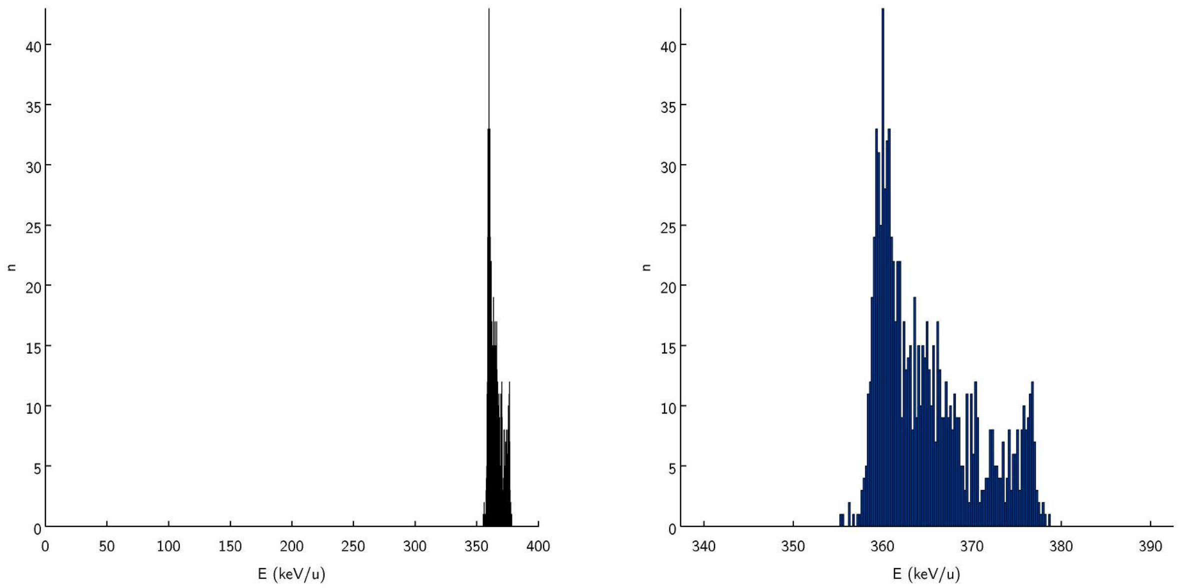

(a) Final energy distribution

(b) Final energy peak detail

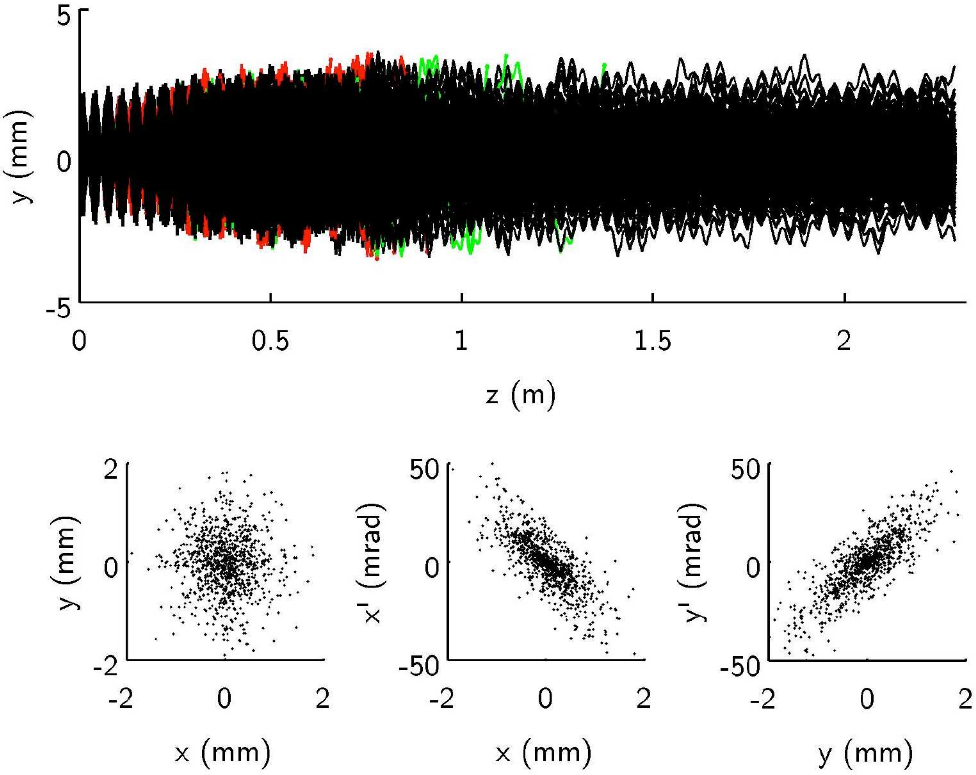

(c) Particle trajectories and final phase space

Figure 8.12: Results of carbon 4+ RFQ simulations using the final *Comsol* field map scaled in *GPT:*
(a) Histogram of energies of particles at the end of the RFQ;
(b) Detailed histogram of energies of fully accelerated particles at the end of the RFQ;
(c) Particle distributions, showing tracks through the RFQ and final phase space, with lost particles marked in colours dependent on the area of the RFQ in which they are lost

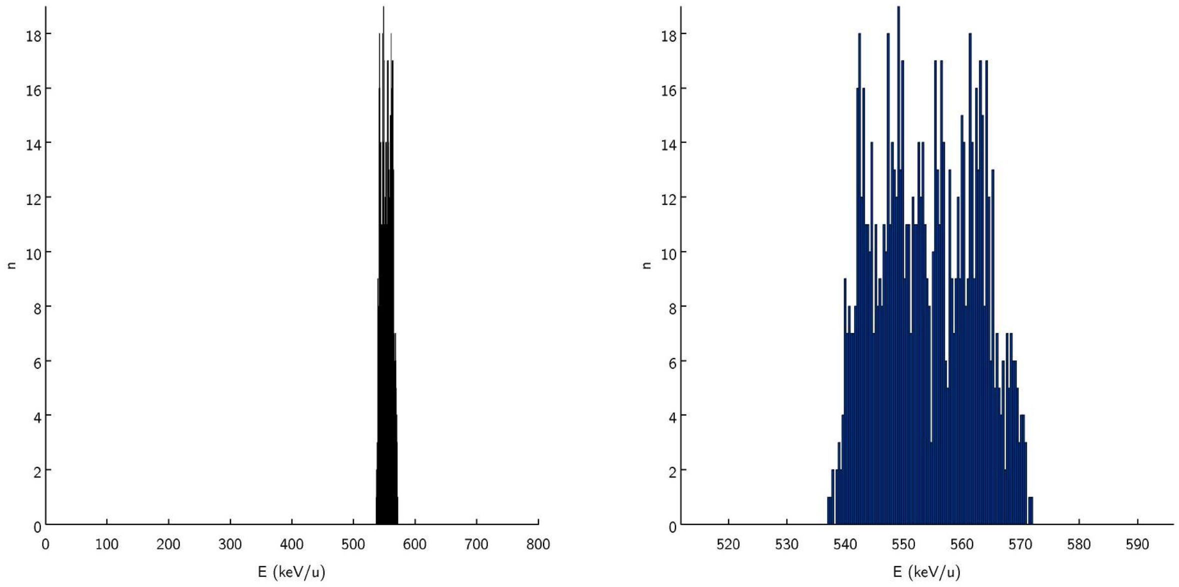

(a) Final energy distribution **(b)** Final energy peak detail

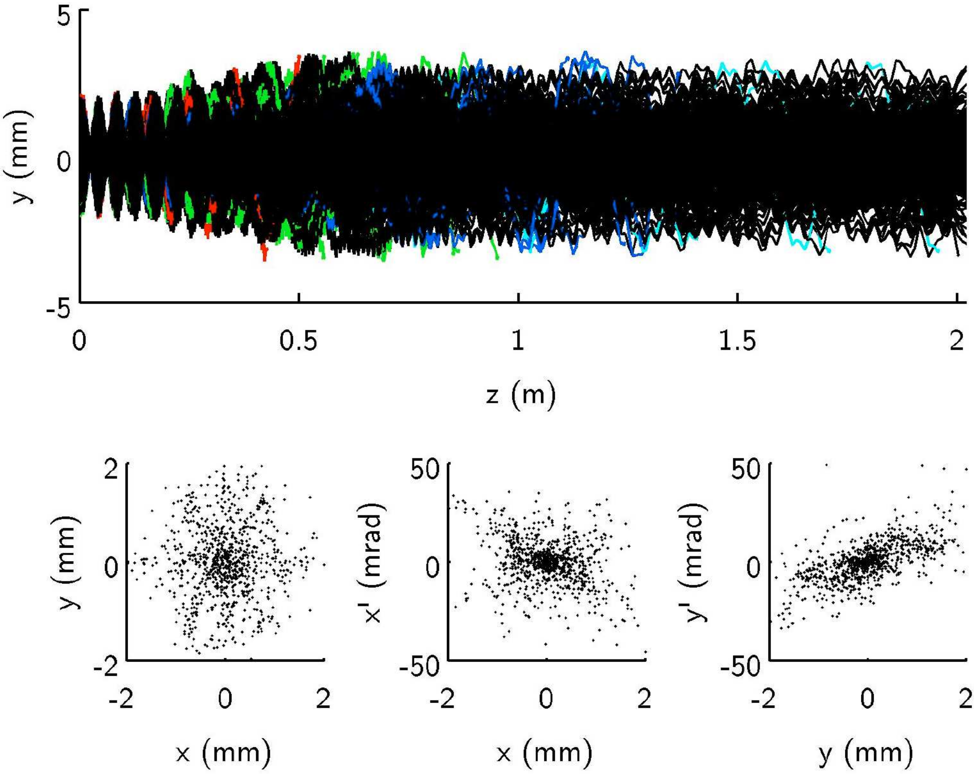

(c) Particle trajectories and final phase space

Figure 8.13: Results of carbon 6+ RFQ simulations using the final *Comsol* field map scaled in *GPT:*
(a) Histogram of energies of particles at the end of the RFQ;
(b) Detailed histogram of energies of fully accelerated particles at the end of the RFQ;
(c) Particle distributions, showing tracks through the RFQ and final phase space, with lost particles marked in colours dependent on the area of the RFQ in which they are lost

8.3 PAMELA RFQ

The methods of modelling RFQ designs for *PAMELA*, and the problems and successes that led from each iteration to the next, are described in § 7.5 above. The aim of this section is to set out the particle tracking results of four of the simulations that marked significant milestones in the development of the RFQ parameters.

The numerical results are summarised in Table 8.5. The RFQ modulation parameters for the four models are compared in Figure 8.18.

8.3.1 Mark 1

The Mark 1 design for the *PAMELA* RFQ took the scaling calculation for carbon 6+ and applied the scaling factor to the modulation parameters of the *FETS* RFQ. The parameters were then converted into a three-dimensional geometry in *Inventor*, solved cell-by-cell in *Comsol* and tracked using *GPT*, with the same method as for the *FETS* RFQ. The results of the tracking simulations are presented in Figure 8.14 and are included in the summary in Table 8.5.

The transmission of 23% was much lower than predicted from the scaled field map, which transmitted 93% of the particles. The difference is due to the redirection of the field (compared to the one-dimensional compression of the *GPT* scaling method), producing larger transverse oscillations for lesser longitudinal accelerating force, such that many particles collide with the vanes or drop out of the accelerating bunches.

	Mark 1	**Mark 2**	**Mark 3**	**Mark 4**
E-field frequency (MHz)	280	280	280	280
Initial particle energy (keV/u)	12	12	12	12
RFQ length (m)	2.021	3.58	2.021	2.033
Electrode potential (kV)	85	85	85	85
Transmission (%)	23.1	97.1	47.7	87.1
Transverse losses (%)	67.9	2.7	51.6	12.8
Longitudinal losses (%)	9.0	0.2	0.7	0.1
Mean energy (keV/u)	552.0	604.0	550.6	549.5
RMS energy spread (keV/u)	9	10	9	11
x-emittance (mm mrad)	0.289	0.279	0.346	0.185
y-emittance (mm mrad)	0.414	0.268	0.261	0.175

Table 8.5: Simulation parameters and results of different model simulations for the *PAMELA* RFQ; see Figure 7.21 for graphical comparison

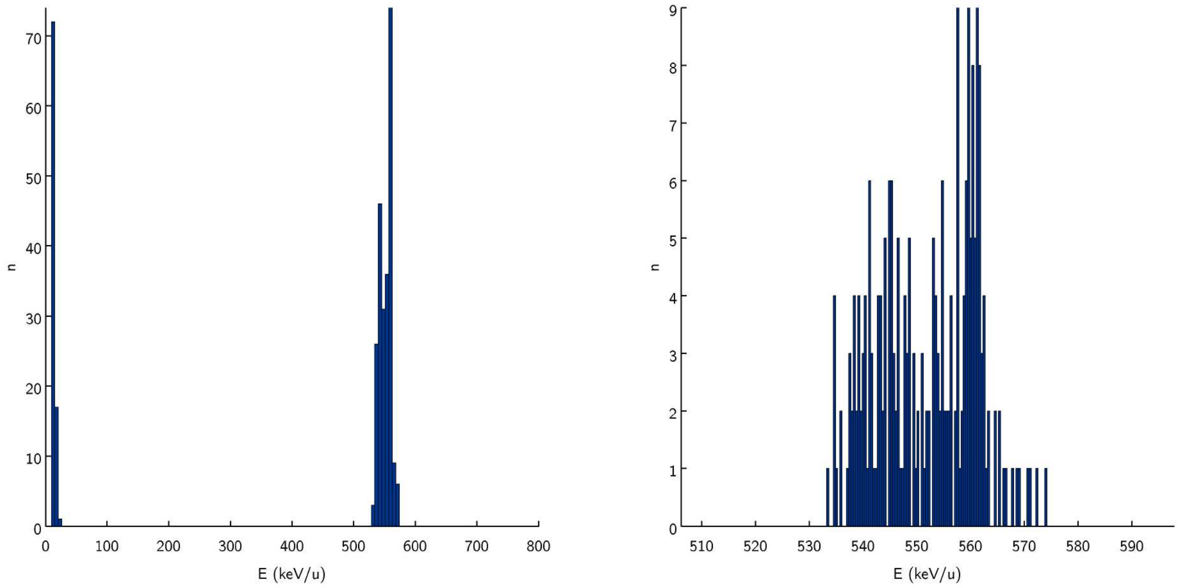

(a) Final energy distribution **(b)** Final energy peak detail

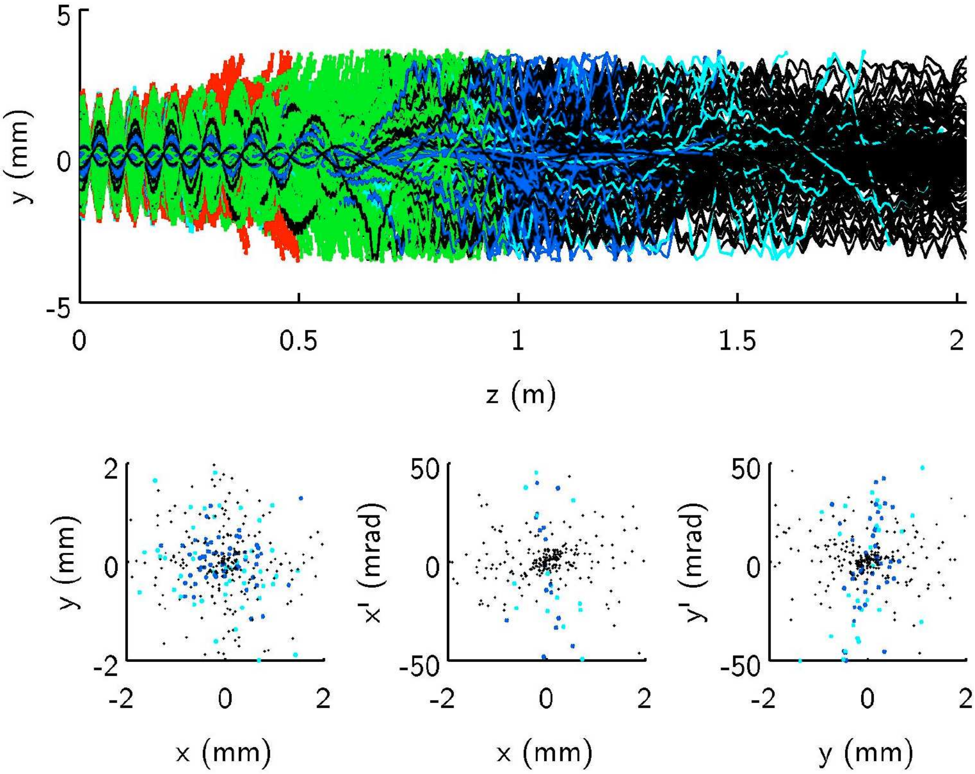

(c) Particle trajectories and final phase space

Figure 8.14: Results of *PAMELA* Mark 1 RFQ simulations:
(a) Histogram of energies of particles at the end of the RFQ;
(b) Detailed histogram of energies of fully accelerated particles at the end of the RFQ;
(c) Particle distributions, showing tracks through the RFQ and final phase space, with lost particles marked in colours dependent on the area of the RFQ in which they are lost

8.3.2 Mark 2

The Mark 2 design was created from scratch in *RFQSIM*, rather than being based on existing modulation parameters. The results of the tracking simulations are presented in Figure 8.15 and are included in the summary in Table 8.5. The energy and transmission are well within parameters, but a much longer RFQ is required, with over 800 cells and a length greater than 3.5 m. This increased complexity and length leads to increased expense and space requirements, as discussed in § 7.5.

8.3.3 Mark 3

The Mark 3 design started from the scaled *FETS* parameters from the Mark 1 design, but adapted them to produce particle dynamics more suitable for the shorter cell length and heavier particles. Many different modifications were compared in the process of finalising the Mark 3 design, and the alterations producing the most effective results were combined together. The results of the tracking simulations are presented in Figure 8.16 and are included in the summary in Table 8.5. The transmission was increased from 23% to 48%.

8.3.4 Mark 4

The Mark 4 simulation redesigned the matching-in section at the very front of the RFQ to better capture the entire phase space of incoming beam. The spacing between vanes was also reduced, to apply a stronger focusing and accelerating force to the carbon ions. The combination of these modifications produced a field map that accelerated 87% of particles to the correct energy, which marks the successful design of a carbon RFQ for *PAMELA*.[1] The results of the tracking simulations are presented in Figure 8.17 and are included in the summary in Table 8.5.

---

[1] Further optimisation could improve this result (see Chapter 9), but 87% is an acceptable transmission for this stage of the design process.

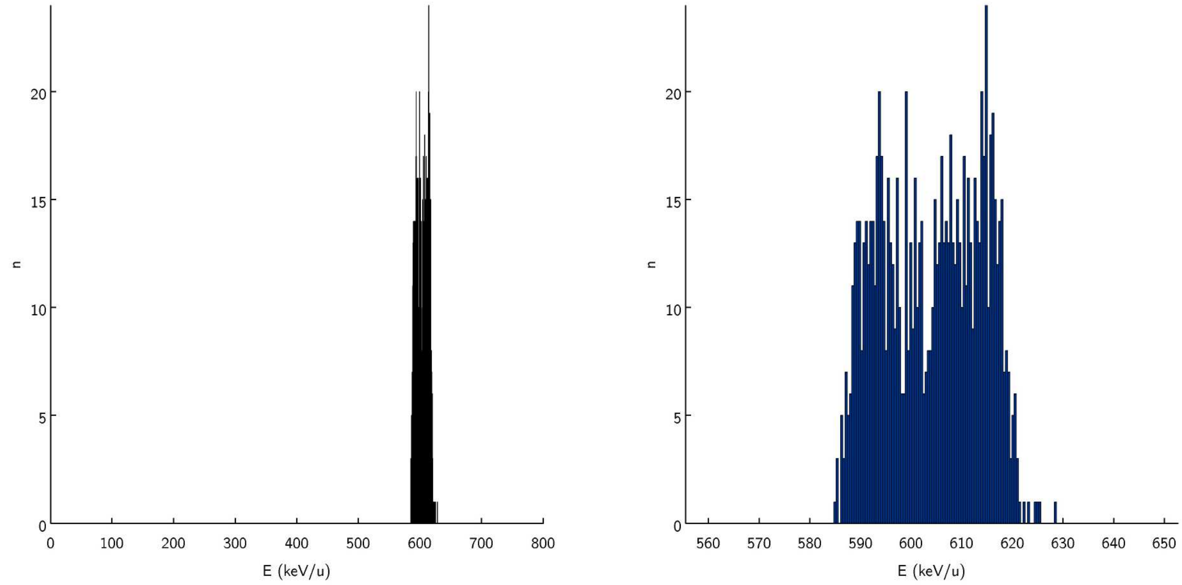

(a) Final energy distribution

(b) Final energy peak detail

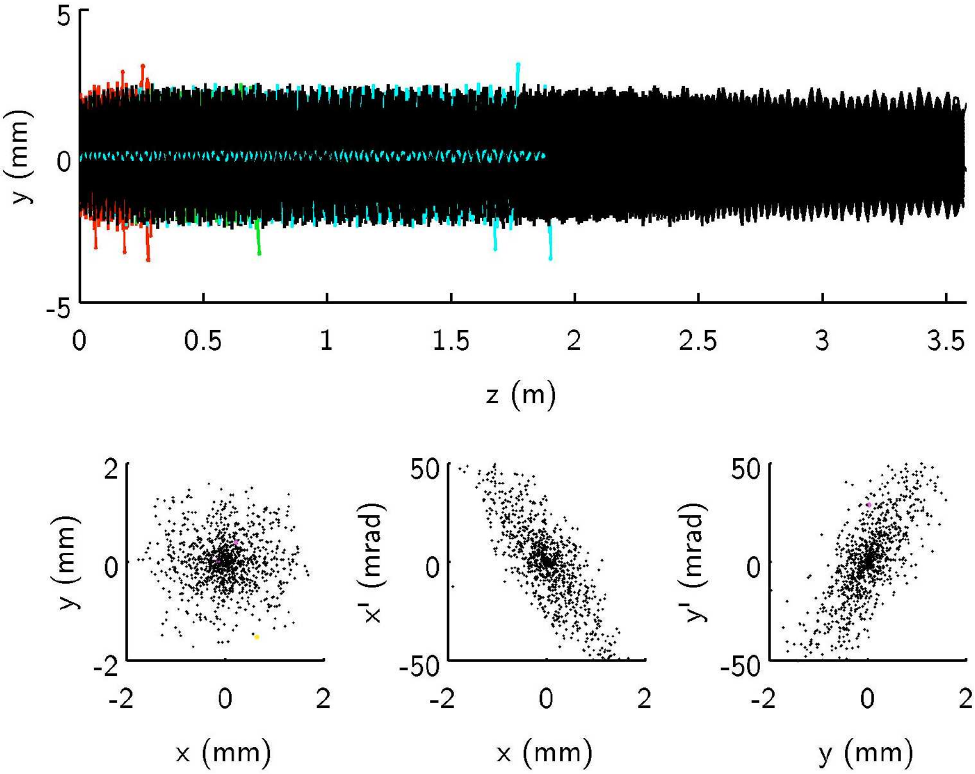

(c) Particle trajectories and final phase space

Figure 8.15: Results of *PAMELA* Mark 2 RFQ simulations:
(a) Histogram of energies of particles at the end of the RFQ;
(b) Detailed histogram of energies of fully accelerated particles at the end of the RFQ;
(c) Particle distributions, showing tracks through the RFQ and final phase space, with lost particles marked in colours dependent on the area of the RFQ in which they are lost

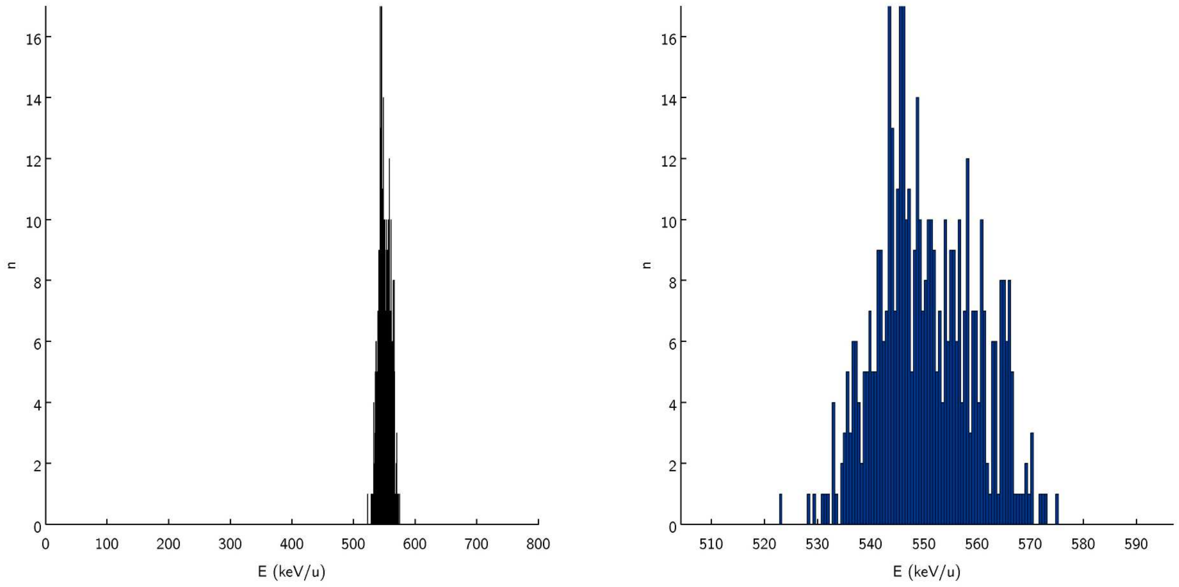

(a) Final energy distribution **(b)** Final energy peak detail

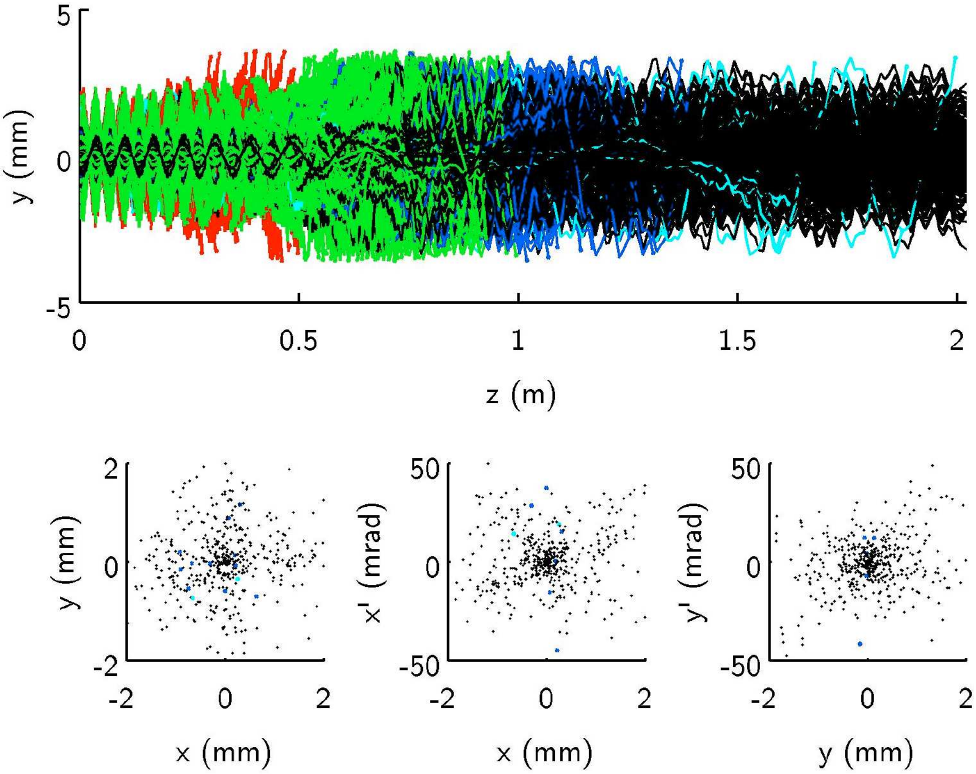

(c) Particle trajectories and final phase space

Figure 8.16: Results of *PAMELA* Mark 3 RFQ simulations:
(a) Histogram of energies of particles at the end of the RFQ;
(b) Detailed histogram of energies of fully accelerated particles at the end of the RFQ;
(c) Particle distributions, showing tracks through the RFQ and final phase space, with lost particles marked in colours dependent on the area of the RFQ in which they are lost

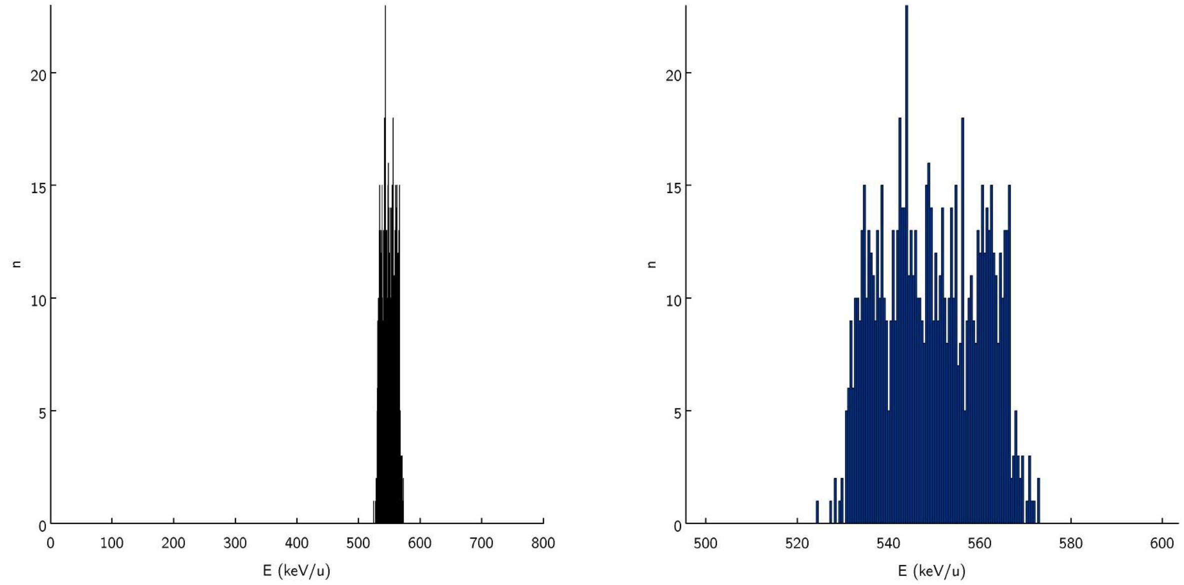

(a) Final energy distribution

(b) Final energy peak detail

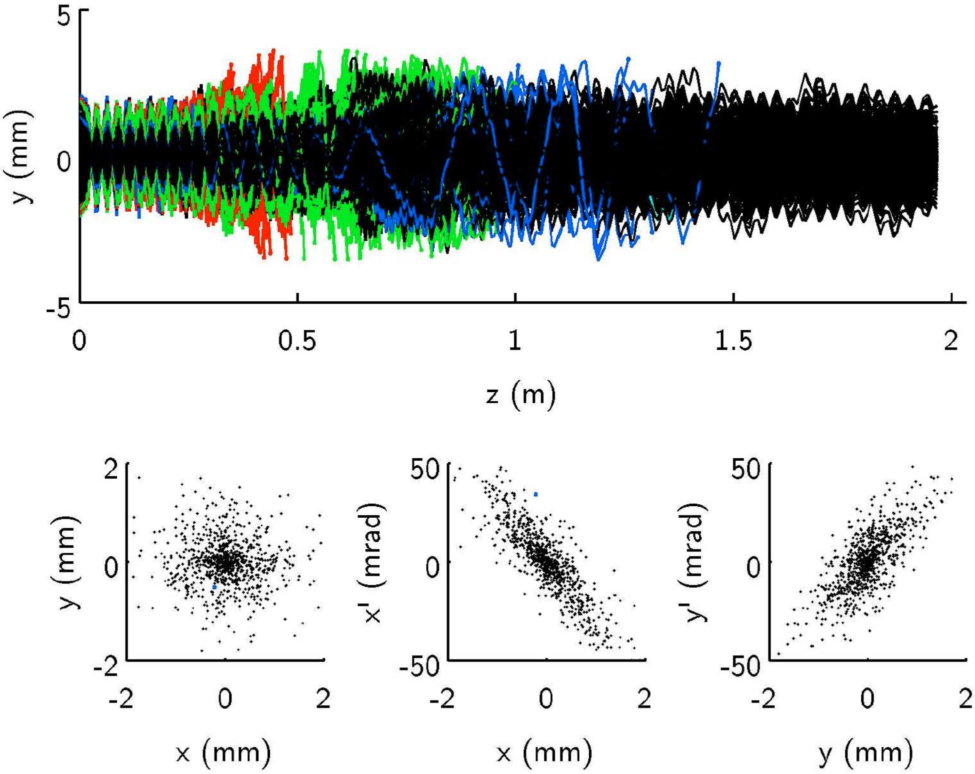

(c) Particle trajectories and final phase space

Figure 8.17: Results of *PAMELA* Mark 4 RFQ simulations:
(a) Histogram of energies of particles at the end of the RFQ;
(b) Detailed histogram of energies of fully accelerated particles at the end of the RFQ;
(c) Particle distributions, showing tracks through the RFQ and final phase space, with lost particles marked in colours dependent on the area of the RFQ in which they are lost

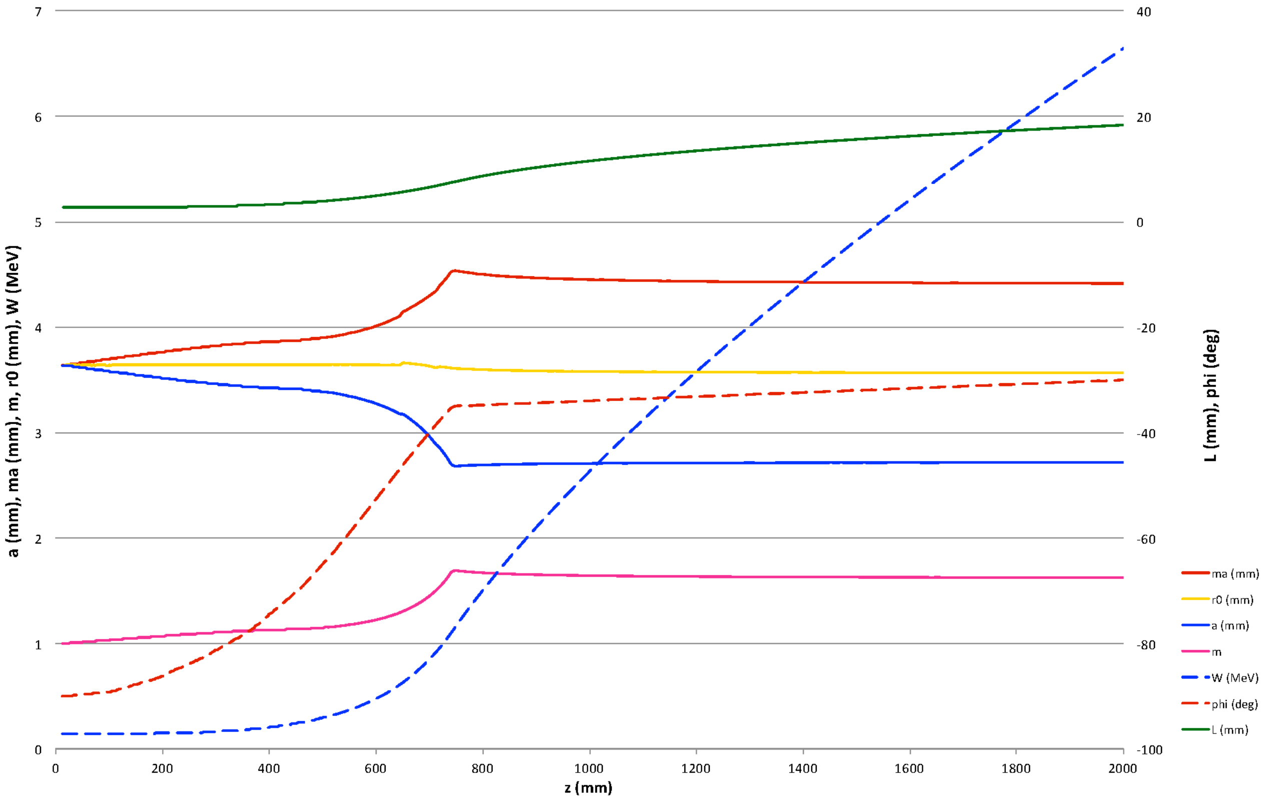

(a) Mark 1

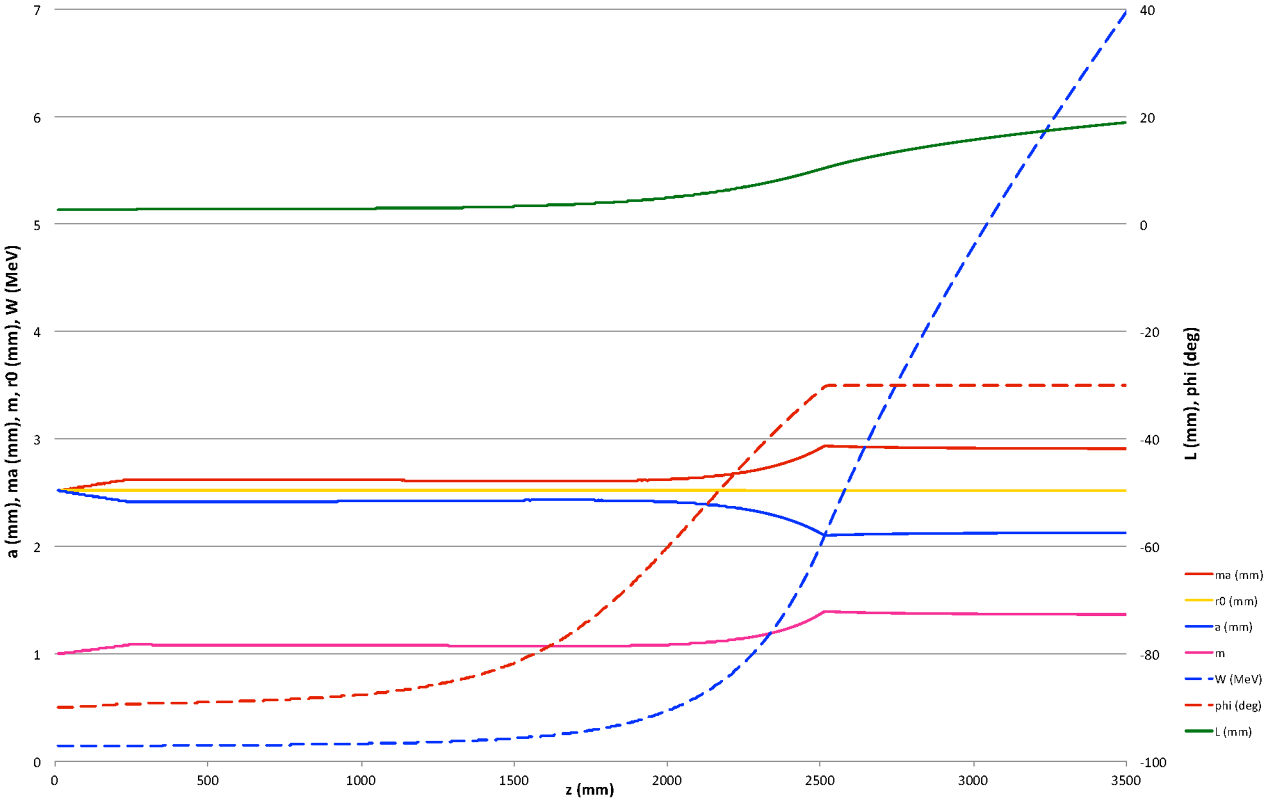

(b) Mark 2

Figure 8.18: Cell modulation parameters for the four versions of the *PAMELA* RFQ; Compare with equivalent parameters for the *FETS* RFQ in Figure 6.5

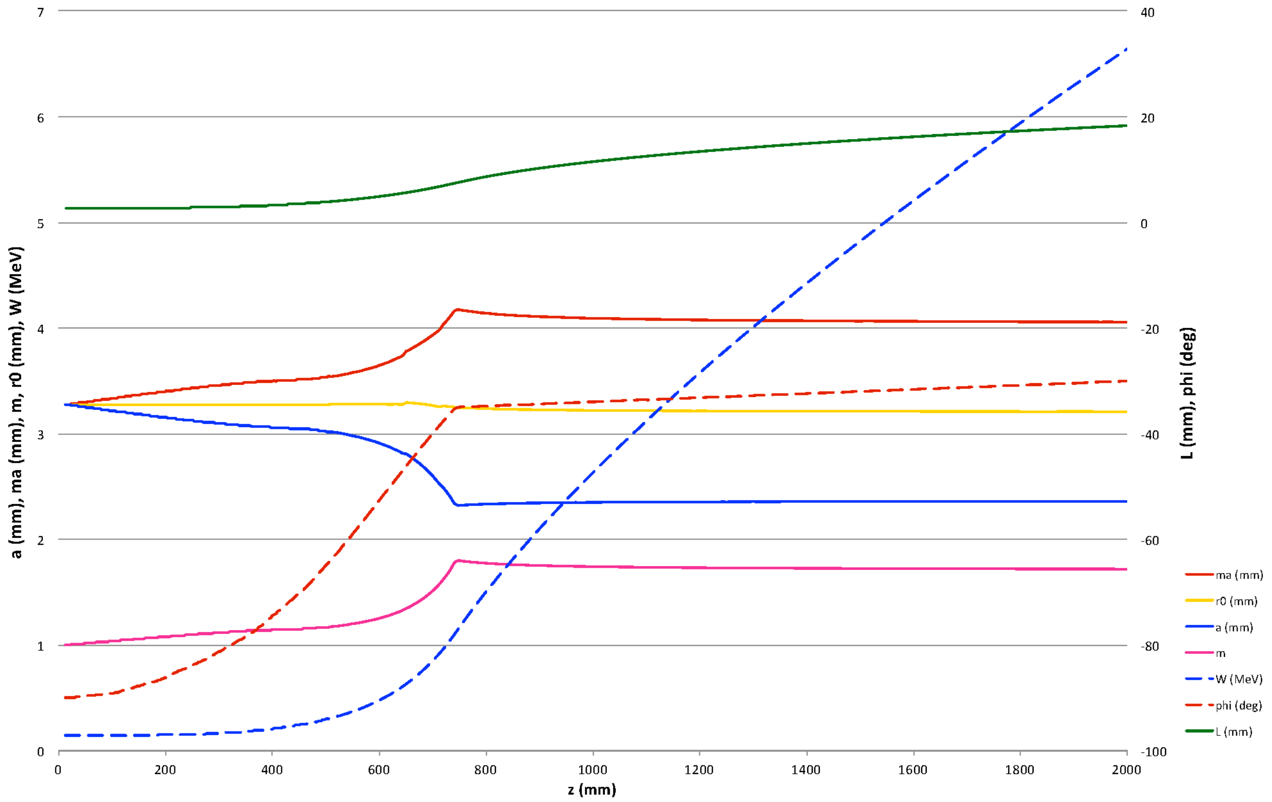

(c) Mark 3

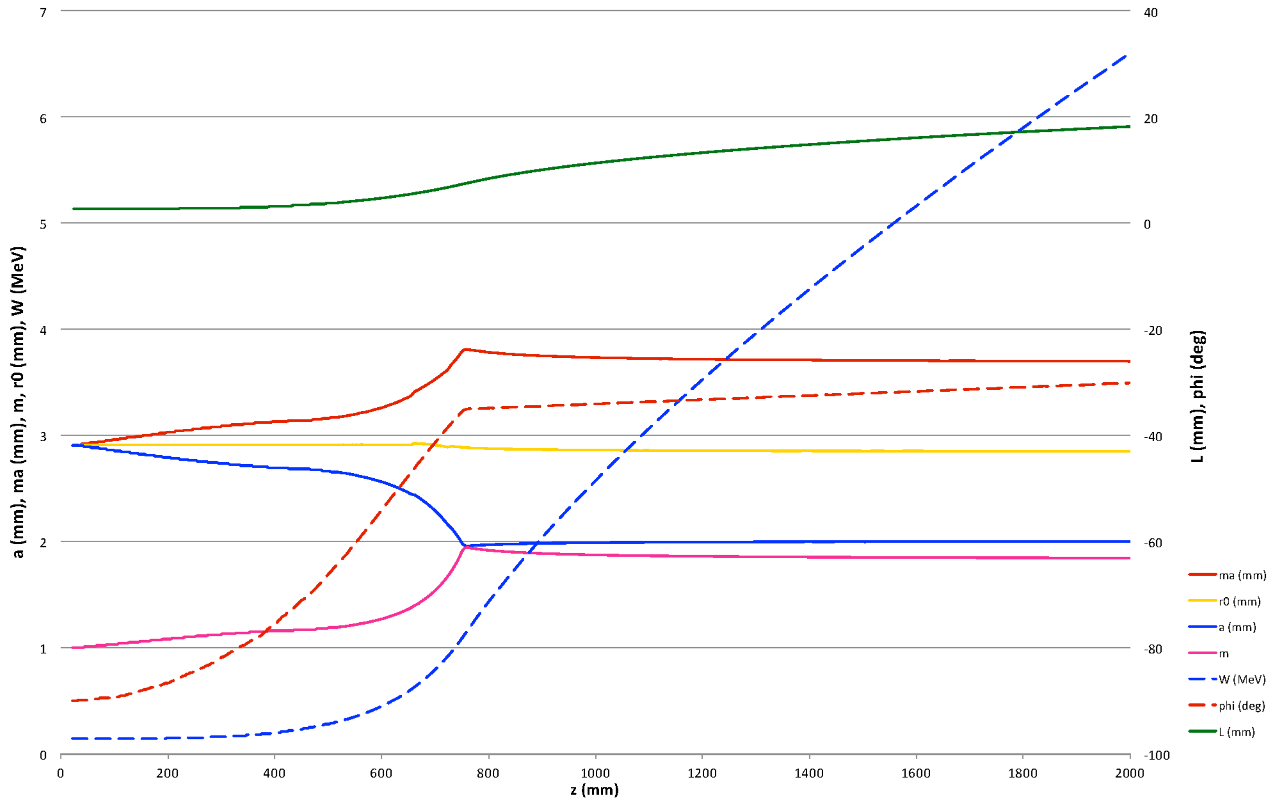

(d) Mark 4

Figure 8.18 (continued): Cell modulation parameters for the four versions of the *PAMELA* RFQ

9 Future Work

Continuation of the work carried out for this thesis would fall into two broad areas: method and application. The former is concerned with the RFQ design and modelling system and code *ModelRFQ*, and the latter is concerned with the specific RFQ design for *PAMELA*.

9.1 ModelRFQ development

The code in its current state allows full and accurate CAD and electrostatic modelling of the RFQ vane tips, and tracking of beams through this field, with or without space charge. This is still a very young code and has many dimensions in which it could be expanded, including:

- exporting the full vane tip geometry to define the boundaries of the tracking simulation for particle losses by collision with the vanes;
- adding image-charge effects;
- improving the space-charge solver;
- automating the CAD update process to remove user interaction requirements;
- incorporating initial modulation parameter generation;
- adding automatic iterative modulation parameter optimisation.

The first three suggestions apply to the particle tracking section of the simulations. In the present implementation, the particles are assumed to be travelling down a cylindrical tube, defined by the narrowest gap between the vanes. This means that the code underestimates the transmission, as some of the particles which stray out of this virtual cylinder may still be captured by the vane tip field and focused back into the main bunch. By exporting the full geometry and using this to define the losses by collision with the vane tips rather than the current cylinder, more accurate transmission figures could be produced. *GPT* does not include standard functions to import this geometry and thereby define a surface in the tracking simulation, but it does provide a programming interface for custom code to be added. Therefore, this development is theoretically possible within the existing *ModelRFQ* framework. Work on this process is already well underway [23]. Another advantage of including this geometry would be for the computation of image-charge effects—the modification of the perceived electric field due to reflection of space charge in the vane tips. This calculation is already included in other RFQ simulation codes [72, 73] using a moving-mesh method for calculating the space charge. As noted in § 7.2.5, the latest versions of *GPT* already include moving-mesh space-charge calculations, which could be modified by custom code to include image-charge effects based on CAD geometry. Work to implement these changes to the space-charge solver using a *Gaus-Seidel* algorithm is in preparation, in partnership with Rostock University [23].

A further development of the simulation process could combine the electrostatic modelling with the space-charge calculations in a unified electromagnetic solving process. This represents a very significant alteration to the current method of simulation, and the gain in accuracy may be very slight, so the efficacy of this modification should be carefully evaluated before being implemented.

The next two suggestions for future work relate to incorporating more areas of the simulation process into the unified *ModelRFQ* code. The current CAD system requires very little interaction from the user, as all the import process is controlled by VBA code when the model is updated. However, to enable full iterative optimisation loops, this process should ideally be invisible to the user and controlled via *Matlab*. Also, the initial generation of modulation parameters is currently carried out by *RFQSIM*, which is external to the *ModelRFQ* system. This procedure could be recreated within *Matlab* to incorporate the field expansion optimisation method as a first stage of the modelling process. This would allow a much wider range of RFQ designs to be automatically generated with full CAD models and particle tracking simulations.

The final suggestion is perhaps the most difficult to realise. If the code could recognise problems with the RFQ design and suggest improvements automatically, then iterative optimisation could be employed, such that the code develops a working RFQ design with minimal user input. At present, the recognition of problems and possible solutions is very specialised, based on a lot of interpretation of the dynamics of the particles by an experienced accelerator physicist. Handing this operation over to a computer would not be a simple task, but if it were achieved, this would greatly improve the usefulness of the *ModelRFQ* code. With this procedure in place it might also be possible to replace the field-expansion-based initial model generation step with a CAD-based optimisation technique, but with current computing resources this would take days rather than hours to complete, so retaining the field expansion as a first step is logical.

The *ModelRFQ* distribution is freely available, subject to licence of the requisite software tools, so it is the author's hope that the code continues to develop into an essential tool for RFQ designers.

9.2 PAMELA RFQ development

The final *PAMELA* RFQ design presented in this thesis has a transmission of 87.1% and an RMS energy spread of 2%, compared to the equivalent *FETS* RFQ results (without space charge) of 100% transmission and an RMS energy spread of 0.5%. Further iterations of the design and modelling process could definitely produce improvements, especially if the *ModelRFQ* development options from the previous section were implemented.

The *PAMELA* project has, up to this point, been a design study for a prototype accelerator. The scope of the project is not to produce fully optimised and tested final designs ready for production, but rather to prove that such could be produced for the design and build phase of the project. In the context of this project, the final RFQ design presented in this thesis surpasses these requirements: the scaled RFQ designs (see § 7.4 and § 8.2) act as a proof of principle that a machine could be produced that generates the correct beam for injection into *PAMELA*; the CAD-based designs (see § 7.5

and § 8.3) take this further and suggest the parameters required to build this machine. As further details of the injector chain are finalised, such as the manufacturer and output distribution of the ion source, these details can inform the further development of the RFQ. The next phase of design would finalise the modulation parameters to improve the transport characteristics even further, and also investigate optimisation for power consumption, cost, space, and other such factors.

The RFQ should not be designed in isolation. Throughout the development process to date, collaboration with the rest of the *PAMELA* team has influenced the RFQ design, setting the requirements for injection and suggesting methods of system-wide optimisation, such as selecting RF frequencies that can be utilised for multiple sections of the acceleration chain. This collaboration should continue, such that the requirements of the downstream components drive the RFQ optimisation, and the output of the RFQ simulation inform the design of the rest of the system. One example of this is the sharing of particle distributions. Work has already begun to integrate the input and output distributions of *ModelRFQ* with other simulations, so that the starting conditions of the RFQ match the output of the LEBT exactly, and likewise the output distribution of particles can be used for the next stage of acceleration.

These improvements to the RFQ design should be carried out in the next phase of the *PAMELA* project, as the design for the rest of the accelerator is also refined.

10 Conclusions

Charged particle therapy (CPT) has been shown to be an invaluable tool in the radiological treatment of cancerous tumours. Chapter 2 introduced the concepts of radiotherapy and its aims of causing irreparable damage to DNA, which can kill cancer cells and block the reproduction mechanism. However, the damaging side-effects of conventional radiotherapy were also discussed. Various ingenious schemes exist to reduce these side-effects by modifying the use of the conventional beams. CPT offers an alternative beam system that reduces some of the dangerous radiation effects on healthy tissue by taking advantage of the Bragg peak in the dose profile, which allows the majority of the dose to be delivered to the tumour rather than the healthy tissue (see Figure 2.1 and Figure 2.2). Treatment centres employing CPT have been steadily increasing in number over the past two decades (see Figure 2.3) and the technology has begun its move out of the physics laboratory and into hospitals and mainstream medical centres. The UK is currently far behind other western countries in its CPT capabilities, but projects are already underway to rectify this situation, such as the *PAMELA* project that forms the motivation for, and application of, this current thesis.

CPT requires larger and more sophisticated particle accelerators than conventional radiotherapy, because the particles that make up the beam are more massive. Chapter 3 introduced the topics of accelerator physics relevant for this thesis, providing a basic guide to the subject for non-specialists, describing the main types of accelerators, and assessing their application as candidates for CPT. Cyclotrons are commonly used for CPT using protons, but have a number of disadvantages relating primarily to the quality of the output beam due to the use of degraders. Synchrotrons are the only current solution for carbon acceleration, but these larger and more complex machines require highly trained staff to run and maintain them. They also have a low repetition rate, which extends the amount of time for which a patient must be immobilised, and reduces patient throughput. Fixed-field, alternating-gradient accelerators (FFAGs) have been proposed as a solution for CPT, combining the high repetition rate and reliability of the cyclotron with the variable energy capability of the synchrotron. However, the type of FFAGs being investigated bring problems of their own, being untested technology, and need to be carefully designed, prototyped and tested before they can be considered for patient treatment.

The *PAMELA* project was set up to investigate the utilisation of this FFAG technology for CPT, and to propose a prototype machine that could be used as the foundation for a UK CPT facility. Chapter 4 introduced the *PAMELA* design and defined the medical and technical design requirements. The proposal is a staged, two-ring, two-species accelerator capable (by the final stage) of treatment with protons and carbon ions. The accelerator requires an injector system to deliver beams of both $\sim 30\,\mathrm{MeV}$ protons and $\sim 8\,\mathrm{MeV/u}$ carbon 6+ ions. The requirements for the injector are stated in Table 4.4.

To realise the *PAMELA* injection requirements, a system comprising ion sources, pre-accelerators and transport lines has been developed at Imperial College London. Chapter 5 describes and compares some of the options considered for the injector, and details the proposed injection system (see Figure 5.4). The proposal is to use two separate pre-accelerators, a cyclotron for proton and a linac for carbon ions, with separate ion sources, and then combine the beams into a single injection line as they enter the FFAG. A staged approach provides the proton beam first, via a simple off-the-shelf cyclotron with built-in ion source, which combines with the first FFAG ring for treatment energies. Secondly, a linear carbon ion injector combines with the first FFAG ring to produce a medium-energy carbon beam for medical and biological experimentation. Finally, a second FFAG ring is added to accelerate carbon ions to energies high enough for cancer treatment. The carbon beam starts at an electron cyclotron resonance ion source (ECRIS) and then is transported through a spectrometer dipole into a radio-frequency quadrupole (RFQ) and a linear accelerator (linac) before merging with the proton beam line for injection into the FFAG. A combined pre-accelerator would be more cost-effective, but beam current considerations (among other difficulties) make this approach prohibitively challenging, technically. In the future, however, the availability of high-current, high-charge-state carbon ion sources may make the combined approach more feasible.

The main body of work for this thesis involved the creation of a method of design and simulation for particle transport through an RFQ, and the application of this method to the *PAMELA* injector RFQ. Chapter 6 introduced the theory of RFQ technology, and methods of design (which are further described in Appendix B). An RFQ provides focusing and acceleration via a combined-purpose field generated by exciting an RF resonance mode in a chamber containing conducting vanes or rods that have been shaped to produce exactly the correct field for accelerating the particle beam in question. The optimisation of the modulation pattern of the RFQ to match the input and required output beams is the subject of the simulation work of this thesis.

The simulation software was developed from a rough set of disparate files, folders and functions requiring hours of user manipulation, to a much more tightly integrated and automated system. The code is still under development and is freely available as a community project.[1] The software used, the automated code written and their development over time are detailed in Chapter 7. The final version of the code is able to convert a spreadsheet full of numerical vane modulation parameters into a full CAD model for manufacture plus a full set of particle tracking results, based on the same CAD model. This allows the simulations to closely match the final machine, and include subtle effects that approximation-based codes might miss. This modelling method also allows accurate investigation of non-linear effects and hypothetical scenarios that would not be readily available to an approximation-based numerical solver, which can aid the development and optimisation of an RFQ design. Investigations into details such as field flatness, temperature distributions and cooling channels, and mechanical stresses could also be integrated into the multi-physics models, although such intricacies are not appropriate for the current status of the *PAMELA* RFQ design. The system also allows for extensive error studies, some of which have already begun [23].

---

[1] `https://launchpad.net/modelrfq`

The parameters spreadsheet is read into *Autodesk Inventor* and a CAD model is automatically constructed by VBA code. The code takes the one-dimensional modulation parameters from the spreadsheet and extrapolates a smooth sinusoidal path, then extracts a few additional parameters to define a two-dimensional profile, and finally combines these to form a three-dimensional model. This model can be combined into a full CAD assembly of the whole RFQ and can influence other design studies for other parameters of the RFQ design. Once the model is built, a suite of *Matlab* functions take over and automate the simulation process. An electrostatic model is constructed in *Comsol*, using the CAD model to define the geometry and a user input file to define the electric properties. This electrostatic model is solved step-by-step in many individual cells to maximise the modelling accuracy, and a vane-tip field map is constructed. This field map is then used as the basis for the particle tracking software, *GPT*, to simulate the beam in the RFQ. The simulated particle tracks are analysed using *Matlab*, and the results are then presented to the user numerically and graphically via statistical results, various plots, and real- and phase-space animations.

The simulation code has been used for three separate scenarios. The first was the *Front-End Test Stand* (*FETS*) RFQ, the second was a scaling law investigation for a carbon RFQ, and the third was the *PAMELA* RFQ. The method for investigating each of these scenarios was described in Chapter 7, and the results were detailed in Chapter 8. A summary of these results is presented in Table 10.1. The *FETS* RFQ simulations transmitted all the particles and accelerated the beam to 3 MeV, with an energy spread of 0.5%. Space charge was excluded from these simulations so that they could be directly compared with the *PAMELA* simulations, for which space-charge forces are not significant. The scaled carbon 6+ simulations, based on the *FETS* design, lost 7% of particles transversally during acceleration, and produced a wider energy spread and final emittance, but did successfully accelerate 93% of the carbon ions. However, this field map was based upon an unphysical scaling transformation. The full *PAMELA* field map, with many parameters in common with the scaled simulation, lost almost twice as many particles transversally, but still accelerated 87% of the carbon ions ready for injection into the linac for the next stage of pre-acceleration. This final RFQ design has been presented as part of the *PAMELA* design review [44].

	FETS	**Scaled Carbon 6+**	***PAMELA*** (Mk. 4)
E-field frequency (MHz)	324	280	280
Initial particle energy (keV/u)	65	12	12
RFQ length (m)	4.06	2.03	2.033
Electrode potential (kV)	85	85	85
Transmission (%)	100	93.0	87.1
Transverse losses (%)	0	7.0	12.8
Longitudinal losses (%)	0	0	0.1
Mean energy (keV/u)	3020	554	549.5
RMS energy spread (keV/u)	15	8	11
x-emittance (mm mrad)	0.168	0.216	0.185
y-emittance (mm mrad)	0.178	0.208	0.175

Table 10.1: Summary of RFQ simulation results

There is further work to be done in developing the simulation code, and in finalising the *PAMELA* RFQ design. Suggestions for this development, detailed in Chapter 9, include adding additional automation and eventual optimisation code, so that the software can automatically optimise an RFQ for the best transmission results in any scenario, without requiring user input; adding extra electromagnetic features such as complex boundaries, image charges and improved space-charge calculations; and amalgamating with the *RFQSIM* code to produce optimised starting points for simulations and so increase the efficiency of the modelling code. The *PAMELA* RFQ could also be further optimised to increase its transmission and acceleration efficiency, and more attention given to important factors such as cost, size, and RF matching with the rest of the acceleration chain. This work would be included in future phases of the *PAMELA* project.

In conclusion, this thesis has presented a novel RFQ design method using computer simulations for accurate testing of successive design models, and has demonstrated that this method can be applied to real RFQ design scenarios. Advantages of this method include the agreement between simulation and manufacture, and the modelling of geometric details using CAD software allowing the testing of various modifications to the RFQ design. Results of simulations for the *FETS* RFQ have been confirmed by comparison with existing trusted codes, and the simulation code has been used to develop a working design for the *PAMELA* RFQ.

Appendices

A Charged Particle Therapy Centres

Table A.1, Table A.2 and Table A.3 contain details of closed, working and proposed charged particle therapy centres, respectively.

Centre	Country	Particle (MeV/u)	Treatment start date	Treatment end date	Patients treated
Berkeley 184, CA	USA	proton	1954	1957	30
Uppsala	Sweden	proton	1957	1976	73
Berkeley, CA	USA	helium	1957	1992	2054
Harvard, MA	USA	proton	1961	2002	9116
Dubna [1]	Russia	proton	1967	1996	124
Los Alamos, NM	USA	pion	1974	1982	230
Berkeley, CA	USA	ion	1975	1992	433
TRIUMF, Vancouver	Canada	pion	1979	1994	367
Chiba	Japan	proton	1979	2002	145
PSI, Villigen	Switzerland	pion	1980	1993	503
Tsukuba (PMRC, 1)	Japan	proton	1983	2000	700
Louvain-la-Neuve	Belgium	proton	1991	1993	21
Bloomington (MPRI, 1), Indiana	USA	proton	1993	1999	34
G.S.I. Darmstadt [2]	Germany	ion	1997	2009	440

Table A.1: Closed charged particle therapy centres worldwide
Data taken from the Particle Therapy Co-Operative Group (PTCOG),
`http://ptcog.web.psi.ch/Archive/Patientenzahlen-updateMar2010.pdf`
[1] Degraded beam
[2] With beam scanning

Centre	**Country**	**Particle**	**Energy** (MeV/u)	**Treatment start date**	**Patients treated**
ITEP, Moscow	Russia	proton	250	1969	4246
St. Petersburg	Russia	proton	1000	1975	1362
PSI, Villigen	Switzerland	proton	72	1984	5458
Uppsala	Sweden	proton	200	1989	929
Clatterbridge	UK	proton	62	1989	2021
Loma Linda, CA	USA	proton	250	1990	15000
Nice	France	proton	65	1991	4209
Orsay	France	proton	230	1991	5216
iThemba Labs	South Africa	proton	200	1993	511
HIMAC, Chiba	Japan	carbon	800	1994	5497
UCSF, CA	USA	proton	60	1994	1285
TRIUMF, Vancouver	Canada	proton	72	1995	152
PSI, Villigen [2,3]	Switzerland	proton	250	1996	704
HZB (HMI), Berlin	Germany	proton	72	1998	1660
NCC, Kashiwa	Japan	proton	235	1998	680
Dubna [1]	Russia	proton	200	1999	720
HIBMC,Hyogo	Japan	proton	230	2001	2382
PMRC(2), Tsukuba	Japan	proton	250	2001	1849
NPTC, MGH Boston	USA	proton	235	2001	4967
INFN-LNS, Catania	Italy	proton	60	2002	174
HIBMC,Hyogo	Japan	carbon	320	2002	638
WERC,Tsuruga	Japan	proton	200	2002	62
Shizuoka	Japan	proton	235	2003	986
WPTC, Zibo	China	proton	230	2004	1078
MPRI(2), IN	USA	proton	200	2004	1145
MD Anderson, TX [4]	USA	proton	250	2006	1700
UFPTI, FL	USA	proton	230	2006	2679
NCC, Ilsan	South Korea	proton	230	2007	648
IMPCAS, Langzou	China	carbon	400	2009	126
HIT, Heidelberg [2]	Germany	carbon	430	2009	treatment started
HIT, Heidelberg [2]	Germany	proton	250	2009	treatment started
RPTC, Munich [2]	Germany	proton	250	2009	446
ProCure, OK	USA	proton	230	2009	21
GHMC, Gunma	Japan	carbon	400	2010	treatment started
CDH, IL	USA	proton	230	2010	treatment started
UPenn, PA	USA	proton	230	2010	150

Table A.2: Working charged particle therapy centres worldwide
Data from the Particle Therapy Co-Operative Group (PTCOG),
`http://ptcog.web.psi.ch/ptcentres.html`
[1] Degraded beam
[2] With beam scanning
[3] Degraded beam for 1996 to 2006; dedicated 250 MeV proton beam from 2007 on
[4] With spread beam and beam scanning (since 2008)

Centre	**Country**	**Particle**	**Energy** (MeV/u)	**Technology**	**Proposed start date**
CPO, Orsay *	France	proton	230	Cyclotron	2011
WPE, Essen *	Germany	proton	230	Cyclotron	2011
PTC, Marburg *	Germany	both	430	Synchrotron	2011
Southern Tohoku *	Japan	proton	230	Cyclotron	2011
Medipolis *	Japan	proton	250	Synchrotron	2011
PMHPTC *	Russia	proton	250	Synchrotron	2011
CMHPTC *	Slovak Republic	proton	250	Synchrotron	2011
PSI, Villigen *	Switzerland	proton	250	SC Cyclotron	2011
HUPBTC, VA *	USA	proton	230	Cyclotron	2011
CNAO, Pavia	Italy	both	430	Synchrotron	2011
Chang Gung, Taipei *	Taiwan	proton	235	Cyclotron	2011
St. Louis, MO *	USA	proton	250	SC Synchro-cyclotron	2011
ProCure, IL *	USA	proton	230	Cyclotron	2011
NRoCK, Kiel *	Germany	both	430	Synchrotron	2012
NIPTRI, IL *	USA	proton	250	SC Cyclotron	2012
PTC Czech s.r.o.	Czech Republic	proton	230	Cyclotron	2013
Trento *	Italy	proton	230	Cyclotron	2013
Skandion Clinic	Sweden	proton	250	Cyclotron	2013
Med-AUSTRON	Austria	both	400	Synchrotron	2014
SJFH, Beijing	China	proton	230	Cyclotron	unknown
RPTC, Koeln	Germany	proton	250	SC Cyclotron	unknown
CCSR, Bratislava	Slovak Republic	proton	72	Cyclotron	unknown
iThemba Labs	South Africa	proton	230	Cyclotron	unknown

Table A.3: Propoesed charged particle therapy centres worldwide
Data from the Particle Therapy Co-Operative Group (PTCOG),
`http://ptcog.web.psi.ch/newptcentres.html`
*Under construction

B RFQ Field and Dynamics

Derivations below primarily follow methods from references [32] and [64].

B.1 Field expansion

In cylindrical polar coordinates, with the beam axis at $r = 0$, the edge of the electrodes at $r = a$ and the start of the RFQ at $z = 0$, it is possible to express the field between the electrodes as a series of infinite terms.

On-axis in the accelerating mode, the magnetic field is zero, and the problem can therefore be treated within the quasi-static approximation, where the electric field is comprised of an electrostatic field varying sinusoidally in time,

$$U(r, \theta, z, t) = V(r, \theta, z) \sin(\omega t + \phi). \tag{B.1}$$

Taking the electrostatic part, we can apply Laplace's equation,

$$\nabla^2 V = \frac{\partial^2 V}{\partial r^2} + \frac{1}{r}\frac{\partial V}{\partial r} + \frac{1}{r^2}\frac{\partial^2 V}{\partial \theta^2} + \frac{\partial^2 V}{\partial z^2} = 0. \tag{B.2}$$

Using separation of variables $V(r, \theta, z) = R(r)\Theta(\theta)Z(z)$ and observing symmetries gives a solution conforming to the boundary conditions of the RFQ,

$$\begin{aligned} V(r, \theta, z) = {} & \frac{V_0}{2} \sum_p A_{0(2p+1)} r^{2(2p+1)} \cos[2(2p+1)\theta] \\ & + \frac{V_0}{2} \sum_m \sum_n A_{mn} I_{2n}(mkr) \cos(2n\theta) \cos(mkz), \end{aligned} \tag{B.3}$$

where V_0 is the potential difference from the positive to the negative vane, $p = 0, 1, 2, \ldots$, $m \geqslant 1$, $m + n = 2p + 1$, $k = 2\pi/\beta_s\lambda$, β_s is the velocity of the synchronous particle, A_{ij} are constants and I_n are modified Bessel functions.

To describe the basic properties of the RFQ field, the first two terms of the expansion are sufficient, giving

$$V(r, \theta, z) = \frac{V_0}{2} \left[A_{01} r^2 \cos 2\theta + A_{10} I_0(kr) \cos kz\right]. \tag{B.4}$$

B.2 Quadrupole focusing and transverse motion

The electric field is calculated from the potential,

$$\mathbf{E} = -\boldsymbol{\nabla} U = -\boldsymbol{\nabla} V \sin(\omega t + \phi). \tag{B.5}$$

Solving for the two-term field function (Equation B.4) gives

$$E_r = -\frac{V_0}{2}\left[2A_{01} r \cos 2\theta + kA_{10} I_1(kr) \cos kz\right] \sin(\omega t + \phi), \tag{B.6}$$

$$E_\theta = V_0 A_{01} r \sin 2\theta \sin(\omega t + \phi), \tag{B.7}$$

$$E_z = \frac{V_0}{2} k A_{10} I_0(kr) \sin kz \sin(\omega t + \phi). \tag{B.8}$$

In cartesian coordinates,

$$\begin{aligned} x &= r\cos\theta, \\ y &= r\sin\theta, \\ \cos 2\theta &= \cos^2\theta - \sin^2\theta, \\ \therefore \quad r^2\cos 2\theta &= r^2\cos^2\theta - r^2\sin^2\theta = x^2 - y^2, \end{aligned}$$

which gives the two-term potential function as

$$U(r,\theta,z,t) = \frac{V_0}{2}\left[A_{01}(x^2 - y^2) + A_{10} I_0(kr)\cos kz\right], \tag{B.9}$$

so that the electric field in cartesian co-ordinates is

$$E_x = -\frac{V_0}{2}\left[2A_{01}x + kA_{10} I_1(kr)\frac{\partial r}{\partial x}\cos kz\right]\sin(\omega t + \phi), \tag{B.10}$$

$$E_y = \frac{V_0}{2}\left[2A_{01}y - kA_{10} I_1(kr)\frac{\partial r}{\partial y}\cos kz\right]\sin(\omega t + \phi). \tag{B.11}$$

To analyse the motion in the x-direction of a particle with mass m and charge q, the displacement is assumed to be small, such that $I_1(kr) \approx kr/2$. For the synchronous particle,

$$kz = \frac{2\pi}{\beta\lambda} z = \omega\frac{z}{v} = \omega t, \tag{B.12}$$

and, using the identities $\partial r/\partial x = x/r$ and $2\cos\omega t \sin(\omega t + \phi) = \sin\phi + \sin(2\omega t + \phi)$,

$$\frac{\partial^2 x}{\partial t^2} - \frac{F_x}{m} = 0, \tag{B.13}$$

$$\frac{\partial^2 x}{\partial t^2} - \frac{q}{m}E_x = 0, \tag{B.14}$$

$$\frac{\partial^2 x}{\partial t^2} + \left[\frac{qV_0A_{01}}{m} x \sin(\omega t + \phi) + \frac{qkV_0A_{10}}{2m}\frac{kr}{2}\frac{x}{r}\cos\omega t \sin(\omega t + \phi)\right] = 0, \tag{B.15}$$

$$\frac{\partial^2 x}{\partial t^2} + \left[\frac{qV_0 A_{01}}{m}\sin(\omega t + \phi) + \frac{qk^2 V_0 A_{10}}{8m}\left[\sin\phi + \sin(2\omega t + \phi)\right]\right] x = 0. \tag{B.16}$$

Integrating the term at twice the resonating frequency across each cell in the RFQ will give zero if x is approximately constant relative to longitudinal motion, so the equation of motion becomes

$$\frac{\partial^2 x}{\partial t^2} + \left[\frac{qV_0 A_{01}}{m}\sin(\omega t + \phi) + \frac{qk^2 V_0 A_{10}}{8m}\sin\phi\right] x = 0, \tag{B.17}$$

which is in fact the Mathieu equation for dynamics in periodic structures,

$$\frac{\partial^2 x}{\partial \tau^2} + \left[B\sin(2\pi\tau) + \Delta_{\mathrm{RF}}\right] x = 0, \tag{B.18}$$

where

$$2\pi\tau = \omega t + \phi, \tag{B.19}$$

$$B = \frac{4\pi^2 q A_{01} V_0}{m\omega^2} = \frac{\lambda^2 q A_{01} V_0}{mc^2}, \tag{B.20}$$

$$\text{and } \Delta_{\mathrm{RF}} = \frac{4\pi^2 qk^2 A_{10} V_0 \sin\phi}{8m\omega^2} = \frac{\pi^2 q A_{10} V_0 \sin\phi}{2mc^2\beta^2}. \tag{B.21}$$

The solution of the Mathieu equation (Equation B.18) is

$$x = C\sin\sigma_{0t}\tau\left[1 + \varepsilon\sin 2\pi\tau\right], \tag{B.22}$$

where σ_{0t} is the zero current betatron phase advance per period,

$$\sigma_{0t} = \sqrt{\frac{B^2}{8\pi^2} + \Delta_{\mathrm{RF}}}, \tag{B.23}$$

and the second sinusoidal term is the ‘flutter factor’ describing a variation at the radio frequency with amplitude $\varepsilon = B^2/4\pi^2$.

Similar derivations for the y-direction show that the quadrupole field successfully contains the beam in both transverse directions.

B.3 Acceleration and longitudinal motion

On the vane tip at a fixed time,

$$V(a,0,0) = V(ma,0,\beta\lambda/2) = \frac{V_0}{2}, \tag{B.24}$$

where $(a,0,0)$ and $(ma,0,\beta\lambda/2)$ are two fixed points (extrema, in fact) in a single acceleration cell (see Figure 6.3).

This allows us to solve the two-term potential function (Equation B.4) for A_{10} and A_{01},

$$V(a,0,0) = \frac{V_0}{2}\left[A_{01}a^2 + A_{10}I_0(ka)\right] = \frac{V_0}{2}, \tag{B.25}$$

$$A_{01}a^2 + A_{10}I_0(ka) = 1, \tag{B.26}$$

$$V(ma,0,\beta\lambda/2) = \frac{V_0}{2}\left[A_{01}m^2a^2 + A_{10}I_0(kma)\cos(k\beta\lambda/2)\right] = \frac{V_0}{2}, \tag{B.27}$$

$$A_{01}m^2a^2 + A_{10}I_0(kma)\cos(k\beta\lambda/2) = 1, \tag{B.28}$$

$$A_{01}m^2a^2 - A_{10}I_0(kma) = 1, \tag{B.29}$$

as $\cos(k\beta\lambda/2) = \cos(2\pi/\beta\lambda \times \beta\lambda/2) = \cos(\pi) = -1$.

Taking (B.26), multiplying by m^2 and subtracting (B.29) gives

$$A_{10}\left[m^2I_0(ka) + I_0(kma)\right] = m^2 - 1, \tag{B.30}$$

$$A_{10} = \frac{m^2-1}{m^2I_0(ka) + I_0(kma)}. \tag{B.31}$$

Substituting into (B.26) gives

$$A_{01} = \frac{1}{a^2}\left[1 - A_{10}I_0(ka)\right], \tag{B.32}$$

$$= \frac{1}{a^2}\left[\frac{m^2I_0(ka) + I_0(kma) - m^2I_0(ka) + I_0(ka)}{m^2I_0(ka) + I_0(kma)}\right], \tag{B.33}$$

$$= \frac{1}{a^2}\left[\frac{I_0(ka) + I_0(kma)}{m^2I_0(ka) + I_0(kma)}\right]. \tag{B.34}$$

To simplify the analyis, further constants χ and A are introduced, with $A_{01} = \chi/a^2$ and $A = A_{10}$, such that

$$\chi = \frac{I_0(ka) + I_0(kma)}{m^2I_0(ka) + I_0(kma)}, \tag{B.35}$$

$$A = \frac{m^2-1}{m^2I_0(ka) + I_0(kma)}, \tag{B.36}$$

$$\tag{B.37}$$

giving

$$U(r,\theta,z,t) = \frac{V_0}{2}\left[\chi\left(\frac{r^2}{a^2}\right)\cos 2\theta + AI_0(kr)\cos kz\right]\sin(\omega t + \phi), \tag{B.38}$$

so the longitudinal field E_z (Equation B.8) becomes

$$E_z = \frac{V_0}{2} kAI_0(kr) \sin kz \sin(\omega t + \phi). \tag{B.39}$$

To find the acceleration of a particle through this field, we find the energy gain for a particle with arbitrary velocity β over a cell (half a period of modulation, from $r = a$ to $r = ma$) with length l and synchronous velocity β_s, by evaluating the work done by the field ΔW and neglecting the transverse motion, such that

$$\Delta W = q \int_0^l E_z \, \mathrm{d}z, \tag{B.40}$$

$$= \frac{qk_\mathrm{s}AV_0}{2} \int_0^l \sin k_\mathrm{s}z \sin(kz + \phi) \, \mathrm{d}z, \tag{B.41}$$

where $k_\mathrm{s} = 2\pi/\beta_\mathrm{s}\lambda$, $k = 2\pi/\beta\lambda$ and $l = \beta_\mathrm{s}\lambda/2$.

For the synchronous particle, $\beta = \beta_\mathrm{s}, k = k_\mathrm{s}$, and

$$\Delta W_\mathrm{s} = \frac{qAV_0\pi \cos\phi_\mathrm{s}}{4}, \tag{B.42}$$

which is commonly written as

$$\Delta W_\mathrm{s} = qE_0Tl\cos\phi_\mathrm{s}, \tag{B.43}$$

where $E_0 = 2AV_0/\beta_\mathrm{s}\lambda$ and $T = \pi/4$. This is the energy gain for the synchronous particle. The real particles in the accelerator move in harmonic motion about the synchronous particle. This can be seen by evaluating the average rate of change of energy and phase,

$$\frac{\partial(W - W_\mathrm{s})}{\partial z} = qE_0T(\cos\phi - \cos\phi_\mathrm{s}), \tag{B.44}$$

$$\frac{\partial(\phi - \phi_\mathrm{s})}{\partial z} = -\frac{2\pi(W - W_\mathrm{s})}{mc^2\beta_\mathrm{s}\lambda^2}. \tag{B.45}$$

Linear approximations are made for small angle phase oscillations, and the equation of motion about the synchronous particle becomes

$$\frac{\partial}{\partial\tau}\left(\beta^2\frac{\partial\Delta\phi}{\partial\tau}\right) + \frac{\pi^2qAV_0\sin(-\phi)}{mc^2}\Delta\phi = 0. \tag{B.46}$$

The solution of this differential equation is harmonic motion with zero current longitudinal phase advance per period of

$$\sigma_{0l} = \sqrt{\frac{\pi^2qAV_0\sin(-\phi)}{mc^2\beta_\mathrm{s}^2}}. \tag{B.47}$$

B.4 Modulation design

The modulation design is described in § 6.3. The sections below give additional mathematical details, following references [63] and [64].

Shaper

The acceleration strength is increased linearly from zero at the end of the matching section to a final value A_{sh} at the end of the shaper,

$$A = A_{\mathrm{sh}} \frac{z}{L_{\mathrm{sh}}}, \tag{B.48}$$

where L_{sh} is the length of the shaper. The synchronous phase is also made to increase linearly from the initial value ϕ_{i} to the value at the end of the shaper, ϕ_{sh},

$$\phi_{\mathrm{s}} = \phi_{\mathrm{i}} + \Delta\phi \frac{z}{L_{\mathrm{sh}}}, \tag{B.49}$$

where $\Delta\phi = \phi_{\mathrm{sh}} - \phi_{\mathrm{i}}$.

Gentle buncher

From Equation B.47, keeping the small angle frequency constant requires

$$\frac{AV_o \sin(-\phi)}{\beta_{\mathrm{s}}} = \text{constant}. \tag{B.50}$$

Constant spatial length of the separatrix ψ implies

$$\beta_{\mathrm{s}}\psi = \text{constant}, \tag{B.51}$$

where the phase length of the separatrix is given by

$$\tan\phi_{\mathrm{s}} = \frac{\sin\psi - \psi}{1 - \cos\psi}. \tag{B.52}$$

Constant transverse focusing strength requires (see Equation B.10, Equation B.11 and Equation B.35)

$$\frac{\chi}{a^2} = \text{constant}, \tag{B.53}$$

which is equivalent to a constant mean radius

$$r_0 = \frac{a + ma}{2} = \text{constant}. \tag{B.54}$$

C Program Code

This appendix sets out the structure of the program code used to automate the RFQ simulation process. The code itself is freely available under the GNU Public Licence—although commercial software packages are also required to run the simulations—and at the time of publication can be found as a community project at `https://launchpad.net/modelrfq`.

The scope of this discussion will be limited to the final working code, rather than describing the many iterations and different systems used over the course of the simulation development process. For example, electrostatic modelling was initially carried out in *CST EM Studio*, with code stored in macros written in *Visual Basic for Applications*, but this code will not be included here.

The *ModelRFQ* code described here was written jointly by the author and Dr Simon Jolly of Imperial College London.

C.1 Software packages

Four commercial software packages are required to make use of the *ModelRFQ* simulation code. To run the whole process, *Microsoft Windows* must be used, although the majority of the process can be run on *Mac OS X* or *Linux*. In addition, software capable of reading and writing *Microsoft Office Excel* spreadsheets is required for setting up the modulation parameters.

Autodesk Inventor This is a computer-aided design (CAD) package that produces the geometric model from the modulation parameters. It only runs on *Windows*. A free version is available to academic institutions, with limitations. *ModelRFQ* includes a number of linked CAD models containing *Visual Basic for Applications* (VBA) code that automatically updates the model from the modulation parameters spreadsheet.

Comsol Multiphysics This is a multi-physics solving engine that finds the electric field based on the CAD model. Discounts are available to academic institutions. *ModelRFQ* contains *Matlab* functions that automatically create and solve *Comsol* models in the background.

General Particle Tracer This is a particle tracking engine that simulations the motion of particles through the field map exported from *Comsol*. *ModelRFQ* contains *Matlab* functions that automatically set up and run *GPT* simulations in the background.

Matlab This is a data-handling mathematical package with its own built-in programming language. This is used to control the *ModelRFQ* process and to handle and process the data after the simulation.

C.2 Procedure

An end user seeking to model an RFQ will carry out the following procedure:

1. Edit the modulation parameter spreadsheet to include the modulation pattern for the particular RFQ to be modelled;
2. Edit the simulation parameters text file to set up the physical scenario;
3. Open the master CAD file and click to update all CAD files from the spreadsheet; and
4. Open *Maltab* and run the command `modelRfq()`.

Limitations of this process are discussed in Chapter 9 as possible future developments of the *ModelRFQ* project, particularly that there is currently no optimisation algorithm for the RFQ modulation parameters, so a starting set of parameters must be known and must be modified by the user for their particular application. The development of this optimisation algorithm is outside of the scope of this thesis. Also, a more complete solution would interface *Inventor* and *Matlab* directly, eliminating the need for step 3 above. Finally, combining steps 1 and 2 into a single input file would make the process more coherent for the end user.

The following sections set out the procedures carried out by the user and the code, and how these simulate the particle dynamics and report the results to the user.

C.2.1 Modulation parameters

A spreadsheet file contains the modulation parameters for each cell of the RFQ.[1] A cell is one period of oscillation. The *FETS* RFQ design contains 307 cells, but *ModelRFQ* can handle up to 1 000 cells.

The spreadsheet has a number of tabs. The first sheet contains a one-dimensional array of parameter values in a very specific order, as this is how the parameters are read into *Inventor* by the VBA script. The data in this sheet is populated from the later sheets, which are edited by the user. The second sheet contains the cell-by-cell modulation parameters that define the shape of the RFQ. These are laid out in such a way that the output of *RFQSIM* or similar field expansion code can be simply pasted in to quickly create a CAD model. A series of operations are carried out on these parameters to produce the values required for *Inventor*. This sheet also includes options to scale the lengths, which are used in this thesis to convert the *FETS* modulation parameters to values appropriate for *PAMELA*. There are additional sheets that calculate the Kilpatrick factor to check for possible electrical breakdown, and charts that display the modulation parameters pictorially.

C.2.2 Simulation parameters

The parameters that are specific to a particular model are entered into a *Matlab* text file.[2] This file is stored in the model directory for each simulation and contains details such as the particle species, charge, mass and initial energy, and the input beam parameters. The eventual aim of the

---

[1] File `CAD/RFQParameters.xls`

[2] File `Matlab/getModelParameters.m`

development process is to include these details in the modulation parameters spreadsheet, so only a single input file is required to describe a complete RFQ simulation.

The majority of *ModelRFQ* is run via *Matlab*. For each stage in the process, the local working directory is interrogated for model-specific files and parameters, and if not found, the default files and parameters are loaded instead. Files that define a particular RFQ model are stored in the model directory so that the process can be repeated in the future if required.

C.2.3 CAD model creation

The process of constructing a three-dimensional model from the one-dimensional modulation parameters is described in § 7.2.2. The code for carrying out this process is written in VBA and extracts the parameters from the spreadsheet, applying these to the CAD models automatically to produce the full geometry of the RFQ. The user needs only to open the master file and click to update, and the code constructs the RFQ models. These models are saved in *Inventor* format and read directly by *Comsol*.

C.2.4 Field map creation

Once the user starts the `modelRfq()` function, *Matlab* loads the simulations parameters and starts the simulation process. The first step is to load *Comsol* as a server application in the background and create an electromagnetic model. This is handled by a separate *Matlab* function that steps through all the stages of model creation and solving.[3] The function loads in the geometry from the CAD model and then selects a single cell for solving and a number of cells on either side to produce the correct boundary conditions. Once the geometry is defined for the cell being solved, *Matlab* takes the simulation parameters and defines the electric potential conditions for solving to produce the electric field. The function next specifies the required mesh density and solver settings for *Comsol*, then runs the solver and extracts the electric field map. The field map is exported as a *Matlab* data file, then converted to a format that *GPT* can use for particle tracking.[4]

C.2.5 Particle tracking

Once the *Comsol* process is complete, *Matlab* calls the *GPT* executable file to run the particle tracking simulation.[5] A generic input file takes the simulation parameters and the field map to define a simulation for a particular RFQ. The basis of the particle tracking is as described in § 7.2.5. *GPT* produces a time- and position-based data file and a trajectory-based data file,[6] which are then loaded into arrays in *Matlab*.

---

[3] File `Matlab/ComsolInterface/buildComsolModel.m`

[4] File `RFQFieldMap.gdf`

[5] File `Matlab/GptInterface/runGptComman.m`

[6] Files `GPT/RFQParticles.gdf` and `GPT/RFQTrajectories.gdf`

C.2.6 Postprocessing

ModelRFQ runs a number of *Matlab* functions that manipulate the particle data arrays to tag the particles that are correctly accelerated, and analyse the tracks of all the particles. These output the transmission and final and emittance results, and produce energy and tracking plots. There is also the option to produce animations of the real- and phase-space particle distributions at each time-step of the tracking simulation, which can be invaluable for the process of optimising the RFQ parameters to find where particles are lost and where the modulations should be modified to produce better transmissions.

C.3 Code objects

This section lists the various objects in the *ModelRFQ* distribution and their functions, as at the time of writing. As the code is still under development, these details may change with time. The distribution contains model files, functions and scripts, data files and batch files.

C.3.1 Models

The `CAD` folder contains the modulation parameters spreadsheet, `RFQParameters.xls`, and a number of `.ipt` and `.iam` files, which are part files and assembly files in *Autodesk Inventor*, respectively. The full assembly is called *RFQFull.iam* and is made up of a number of part files, which are themselves based on smaller assemblies that are also based on smaller part files. The part files all contain links to the spreadsheet, and opening the full assembly and updating all links pulls in all the modulation data and produces a final CAD model. The VBA code is included in the model files. For Mac or Linux systems, the CAD model needs to be exported as a `.sat` file before importing into *Comsol*.

The `Comsol` folder contains the electrostatic for a section of the RFQ, called `RFQQuadrant.mph`. This model is normally built by *Matlab* functions, but a template is included in the *ModelRFQ* distribution as an alternative to building automatically. The model contains a quadrant of a single cell, surrounded by other cells for boundary conditions, and the full field map is built in *Matlab* from the individual cell quadrant field maps.

The `GPT` folder contains the `RFQ.in` input file, which specifies the static parameters of the *GPT* simulation. The dynamic parameters are set by *Matlab*.

C.3.2 Functions

The `Matlab` folder contains a number of *Matlab* functions, which carry out the process of modelling the RFQ.

modelRfq This is the master function, called by the command `modelRfq()`, which forms the shape of the process and calls sub-routines to carry out the simulation tasks.

getModelParameters This function will be different for different RFQ models, and is saved to the local working folder so that the simulation can be repeated in the future. This file contains everything that is particular to one RFQ design, and the rest of the code is generic.

ComsolInterface/buildComsolModel This is the master function for the *Comsol* modelling section of the simulation, which forms the shape of this process, looping through a number of steps carried out by sub-routines for each cell and saving the field map.

ComsolInterface/buildCell This function is called by `buildComsolModel` for each cell in the RFQ. It calls a number of sub-routines that create and solve the *Comsol* model for the current cell.

ComsolInterface/createGeometry This function imports the full RFQ CAD model and cuts out the quadrant of the current cell and its boundary cells.

ComsolInterface/createMesh This function creates the mesh of elements that define the points on which the solver will calculate the field.

ComsolInterface/createParameters The *Comsol* model uses parameter values to select the current cell from the full CAD model. This function passes the coordinates of the current cell in the loop, among other parameters used in the model.

ComsolInterface/fillFieldMapFromQuadrant This function takes the solution from *Comsol* and reflects it in two axes to produce a field map for the whole cell.

ComsolInterface/findVaneEnd This function interrogates the *Comsol* geometry to find the model objects of each of the vanes so that *Matlab* can interact with the vanes.

ComsolInterface/findVaneObjects This function interrogates the *Comsol* geometry to find all the model objects for a particular vane so that *Matlab* can interact with the vanes.

ComsolInterface/getCellParameters This function returns the parameters for the current cell from a list loaded in memory of all the parameters for all the cells. These parameters are required to set up the *Comsol* model and to manipulate the resultant field map for the current cell.

ComsolInterface/getFieldMap This function extracts the solved field map data from *Comsol* at specific co-ordinates, such that accuracy of solution and efficiency of processing power are both maximised.

ComsolInterface/getModulationParameters This function reads the modulation parameters from the spreadsheet and loads them into memory.

ComsolInterface/initialiseModel This function is the first to be called in setting up a *Comsol* model, and creates the empty model file into which the CAD geometry is imported.

ComsolInterface/loadFieldMap This function loads all of the single-cell field maps and combines them into a full coherent field map for the length of the RFQ.

ComsolInterface/meshCell This function runs the commands to build the solver mesh for the current cell, and also tests the mesh for errors and refines it if necessary.

ComsolInterface/outputFieldMap This function saves the current cell mesh to a *Matlab* data file, ready to be read in by `loadFieldMap` or to be saved for future reference. The file format is both compact and efficient, as single cell maps can be extracted easily from the file, or the whole field map loaded.

ComsolInterface/setSelections Selections in *Comsol* are used to apply attributes and boundary conditions to geometry objects. This function ensures that the correct objects are selected.

ComsolInterface/setupModel This function calls a number of sub-routines to define the *Comsol* model, starting with `initialiseModel`, so that the cell-by-cell process can start.

ComsolInterface/setupPlots This function defines the plots that visualise the final field and potential data. The *Comsol* model is saved in the working directory, and the plots are available for the user to inspect at the end of the *ModelRFQ* process.

ComsolInterface/setupSolver This function sets the attributes and parameters of the solver, which translates the geometry and physical conditions into a field map for particle tracking.

ComsolInterface/specifyAirVolumes This function sets the parameters of the model that relate to the physical properties of the vacuum in the RFQ.

ComsolInterface/specifyTerminals This function sets the parameters of the model that relate to the electrical conditions on the vanes in the RFQ.

GptInterface/importGdf This function reads data from a *GPT* binary `.gdf` file and loads the data into memory for post-processing.

GptInterface/readGdf This function carries out the binary read and translate process for a `.gdf` file.

GptInterface/readGdfHeader This function interrogates a `.gdf` file to find the file structure, and therefore shapes the action of `readGdf`.

GptInterface/runGptCommand This function calls the *GPT* engine and runs a given command. This is used by *ModelRFQ* to run the particle tracking and to convert field maps and particle data.

TwitterInterface/twit The *Twitter* interface functions are provided free of charge by the *Matlab* programming community. Copyright details are included in the *ModelRFQ* distribution. This function sends a message to a given *Twitter* account for notification and logging purposes.

TwitterInterface/twitpref This function is used to enter the user's *Twitter* credentials to enable reporting via the *Twitter* service.

Functions/buildMovies This function creates animations of particle motion through real- and phase-space for analysis of particle dynamics.

Functions/calculateEmittance This function calculates the emittance of a bunch by statistical analysis of the ensemble of particles.

Functions/combineFieldMaps This utility function can be used to combine separate field map text files into a single text file.

Functions/convertSecondsToText This utility function converts numerical seconds into descriptive text containing days, hours, minutes and seconds. It is used throughout *ModelRFQ* to report on elapsed time for progress checking and benchmarking.

Functions/currentTime This utility function returns the current time as descriptive text containing days, hours, minutes and seconds. It is used throughout *ModelRFQ* to report on current progress.

Functions/enhanceFigure This utility function formats a *Matlab* figure for legibility and file size optimisation before saving as an image file.

Functions/findFile This utility function finds a file in either the local working folder, its subfolders, or a master folder. This is used by *ModelRFQ* to keep master copies of important data files but to give priority to local versions so that different RFQ parameters can easily be specified by placing the relevant files in the working folder. For example, a working folder could contain only a modified `getModelParameters` but use the default field map, which would allow the tracking of different particles through the same RFQ field without duplicating large data files.

Functions/getComputerName This utility function returns the hostname of the current computer. This is used by *ModelRFQ* to specify different master folders on different installations.

Functions/getComsolPort This utility returns an available port for *Comsol* to run as a server, allowing multiple servers to run concurrently.

Functions/logMessage This utility function sends messages to the user via screen displays, log files and *Twitter* notifications. Different levels of notifications can be sent, and different verbosity settings can be defined for each reporting modality, as the user prefers. For example, notifications of starting and completion only could be sent to *Twitter* to prompt the user to action, while the screen displays the progress towards completion and the log file contains all warnings, errors and detailed information of each step of the process. This function is used extensively throughout *ModelRFQ*.

Functions/makeFolder This utility function creates a subfolder if it does not already exist.

Functions/plotEnergies This function plots the final energies of the tracked particles at the output of the RFQ as a histogram. This function was used to produce the histograms presented in this thesis.

Functions/plotTrajectories This function plots the trajectories and final phase space of the tracked particles. This function was used to produce the trajectory plots presented in this thesis.

Functions/saveFigure This utility function saves a *Matlab* function as an image file. It is used by both *plotEnergies* and `PlotTrajectories`.

Functions/tagColours This function tags particle tracks with a colour based on the position in the RFQ they reached.

Functions/tagLosses This function classifies particle tracks based on the position in the RFQ at which they were lost, ready for colour tagging by `tagColours` for `plotTrajectories`.

Functions/writeResults This function outputs the simulation results to a log file for easy comparison between models.

C.3.3 Data files

GPT/RFQFieldMap This binary data file contains the field map for the RFQ being modelled. The master folders contain the *FETS* RFQ field map, which can be used as part of the scaling process, or to verify the correct running of the code. In the process of running *ModelRFQ*, this data file is generated anew in the working directory by solving the *Comsol* model of the CAD geometry.

GPT/RFQParticles This binary data file contains the dynamics of the simulated particles. This is produced anew by *ModelRFQ*, although default files can be used for verification purposes.

GPT/RFQTrajectories This binary data file contains the trajectories of each of the simulated particles. This is produced anew by *ModelRFQ*, although default files can be used for verification purposes.

Comsol/RFQFieldMap This *Matlab* data file is created at the end of the *Comsol* modelling process to contain the field map. The next phase of the simulation converts this file via a text format into binary data for tracking simulations in *GPT*. No default versions are included as all the data is contained in the `.gdf` files.

C.3.4 Batch files

Matlab/Functions/runBatch This function loops through all subfolders in a working folder and runs `modelRfq()` in each one, and finally collates and compares the results in a log file. A special folder named `Include` can be used to include common files for each simulation. For example, a set of folders could contain different scaling factors, but the particle definition would be common to all folders.

Batch/runRfqBatch This *Windows* batch file carries out the same function as *runBatch*, but it closes and opens *Matlab* between each run. This can be required to conserve computer memory and avoid instabilities in lower-memory systems.

Batch/modelRfqRfqInFolder This *Windows* batch file runs `modelRfq()` in the given folder. It is called by a loop in `runRfqBatch`.

Batch/setRfqPath This *Windows* batch file ensures that the *ModelRFQ* batch programs are registered with the *Windows* operating system.

REFERENCES

[1] WHO, *Radiotherapy in Cancer Management*, Published on behalf of the World Health Organisation by Chapman and Hall Medical, 1997.

[2] G G Steel, *Basic Clinical Radiobiology (3rd Edition)*, Arnold, 2002.

[3] C K Bomford and I H Kunkler, *Walter and Miller's Textbook of Radiotherapy (6th Edition)*, Churchill Livingstone, 2003.

[4] M Haas *et al.*, *Radiation Therapy: A Guide to Patient Care*, Mosby Elsevier, 2007.

[5] E Halperin, C Perez, and L Brady, *Perez and Brady's Principles and Practice of Radiation Oncology (5th Edition)*, Wolters Kluwer Health, 2008.

[6] R R Wilson, "Radiological use of fast protons", *Radiology*, 47:487–491, 1946.

[7] H Bethe, "Zur Theorie des Durchgangs schneller Korpuskularstrahlen durch Materie", *Annalen der Physik*, 397(3):325–400, 1930.

[8] F Bloch, "Zur Bremsung rasch bewegter Teilchen beim Durchgang durch Materie", *Annalen der Physik*, 408(3):285–320, 1933.

[9] M Chalmers, "How particles can be therapeutic", *Physics World*, August, 2003.

[10] A Lennox, "Accelerators for cancer therapy", *Radiation Physics and Chemistry*, 61:223–226, 2001.

[11] B Jones, "The case for particle therapy", *British Journal of Radiology*, 2006.

[12] B Jones and I Rosenberg, "Particle Therapy Co-operative Oncology Group (PTCOG 40) meeting, Institute Curie 2004", *The British Journal of Radiology*, 78(926):99, 2005.

[13] R Miralbell *et al.*, "Potential reduction of the incidence of radiation-induced second cancers by using proton beams in the treatment of pediatric tumors", *International Journal of Radiation Oncology*, 2002.

[14] B Jones, "The potential clinical advantages of charged particle radiotherapy using protons or light ions", *Clinical Oncology*, 2008.

[15] B Jones, R Dale, and A Cárabe-Fernández, "Charged particle therapy for cancer: The inheritance of the Cavendish scientists?", *Applied Radiation and Isotopes*, 2009.

[16] M Goitein and M Jermann, "The relative costs of proton and x-ray radiation therapy", *Clinical Oncology*, 2003.

[17] Particle Therapy Co-Operative Group (PTCOG), "Particle therapy facilities", retrieved July 2011, `http://ptcog.web.psi.ch/ptcentres.html`.

[18] J M Lagniel, "Status of the hadron-therapy projects in Europe", PAC'07, Albuquerque, New Mexico, USA, 2007, MOZBC02, pp. 127–131.

[19] E Bressi, M Pullia, and C Biscari, "Status report on the Centro Nazionale di Adroterapia Oncologica (CNAO)", PAC'09, Vancouver, Canada, 2009, TU6PFP005, pp. 1297–1299.

[20] University College London Hospitals, "Proton beam therapy", 2010, `http://www.uclh.nhs.uk/aboutus/newdev/pages/pbt.aspx`.

[21] S Jolly, Imperial College London, personal communication, 2011.

[22] Daniel Brandt, CERN, personal communication, 2011.

[23] J Pozimski, Imperial College London, personal communication, 2011.

[24] E Wilson, *An Introduction to Particle Accelerators*, Oxford University Press, 2001.

[25] K Wille, *The Physics of Particle Accelerators: An Introduction*, Oxford University Press, 2000.

[26] S Humphries, *Charged Particle Beams*, Wiley, 1990.

[27] R Tolman, *The Principles of Statistical Mechanics*, Oxford Clarendon Press, 1938.

[28] H Goldstein, C Poole, and J Safko, *Classical Mechanics*, Addison Wesley, 2002.

[29] F Sacherer, "RMS envelope equations with space charge", *Nuclear Science*, 1971.

[30] A W Chao and M Tigner, *Handbook of Accelerator Physics and Engineering, Third printing*, World Scientific, 2006.

[31] E D Courant and H S Snyder, "Theory of the alternating-gradient synchrotron", *Annals of Physics*, 1958.

[32] S Humphries, *Principles of Charged Particle Acceleration*, John Wiley and Sons, 1986.

[33] J LeDuff, "Phase stability", *CERN Accelerator School 2003, Brunnen, Switzerland*, 2003.

[34] Wolfram MathWorld, "Separatrix", retrieved July 2011, `http://mathworld.wolfram.com/Separatrix.html`.

[35] A Geisler *et al.*, "Superconducting 250 MeV proton cyclotron for cancer treatment", *IEEE Transactions on Applied Superconductivity*, 15(2):1342–1345, 2005.

[36] M O Oliphant, "The acceleration of particles to very high energies". Classified memo submitted to DSIR, 1943. University of Birmingham Archive.

[37] J Livingood, *Principles of Cyclic Particle Accelerators*, D Van Nostrand Company Inc., 1962.

[38] H Eickhoff *et al.*, "The proposed dedicated ion beam facility for cancer therapy at the clinic in Heidelberg", EPAC'00, Vienna, Austria, 2000, WEP3A13, pp. 2512–2514.

[39] L Thomas, "The paths of ions in the cyclotron I—orbits in the magnetic field", *Physical Review*, 54(8): 580–588, 1938.

[40] K Symon, "The FFAG synchrotron—Mark I", *Midwestern Universities Research Assn. report MURA-KRS-6*, 1954.

[41] Shinji Machida, "Scaling fixed-field alternating gradient accelerators with a small orbit excursion", *Phys. Rev. Lett.*, 103(16):164801, 2009.

[42] C Johnstone, W Wan, and A Garren, "Fixed field circular accelerator designs", PAC'99, New York, USA, 1999, THP50, pp. 3068–3070.

[43] S Sheehy *et al.*, "PAMELA: Lattice solution for a medical C6+ therapy facility", IPAC'10, Kyoto, Japan, 2010, MOPEA022.

[44] K Peach *et al.*, *PAMELA Design Report*, unpublished, 2011.

[45] K Peach *et al.*, "PAMELA overview: Design goals and principles", PAC'09, Vancouver, Canada, 2009, TH4GAC03.

[46] S Machida *et al.*, *Acceleration in the linear non-scaling fixed field alternating gradient accelerator EMMA*, unpublished, 2011.

[47] G Morgan, "Non-scaling FFAG: Design and development", *MPhys Project Report of Oxford University*, 2007.

[48] B Gottschalk *et al.*, "Multiple coulomb scattering of 160 mev protons", *Nuclear Instruments and Methods B*, 74(4):467–490, 1993.

[49] M Muramatsu *et al.*, "The compact electron cyclotron resonance ion source KeiGM for the carbon ion therapy facility at Gunma University", *Review of Scientific Instruments*, 81(2):02A327, 2010.

[50] Pantechnik, "Supernanogun guaranteed intensities". Product website, retrieved 13 September 2011, `http://www.pantechnik.fr/joomla/index.php?option=com_content&task=view&id=14&Itemid=65&limit=1&limitstart=1`.

[51] IBA SA, "Cyclone 30". Product brochure, 2011, `http://www.iba-cyclotron-solutions.com/products-cyclo/cyclone-30/`.

[52] B Schlitt and U Ratzinger, "Design of a carbon injector for a medical accelerator complex", EPAC'98, Stockholm, Sweden, 1998, WEP08C, pp. 2377–2379.

[53] A Bechtold *et al.*, "Development of an RFQ-injector for a therapy-synchrotron", EPAC'00, Vienna, Austria, 2000, WEP3B05, pp. 2500–2502.

[54] M Maier *et al.*, "Commissioning of the linac for the Heidelberg Heavy Ion Cancer Therapy Centre (HIT)", PAC'07, Albuquerque, New Mexico, USA, 2007, THPMN014, pp. 2734–2736.

[55] D Auria, G Rossi, and CS Trieste, "A 100 MeV multitank drift tube linac for proton acceleration", PAC'97, Vancouver, Canada, 1997, 5W030, pp. 1180–1181.

[56] U Ratzinger, "Effiziente Hochfrequenz-Linearbeschleuniger für leichte und schwere Ionen". Post-doctoral thesis, 1998. Johann Wolfgang Goethe University, Frankfurt.

[57] Thomas P Wangler, *RF linear accelerators*, Wiley, 2008.

[58] N Hayashizaki and T Hattori, "IH linac with higher order modes", EPAC'08, Genoa, Italy, 2008, THPP022, pp. 3419–3421.

[59] M Aslaninejad *et al.*, "Injection of proton and carbon 6+ into the non-scaling FFAG", IPAC'10, Kyoto, Japan, 2010, THPEB033.

[60] K Tinschert, R Iannucci, and R Lang, "Electron cyclotron resonance ion sources in use for heavy ion cancer therapy", *Review of Scientific Instruments*, 79:02C505, 2008.

[61] M Muramatsu *et al.*, "Compact ECR ion source with permanent magnets for carbon therapy", *Review of Scientific Instruments*, 75:1925–1927, 2004.

[62] M Muramatsu *et al.*, "Development of the compact electron cyclotron resonance ion source for heavy-ion therapy", *Review of Scientific Instruments*, 71(2):984–986, 2000.

[63] K R Crandall, R H Stokes, and T P Wangler, "RF quadrupole beam dynamics design studies", LAC'79, Montauk, NY, 1979, 790927-17.

[64] I M Kapchinskij and V A Teplyakov, "Linear ion accelerator with spatially homogeneous strong focusing", *Pribory i Teknika Éksperimenta*, 2:19–22, 1969.

[65] R A Jameson, "Beam-intensity limitations in linear accelerators", *IEEE Transactions on Nuclear Science*, 28(3):2408–2412, 1981.

[66] R A Jameson, “Equipartitioning in linear accelerators”, LINAC’81, Sante Fe, NM, USA, 1981, LA-UR-81-3073.

[67] R A Jameson, “Self-consistent beam halo studies & halo diagnostic development in a continuous linear focusing channel”, US-CERN-Japan Topical Course on Accelerator Physics and Technology, 1994, LA-UR-94-3753.

[68] R A Jameson, “Beam losses and beam halos in accelerators for new energy sources”, *Fusion engineering and design*, 32:149–157, 1996.

[69] A Kurup and A Letchford, “Electromagnetic design of a radio frequency quadrupole for the Front End Test Stand at RAL”, EPAC’06, Edinburgh, Scotland, 2006, MOPCH116.

[70] Y Cheng *et al.*, “RFQ cold model RF measurements and waveguide-to-coaxial line transition design for the Front-End Test Stand at RAL”, PAC’07, Albuquerque, New Mexico, USA, 2007, TUPAS002.

[71] S Jolly *et al.*, “Detailed study of the RF properties of the FETS RFQ cold model”, EPAC’08, Genoa, Italy, 2008, THPP024.

[72] J Maus *et al.*, “RFQ particle dynamic simulation development”, PAC’09, Vancouver, Canada, 2009, TH5PFP058.

[73] J Maus, R A Jameson, and A Schempp, “PteqHI development and code comparing”, ICAP’09, San Francisco, USA, 2009, THPSC031.

[74] A Letchford and A Schempp, “A comparison of 4-rod and 4-vane RFQ fields”, EPAC’98, Stockholm, Sweden, 1998, THP11E, pp. 1204–1206.

[75] S B van der Geer and M J de Loos, *GPT User Manual 2.8.3*, Pulsar Physics, 2008, `http://www.pulsar.nl/gpt`.

[76] W H Press *et al.*, *Numerical Recipes: the Art of Scientific Computing*, Cambridge University Press, 2nd Edition, 1992.

[77] J Lawson, “Perveance and the Bennett pinch relation in partially-neutralized electron beams”, *International Journal of Electronics*, 5(2):146–151, 1958.

[78] W Kilpatrick, “Criterion for vacuum sparking designed to include both RF and DC”, *Review of Scientific Instruments*, 28:824–826, 1957.